Tropical Southeast Pacific Continent-Ocean-Atmosphere Linkages Since the Pliocene Inferred from Eolian Dust

Dissertation
zur Erlangung des Doktorgrades der Naturwissenschaften
am Fachbereich Geowissenschaften
der Universität Bremen

vorgelegt von Cornelia Saukel
Alfred-Wegener-Institut für Polar- und Meeresforschung
Columbusstraße, 27568 Bremerhaven

Bremen, Januar 2011

Gutachter:
Prof. Dr. Ralf Tiedemann
Prof. Dr. Dierk Hebbeln

The Present Is the Key to the Past Is the Key to the Future.
(E. L. Mathieson, GSA, 2002)

Front image taken from
http://130.166.124.2/world_atlas/3/files/3-1012-full.html; Dr. William Bowen, 2005

Meinen Eltern

Abstract

Paleo-changes in trade-wind strength play a key role in the process of Pliocene and Pleistocene climate reorganization in the tropical oceans. In the Southeast Pacific, knowledge about changes in southeast trade-wind strength is one of the missing links to understand paleo-changes in oceanography and productivity, and associated variations in thermocline depth and upwelling. The area has long been in focus of the paleoclimate studying community due to the warm Pliocene's similarities to modern El-Niño conditions that turned into a dominant La-Niña-like state during the Pleistocene ice ages.

Eolian dust is a valuable indicator of paleo-changes in atmospheric circulation and continental aridity. This thesis examines continent-ocean-atmosphere linkages in the tropical Southeast Pacific at selected time intervals during the Pliocene and Pleistocene epochs on the basis of eolian dust as preserved in marine sediments. The main objectives of this study are the reconstruction of changes in (1) southeast trade-wind strength and dust transport, and changes in (2) western South American continental aridity over time.

Terrigenous proxy records from Ocean Drilling Program (ODP) Leg 202, Sites 1237 and 1239 in the tropical East Pacific, are generated and studied. For the first time, a sediment record of the Southeast Pacific (ODP Site 1237) of the past 5 Ma is investigated for siliciclastic grain-size distributions and changes in geochemical composition to reconstruct southeast trade-wind variability. Previously published records from ODP Sites 846, 849, 1241, as well as several other sediment cores are included for further interpretations. In addition, a set of surface sediment samples from the East Pacific is investigated to reconstruct the modern spatial pattern of eolian-derived marine sediments as a prerequisit for the interpretation of paleo-dust records. These show that wind is the dominant transport agent of terrigenous matter and eolian material the dominant terrigenous sediment component west of the Peru-Chile Trench south of 5°S.

Wind strengths reconstructions reveal that there is a difference in timing of the development of the modern eastern equatorial Pacific cold tongue, the onset of stronger southeast trade winds and the mid-Pliocene intensification of the Northern Hemisphere Glaciation. Paleoceanographic studies reveal a thermocline shoaling in the eastern equatorial Pacific to have already commenced between 4.8 and 4.0 Ma related to a strengthening of the Atlantic Meridional Overturning Circulation that in turn was initiated by the closure of the Central American Seaway. The southeast trade winds, however, were only strong enough to control upwelling in the East

Pacific cold tongue area after ∼3.3 Ma, when the thermocline was at a stable shallow state. An abrupt switch to enhanced wind strength at ∼3.3 Ma is concurrent with Marine Isotope Stage M2. From ∼3.3 Ma onwards, wind strengths keep increasing gradually until 1.6 Ma. With the intensification of Northern Hemisphere Glaciation, the southeast trade winds start to control upwelling in the eastern equatorial cold tongue and thereby further decrease sea surface temperatures and allow productivity to increase. After ∼1.6 Ma, however, this relationship is no longer apparent.

During the intensification of Northern Hemisphere Glaciation (3.1 - 2.4 Ma), wind strength co-vary with dust accumulation rates. An end-member analysis of terrigenous grain-size distributions allows the identification of a fine and very fine eolian dust end member. The coarser dust end member varies with iron and titanium accumulation rates and with sea surface temperatures in the East Pacific cold tongue on glacial-interglacial cycles after 2.7 Ma. This indicates stronger southeast trade winds and drier continental conditions during cold periods, and less intense wind strength and more humid continental conditions during warm stages between 2.7 and 2.0 Ma. Long-term increases in southeast trade-wind strength from ∼2.7 - 2.5 and 2.2 - 2.0 Ma are associated with enhanced pole-to-equator temperature gradients during times of global climate cooling.

Late Quaternary variability in dust accumulation rates at ODP Site 1237 depicts the glacial-interglacial cyclicity of western South American climate change. Glacial dust fluxes are twice as high as interglacial fluxes, suggesting drier glacials and more humid interglacials during the past 500 ka. Grain-size distributions of the terrigenous sediment fraction, however, do not indicate any distinct changes in mean trade-wind speed or direction during the same time interval. An extension of the dust source area and enhanced gustiness as well as a northern shift of the Southeast Pacific atmospheric circulation system are responsible for a glacial two-fold increase in dust flux.
In agreement with results from ODP Site 1237, multiproxy reconstructions of equatorial ODP Site 1239 sediments for the past 500 ka display more humid conditions during interglacials than during glacials. Sea surface temperature gradients across the equatorial front suggest a glacial northern shift of the ITCZ.

The onset of hyper-aridity in South America between 4 and 3 Ma is related to a combination of global climate cooling and enhanced upwelling in the Humboldt Current system that is controlled by strengthening southeast trade winds after 3.3 Ma. Changes in ocean circulation and thermocline depth adjustments in the tropical East Pacific, however, happened at least 700 ka earlier. After ∼1.6 Ma, wind

strength decreased to a lower level but productivitiy and dust supply kept increasing at ODP Site 1237. A single valid chain of forcing mechanisms for changes in western South American climate during the past 5 Ma is therefore not apparent.

Kurzfassung

Die Passatwinde spielen eine Schlüsselrolle im Prozess Pliozäner und Pleistozäner Klimaveränderungen im tropischen Ozean. Das Verständnis der Veränderungen in den Windstärken des Südost-Passats ist von essentieller Bedeutung im Verstehen südostpazifischer Paläo-Ozeanographie, Paläo-Produktivität und damit verbundener Veränderungen in der Thermoklinentiefe und im Auftriebsgeschehen. Aufgrund von dort vorherrschenden El Niño-ähnlichen Bedingungen während des warmen Pliozäns, die in den Pleistozänen Eiszeiten in La Niña-ähnliche Zustände umschlugen, genießt der tropische Pazifik besondere Aufmerksamkeit im Studium globaler Paläoklima-Rekonstruktionen.

Veränderungen in der atmosphärischen Zirkulation und der kontinentalen Trockenheit auf geologischen Zeitskalen können anhand von Staubablagerungen rekonstruiert werden. Die vorliegende Arbeit basiert auf Untersuchungen von äolisch eingetragenen marinen Sedimenten und dient der Erforschung von klimatischen Kopplungen zwischen Kontinent, Ozean und Atmosphäre im tropischen Südostpazifik während ausgewählter Zeitintervalle im Pliozän und Pleistozän.

Die im Rahmen dieser Arbeit entstandenen Datensätze terrigener Klimaindikatoren (Proxies) wurden durch sedimentologische und geochemische Analysen von Sedimentmaterial aus Ocean Drilling Program (ODP) Leg 202 Sites 1237 und 1239 im tropischen Ostpazifik gewonnen. Die Proxy-Kurven von ODP Site 1237 reichen fünf Millionen Jahre in die Vergangenheit und stellen den ersten Datensatz dieser Länge zur Rekonstruktion der Südost-Passatwind-Variabilitäten im Pazifik dar. Bereits veröffentlichte Datensätze von ODP Sites 846, 849 und 1241, sowie von anderen Sedimentkernen aus dem Ostpazifik werden zur weiteren paläoklimatischen Interpretation von ODP Site 1237 hinzugezogen. Zusätzlich dient ein Probensatz von Oberflächensedimenten aus dem Ostpazifik als Referenzdatensatz hinsichtlich heutiger Staubeinträge in den Ozean und liegt den Interpretationen paläoklimatischer Bedingungen zu Grunde. Die Ergebnisse der Analysen spiegeln eine deutliche Staubeintragsfahne westlich des Peru-Chile-Tiefseegrabens und südlich von 5°S wider.

Die Rekonstruktion relativer Veränderungen in den Windstärken im Vergleich zu paläozeanographischen Temperaturdaten legt eine unterschiedliche Terminierung klimatischer Ereignisse offen, die zuvor in kausalen Zusammenhang gebracht wurden. So setzte eine Verflachung der Thermoklinentiefe im Ostpazifik bereits zwischen 4.8 und 4.0 Ma vor heute als Konsequenz der globalen Anpassung an die Verstärkung der Thermohalinen Zirkulation im Nordatlantik ein, die wiederum

durch die Schließung des Panama-Seeweges initiiert wurde. Die Südost-Passatwinde waren jedoch erst nach 3.3 Ma stark genug um den Auftrieb kalten, nährstoffreichen Wassers zu beeinflussen. Die abrupte Verstärkung der Windintensitäten fällt in das Marine Isotopenstadium M2. Ab diesem Zeitpunkt ist ein gradueller Anstieg der Windstärken bis 1.6 Ma vor heute in den Proxy-Kurven zu verzeichnen. Mit der Intensivierung der Nordhemisphären-Vereisung begannen die Südost-Passate das Auftriebsgeschehen in der äquatorialen Kaltwasserzunge zu kontrollieren, die damit verbundenen Oberflächenwasser-Temperaturen weiter zu reduzieren und eine Erhöhung der Produktivität zu ermöglichen. Anschließend ist dieser Zusammenhang in den Paläoklima-Daten nicht mehr zu erkennen.

Während der Nordhemisphären-Vereisung (3.1 - 2.4 Ma) verändern sich die Windstärken parallel zu den Staubakkumulationsraten. Eine Endmember-Analyse der terrigenen Korngrößenverteilungen ermöglichte die Bestimmung eines feinkörnigen und eines sehr feinkörnigen Staub-Endmembers. Nach 2.7 Ma variiert das gröbere Staub-Endmember auf Glazial-Interglazial-Zyklen parallel zu Eisen- und Titan-Akkumulationsraten sowie zu Oberflächenwasser-Temperaturen in der ostäquatorialen Kaltwasserzunge. Davon lassen sich stärkere Südost-Passatwinde und aridere Bedingungen im westlichen Südamerika während der Kältephasen ableiten, die geringeren Windstärken und feuchteren Bedingungen auf dem Kontinent während der Warmzeiten gegenüberstehen. Langzeitige Anstiege in den Windstärken der Südost-Passate zwischen $\sim$2.7 - 2.5 und 2.2 - 2.0 Ma stehen indessen im Zusammenhang mit erhöhten meridionalen Temperaturgradienten in Phasen globaler Abkühlung.

Spät-Quartäre Veränderungen der Staubakkumulationsraten an ODP Site 1237 repräsentieren die glazial-interglazialen Klimaschwankungen im westlichen Südamerika. Glaziale Staubflüsse sind doppelt so hoch wie interglaziale Staubeinträge und weisen auf generell trockene Kälte- und feuchte Wärmeperioden während der letzten 500 ka hin. Korngrößenverteilungen der terrigenen Sedimentfraktion zeigen im selben Zeitraum jedoch keine Veränderungen in Windgeschwindigkeit und/oder -richtung an. Die Verdopplung der Staubflüsse während der Glaziale ist stattdessen auf eine Ausbreitung der Staubquellgebiete, erhöhtes Auftreten von Staubstürmen und die Nordverschiebung des südostpazifischen atmosphärischen Zirkulationssystems zurück zu führen.
Übereinstimmend mit den Ergebnissen von ODP Site 1237 zeigen Multi-Proxy-Rekonstruktionen an Sedimentproben von ODP Site 1239 feuchtere Bedingungen während der Interglaziale als während der Glaziale. Gradienten in Oberflächenwasser-Temperaturen über die äquatoriale Front hinweg weisen ebenfalls auf eine glaziale Nordverschiebung der Innertropischen Konvergenzzone hin.

Das Einsetzen hyperarider Bedingungen im westlichen Südamerika zwischen 4 und 3 Ma wurde durch eine Kombination globaler Abkühlung und erhöhten Auftriebs im Humboldt-Strömungssystem entlang der Westküste Südamerikas bedingt. Der erhöhte Auftrieb wiederum ist ein Resultat der sich verstärkenden Südost-Passatwinde nach 3.3 Ma. Veränderungen in der Ozeanzirkulation und der Thermoklinentiefen-Anpassungen im tropischen Ostpazifik setzten jedoch ca. 700 ka früher ein. Nach $\sim$1.6 Ma schwächten die Passatwinde ab, während Produktivität und Staubeintrag weiter anstiegen. Die Mechanismen, welche den Veränderungen des Klimageschehens in Südamerika während der letzten 5 Millionen Jahre zu Grunde liegen, sind vielfältig und nicht anhand einer einzelnen Kausalkette zu erklären.

Acknowledgements

This study would not have been possible without the support of many people whom I would like to thank.
First of all I would like to thank my supervisor Prof. Dr. Ralf Tiedemann, who initiated the project of which this thesis is a part of. He helped me to arrange a research stay at the Lamont-Doherty Earth Observatory and supported my contributions to several international scientific meetings. I also want to thank Dr. Frank Lamy. Despite their busy schedules both offered great scientific support and had time for discussion, especially within the last year.
I thank Prof. Dr. Dierk Hebbeln, the Graduate Dean of GLOMAR, for valuable contributions during my thesis committee meetings and for his agreement to act as the second reviewer of this thesis.
Further, I would like to thank the other members of my thesis committee, Dr. Jan-Berend Stuut and Dr. Christoph Vogt. They gave great advice in the lab and concerning data processing issues, and provided important moral support. Thanks to Jan-Berend I could spend some productive days for discussion and writing at the NIOZ.
I thank Dr. Gisela Winckler for hosting me in the Geochemistry Department at the Lamont-Doherty Earth Observatory in Palisades, NY, for two months. I was offered enormous support by her and Prof. Jerry McManus in generating and discussing a new data set that turned out to be of great value for the interpretation of the dust records.
Dr. Daniela Schmidt hosted me at the University of Bristol twice and offered a great deal of scientific and moral support as well as last minute corrections. Thank you.
GLOMAR is thanked for offering a large schedule of scientific and soft skill education, the initiation of a thesis committee for each PhD student, and the opportunity to enlarge one's network. I especially thank Dr. Uta Brathauer for her support.
Dr. Silke Steph, Dr. Arne Sturm, and Dr. Anna Wegner were always open for questions concerning data from the SE Pacific and dust, respectively, for which I want to thank them.
The IODP core repository staff at the MARUM in Bremen and at the IODP head quarters in College Station, TX, made sampling-life very easy. Special thanks to Vera Lukies for technical support at the scanner at the MARUM.
Working at the Alfred Wegener Institute for Polar and Marine Research was of great pleasure and profit. First, I would like to thank the laboratory staff, including Susanne Wiebe, Rita Fröhlking, Ute Bock, Ingrid Stimac, and Ilsetraut Stölting for technical help. Second, I want to thank my fellow PhD colleagues for sharing good and bad, especially Inès Borrione and David Naafs.
I further want to thank all my friends for sharing wonderful times in Bremen and for bearing with me during the hard times. Special thanks to Oliver Hach, Kevin Pöhlmann, Katharina Jantzen, Theresa Weidner, Frauke Scharf, and Cornelia Roder.
Last but not least I want to thank my family. I am very grateful for their never-ending support and belief in me.

Contents

Abstract **v**

Kurzfassung **viii**

1 Introduction **1**
1.1 Motivation and Objectives of Research 1
1.2 Strategy of the Thesis - The Eolian Component in Marine Sediments: The Concept of Dust as a Proxy for Changes in Atmospheric Circulation and Continental Aridity 2
1.3 The Pliocene and Pleistocene Epochs 4
1.4 Structure of the Thesis 5

2 The Study Area **7**
2.1 Tropical Southeast Pacific Ocean-Atmosphere Linkages 7
2.2 Southeast Pacific Tectonic Processes and their Relevance for Paleoclimate Evolution 9
2.3 Source Areas of Dust - The Atacama Desert 11
2.4 Andean Geology 13

3 Sample Material and Methods **15**
3.1 Site Locations and Sample Material 15
3.2 Sedimentological and Geochemical Analyses of Sediments of ODP Site 1237 18
3.3 Sedimentological Analyses of Surface Sediment Samples 26
3.4 Statistical Analysis 27

4 Manuscripts and Publications **28**
4.1 Distribution and Provenance of Wind-Blown SE Pacific Surface Sediments 28
4.2 Late Quaternary Glacial-Interglacial Climate Variability of Western South America 62
4.3 Glacial-Interglacial Variability in Dust Supply to the SE Pacific during the Plio-Pleistocene Transition (2-3.1 Ma) 84
4.4 More humid interglacials in Ecuador during the past 500 kyr linked to latitudinal shifts of the equatorial front and the Intertropical Convergence Zone in the eastern tropical Pacific 103
4.5 Early Pliocene increase in thermohaline overturning: A precondition for the development of the modern equatorial Pacific cold tongue 119

5 Changes in Dust Supply on Tectonic and Orbital Timescales during the Past 5 Ma - A Synthesis **137**

6 Perspectives **146**

Bibliography **148**

List of Figures **160**

1 Introduction

1.1 Motivation and Objectives of Research

The variability of trade winds has long been considered a missing link in understanding past oceanographic and productivity changes in the upwelling areas of the eastern boundary currents along the western continental margins. Climate, upper ocean stratification and trade wind intensities are linked in that the occurrence of upwelling depends on thermocline depth and wind strength, which in turn depend on the large-scale climate conditions. The low-latitude Southeast Pacific is one of the major upwelling areas on earth and of special interest due to its strong appearance throughout the year.
The tropical Pacific plays an important role in the global climate system as the global atmospheric circulation is highly sensitive to tropical Pacific sea surface temperature anomalies (Cane, 1998; Mix, 2006). The teleconnections of changes in the Pacific temperature pattern with the global climate is evident and best studied in the context of the El Niño-Southern Oscillation in past and present. Because of tight connections of the atmospheric and oceanic surface circulation systems (Wyrtki and Meyers, 1976; Strub et al., 1998), paleo-changes in southeast trade-wind strength and dust transport are considered a missing link to understand changes in tropical Southeast Pacific oceanography, El Niño-behavior, productivity, and associated variability in thermocline depth, upwelling, and dust fertilization.

The major goals of this thesis are the reconstruction of changes in the atmospheric and continental components of the coupled continent-ocean-atmosphere system, i.e. (1) the trade wind strength and dust transport and (2) the South American continental aridity. This study covers the past 5 Million years (Ma) before present, focussing on two selected time intervals, the Plio-Pleistocene transition including the intensification of the NHG (3.1 - 2 Ma), and the Pleistocene ice ages of the past 500 thousand years (ka).
In detail, the aims and questions to be answered are:

- Reconstructing the modern spatial pattern of siliciclastic grain-size variability in the southeastern Pacific from surface sediment samples to identify the eolian signal and regions of possible fluvial overprints. A detailed analysis of the regional grain-size pattern is considered a prerequisite for the interpretation of the paleo-dust records.

- Establishing records of siliciclastic accumulation rates and grain sizes at ODP Site 1237 to reconstruct changes in continental aridity and trade-wind strength, respectively.

- Distinguishing between continental aridity and wind strength changes by comparing compositional (geochemical) and grain-size data of the terrigenous sediment input involving an end-member modelling approach. Are changes in continental climate and wind intensity in phase or decoupled?

- What are the forcing mechanisms that controlled changes in South American aridity/humidity and trade wind intensity?

- How do changes in wind strength relate to changes in thermocline depth and ocean productivity?

1.2 Strategy of the Thesis - The Eolian Component in Marine Sediments: The Concept of Dust as a Proxy for Changes in Atmospheric Circulation and Continental Aridity

The approach of this thesis follows the geological paradigm of the present providing 'a key to the past' (uniformitarianism after James Hutton) (Mathieson, 2002; Haywood, 2005). Marine sediments provide first-order archives of deposition changes in mineral dust among other components over long timescales due to their mostly continuous sedimentation histories (Kohfeld and Tegen, 2007). Therefore, they represent the majority of Plio-Pleistocene records of long-distance transported dust. Mineral dust as detected in marine sediments is mainly derived from arid and semi-arid tropical and subtropical areas of sparse vegetation (Rea, 1994; Kohfeld and Harrison, 2001; Harrison et al., 2001; Prospero et al., 2002). For this study, sedimentary material of Ocean Drilling Program (ODP) Site 1237 (Leg 202) located in the vicinity of the Atacama Desert (chapter 3.1) was sampled to investigate the variability of the southeast trade winds in the tropical Southeast (SE) Pacific. Previously, the modern spatial distribution of dust across the SE Pacific was reconstructed analyzing surface sediments from numerous cores obtained on different cruises to the tropical East Pacific since 1969. The surface sample data set has been used as a reference data set for the interpretation of the paleo-dust records.

Eolian dust has been defined as 'a suspension of solid particles in a gas, and/or the deposit of such particles' (Pye, 1987). In the following chapters, 'dust' refers to only the lithogenic fraction, i.e. eolian-derived mineral and soil dust. Dust is an active feature of the climate system (Harrison et al., 2001) that represents part of the physical and biogeochemical linkages of the atmosphere, the lithosphere, and the hydrosphere (Arimoto, 2001). The variation of the atmospheric dust load is usually a response to climate change, in that aridity, precipitation, vegetation cover, and

winds control the dust cycle (Clemens, 1998; Kohfeld and Tegen, 2007).
Dust production is dependent on the availability of wind-erodible material. This in turn requires humidity for sufficient weathering and subsequent drying and loss of vegetation (Jickells et al., 2005). The entrainment of dust from the ground is then controlled by the nature of the soil, the presence of any obstacle, and most importantly wind speed and gustiness (Laity, 2008). Dust itself can also directly and indirectly influence climate, such as the radiative forcing through absorption and scattering of light, or the cloud cover through the availability of more or less condensation nuclei. Furthermore, it can provide nutrients to marine or terrestrial ecological systems (Harrison et al., 2001). Dust transport and deposition to the ocean are further controlled by the atmospheric structure, wind speed, and precipitation that regulate its entrainment and removal (Jickells et al., 2005). Because of their close dependence, dust emission, transport and deposition changed concurrent with climatic changes on geological timescales, and can be retrieved from natural archives such as marine or lake sediments, ice cores, or loess deposits.
The linkage of the climate system and the dust cycle makes eolian dust as retrieved from natural archives a valuable proxy to learn about past climatic variability, especially changes in atmospheric circulation patterns. Dust accumulation rates provide information on changes in the dust cycle, comprising dust source, transport and deposition. Grain-size distributions of dust, on the other hand, are more specific and frequently used as indicators of changes in wind strength and/or changes in the distance of the deposited dust from the source area (Sarnthein et al., 1981; Rea, 1994; Prins and Weltje, 1999; Kohfeld and Tegen, 2007). Clemens (1998) made three fundamental observations: (1) the eolian flux and grain size are independent, (2) eolian flux is related primarily to aridity and vegetation cover at the source, (3) grain size is primarily a function of atmospheric transport capacity. These observations are incomplete in that they are missing a relation of the vorticity of winds and eolian flux, as enhanced gustiness can also increase eolian fluxes enormously and may even be more relevant to flux variability than changes in the source in terms of aridity and vegetation cover (McGee et al., 2010).
Using eolian grain size as a paleoclimate proxy for changing wind strength is based on the assumption that far from the dust source ($>$1000 km) grain-size distribution has stabilized and is in pseudoequilibrium with the transporting winds, because larger grains have already settled out due to gravitational fallout. As a consequence, downcore changes in grain size of the eolian-derived marine sediment component at a certain location record changes in wind strength (Rea, 1994; Clemens, 1998; Hovan, 1995). Clemens (1998), e.g., found strong positive correlations between median grain size in sediment trap samples, overlying wind speed, and the regional barometric pressure in the Indian Ocean.
In this study, grain-size distributions of the lithogenic fraction were analyzed to re-

construct relative changes in southeast trade-wind strength during the past 5 Million years. Additionally, siliciclastic, iron, and titanium accumulation rates were generated to represent the variability in dust supply to the SE Pacific to draw inferences about changes in western South American continental climate.
For provenance studies of the modern input of eolian dust to the SE Pacific the geology is of interest to trace transport pathways. Therefore, a short passage on Andean geology follows in chapter 2.4.

1.3 The Pliocene and Pleistocene Epochs

During the past five Million years (Ma) the global climate experienced a transition from relatively warm conditions with 2 - 3°C higher temperatures than today (Haywood and Valdes, 2004) to much more variable conditions with alternating cold and warm periods. The past 5 Ma b.p. in Earth's history are represented by the Pliocene (5.3 - 2.6 Ma) and Pleistocene (2.6 to 0.01 Ma) epochs. In the Early Pliocene climate was much more equable than after 3 Ma, when mid- and high-latitude areas began to cool significantly and major continental ice sheets started to build up in the Northern Hemisphere, leading to the development of distinct alternating glacial and interglacial intervals between 3.1 and 2.4 Ma (e.g., Raymo, 1994; Poore, 2007), as inferred from δ^{18}O in benthic foraminifera (Lisiecki and Raymo, 2005) (Fig. 1).

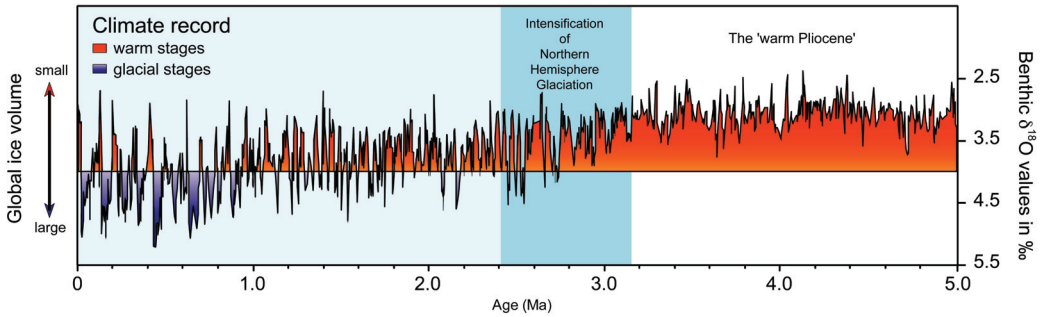

Figure 1: Climate variability over the past five Million years as recorded in benthic oxygen isotopes (Lisiecki and Raymo, 2005). Glacials are indicated by blue shading, interglacials and warm stages in red. (courtesy of R. Tiedemann).

While the distribution of continents was almost identical to the modern situation during the warm Pliocene, mean global surface temperatures were ~3°C warmer than today, ice sheets were absent in the Northern Hemisphere, sea level was approximately 25 m higher than today (e.g., Dowsett et al., 1999; Ravelo et al., 2004; Mudelsee and Raymo, 2005), and CO_2 concentrations were close to the modern

(Foster et al., 2009). The Mid-Pliocene (3.3 - 3.0 Ma) is often referred to as the last period in Earth's history that can be used as a scenario for a warming global climate in the future (Dowsett et al., 1999; Haywood, 2005; Robinson et al., 2008; Dowsett and Caballero Gill, 2010). To capture the development from these much warmer and equable climate conditions in the Early and Mid-Pliocene to the Pleistocene ice ages including the intensification of Northern Hemisphere Glaciation (NHG), the entirety of the Plio-Pleistocene epochs is important to study.

1.4 Structure of the Thesis

This thesis consists of three major sections, an introductory part (chapters 1 - 3), a part including manuscripts for publications and actual publications in scientific journals (chapter 4), and a third part (chapter 5 and 6) summarizing the main conclusions of the previous chapters in a synthesis of 5 Million years of southeast trade-wind variability in the Pacific.

Chapter 1 includes the motivation and research objectives, as well as the strategy and outline of this thesis. Dust is introduced as a proxy of paleoclimate research in chapter 1.2.

Chapter 2 contains background information about the study area, including the source areas of eolian dust.

Chapter 3 provides an overview of the sample material used for analyses, and an insight into the methods applied that are not elaborated in detail in the first-authorship manuscripts.

Chapter 4 comprises results in manuscripts and publications.

Chapter 4.1 presents the modern spatial pattern of eolian-derived marine sediments in the eastern equatorial and south-tropical Pacific as a reference data set for the interpretation of ODP Site 1237 paleo-dust records. The article is published in *Marine Geology*.

Chapter 4.2 focusses on dust flux variability in the SE Pacific of the past 500 ka as investigated on sediment samples from ODP Site 1237. The manuscript is in review with *Quaternary Science Reviews*.

Chapter 4.3 discusses the variability of dust supply to the SE Pacific during the Plio-Pleistocene transition and its implications for the history of global climate cooling, especially during the Northern Hemisphere Glaciation intensification. This manuscript is in preparation and will be submitted to *Aeolian Research*.

Chapters 4.4 and 4.5 contain articles of co-authorship that are published in *Paleoceanography*.

Chapter 4.4 (Rincón-Martinez et al., 2010) examines changes in the eastern

equatorial Pacific Ocean dynamics and their impact on continental precipitation during the past 500 ka based on a multi-proxy approach.

Chapter 4.5 (Steph et al., 2010) elucidates the Pliocene Climate switch presenting Pliocene oceanographic proxy data and climate model results that suggest an alternative chain of forcing mechanisms to previous studies.

The synthesis in **chapter 5** is followed by a research outlook (**chapter 6**) containing open questions and suggestions for further investigations.

The references of chapter 4 are listed at the end of each manuscript or publication, while all other references are listed in the bibliography at the end of the thesis. The data generated within the framework of this thesis are available in the PANGAEA database (http://www.pangaea.de).

This thesis is part of the project *SE trade wind strength and dust transport (Leg 202)* funded by the German Science Foundation (DFG Ti240/17-1) within the program 'Integrated Ocean Drilling Program/Ocean Drilling Program'.

2 The Study Area

2.1 Tropical Southeast Pacific Ocean-Atmosphere Linkages

Southeast (SE) Pacific Ocean surface circulation is strongly influenced by wind forcing (Kessler, 2006). The large-scale atmospheric circulation in the tropical Pacific comprises two interacting circulation cells, a zonal (Walker) and a meridional (Hadley) cell. Together with the topography of the Andes that deflects the Intertropical Convergence Zone (ITCZ) to the Northern Hemisphere (Takahashi and Battisti, 2006), these cells strongly determine the near-surface winds (Pierrehumbert, 2000) and thus the seasonal shifting latitudinal position of the ITCZ. The ITCZ in turn largely affects the distribution of precipitation over the tropical ocean and the adjacent continent as well as the pattern and strength of ocean surface currents in the equatorial and subtropical regions.
The ocean surface circulation dynamics and surface wind patterns are linked in that the eastern branch of the southeastern Pacific subtropical anticyclone, confined by the ITCZ in the north and by the strong eastward zonal flow of the West Winds in the south (Fig. 2), provides the vorticity for the large-scale surface structure of the South Pacific gyre (Sepulchre et al., 2009). The eastern part of the SE Pacific anticyclonic gyre, the Humboldt Current system, is bounded to the north by the equatorial current system and to the south by the West Wind Drift. The southeast trade winds are the major trigger for the eaquatorward flow of the surface waters along the coast of Peru and enhance coastal upwelling through Ekman transport of surface waters (McGregor and Nieuwolt, 1998). The equatorward Humboldt or Peru Current feeds the South Equatorial Current (SEC), which carries most of the water flowing west from the eastern Pacific. These currents represent a combination of upwelling and advection of subantarctic waters and thereby form a cold tongue, that extends from $\sim$40°S to $\sim$5°S (Thiel et al., 2007). Its cold sea surface temperatures (SSTs) are a relevant feature in South American hydrology and climate, and are one of the main factors made responsible for the aridity along the adjacent western coast of South America (see chapter 2.3). The currents are strongest in austral winter, concurrent with the southeast trade winds, which represent the lower branch of the Hadley cell circulation, and are generally maintained by a steep air-pressure gradient between the east and west Pacific (Laity, 2008).

These ordinary circulation patterns are regularly disrupted by the El Niño-Southern Oscillation (ENSO), one of the most important modes of interannual variability in the South Pacific. The Southern Oscillation (SO) describes changes in the pressure differences between the South Pacific (high pressure) and Indonesia (low pressure). When this relationship reverses, an El Niño occurs. During El Niño-years the ocean-atmosphere system in the tropical Pacific is disrupted. SSTs in

Figure 2: Schematic view of atmospheric large scale circulation in the SE Pacific. The southeast trade winds blowing from the Atlantic across South America are blocked by the Andes. This causes a rain shadow effect on the eastern side of the mountain range. Range of the Intertropical Convergence Zone reflects annual movement; Atacama Desert indicated in orange, ODP Site 1237 indicated by a red dot (courtesy of R. Tiedemann).

the Equatorial East Pacific (EEP) are unusually warm, the temperature gradient between the West Pacific Warm Pool (WPWP) and the EEP is strongly reduced, the thermocline in the East Pacific is rather deep, and the southeast trade winds are relaxed compared to average conditions (Wallace et al., 1998) (Fig. 3). It is further characterized by torrential precipitation in Ecuador and northern Peru (and sometimes in north-central Chile), but extremely dry conditions in the Altiplano (Cane, 2005). It has further consequences for weather and climate conditions around the globe through teleconnections, e.g. warm winters in Alaska and Canada, and cool, wet winters near the Gulf of Mexico (Molnar and Cane, 2002).
Complementary to the El Niño phases, La Niña phases occur as part of the SO. La Niña reveals the same features as the ordinary ocean-atmosphere circulation patterns in the Pacific, but much amplified. Trade winds are most intense during such periods, enhancing the upwelling of cold, nutrient-rich waters in the central and eastern tropical Pacific, while warm sea surface temperatures and heavy precipitation are confined further to the west in the WPWP.

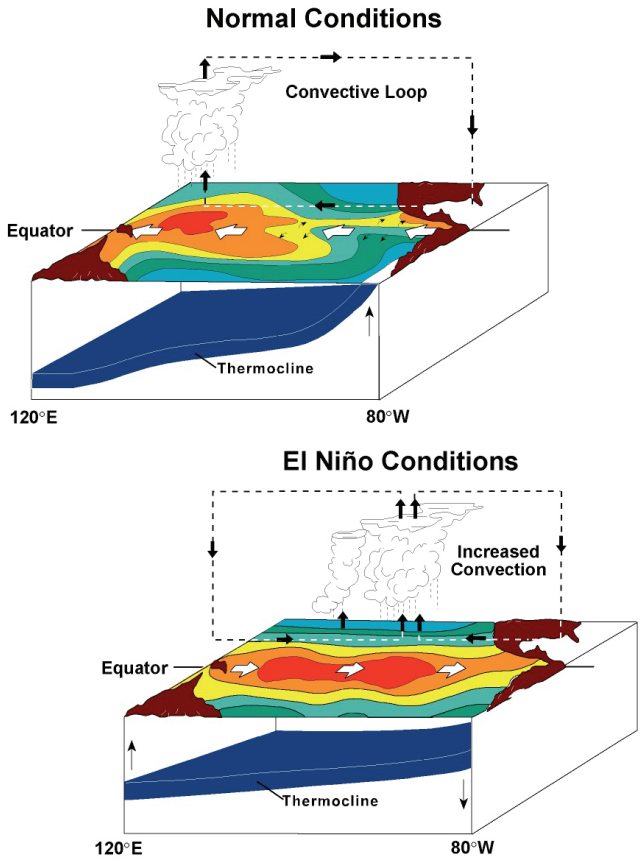

Figure 3: Ocean-atmosphere circulation patterns in ordinary conditions and during El Niño phases in the equatorial Pacific (NOAA, http://www.pmel.noaa.gov/tao/elnino/nino_normal.html)

2.2 Southeast Pacific Tectonic Processes and their Relevance for Paleoclimate Evolution

On time-scales of millions of years climate-forcing mechanisms include tectonic processes, such as mountain uplift or the opening and closing of oceanic gateways that may trigger changes in oceanic and atmospheric circulation (Raymo, 1994; Ruddiman and Prell, 1997). Even though these processes are only noticeable over the long-term and happen gradually, there might be thresholds, such as critical heights of mountain ranges or sill depths, to have abrupt effects on the climate. Investigating climate records retrieved from marine sediments of the tectonically active SE Pacific Ocean of the past 5 Ma therefore must consider the uplift history of the Andes, the closure history of the Central American Seaway (CAS) and how they might have influenced the paleoceanographic and continental climatic environment.

Andean Uplift The Andes' genesis is characterized by relatively short tectonically active phases that may have lasted a few hundred thousand years to a few million years (Jaillard et al., 2000; Megard, 1984), interrupting longer periods of relative tectonic quiescence (Wipf, 2006). These tectonic "events" might have served as triggers in the climate history of the SE Pacific. It is still unclear to which extend the Andes' uplift changed paleoceanographic features in the SE Pacific. However, paleoceanographic changes are supposed to derive mainly from reorganizations in atmospheric circulation caused by a progressive uplift of the mountain range. The Andes undoubtedly started forming a barrier for the trade winds, which forced the low-level high-velocity winds on the western continental margin to follow the coastline, enhancing coastal upwelling. The orographic rain shadow effects as well as decreased sea surface temperatures caused by the upwelling of cooler water masses are probable causes and amplifiers of onshore (hyper-)arid conditions and the maintenance of the Atacama Desert of northern Chile and Peru (Hay, 1996; Gregory-Wodzicki, 2000).

Most of the uplift of the Andean mountain range had already occurred during the middle and late Miocene (Picard et al., 2008). While the Altiplano had supposedly reached its current elevation by 6.8 Ma (Garzione et al., 2006), all other segments of the Andes have experienced uplift also during the Pliocene (and Pleistocene) epoch(s) (Jaillard et al., 2000; Gregory-Wodzicki, 2000). The subduction of the Nazca Ridge beneath the south-central Peruvian margin started deforming the upper part of the central Andean forearc around 4 - 5 Ma ago, reaching uplift rates of 7 cm ka^{-1} (Macharé and Ortlieb, 1992). At this time, the Northern Andes in Colombia had only reached 40% of their modern height and experienced a rapid uplift phase between 5 and 2 Ma at rates of 0.5 - 3 mm a^{-1}, to reach modern elevation by 2.7 Ma.

Closure of the Central American Seaway (CAS) Opening and closing of oceanic gateways have long been considered to have a large influence on climate change (Berggren and Hollister, 1974; Berger et al., 1981; Haq, 1981; Hay, 1996) by respectively conveying and restricting the flow of water masses. The Central American (or Panama) gateway has often been suggested to have played a role in the transition from the warm Pliocene to the intensification of Northern Hemisphere Glaciation (NHG) (Berggren and Hollister, 1974; Haug and Tiedemann, 1998; Tiedemann and Mix, 2007).
Reconstructions from rock records suggest the existence of a deepwater passage between the Pacific and Atlantic oceans, i.e. the Carribean Sea, until at least $\sim$7-10 Ma (Molnar, 2008). By 5 Ma, the final closure phase commenced, initiated by the subduction of the Cocos Ridge (Dengo, 1985). A shallowing of the sill depth

changed the oceanic circulation during the Pliocene (Groeneveld et al., 2006; Steph et al., 2006) and has most likely intensified the Pacific gyral circulation. A critical threshold for the exchange of upper ocean water masses was reached by 4.6 - 4.2 Ma, when surface water salinity (Haug et al., 2001) and sea surface temperatures (SST) (Steph et al., 2010) increased significantly in the Caribbean. Farrell et al. (1995) suggested a displacement of maximum opal accumulation from the Pacific Basin towards the Galapagos region around 4.4 Ma related to the CAS, while modeling studies by Lunt et al. (2008) (online available material) showed a decrease in Pacific SSTs of 1.5 - 2°C between 15 and 30°S when Panama is closed. Estimations for the closing of the CAS range mostly from 3.5 to 2.6 Ma (Keigwin, 1978; Tsuchi, 1997; Ibaraki, 1997; Bartoli et al., 2005; Lunt et al., 2008), but are only certain for the period of the 'Great American Exchange' of vertebrates at $\sim$2.7 Ma (Lundelius, 1987; Marshall et al., 1982; Marshall, 1988).
Since atmospheric circulation patterns change with surface water circulation, the closure of the CAS indirectly influenced the prevalent wind system in the equatorial East Pacific and the average position of the ITCZ. Hovan (1995), e.g., found evidence for a southward shift of the ITCZ at the time of the critical threshold between 5 and 4 Ma inferred from latitudinal shifts in dust deposition below the doldrums.

2.3 Source Areas of Dust - The Atacama Desert

The source area of dust transported to the SE Pacific by the southeast trade winds is the Peruvian-Chilean desert. It extends 3700 km along the coast from southern Ecuador / northern Peru to central Chile (Fig. 4) and belongs to the driest regions on Earth (Laity, 2008). There are three coexisting and interacting factors causing the aridity in the desert region: (1) The area's location in the latitudinal belt of the subtropical anticyclone (atmospheric subsidence), (2) the cold ocean current along the coast, the Peru or Humboldt Current, which causes a temperature inversion preventing onshore penetration of moisture from the Pacific, and (3) the orographic rain shadow caused by the Andean mountain chain, allowing only sparse precipitation originating in the Amazon Basin (Bobst et al., 2001).

Cold upwelling waters from the eastern boundary current suppress evaporation and convection, while the anticyclone brings dry air from the subtropical jet and blocks winter storm incursions from the south at the same time (Latorre et al., 2005). The Andes stabilize the position of the anticyclone and are a barrier to moisture transport from the east. These factors taken together result in a strong inversion layer at around 1000 m height (Laity, 2008).

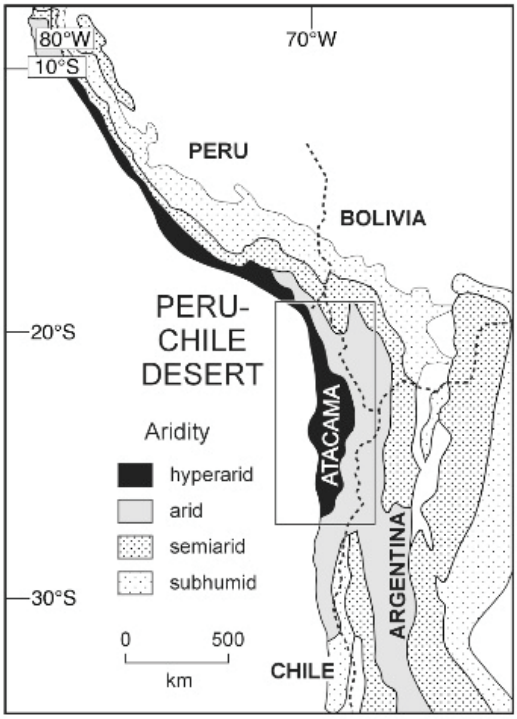

Figure 4: Present-day climatic zones of western South America from Hartley (2003)

In the core of the Atacama Desert in northern Chile, where annual precipitation is less than 10 mm/a (Larrain et al., 2002), hyperaridity prevails (Fig. 4). There is an almost complete lack of vegetation from 0 to 2500 m above sea level (a.s.l.). The desert's soils are unique in that they consist of silicate dust and salts from regional source rocks (chapter 2.4) that accumulated over long periods of time without significant losses from weathering (Laity, 2008).
According to Tanaka and Chiba (2006) dust emission flux from the Atacama ranges between 10 - 100 g m^{-2} a^{-1}, while the deposition flux above the adjacent ocean varies between 0.1 - 10 g m^{-2} a^{-1}. Only one hundredth of what is emitted reaches the ocean. Barkan and Alpert (2010) found a high correlation between insolation and dust in the Atacama Desert and inferred radiation as a cause for atmospheric dust loadings. Since the spatial and seasonal distribution of incoming solar radiation is controlled by orbital parameters (Lisiecki and Raymo, 2007), the relation of radiation and dust loading suggests that dust supply to the oceans follows the orbital cycles on geologic timescales.
Across the Western Cordillera, the arid and semiarid Altiplano stretches from 15 to 28°S. This volcanic plateau (3800 m a.s.l.) is often considered an extension of the Atacama Desert (Berger, 1997). Precipitation mainly occurs in austral summer and varies between 50 and 500 mm a^{-1}. Moisture is a very effective agent of weathering and thus an important factor for dust production available for transport. Eolian

deflation is noticable in numerous playas. Dust storms are frequent and local wind velocities can exceed 25 m s^{-1} (Laity, 2008).

2.4 Andean Geology

The Andes are the major climatic divide and watershed in South America. The short distance from their highest peaks of >6000 m to the Peru-Chile Trench makes them the largest relative relief on earth. While Neogene igneous intrusives are present in Costa Rica and western Panama, they are absent in eastern Panama. There, Cenozoic sediments that extend into Colombia overlay the Mesozoic igneous basement. A Quaternary volcanic range dominates northern Central America with a volcanic gap in southern Costa Rica/Western Panama (Bundschuh et al., 2007). This gap coincides with the Talamanca Cordillera, characterized by an exceptional occurrence of intrusive bodies in the sedimentary and volcanic series. These batholiths and granitoid stocks embody quartz-diorites and monzonites as well as granites and gabbros in subordinate abundance (Abratis, 1998). They represent the source rocks of quartz and chlorite in Central America, while the volcanic range delivers large amounts of smectite (chapter 4.1).
In Colombia, the undulating Pacific coastal area is built of mighty marine Tertiary rocks. It changes to a wide coastal low land of Cretaceous and Tertiary sediments in Ecuador. The Western Cordillera comprises Cretaceous clay shales and cherts in these latitudes, overlain by basaltic volcanic rocks in Colombia and alternating volcanites and fine-grained pelites in Ecuador. Massive tholeiitic basalts are attributed to accretions of oceanic crusts (Zeil, 1986). Wet-chemical weathering produces mainly smectites in this area (chapter 4.1).
North of 12°S, the Central Cordillera in Peru is formed of young plutonic rock massifs of the Cordillera Blanca. The Western Cordillera is composed of Mesozoic volcanites, volcanoclastic series and sediments, and is divided into single Jurassic and Cretaceous basins (Zeil, 1986). The Coastal Batholith in Peru intruded the cordillera during the Cretaceous. It is >1000 km in length and consists of gabbros and diorites of the early Cretaceous, followed by tonalites, granodiorites, monzodiorites and leukogranites. The Coastal Cordillera begins at the southern coast of Peru and extends into northern Chile. It has a Precambrian basement with several outcrops in Peru displaying the oldest gneisses and granulites of the Andes. By contrast, metamorphic Paleozoic rocks and sediments build the Chilean basement. Massive andesitic volcanites with numerous Jurassic and Cretaceous plutonic intrusions build their cover (Zeil, 1986). Between the Coastal Cordillera and the foothills of the Andes lies the Pampa de Tamarugal, the northern segment of the Atacama Desert. This pronounced basin is filled with 900 m of Tertiary and Quaternary sedi-

ments (Aravena, 1995) bordered by the Precordillera. The Precordillera is built on a basement of Paleozoic series with metamorphic Precambrian break-ups that is covered with Mesozoic marine and volcanic rocks (Zeil, 1986). The Precordillera and the High Cordillera are separated by another depression parallel to the Pampa de Tamarugal, displaying big salars such as the Salar de Atacama. It contains 10000 m of Permian to Holocene continental debris (Orme, 2007). Further inland between 12°S and 27°S, the High Cordillera is largely covered with massive series of Cenozoic volcanites, i.e. mostly ignimbrites. The wide Altiplano is filled with predominantly upper Cretaceous and Tertiary continental sediments (Zeil, 1986).

Volcanism The spatial distribution of the volcanic vents in the Central Andes can be related to differential block uplifting, especially during the Late Pliocene, but also the Pleistocene epoch (Lahsen, 1982). Recent Andean volcanism can be distinguished into distinct volcanic zones, the northern most of which extends NNE-SSW from 5°N to 3°S. It is mostly of basaltic, andesitic composition (Orme, 2007). Volcanism is absent in zones of flat subduction, i.e. between 5°S and 14°S (Lahsen, 1982) in the study area. South of 14°S, the central volcanic zone spreads along the Western Cordillera (central Peru) around the Arica Bend to 27°S (northern Chile). Here, volcanic activity has returned episodically ever since the Lower Miocene. Ignimbrites are common and stratovolcanoes crowning the Andes are mostly andesitic to dacitic in composition (Orme, 2007). The arc zones of Ecuador (Steinmann et al., 1999) northern and Central Peru display an effusive pulse in the early Pliocene, between 5 - 4 Ma (Jaillard et al., 2000; Lahsen, 1982). Volcanic ash layers found in SE Pacific marine sediments consist mostly of silt- to sand-sized volcanic glass and minor amounts of plagioclase, biotite, quartz, amphibole, and pyroxene (Mix et al., 2003), and point to active phases of uplift during the Plio- and Pleistocene epochs (Tiedemann and Mix, 2007).

3 Sample Material and Methods

3.1 Site Locations and Sample Material

This study is based on a set of surface sediment samples of the Southeast Pacific (10°N - 25°S, 100°W - 70°W), on Ocean Drilling Program (ODP) Site 1237 (Leg 202) (Mix et al., 2003) (Fig.5), and core RRV9702A-69PC. In the following, the relevance of the core locations for reconstructing the history of the southeast trade-wind system in the Pacific is outlined.

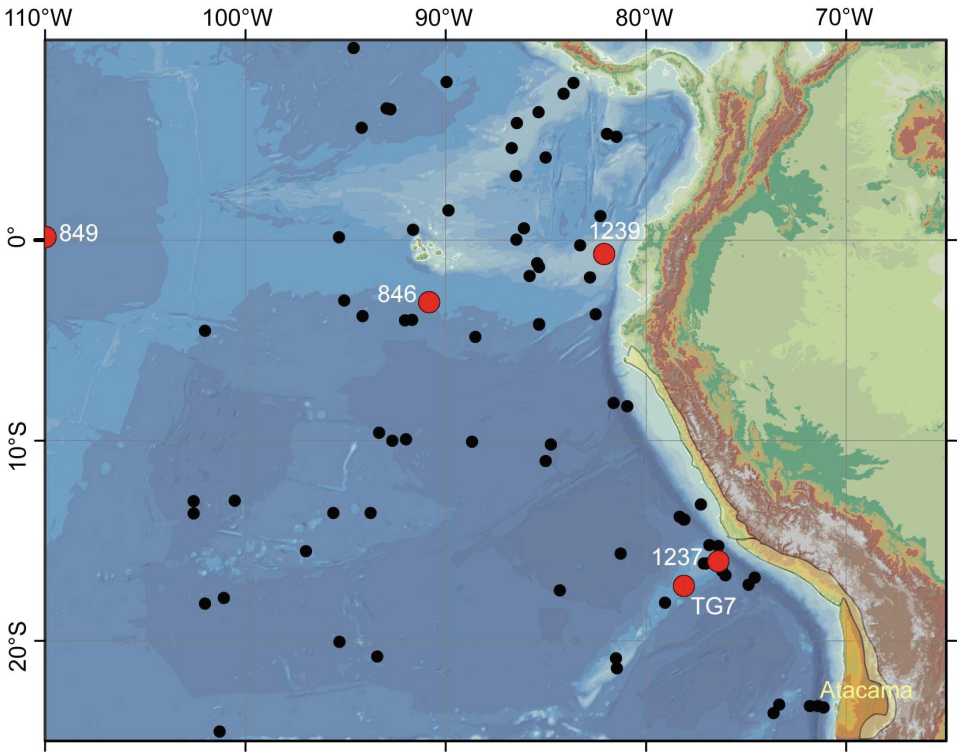

Figure 5: Sample locations of material analyzed and/or discussed in this study. Red dots represent ODP cores and gravity core TG7; black dots represent surface sediment samples. The Atacama Desert and the arid coastal areas of Peru are indicated by brown-yellow shading.

Surface Sample Material 75 surface sediment samples were analyzed for the reconstruction of the modern spatial pattern of siliciclastic grain-size variability in order to identify the eolian signal of the southeast trade-winds (chapter 4.1). The sample material was obtained by means of multi-corers, box-corers, gravity or piston corers. Water depths of sampled sites range from 904 m bsl to 7597 m bsl (chapter 4.1). Sedimentation rates are generally comparably low in this study area,

especially in the basins of the Southeast (SE) Pacific (below 3 cm/ka Mix et al. (2003)).

ODP Site 1237 (16.01°S, 76.37°W) Site 1237 is located ∼140 km off the southern Peruvian coast on the eastern flank of Nazca Ridge (Mix et al., 2003). Three holes were drilled at a water depth of 3212 m, leading to full recovery for the past 5 million years (Ma) (Mix et al., 2003). The tectonic backtrack path of the Nazca Plate moves Site 1237 approximately 5° further west relative to South America at 5 Ma b.p. (calculated from velocities given in Breitsprecher and Thorkelson (2009), Fig. 6). Following the NUVEL-1A prediction (Norabuena et al., 1998), the average closing velocity of the Nazca and South American plates has been 75±2 mm/a for the past 3 Ma, and ∼79 mm/a before 3 Ma. The distance of several hundred kilometers further to the west places Site 1237 somewhat closer towards the centers of the South Pacific anticyclone and the oceanic gyre 5 Ma ago, below possibly different overlying paleoceanographic and atmospheric conditions.

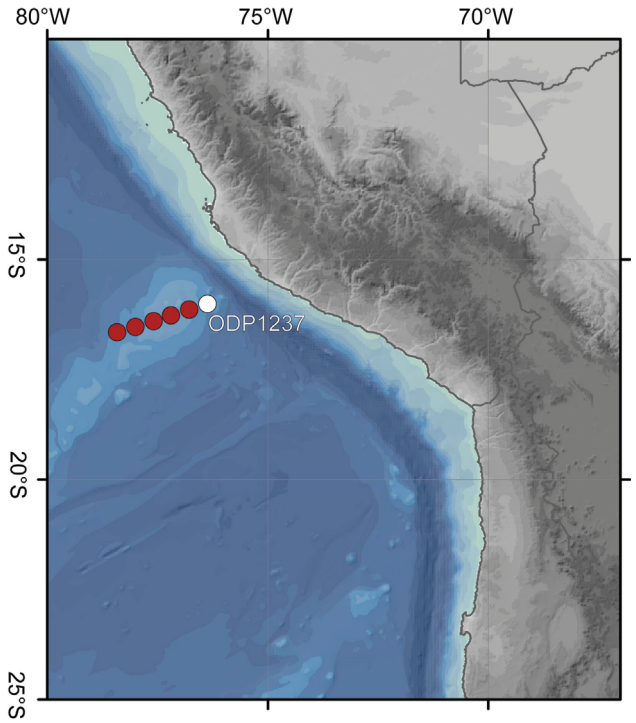

Figure 6: Tectonic backtrack of ODP Site 1237 for the past 5 Ma. Red dots indicate the position of the study site in 1 Ma steps. The modern location is indicated by a white dot.

Despite the tectonic backtrack, this site is perfectly situated to record changes in dust flux and trade-wind intensity because of its proximity to the dust source area,

which allows the recording of changes in wind intensities via grain-size variability in the eolian silt fraction. The adjacent coastal deserts of Peru and Chile as well as the Atacama are characterized by arid conditions since the late Miocene (Hartley and Chong, 2002) (chapter 2.3). Due to the site's location west of the Peru-Chile deep-sea trench and no major rivers draining into the Pacific between 5° and 25°S, sediment supply by gravity flows from the continental margin as well as fluvial supply can be largely excluded, as continental debris is trapped within the trench system.
Sedimentation rates at pelagic Site 1237 vary from 1-3 cm/ka (Mix et al., 2003). The uppermost 92 meters composite depth (mcd) of the core that correspond to 5 Ma consist of calcareous and/or siliceous (silty) clays and clayey oozes, disrupted by 37 ash layers that are characterized by rapid sedimentation rates. The ash layers usually display sharp basal, but diffuse upper contacts, rendering the interpretation of results from sedimentological analyses difficult. Even though it has been tried to omit ash layer samples, it was not possible to detect all until geochemical and sedimentological measurements were conducted. Especially in core depth where bioturbation is an issue, samples occasionally contained ash. However, they were identified by very coarse grain-size distributions and peaks in K content (Hart and Miller, 2006).

The age model for Site 1237 was established by correlating high-frequency variations in gamma ray attenuation density, percent sand of the carbonate fraction, and benthic δ^{13}C to variations in Earth's orbital parameters (orbital solution after Laskar (1993)). The excellent paleomagnetic stratigraphy at Site 1237, with all chrons and subchrons clearly defined for the past 5 Ma, led to a satisfying temporal classification of the sediment.
Sample spacing was adjusted to the age model in order to achieve a resolution of $\sim$3000 ka (Tab. 7(a)). Since both working and archive halves of all Site 1237 cores were completely depleted between 3.3 and 8.1 meters composite depths (mcd), the corresponding sections of pre-site survey core RRV9702A-69PC were sampled for compensation (Tab. 7(b)).

RRV9702A-69PC (16.01°S, 76.33°W) The position of pre-site survey core for ODP Leg 202 is located in the vicinity of Site 1237 on Nazca Ridge. The age model of Site 1237 was transfered to RRV9702A-69PC by aligning it to Site 1237 via the well correlating Magnetic Susceptibility records of both cores. Just as the different bore holes of ODP Site 1237, not all ash layers of RRV9702A-69PC could be found in Site 1237 samples and vice versa. The core was sampled with a spacing of 10 cm from 2.3 - 6.4 m (57.2 - 274.7 ka) to fill a sample gap of Site 1237,

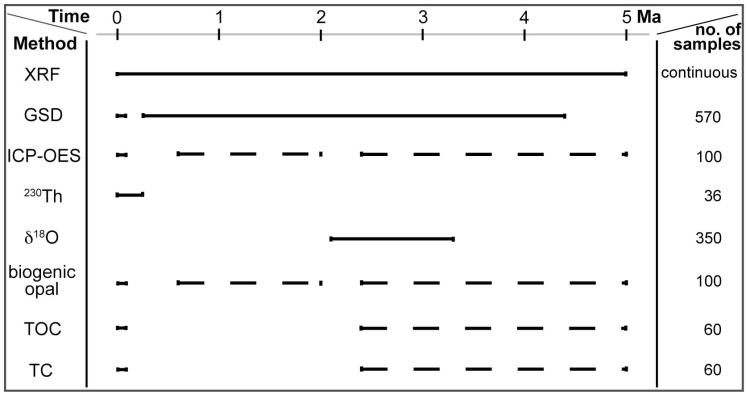

(a)

Method	number of samples
GSD	42
ICP-OES	16
biogenic opal	42
TOC	42
TC	42

(b)

Figure 7: Processed samples of **a** ODP Site 1237 and **b** RRV9702A-69PC. GSD - grain-size distribution.

resulting in 42 samples (Tab. 7(b)).

ODP site 1239 (0.67°S, 82.09°W) Site 1239 was drilled approximately 120 km off the coast of Ecuador, close to the crest of Carnegie Ridge at a water depth of 1414 m (Mix et al., 2003). Due to its proximity to the Gulf of Guayaquil it is ideally located to record changes in fluvial supply related to the variability of precipitation in northwestern South America. Sedimentation rates are considerably higher on Carnegie Ridge than on Nazca Ridge, ranging from 5-18 cm/ka. The site is located within the highly productive equatorial upwelling system. Sediments consist of foraminifer and nannofossil oozes with variant amounts of clay, diatoms, and micrite.

3.2 Sedimentological and Geochemical Analyses of Sediments of ODP Site 1237

Nondestructive Down-Core Geochemical Analysis - XRF The stratigraphically complete sediment record of ODP Site 1237 corresponding to the past 5.16 Ma as well as the complete sediment record of ODP Site 1239 corresponding to the past 5 Ma were scanned with an Avaatech Core Scanner (2nd generation, XRF-CS) at the Alfred-Wegener-Institute in Bremerhaven in a resolution of 1-2 cm and 1-5 cm, respectively. Energy settings used were 10 and 50kV to cover all elements of interest.

The Avaatech X-ray fluorescence (XRF) Core Scanner II is a nondestructive analytic system for fast semi-quantitative and quasi-continuous high resolution analy-

ses of the chemical composition of split sediment cores. XRF measurements of the entire suite of elements between aluminum (Al) and uranium (U) can be recorded. The principle of XRF core scanning is the ejection of electrons from the inner shells of atoms, initiated by incoming X-ray radiation. The vacant spot on the inner shell is subsequently filled by an electron from an outer shell, thereby emitting the energy difference of the two shells as electromagnetic radiation, which is detected. Each element displays specific wavelengths of radiation. The amplitudes of the peaks of different wavelength (i.e. elements) in the XRF spectrum then are proportional to the concentration of the elements in the sediment (Richter et al., 2006).The set-up of the machine specific XRF logging system and the sample preparation (core scanner at the AWI Bremerhaven) are described in detail in Monien (2010).
XRF scanning provides a means for preliminary stratigraphic interpretations comprising orbital tuning of sedimentary sequences (Pälike et al., 2001) and in this case the detection of terrigenous input patterns and provenances. It is also useful for the identification of sedimentological events, such as ash layers (Richter et al., 2006). For this study, element intensities and element ratios indicative of dust deposition at Site 1237 and terrigenous input at Site 1239 are of special interest. These predominantly include element concentrations of Fe, Ti, K, Al and Si. Ca and Ba, on the other hand, can be useful for inferences about changes in productivity and/or preservation at the study site.
Each working area displays its specific geochemical composition so that different elements can be used as proxies for different mechanisms and potential sources. Potassium (K), for example, is used as an indicator of fluvial terrigenous input off northwestern Africa (Mulitza et al., 2008), whereas it serves as a proxy for ash layers at Site 1237 in SE Pacific sediments originating from andesitic volcanism that is rich in potassium in this study.

All samples were freeze-dried before processing (Fig.8). Results from all analyses are presented in the manuscripts in chapter 4.

ICP-OES Measurements Results from Inductively Coupled Plasma - Optical Emission Spectrometry (ICP-OES) were used to convert XRF scanner counts to element concentrations in mg/g of sediment by means of linear regression (Fig. 9). For ICP-OES measurements samples were dissolved in acid. About 50 mg of homogenized bulk sediment were weighed into tevlon vials and fully digested in a mixture of 3 ml HNO_3 (concentrated, subboiling distilled), 2 ml HCl (30%, suprapur), and 0.5 ml HF (40%, suprapur) by heating to 225°C for two hours, applying a pressure-assisted microwave digestion system (CEM MARSXpress) (Kretschmer et al., 2010). The remaining acid was fumed off in the same microwave. Subsequently, the samples were re-dissolved in 5 ml 1M HNO_3 (subboiling distilled) and

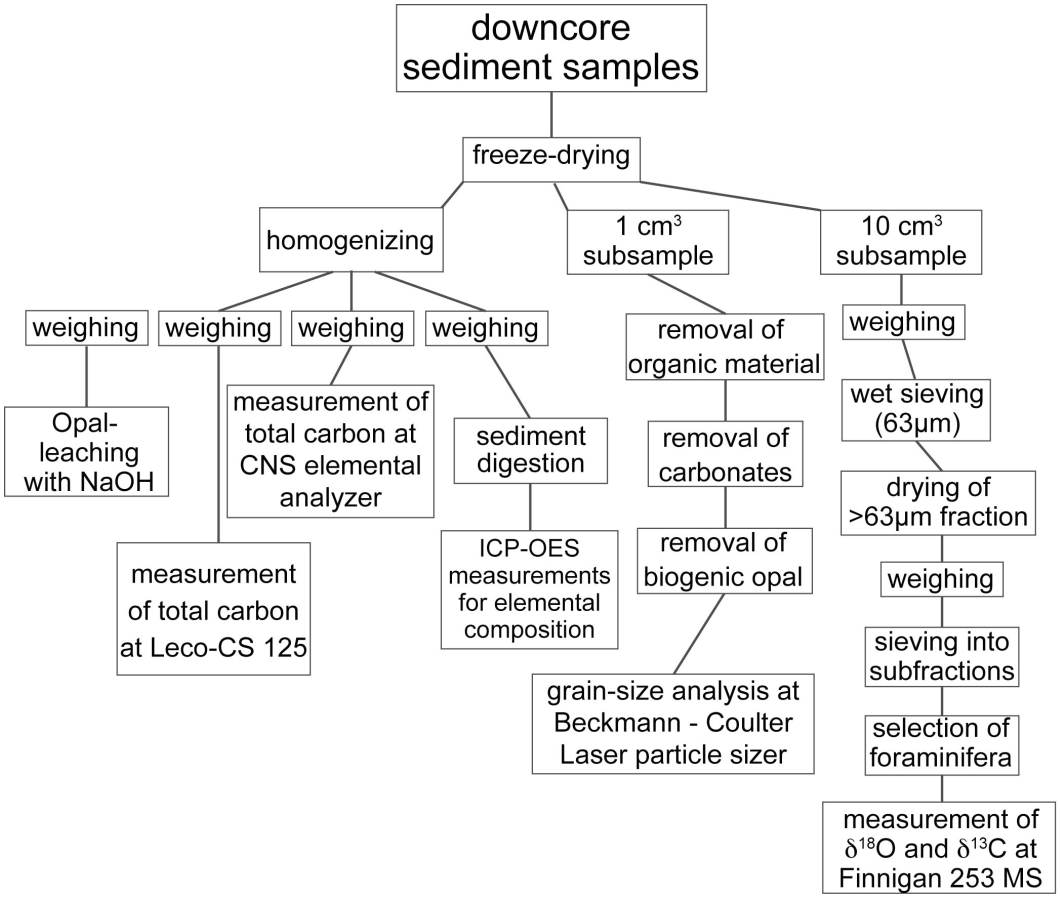

Figure 8: Summary of the individual preparation steps for analyses of ODP Site 1237 sample material

heated to 150°C for 45 minutes, before the solution was transferred to 50 ml Erlenmeyer flasks. The latter were filled to 50 ml with 1M HNO_3 (suprapure, single distilled). Measurements were carried out at an IRIS Intrepid spectrometer (Thermo Fisher Scientific Inc., USA) at the geochemistry laboratories of the AWI.

Conversion of element intensities from XRF scans to element concentrations obtained from ICP-OES measurements is often problematic, as the relationship is often nonlinear. For example, if there are no distinct lithologies, i.e. obvious changes in the sediment matrix, but the same sediment components throughout the core in extremely variable quantities, a correct conversion fails (Fig. 9). In order for the relationship to be correct, the regression line would have to cross the point of origin, which it does not. Weltje and Tjallingii (2008) proposed a log-ratio calibration model for this conversion problem. According to their study, it is sufficient to use log-ratios of element intensities from XRF-scans for a qualitative interpretation of the data (chapter 4.3).

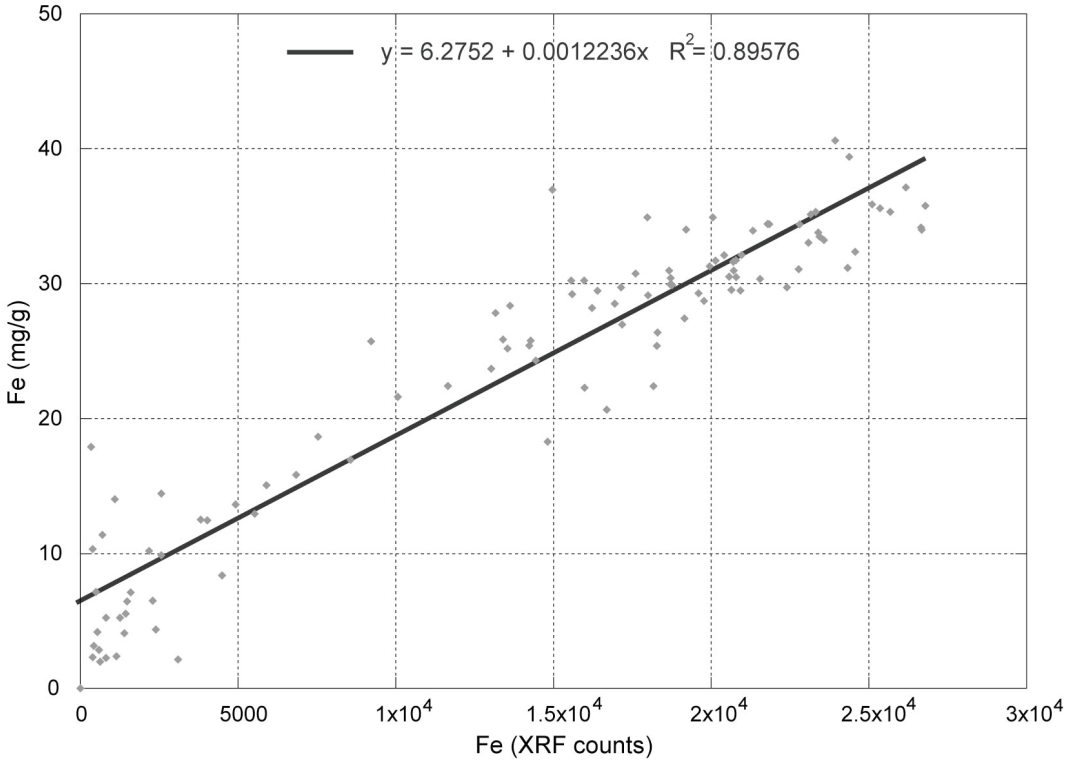

Figure 9: Linear correlation of Fe counts from XRF scans and Fe contents in mg/g from ICP-OES measurements.

Mass Accumulation Rates Fluxes to the sea floor of single sediment components are often estimated from mass accumulation rates (MAR) between dated sediment horizons (Sarnthein et al., 1988). Dust flux was approximated in two different calculations. Firstly, assuming the lithogenic fraction in the marine sediment is solely of eolian origin, dust accumulation rates were calculated as the product of linear sedimentation rates (LSR) (g ka^{-1}), percentage of the eolian lithogenic fraction, and dry bulk density values (g cm^{-3}) (chapter 4.2). LSRs are derived from the age models. High-resolution dry bulk density (ρ_{dry}) records are available from ODP Leg 202 shipboard measurements (Mix et al., 2003). Secondly, dust flux was calculated applying the Th-profiling method (Henderson and Anderson, 2003; Francois et al., 2004)) to have an independent measure of dust flux to control the results for the accumulation rates (ARs).

Th-Profiling ^{230}Th is produced by the decay of ^{234}U in the water column. It is extremely insoluble but adheres to the surface of other particles in the water column and is thus scavenged to the ocean floor rapidly soon after its formation. The assumption therefore is that ^{230}Th production equals its downward flux, so that the accumulation of $^{230}Th_{xs}$ in marine sediments provides an assessment of their

sedimentation rate (Henderson and Anderson, 2003). The excess ^{230}Th activity in sediments can thus be used as a reference against which fluxes of other sedimentary components can be estimated. This method has originally been proposed by Bacon (1984). It's application is limited to sediments no older than ∼300 ka, due to the half-life of ^{230}Th of 75.7 ka (Francois et al., 2004). However, the downcore flux of ^{230}Th consists not only of that produced by the decay of ^{234}U in the water column, but also a small component of ^{230}Th that is contained in detrital material and supported by decay of ^{234}U. Measured ^{230}Th values must be corrected for this detrital addition as well as for ingrowth from authigenic ^{234}U in the sediment and for decay of excess ^{230}Th. For the correction, measurements of ^{234}U and ^{232}Th at the same samples and a rough knowledge of the age-to-depth relationship of the investigated sediment core are required (Henderson and Anderson, 2003). Taking all of this into account, downward fluxes of sediment components are calculated after Bacon (1984) as follows:

$$F_i = Z * (^{234}U) * \lambda_{230} * f_i / {}^{230}Th_{xs}0$$

where
F_i : normalized flux of i to the sediment in g*yr^{-1}*m^{-2}
Z: water depth in m
(^{234}U): seawater activity of ^{234}U in dpm*m^{-3}
λ_{230}: decay constant of ^{230}Th
f_i: weight fraction of i in the sediment
$^{230}Th_{xs}0$: ^{230}Th activity of the sediment in dpm*g^{-1}

Th and U isotopes were analyzed on the fine fraction (<63 μm) of 36 freeze-dried and homogenized samples by Inductively-Coupled Plasma Mass Spectrometry (ICP-MS). Because measurements were wanted at the same depths for which δ^{18}O data already existed and no more bulk sediment was available, the fine fraction collected from washing the δ^{18}O samples through a 63 μm mesh was used for analysis. According to Kretschmer et al. (2010) the fine sediment fraction is the main carrier for the sedimentary $^{230}Th_{xs}$-signal, especially in siliceous and lithogenic-rich sediments. Investigations on the distribution pattern of dust across the SE Pacific (chapter 4.1) showed that terrigenous desert dust occurs only as silt and clay in our study area and is thus well represented in the fine fraction (<63 μm) used for Th and U isotope measurements.

Sample Preparation for Radiogenic ICP-MS Measurements Measurements were conducted on a quadropole ICP-MS at the ICPMS-Lab in the Geochemistry Department of the Lamont-Doherty Earth Observatory in Palisades, NY. Highly accurate quantitative and semi-quantitative analyses of elemental concentrations have

a precision of 1-2%.
Before measurements, spikes of ^{229}Th and ^{236}U were added as internal standards. Both samples (100 μg) and spikes (100 μl) were weighed into tevlon beakers. For sediment digestion, some HNO_3 was added to each sample, and heated to 150°C until almost dry. 5 ml $HClO_4$ and a little more HNO_3 were added before heating up to 230°C to fume the samples. Subsequently, 1 ml HF was added and heated back to $HClO_4$ fumes. This last step was repeated three times to ensure full digestion. Finally, samples were heated until thickening to small amounts ('blobs'), which were then dissolved in 0.5 ml HCl and 5 ml Milli-Q H_2O. NH_4OH was added to raise the pH to 7-8, where $Fe(OH)_3$ precipitates, scavenging the elements of interest. The precipitates were then centrifuged in Milli-Q H_2O. Prior to column chemistry, the Fe precipitates were re-dissolved in HNO_3 and reduced to 0.5 ml at $\sim$150°C, and cooled before another 2 ml 8N HNO_3 were added. The columns were conditioned with 8N HNO_3 before they were loaded with the samples and rinsed with 2 ml 8N nitric acid to elute Fe and everything else unwanted. Th and U were eluted with 12.2 ml concentrated HCl and 12 ml 0.12N HCl, respectively. Finally, 3 drops of $HClO_4$ were added and the samples were left on the hot plate overnight at 100°C to dry down to $HClO_4$ only. A few ml HNO_3 were added and the samples heated to $HClO_4$ fumes at 180-200°C. Heating was continued until there was a really small drop left. This was then re-dissolved in 2 ml of a 1% HNO_3/0.1% HF solution (ultra-clean acids).

Grain-size Analyses of Down-Core Sediment Material Grain-size distributions of sediments are often used to determine the sediment's provenance and/or transport processes (Sarnthein et al., 1981; Weltje and Prins, 2007). In this case the grain-size distribution of the siliciclastic fraction was measured with a Beckman-Coulter laser particle sizer at the Center for Marine Environmental Science (MARUM) in Bremen. Measurements can be conducted in a short amount of time and they are precise and accurate (Prins and Weltje, 1999; Stuut, 2001).
About 1 cm^3 subsamples were taken of bulk down-core sample material of ODP Site 1237 splice and pre-site survey core RRV9702A-69PC for grain-size distribution analyses of the lithogenic fraction (8). The latter was obtained by removing organic carbon, carbonates, and biogenic opal, boiling the samples with excess of a 10% H_2O_2 solution until reaction stopped, with excess of a 10% HCl- solution for one minute, and with excess NaOH pellets for 22 minutes, respectively. A few mg of Na-Polyphosphate were added to the samples and brought to boil in order to avoid coagulation of particles shortly before the analysis, which resulted in grain-size distributions from 0.4 to 2000 μm in 92 size classes.

Difficulties with Radiolarians and Sponge Specules The down-core sample material in some intervals was very rich in biogenic opal in the form of sponge spicules and radiolaria. Opal did not dissolve, even with excess NaOH, and distorted the grain-size distributions of the terrigenous fraction. In order to remove biogenic opal, the boiling time with NaOH was optimized at 22 minutes in numerous trials by increasing the boiling time gradually in steps of 5 minutes from 10 to 30 minutes total, comparing the measurements after each treatment (Fig. 10). After 20 minutes, the distribution is characterized by a coarser mode and an increased proportion of the very fine fraction, suggesting the dissolution of most of the biogenic opal. Microscopic inspection, however, revealed the presence of biogenic opal. At 25-30 minutes, the fine fraction completely disappeared and the whole distribution shifted into coarser size classes. This behavior suggests that not only the sponge spicules and radiolaria, but also the terrigenous clay minerals were destroyed at this point. At 22 minutes, the fine fraction was still present in the samples tested, while biogenic opal was no longer detected through the microscope. It thus displayed the sediment composition as representative for the terrigenous fraction.
This method was not applicable for samples from ODP Site 1239 because of too much biogenic opal that could not be resolved without destroying the lithogenic fraction considerably.

Biogenic Opal Measurements The concentration of biogenic opal in the bulk sediment was determined applying the automated leaching method according to Müller and Schneider (1993). Biogenic silica was extracted heating the samples with sodium hydroxide (1 N NaOH) in a water bath at 85°C for ∼45 minutes, continuously analyzing the leaching solution for dissolved silicon by molybdenum-blue spectrophotometry.

Carbonate Measurements Total carbon (TC) was determined with a CNS elemental analyzer (Elementar Vario EL III). Total organic carbon (TOC, wt%) was measured with a LECO Carbon Sulfur Analyzer (LECO-CS 125). Prior to analysis, calcium carbonates ($CaCO_3$) were dissolved by adding 1M solution of HCl, leaving it on the hot plate at 150°C for two hours. $CaCO_3$ (wt%) was calculated - assuming that calcite/aragonite are the main carbonate phase - from both measurements as follows:

$$CaCO_3 \text{ (wt\%)} = (\%TC - \%TOC) * 8.33$$

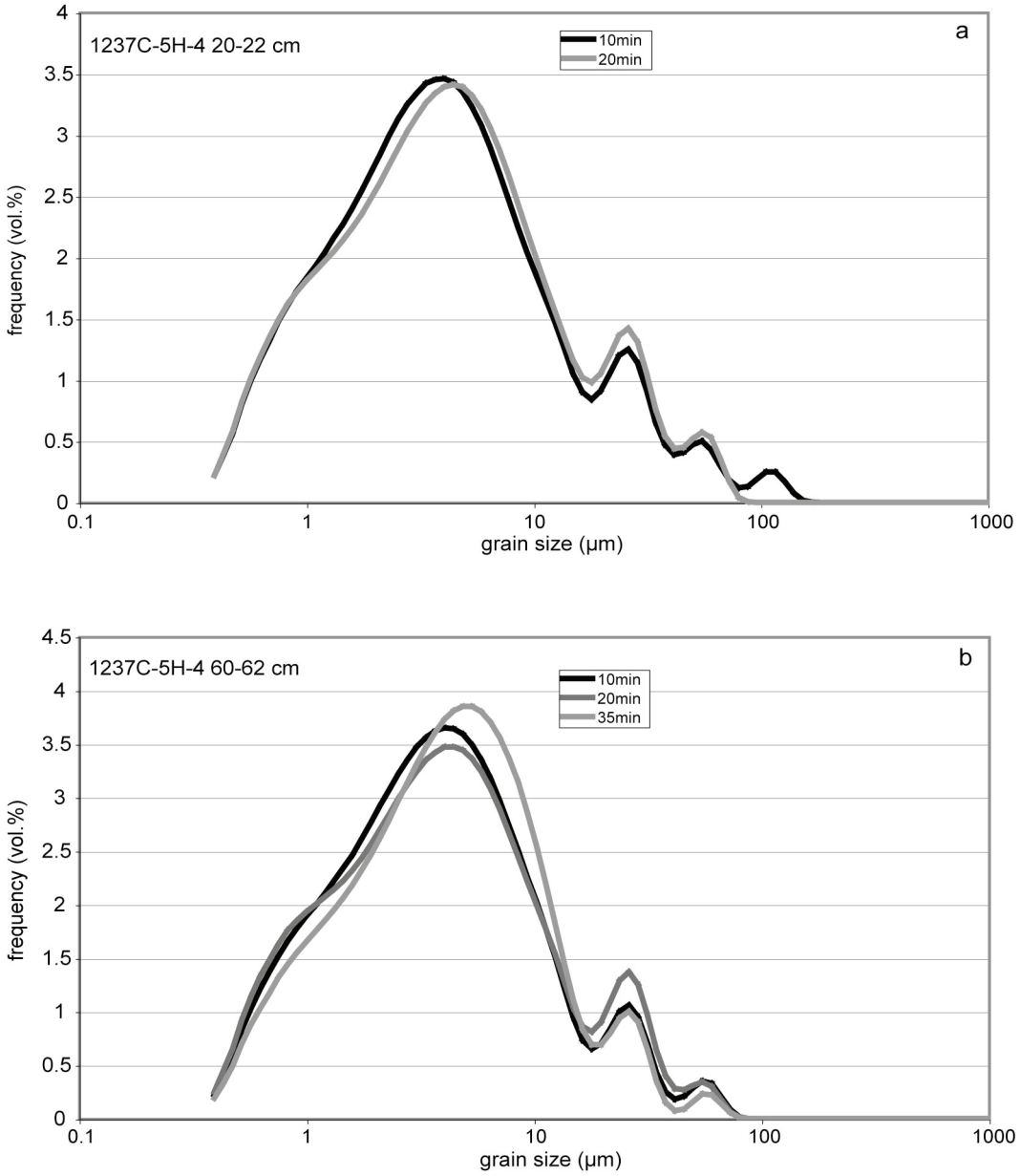

Figure 10: Test results for optimal boiling time to remove biogenic opal without destroying the lithogenic fraction. **a** sample 1237C-5H-4 20-22cm, measured after 10 and 20 minutes; **b** sample 1237C-5H-4 60-62cm, measured after 10, 20, and 35 minutes.

3.3 Sedimentological Analyses of Surface Sediment Samples

Because sample material was sparse and foraminifera of the surface sediment material were needed for another study (Rincón Martínez et al., accepted), the samples were washed through a 63 μm mesh, collecting the fine fraction (<63 μm). In order to retrieve the lithogenic fraction of the fine sediment, it was subsequently treated with excess of a 10% hydrogen peroxide (H_2O_2) and a 10% acetic acid solution (H_3C-COOH) to remove organic matter and carbonates, respectively. The samples were then separated into their clay (<2 μm) and silt (2-63 μm) fractions with the Atterberg settling method, applying Stoke's law. A weak ammonia solution was used to avoid coagulation of clay particles. The clay fraction (<2 μm) was treated with $MgCl_2$ in order to attain a uniform cation charge. It was then centrifuged twice in de-ionized water to remove free ions before the different fractions were dried and weighed (Fig. 11).

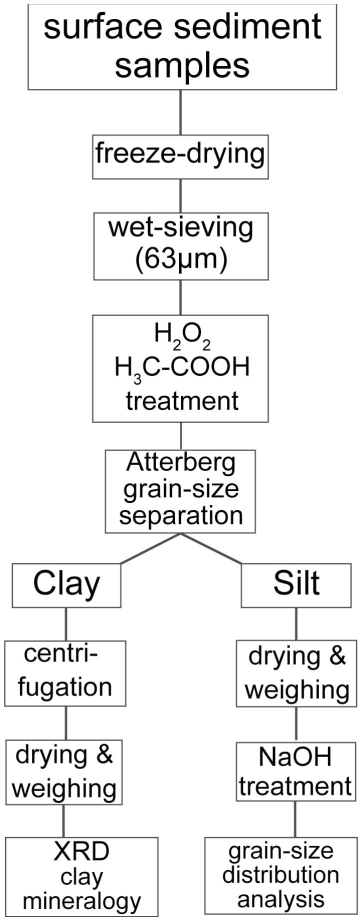

Figure 11: Summary of the individual preparation steps of the surface samples

Sample preparation for clay-mineral composition analyses is elaborated in chapter 4.1. For grain-size distribution analyses of the lithogenic silt fraction, the latter

was boiled with excess NaOH for 10 minutes in order to remove any biogenic opal, before they were analyzed with a Beckmann-Coulter laser particle sizer (chapter 3.2).

3.4 Statistical Analysis

Statistical tools are applied for the collection, organization and interpretation of data. Their purpose is a more comprehensive understanding of the characteristics of a data set. Here, data sets from the ocean floor that consists of a mixture of different sediment 'populations' originating from different sources and selectively transported by different agents and/or mechanisms are concerned. Especially terrigenous proxies used for (paleo-)climate reconstructions are often difficult to 'unmix' (Weltje and Prins, 2003). In this study, two different statistical approaches were chosen to identify source areas and original sediment populations of eolian-derived sediments (chapter 4.1).

End-member Analysis Instead of simply looking at the medians, means or modes of grain-size distributions, the end-member modeling algorithm after Weltje (1997) was applied, taking into account the compositional character of the data set and thus its non-negativity, leading to a realistic geological interpretation. It has been applied to the surface sample grain-size data set as well as the downcore samples of ODP site 1237 in order to identify the eolian contribution to the sediment and relative changes in southeast trade-wind intensity over geologic time.
To detect the variation of the contribution of different original types of sediments or 'subpopulations' (Prins and Weltje, 1999) to the bulk sediment deposited on the ocean floor, and their agents of transport, the grain-size data set is modeled as a combination of different proportions of statistically determined end members. These end members are fixed compositions of grain-size classes representing the different subpopulations. No prior knowledge of the end members is required. They are attributed to the respective provenances or transport mechanisms according to their character and correlation with, e.g., geochemical data sets of the same sediment after the modeling.

The number of end members necessary to satisfactorily represent the variation of the original grain-size distribution data set is determined by goodness-of-fit statistics. The applicant thereby experiences a trade-off between the reproducibility of the data set and the number of interpretable end members (Prins and Weltje, 1999), as the mean coefficient of determination across the grain-size classes increases with the number of end members.

4 Manuscripts and Publications

4.1 Distribution and Provenance of Wind-Blown SE Pacific Surface Sediments

Cornelia Saukel, Frank Lamy, Jan-Berend W. Stuut, Ralf Tiedemann, Christoph Vogt (*Marine Geology* doi:10.1016/j.margeo.2010.12.006, published)

Abstract The reconstruction of low-latitude ocean-atmosphere interactions is one of the major issues of (paleo-) environmental studies. The trade winds, extending over 20° to 30° of latitude in both hemispheres, between the subtropical highs and the intertropical convergence zone, are major components of the atmospheric circulation and little is known about their long-term variability on geological timescales, in particular in the Pacific sector. We present the modern spatial pattern of eolian-derived marine sediments in the eastern equatorial and subtropical Pacific (10°N to 25°S) as a reference data set for the interpretation of Southeast Pacific paleo-dust records. The terrigenous silt and clay fractions of 75 surface sediment samples have been investigated for their grain-size distribution and clay-mineral compositions, respectively, to identify their provenances and transport agents.
Dust delivered to the Southeast Pacific from the semi- to hyper-arid areas of Peru and Chile is rather fine-grained (4-8 μm) due to low-level transport within the southeast trade winds. Nevertheless, wind is the dominant transport agent and eolian material the dominant terrigenous component west of the Peru-Chile Trench south of $\sim$5°S. Grain-size distributions alone are insufficient to identify the eolian signal in marine sediments due to authigenic particle formation on the sub-oceanic ridges and abundant volcanic glass around the Galapagos Islands. Together with the clay-mineral compositions of the clay fraction, we have identified the dust lobe extending from the coasts of Peru and Chile onto Galapagos Rise as well as across the equator into the doldrums. Illite is a very useful parameter to identify source areas of dust in this smectite-dominated study area.

Keywords: SE Pacific, clay-mineral assemblages, eolian dust, grain-size distribution, trade winds

1. Introduction

The Peruvian and Chilean coasts as well as the Altiplano of Peru, Bolivia and Chile belong to the most arid areas worldwide and are recognized emission sources of eolian dust (e.g., Joussaume 1990; Prospero et al. 2002; Jickells et al. 2005; Goudie and Middleton 2006; Li et al. 2008). This region has experienced much less atten-

tion within the dust-studying community (e.g., Pye 1987; Tegen et al. 2002; Werner et al. 2002; Maher et al. 2010), as dust transport to the tropical East and subtropical Southeast Pacific is considerably smaller than, e.g., that off west Africa, in the Arabian Sea, off east China or Australia. However, basins such as the Salar de Uyuni on the Bolivian Altiplano are comparable in size to the Bodélé depression in Chad, one of the major dust sources in Africa, or to Lake Eyre in Australia (Goudie and Middleton, 2006). Nevertheless, dust sources in the Southern Hemisphere are generally smaller than those of the Northern Hemisphere (Maher et al. 2010). The tropical East Pacific, however, is a key location for (paleo-) climate research, as atmosphere-ocean linkages such as the El Niño-Southern Oscillation system or past shifts of the intertropical convergence zone (ITCZ) on glacial-interglacial time scales are still controversial (e.g., Leduc et al., 2009; Rincón et al., 2010). Therefore, the role of eolian dust may be larger than hitherto acknowledged, and forms a vital gap in our knowledge and understanding of the region.

Atmospheric dust particles represent a link between the atmosphere, lithosphere and the hydrosphere (Arimoto, 2001; Ridgwell, 2002; Maher et al., 2010) and are thus a valuable parameter in the pursuit of understanding the climate system. The concentration of mineral aerosols (dust) is a relevant feature within the global climate system. Its variability may cause changes in, e.g., the radiative forcing through absorption and scattering of light, in the provision of nutrients to marine ecological systems or in cloud cover through the availability of more or less condensation nuclei (Harrison et al., 2001). Furthermore, dust and its grain-size distribution can be used to study changes in continental aridity/humidity, spatial variations of major wind patterns as well as changes in wind intensity (Sarnthein et al., 1981; Rea, 1994; Arimoto, 2001; Stuut et al., 2002). Hence, proxy-based reconstruction of atmospheric changes in the (sub-) tropical East Pacific provide important clues for understanding past changes in ocean-atmosphere dynamics related to e.g. the Southern Oscillation, the trade winds and associated ITCZ shifts.

In order to tackle the importance of recent wind-transported material in the eastern equatorial Pacific and its sources, Prospero and Bonatti (1969) sampled atmospheric dust during a cruise of RV Pillsbury in 1967. They concluded that the supply of eolian dust to ocean sediments south of the ITCZ is less than on its northern side, and identified the arid coastal areas of Peru and northern Chile (Atacama Desert) as the source for those samples collected south of the ITCZ. Several subsequent studies, however, stressed eolian dust to be a noteworthy contributor to (south-) eastern Pacific deep-sea sediments (e.g., Heath et al., 1974; Rosato et al., 1975; Molina-Cruz and Price, 1977; Krissek et al., 1980; Scheidegger and Krissek, 1982; Dauphin, 1983; Rea, 1994; Prospero et al., 2002). Molina-Cruz and Price (1977) described the quartz distribution in surface sediments extending in a tongue similar in direction and position as the prevailing trade winds and interpreted the quartz-

rich sediments to be of eolian origin. Rosato and Kulm (1981) investigated the clay-mineral assemblages of surface sediments on the continental margin and Nazca Plate. Krissek et al. (1980) could not distinguish different agents of transport for terrigenous input with the help of grain-size and element analyses in the area but found bottom nepheloid layers in the Peru Basin. Scheidegger and Krissek (1982) concentrated on quartz and feldspar contents in different grain-size classes inferring dispersal patterns and deposition of eolian and fluvial sediments off Peru and northern Chile. According to their interpretations, eolian-derived material dominates sediments west of the Peru-Chile Trench. Dauphin (1983) used the size of quartz grains as an indicator of provenance and paleo-winds. Besides the South American arid areas, he identified another dust source north of the equator for sediments around the East Pacific Rise. Boven and Rea (1998) attempted to separate the eolian and hemipelagic components in a sediment core 300 km west of the mouth of the Gulf of Guayaquil. Even though the core is largely influenced by hemipelagic sedimentation (Boven and Rea, 1998) due to enormous river discharges through the gulf (Rincón et al., 2010), they identified the eolian component as the dominant contributor of terrigenous material after 15ka.

The focus of our study is to retrieve the modern spatial pattern of mineral dust as preserved in deep-sea sediments of the SE Pacific, in order to investigate the relation of the southeast trade winds and their dust transport. Our approach differs from former studies in that we used two independent parameters: We measured grain-size distributions of the siliciclastic silt fraction (2-63 μm) with a laser particle sizer and the clay-mineral composition of the clay fraction (<2 μm) with X-ray diffraction (XRD) to identify the eolian signal in sea surface sediments. Subsequently, we applied an end-member analysis (Weltje, 1997) to the grain-size data and a cluster analysis to the clay-mineral composition data. This enabled us to relate different grain-size populations (end-members) to distinct sources and means of transport. The end-member modeling algorithm (EMMA) has been successfully applied on Atlantic surface sediment samples offshore West Africa before (Weltje and Prins, 2003; Holz et al., 2004). We used it to interpret a set of surface sediment samples from the SE Pacific for the first time.

The tropical and subtropical East Pacific comprises upwelling regions as well as sub-aqueous volcanism and areas of strong bottom water currents, among other features. It thus has a very complex sedimentary environment experiencing coeval and subsequent sedimentation and redistribution processes (Krissek et al., 1980; Scheidegger and Krissek, 1982), especially by bottom-water currents in the Panama Basin (Lonsdale, 1977; Honjo, 1982; Kienast et al., 2007; Lyle et al., 2007). This complicates the detection of the lithogenic eolian fraction and its distinction from fluvial input and sub-aqueous volcanic debris.

2. Physical Setting

Our study area extends from 10°N - 25°S and 70° - 100°W (Fig. 12). It stretches from the equatorial doldrums in the north to the tropic-subtropical transition in northern Chile, covering the entire length of the Southern Hemisphere tropics in the east Pacific, plus the inner tropics of the Northern Hemisphere. Surface ocean circulation in the eastern tropical and subtropical Pacific is strongly influenced by wind forcing (Kessler, 2006), which, in turn, is determined by the topography of the Andes (Figs. 12 and 13). The continental topography and the Humboldt Current (Fig. 12) both largely influence the region's climatic conditions.

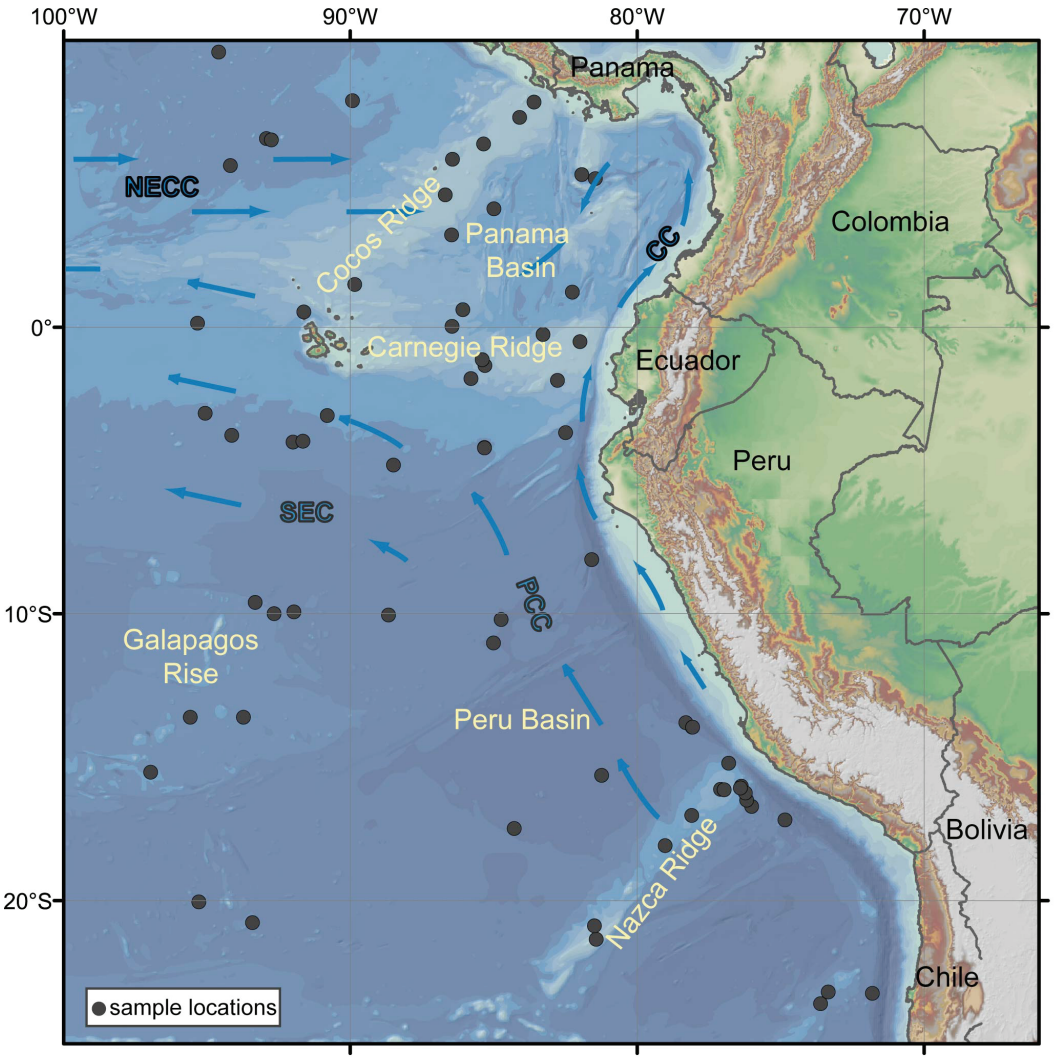

Figure 12: Working area. Black dots show surface sample locations, blue arrows represent surface water currents. NECC - North Equatorial Counter Current; SEC - South Equatorial Current; PCC - Peru-Chile Current (Humboldt Current); CC - Coastal Current

2.1 The Climate of Central and (north-) western South America

Besides orographic effects, latitudinal shifting atmospheric pressure belts and prevailing winds determine precipitation and its distribution in Central and northern South America. The climate is generally seasonal, with distinct (boreal) winter dry periods, dominated by the subtropical high pressure, and wet summers, controlled by the equatorial low pressure (Bundschuh et al., 2007). Between 10°N and 10°S rains follow the overhead passage of the sun, and the equator experiences two wet and dry seasons (Schwerdtfeger, 1976). Colombia experiences rainfall of several mm a^{-1} (Potter et al., 1994; Schwerdtfeger, 1976).

In Ecuador, the area north of 3°S is also very humid. The elongated coastal desert, however, begins at ∼1°S with cool Pacific waters offshore and a precipitation of 172 mm/a (Schwerdtfeger, 1976). At the immediate coast, sand and dust are omnipresent, while the northern banks of the Gulf of Guayaquil and the northern coastline of Ecuador are covered by tropical rain forest (Schwerdtfeger, 1976).

South of 3°S, a wet and dry seasonal regime with the rainy season lasting from November through April is prevalent, as typical for the Southern Hemispheric (sub-) tropics. Northern Peru is similar in relief and precipitation patterns to Ecuador. Central and South Peru are no longer affected by the ITCZ and the Western Cordillera forms a barrier for the atmospheric circulation south of 8°S. The Peruvian highlands experience moderate rainfall and the western slopes represent a transitional zone between the wet eastern regions and the extremely dry coastal plain. The central Peruvian coastal plain receives some precipitation in the form of drizzle through dense stratocumulus clouds, which are always present between May and October and frequent in April and November (Schwerdtfeger, 1976). During the normally dry summers, the sparse vegetation disappears from November on, and the landscape transforms back into a desert, which is characteristic for the lower western slopes of the Andes (Schwerdtfeger, 1976). North of 12°S, however, heavy sierra rains occasionally spill over the Andes reaching the coastal plain. The regular switch of humid and dry conditions in this semi-arid part of Peru is a prerequisite for dust production as water-involved weathering processes are much more efficient in producing aerosols than eolian processes (Pye, 1987; Maher et al., 2010).

Generally, the south is drier than the north, so that the dust and rock plateau around Arequipa is mostly without vegetation. This plateau and the coastal desert, stretching south along the entire coastline to 27°S, belong to an extensive arid zone that extends from southernmost Ecuador across the Andes in southern Peru, Bolivia and northern Chile to southern Argentina (Schwerdtfeger, 1976) into the so-called 'Arid Diagonale' (Bruniard 1982). As a consequence, rainfall in the Atacama Desert, one of the driest areas on earth, reaches only a few mm/yr (Potter, 1994; Schwerdtfeger, 1976).

2.2 The Wind Regime in Western South America and the SE Pacific

The southeastern Pacific subtropical anticyclone (SPSA) largely determines the atmospheric circulation in the study area. It influences the (sub-)tropical west coast of South America year-round. This results in predominant southerly low-level winds, which turn into the southeast trade winds further offshore (Garreaud and Muñoz, 2005). The Pacific trade winds represent one of the largest and most consistent wind fields on earth. They are strongest during their respective winter and spring months (Wyrtki and Meyers, 1976) (Fig.13).

The SPSA is confined by the Intertropical Convergence Zone (ITCZ) and the polar

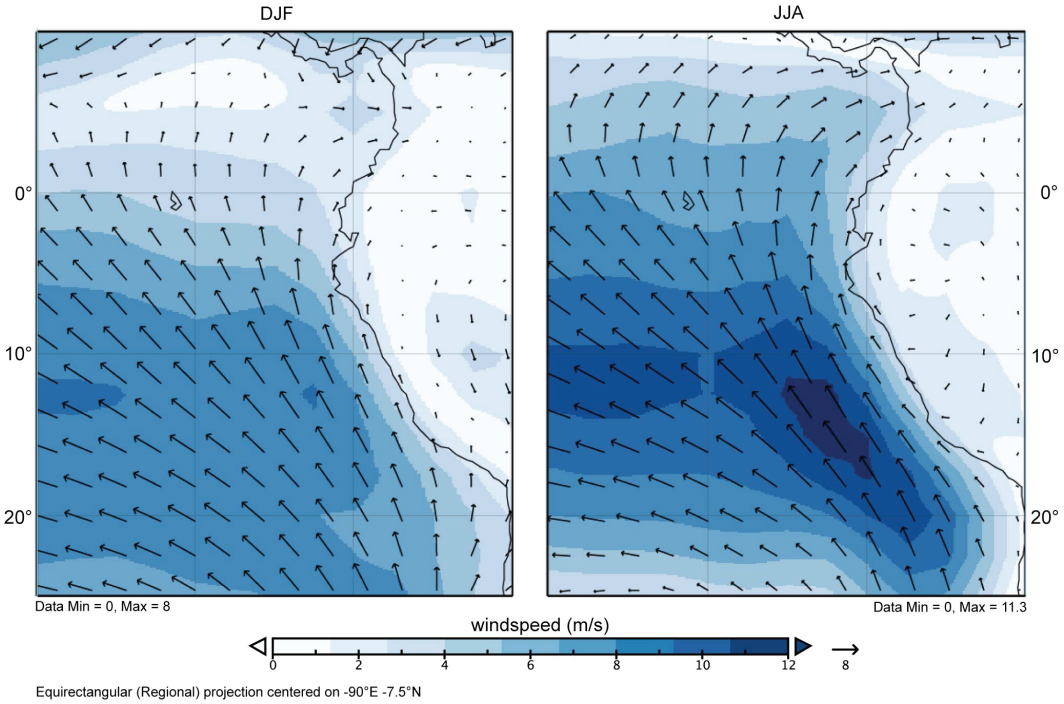

Figure 13: Climatological winds during austral summer and winter in the (sub-)tropical east Pacific. Winds are averaged from the NCEP reanalysis (Kalnay et al., 1996). Average wind speed during summer (December - February) and winter (June -August).

front, to the north and south respectively. The ITCZ, coinciding with the northern boundary of the study area, shifts from roughly 13°N in austral winter (June - September) to 5°N in austral summer (December - March) (Kalnay et al., 1996; Strub et al., 1998) (Fig.13). Together with the land-sea thermal contrasts, it influences surface winds as far as 5°S (Strub et al., 1998).

The eastern flank of the low-level anticyclonic circulation with southerly to southeasterly directions is very consistent in speed and direction above southern and alongshore Peru and northern Chile throughout the year. It is responsible for the distribution of dust over the ocean. According to Howard (1985), Lettau and Costa

(1978), and Garreaud and Muñoz (2005), the coastal southerlies represent a low-level jet that is oriented along the coast within the maritime layer. It is characterized by a maximum of ∼10 m/s surface wind speed about 150 km offshore (Garreaud and Muñoz, 2005) (Fig.13). This flow induces near-shore upwelling of cold water, which, in turn, is important for the thermal balance of the jet and strongly contributes to the aridity on land. At heights of 3-4 km, winds result from subsiding foehn circulation over the Andes from the Amazon basin and are thus easterly in direction (Howard, 1985; Rutllant, 2003). There are two circulation cells, above and beneath the subsidence inversion base, the upper of which is the more energetic. Its circulation is caused by the thermal contrast between the top of the marine boundary layer and the heated arid western slope of the Andes (Rutllant, 2003; Fig.9). Dust from Peru and Chile is incorporated in the lower atmosphere by local relief and southern winds, which often have an onshore and upslope component (e.g., Howard, 1985; Schwerdtfeger, 1976; Garreaud et al., 2003; Flores-Aqueceque et al., 2010). Wind erosion is associated with wind gusts (Flores-Aqueveque et al., 2010; Kurgansky et al., 2010). Supposedly, the dust is lifted into higher air layers and carried by the SE trade winds, which distribute it above the ocean.
Wind speeds at the southern coasts of Peru vary between 4-8 kn (2-4 m/s), becoming stronger further north, reaching an average of 13 kn (6.7 m/s) at 9°S and up to 10 kn (5.1 m/s) elsewhere along the coast (Schwerdtfeger, 1976) (Fig. 13).

2.3 Andean Geology

The clay mineral composition of terrigenous sediments as investigated in this study is - among other factors such as weathering conditions - dependent on its source-rocks on land (Chamley, 1989). The Andes are a magmatic mountain range with omnipresent metamorphic rocks. Their surface is mostly formed by volcanoes and granitic peaks. The absence of stratovolcanoes between 2°S and 15°S, representing a change in rock composition, is of particular interest. This volcanic gap in north-central Peru is caused by a flat subduction angle of the oceanic plate (Nur et al., 1981). While the volcanic cover of the northern Andes is composed of more basic andesites and quartzandesites, ignimbrites consisting of andesites as well as alkaline rhyolites to rhyodacites cover the Central Andes (Zeil, 1986). Precambrian shields outcrop in places in southern Peru and Chile.
Central Andean soils are mostly immature due to the combination of aridity, low temperatures, intense erosion, and frequent ash falls in and adjacent to the volcanic zones. The Pacific lowlands bordering the mountain range often display thick alluvial deposits (Potter, 1994).

2.4 Potential Dust Sources and Source Rocks

Besides the semi-arid and arid coastal areas of Peru and northern Chile, the Atacama Desert and the Altiplano Plateau (15-22°S) with its Salars and desert clay soils are favorable for dust production. Dust exported from the Altiplano can directly be entrained in tropospheric winds (Maher et al., 2010). Dust storms and dust devils are frequent there as well as around Iquique (20°S) at the Chilean coast (Goudie and Middleton, 2006; Kurgansky et al., 2010). Other acknowledged sources are reactivated desert dunes that have been produced under former drier conditions when clay aggregates were deposited during their formation or through post-depositional weathering (Goudie and Middleton, 2006; Pye, 1987). Such dunes are widespread in southern Peru and northern Chile (Howard, 1985). They provide silt and clay in substantial quantities, which can be entrained in the southeast trade winds during dust storms.

3. Materials and Methods

The surface sediment material was sampled at the Oregon State University Marine Geology Repository. It was originally obtained during 16 different cruises to the tropical (south-)east Pacific between 1969 and 2000 (S2). We assume all samples to be of late Holocene age from results of isotope measurements on foraminifera (Rincón et al., 2010), and because only the uppermost 2 cm were used for analyses. Grain-size distributions and clay-mineral compositions were analyzed on 75 and 70 samples, respectively. The samples were washed through a 63 μm mesh for foraminiferal studies published elsewhere (Rincón et al., 2010). Organic carbon and calcium carbonate (CaCO3) were removed from the fine fraction ($<$63 μm) with a 10% hydrogen peroxide (H_2O_2) solution and a 10% acetic acid (H_3C-COOH) solution, respectively. The silt (2-63 μm) and clay ($<$2 μm) fractions were separated using the Atterberg settling method (Ehrmann et al., 1992).

We measured the grain-size distribution of the siliciclastic silt fraction with a Beckman-Coulter laser particle sizer. Besides organic matter and calcium carbonates, biogenic opal was removed boiling the samples with excess NaOH for 10 minutes. Microscope analyses confirmed that this method successfully removed all biogenic components. Shortly before the analysis, a few mg of $NaPyPO_4$ were added and brought to boil in order to avoid coagulation of particles. In order to prevent a bias caused by a different scattering behavior of elongated (or other shaped) particles, grain-size measurements with a laser particle sizer lasted 90 s each, during which the sample suspension was continuously pumped through the lense.

For clay-mineral composition analyses, the clay fraction was homogenized in an agate mortar. 40 mg of each sample together with an internal standard (1 ml of 0.4% molybdenite suspension (MoS_2)) were re-suspended for more consistent semi-quantitative measurements. Vacuum filtration of the suspension on membrane filters

produced texturally oriented clay films with thicknesses of 50 to 100 μm (Petschick et al., 1996), which were then dried and transferred onto aluminum platelets (see Ehrmann et al., 1992). The samples were measured with CoKα-radiation (40kV, 40 mA; λ=1.79Å) on a Philips PW 1710 goniometer equipped with an automatic divergence slit, and a graphite monochromator. To identify overlapping (clay) mineral peaks such as smectite and chlorite, the samples were glycolated at 60°C for at least 12 h with the effect of widening the basal distance of smectite to 17Å (Tucker, 1996) and measured from 2 to 40° 2θ with a step size of 0.02° 2θ. To distinguish the (002) kaolinite (3.58Å) and (004) chlorite peaks (3.54Å), the area between 28° and 30.5° 2θ was additionally scanned with steps of 0.005° 2θ. The diffractograms were later processed with the graphically based Macintosh Apple computer program 'MacDiff 4.2.5' (Petschick et al. 1996, available at http://www.geologie.uni-frankfurt.de/Staff/ Homepages/Petschick/Classicsoftware.html).
The relative clay-mineral contents (rel%) of illite, smectite, chlorite and kaolinite were determined semi-quantitatively by calculating the integrated peak areas of the clay-mineral basal reflections, weighted with the empirically determined factors after Biscaye (1964, 1965). These factors were used to ensure comparability with previous research (Petschick et al., 1996; Lamy et al., 1999). Despite of several former studies (Dauphin, 1983; Molina-Cruz and Price, 1977; Prospero and Bonatti, 1969) that already considered the quartz content in SE Pacific sediments as an indicator for eolian-derived material, we also investigated the quartz and feldspar distributions in the clay fraction, which represent two noteworthy components of SE Pacific sediments containing valuable information. We built the ratios of the peak area of each of the considered (clay)-minerals to the sum of all peak areas, assuming them to represent 100%. Quartz contents are generally low in the clay fraction due to the presence of clay minerals.

3.1 Statistical Analysis

We applied the end-member modeling algorithm (EMMA) of Weltje (1997) to the siliciclastic grain-size data set in order to identify the original sediment populations that contribute to the terrigenous fraction of surface sediments. The minimum number of end members needed to model the variance in the data set satisfactorily is determined by the coefficients of determination for several different models. This 'goodness of fit' is calculated for each size class and represents the squared correlation coefficient (r^2) of the input variables and their approximated values (Prins and Weltje, 1999; Weltje, 1997).

For a more comprehensive understanding of the sediment provenance, we performed a K-means cluster analysis on the Biscay-factor weighted clay-mineral assemblage data. This allows a more precise characterization of the source areas,

as the composition of the cluster center ideally represents an approximation of the source material composition. The clay-mineral assemblage data is a compositional data set, summing to 100%. To carry out multivariate statistical analyses, this data set has to be transformed to a vector space structure applying a log-ratio (Pawlowsky-Glahn and Egozcue, 2006 and references therein). In case of a K-means cluster analysis, the transformation of choice is a centered log-ratio. Different cluster configurations (2 to 10 clusters) were calculated with 100 replicates each. In order to obtain the optimal number of interpretable clusters, we calculated the Davies-Bouldin Index (Davies and Bouldin, 1979) (S3). The lower the index, the more compact are the clusters and the greater are the distances between the cluster centers. Starting with the least number of clusters, the first local minimum of the index thus represents the cluster number of choice. Each sample belongs to only one cluster.

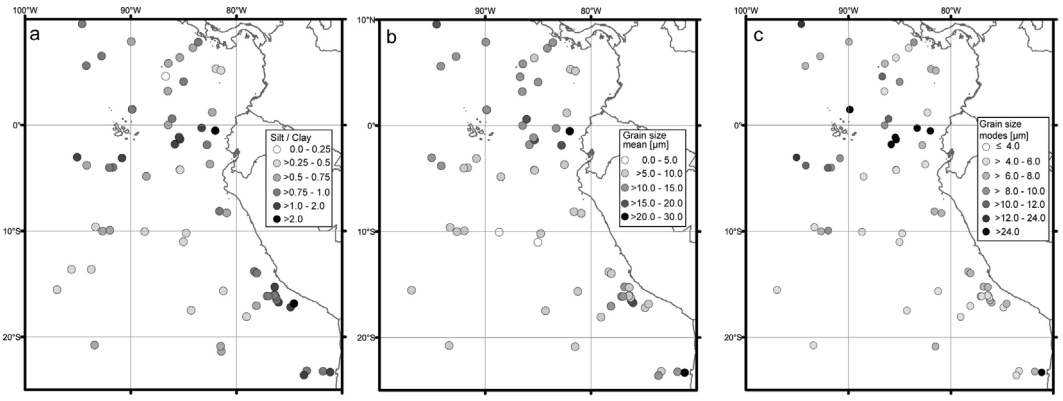

Figure 14: Grain-size analyses. Weight percentages from Atterberg settling method **a** Siliciclastic silt/clay ratio, **b** Grain-size means show comparable results to the silt/clay ratio, **c** Grain-size modes.

4. Results

A first rough grain-size analysis, separating the lithogenic silt and clay fractions with the Atterberg settling method resulted in higher silt contents close to the South American continent. Silt/Clay ratios exceed 2.0 even west of the Peru/Chile Trench. The silt content decreases with increasing distance from the coast in the Peru Basin but remains high around Carnegie Ridge and the Galapagos Islands (Fig. 14). Grain-size analysis of the silt fraction with a laser particle sizer resulted in grain-size distributions of 0.4 μm to, at most, 96.5 μm in 60 size classes. Even though the samples were sieved with a 63 μm mesh, up to three size classes larger than the cut-off value were measured due to elongated shapes of the particles that fit through the mesh, while the idealized spheric shapes do not. Grain-size distributions turned out

to be polymodal, but always displayed one dominating mode. If 'mode' or 'modal grain-size' is not specified, we always refer to the dominant modes of the grain-size distributions. The minor modes are residues of the end-member analysis and not of interest here. Modal grain-size of the dominant modes varies between 4.05 and 60.5 μm, with offshore fining trends in the Peru Basin, while there is no trend visible north of the equator and values (up to 24 μm) are extremely high around the Galapagos Islands, Carnegie Ridge and Galapagos Rise (Fig. 14). Finest sediments are found in the deepest areas of the central Peru Basin, with medians of 4.4 μm and less (not shown). Grain-size analyses of a few sediment samples including all size fractions to test the validity of silt representing the eolian-derived sediment fraction resulted in comparable distributions (S4), with the dominant modes ranging between 2 and 5 μm. The fraction >63 μm that remained after dissolution of carbonate, biogenic opal, and organic carbon is composed of volcanic glass and/or authigenic particles, but not of terrigenous sand, and therefore does not influence our inferences about terrigenous sediments transported to the ocean.

For the end-member model the number of input variables, i.e. the number of size classes, was reduced to 58, due to the general fine-grained nature of the sediments. According to the results for the coefficients of determination we determined the 4 end-member model to best approximate our data (Fig. 15). Figure 15 displays the grain-size classes plotted against the coefficients of determination. The models with 2 and 3 end-members show a weak approximation (r^2 <0.6) of grain-sizes between 20 - 30 μm. The 4 end-member model is the one of choice because it reproduces the data well, with a mean coefficient of determination of r^2 = 0.88, still comprising an interpretable number of end members (EM) (Fig. 15).
Figure 16 shows the four end members, i.e., the distributions of the original grain-size populations (Fig. 16a), as well as their proportions (Fig. 16b-e), which, in sum, approximate the measured grain-size distribution of each sample. EM1 represents nearly all the samples in the central Peru Basin and the most western locations on Nazca Ridge (proportions of 0.8-1). It is the finest of the four end members with the dominant mode of 4.88 μm. EM2 largely overlaps with EM1, but has a distinctly coarser dominant mode of 5.88 μm. It shows the largest proportions in the locations closest to South America - also in the Panama Basin, and on and around the Galapagos Rise. The most distinct and the coarsest of all is EM3, being confined to the Carnegie Ridge and northwest of the Galapagos Islands. Like EM2, EM4 does not show a clear pattern north of the equator but concentrates around the ridges and the Galapagos Islands. These end members overlap considerably in their peak area, but have distinctly different dominant modes, of 5.88 and 9.37 μm, respectively (Fig. 16a).
Quartz, plagioclase and K-feldspar contents in the clay fraction all decrease from

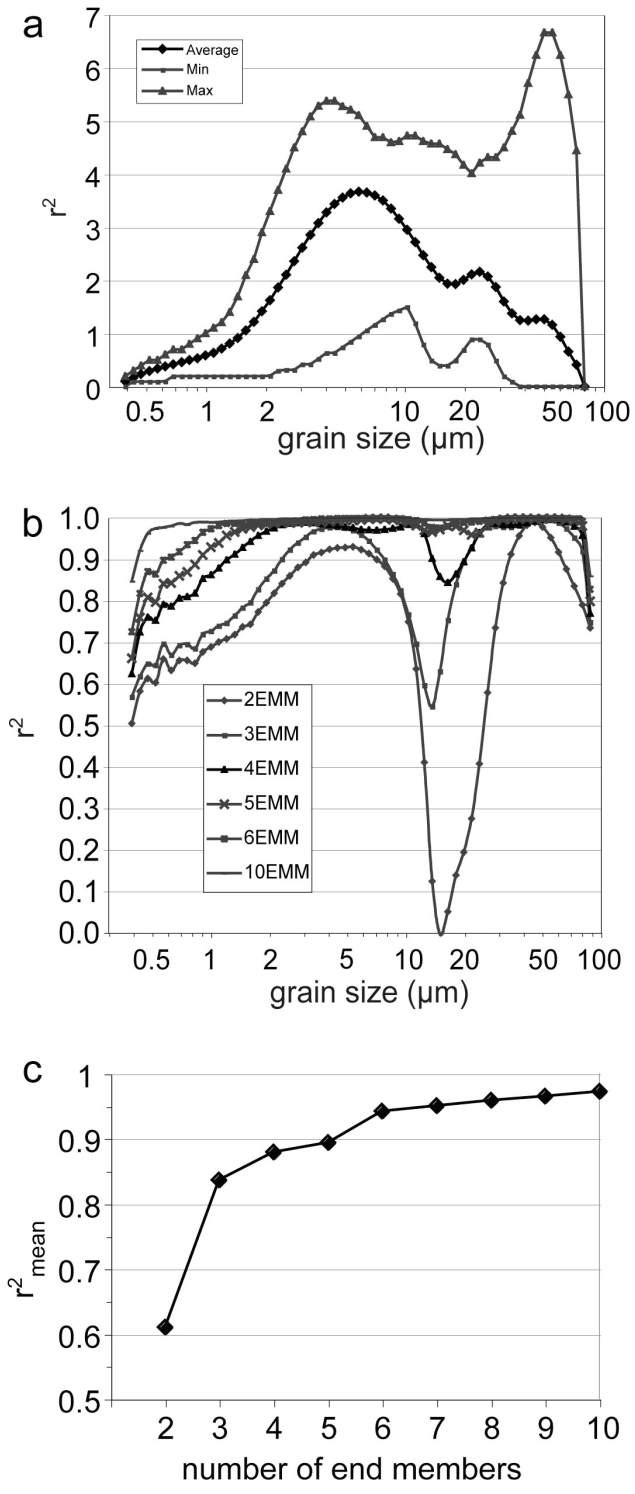

Figure 15: End-member modeling results of surface sediment samples. **a** Summary statistics of input data (grain-size distributions, n = 75), maximum, mean and minimum frequency recorded in each size class; **b** coefficients of determination (r^2) for each size class of model with 2-10 end members; **c** mean coefficient of determination (r^2) of all size classes for each end-member model

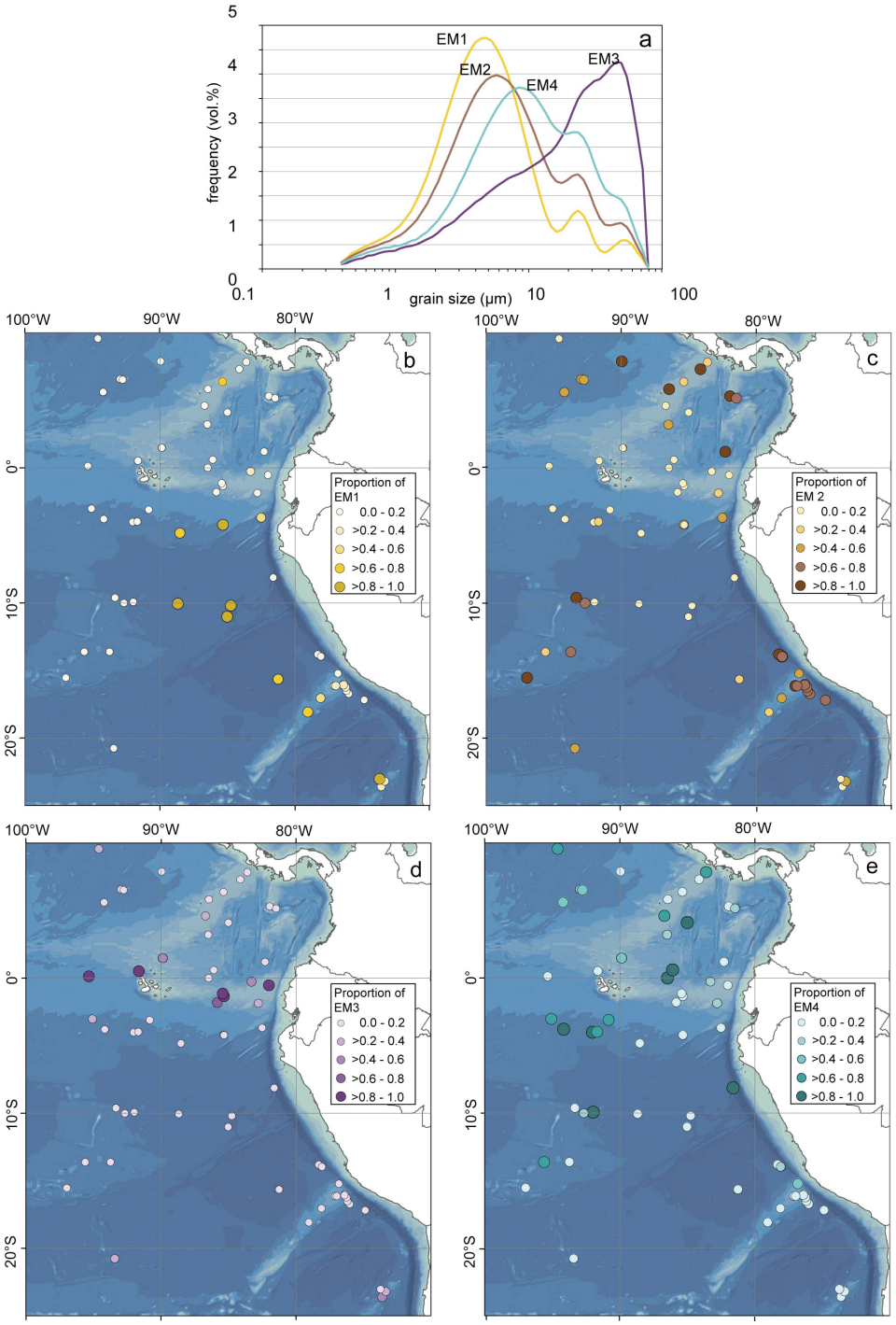

Figure 16: Modeled end members of the terrigenous silt fraction from the Southeast Pacific. **a** grain-size distributions of the 4 end members; **b-e** spatial distribution of the proportions of each end-member.

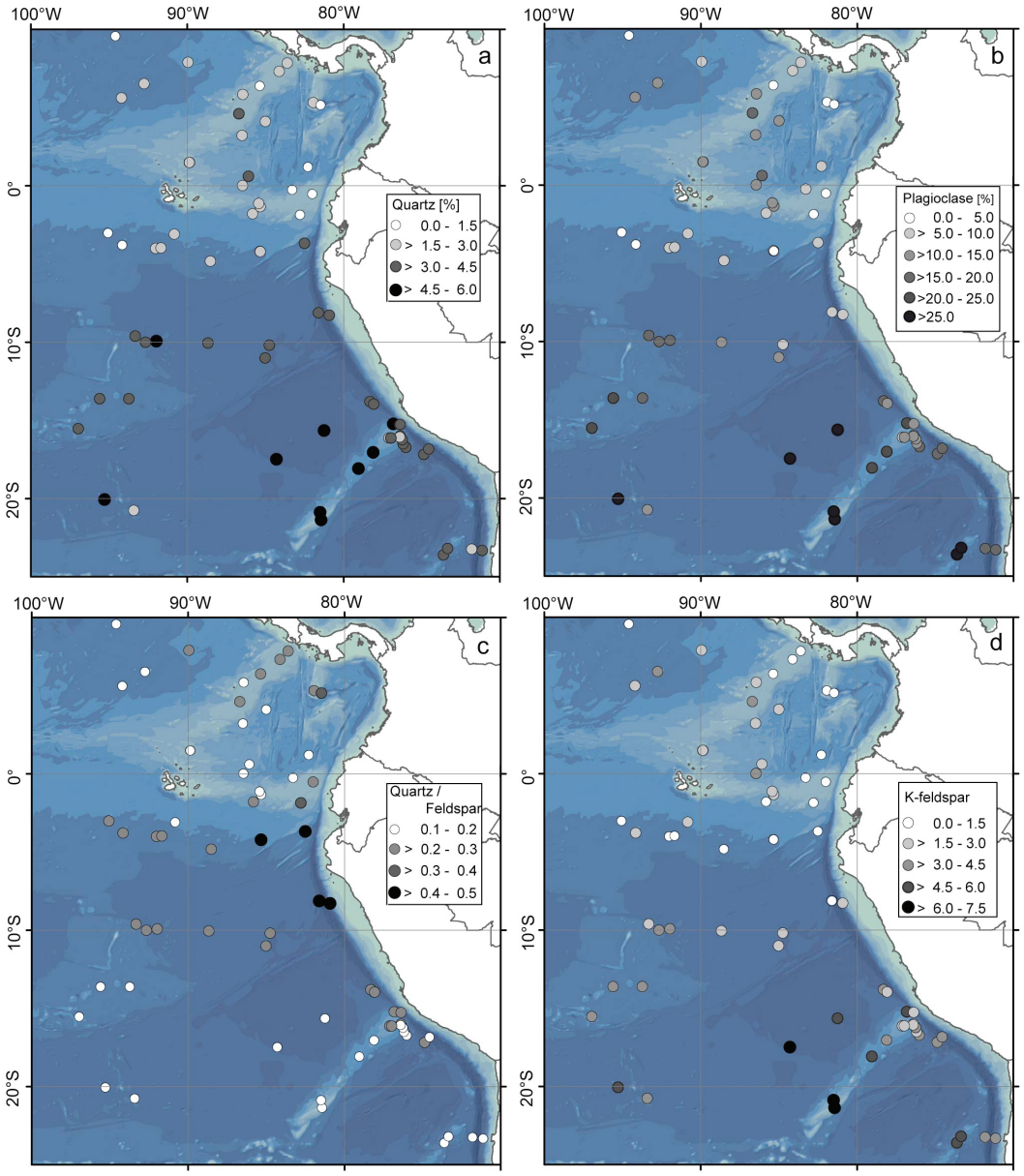

Figure 17: Quartz and feldspar contents in the clay fraction of the surface sediment samples. **a** quartz; **b** plagioclase; **c** quartz/feldspar ratio; **d** k-feldspar

the Nazca Ridge towards the Carnegie Ridge, pointing to southeastern terrigenous sources (Fig. 17). In our study, lowest quartz contents (<3%) appeared north of about ∼5°S with two exceptions on Cocos Ridge (4.6°N, 86.7°W) and just north of the Carnegie Ridge (0.6°N, 86.09°W). Even though generally very low in the clay fraction, plagioclase and quartz both revealed relatively high values on Galapagos Rise.

Considering the four major clay-mineral groups, i.e., smectite, illite, chlorite

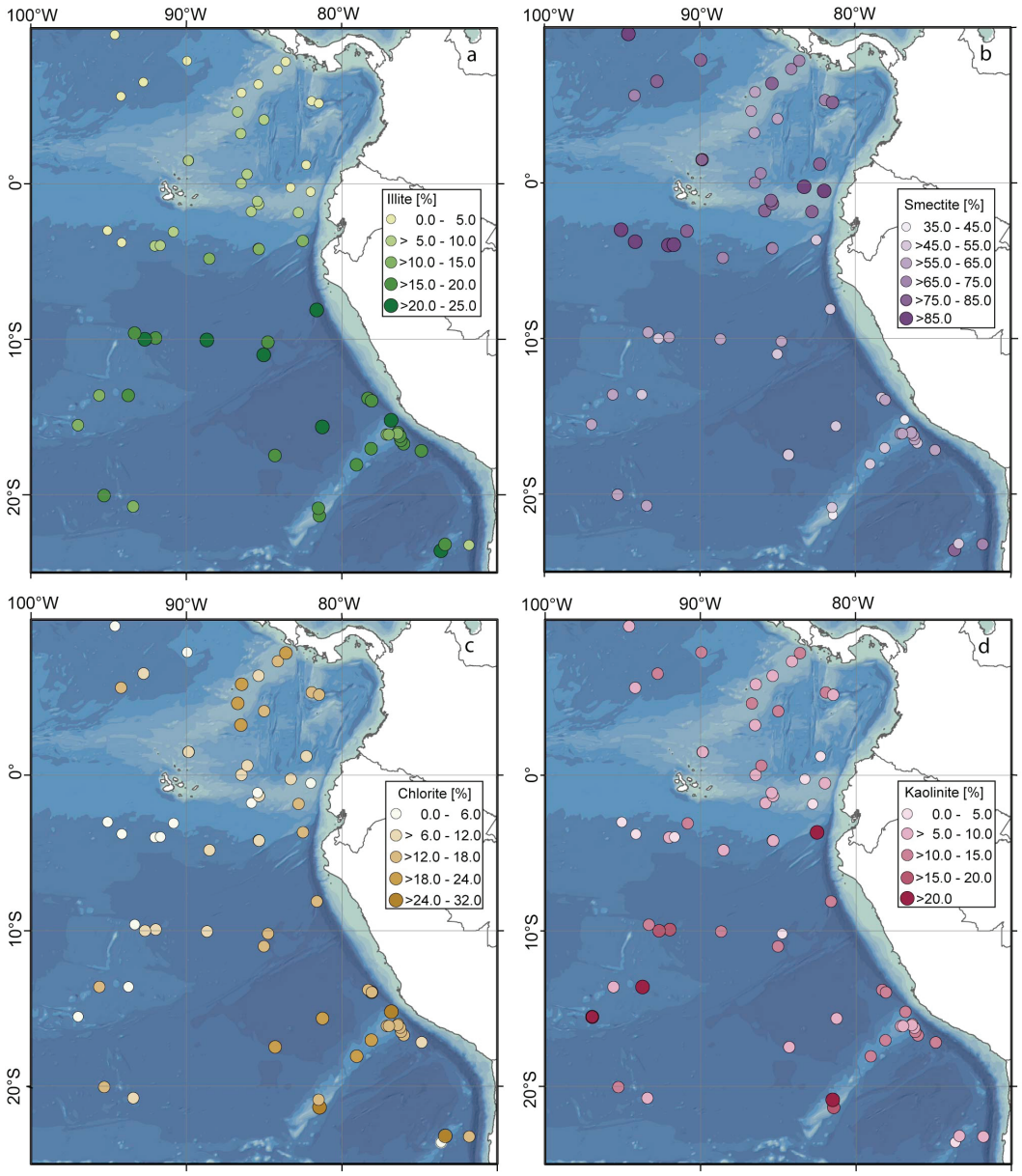

Figure 18: Clay-mineral distributions in the Southeast Pacific: **a-d** contents (%) of **a** illite, **b** smectite, **c** chlorite, and **d** kaolinite in the clay fractions

and kaolinite, and applying the factor weighting after Biscay (1965), our analyses

mostly corroborate global clay-mineral compositions of recent ocean sediments, with the exception of kaolinite (Chamley, 1989) (Fig. 18d). Smectite is by far the most abundant clay mineral in the whole study area, with contents spanning from 35% in the south to up to 97.5% around the Galapagos Islands and on the Carnegie Ridge. Contents are elevated along the Galapagos Rise, but low in the central Peru Basin and on the Nazca Ridge. Values from 55% to 85% north of the equator point to an additional source located between 5 and 10°N. Illite, in contrast, is most abundant in the southern half of the study area, decreasing in a north-northwestern direction (Fig. 18a). Values reach up to 25% off Peru and on the Nazca Ridge in the southeast. Lowest contents have been recorded in the Panama Basin.

Chlorite points towards the same source areas as illite, although its distribution pattern is less well defined and constrained further to the south. It is the second most abundant clay-mineral group with values spanning from 0% south of the Galapagos Islands to 32% on Nazca Ridge. In contrast to illite, there is a source of chlorite in central America, as elevated contents of $>$20% have been recorded on the Cocos Ridge, while chlorite is not present around the Galapagos Islands and the Carnegie Ridge (Fig. 18c). Kaolinite does not show the typical distribution connected to extensive chemical weathering expected in tropical areas (Chamley, 1989). It depicts a patchy pattern without any distinct areas as the other mineral groups. Kaolinite reaches contents of $>$15% on the Galapagos Rise, north of the Galapagos Islands and the southern end of the Nazca Ridge, suggesting submarine sources there (Fig. 18d).

The Davies-Bouldin Index that we used as goodness of fit statistics for the K-means cluster analysis (S5) of the clay-mineral composition data suggests 4 clusters to best represent the data with a minimum number of clusters. Figure 19 shows the four cluster centers. Cluster 1 represents surface sediments from the Nazca Ridge and the Peru Basin and possibly also offshore northern Chile, where samples are scarce. Its cluster center comprises relatively high contents of illite and chlorite, while smectite is reduced to 53%. By contrast, cluster center 2 is largely dominated by smectite (84%) while the other three clay mineral groups are almost negligible. Samples clustering around this center are confined to the Carnegie Ridge and the Galapagos Islands. It is closest in composition to cluster center 4, which differs mainly in its much higher content of chlorite (16%). Its spatial distribution is confined to the Panama Basin. Cluster center 3 is characterized by its relatively large contents of kaolinite (17%) and illite (15%). It is the least confined cluster, including patches of sediment samples on the northern and southern rim of the Carnegie Ridge and most samples from the Galapagos Rise as well as one single sample off southern Peru.

5. Discussion

Dust plumes in the atmosphere above the SE Pacific are rarely caught on satellite images (http://visibleearth.nasa.gov/view_rec.php?id=999), and haze recordings more than a few hundred kilometers offshore are sparse (Prospero and Bonatti, 1969). Nevertheless, because of the results of clay mineralogical analyses and the fine-grained nature of our sediment samples (see below), we believe that our results for recent sediments from west of the Peru-Chile Trench south of $\sim$5°S solely depict eolian dust from the coastal deserts of Peru, but do not incorporate fluvial input signals. First of all, there are no major rivers to be found in the arid areas of South America. Macharé and Ortlieb (1992) found evidence for eolian deflation - not precipitation and runoff - to be the dominant erosive agent at the central coast of Peru. The existing streams are short and mainly transport coarse debris (Potter, 1994; Dunne and Mertes, 2007). Second, the Peru-Chile Trench forms a physiographic barrier, catching the majority of fluvial sediments. The little fluvial material transported offshore in nepheloid layers is outweighed by the eolian-derived sediment component (Krissek et al., 1980; Scheidegger and Krissek, 1982).

5.1 The Provenance of Dust in SE Pacific Sediments

The lobes formed by the quartz, illite, chlorite, and - more southern - the plagioclase distribution (Figs. 17, 18) and their decreasing tendencies from south(east) to north(west) in our study area reflect the major wind field of the SE trade winds and point to them as the major agent of transport of terrigenous material (compare Figs. 13 and 17, 18). Prospero and Bonatti (1969) found quartz to be the prevalent mineral in atmospheric dust collected in the northern Peru basin, followed by plagioclase, muscovites (i.e., illites), smectites and chlorites. Flores-Aqueveque et al. (2009) also determined quartz and feldspars as the prevalent minerals in sands of the coastal desert of northern Chile. This corresponds to our findings (Figs. 17, 18). The sources and transport pathways of the terrigenous components deposited on the Nazca Ridge and in the Peru Basin, are to be distinguished into two separate areas latitudinally. This difference is not as clearly visible in the grain-size distributions, nor shown in previous studies (e.g., Molina-Cruz and Price, 1977; Dauphin, 1983) using quartz contents to represent patterns of terrigenous input. Quartz, feldspars and illite are all products of physical weathering as typical for arid areas, and are among the main components of desert dust (e.g., Flores-Aqueveque et al., 2010). From modeling studies (e.g., Tanaka and Chiba, 2006) we know that the Peruvian coasts, the arid inland areas of southern Peru, the coastal areas of Chile and the semi-arid areas along the western Andean foothills are potential sources of dust. While both source areas, the northern/central Peruvian coast and the Atacama/Altiplano region further south, deliver quartz to our study area, highest quartz contents on the Nazca Ridge and in the southern Peru Basin a few hundred kilome-

ters offshore point to the southern area as the stronger source. Closer to the coast smectite derived from the volcanic chain, restarting in the latitude of the Nazca Ridge, dilutes the quartz signal. The general decreasing trend of quartz contents in a north-northwestern direction was not recognized in the study of Molina-Cruz and Price (1977), which includes samples from the continental margin, and thus fluvial material, overprinting the eolian signal. Scheidegger and Krissek (1982) found latitudinal geological differences mirrored in the quartz/plagioclase ratio of marine surface sediments. We confirm the higher quartz/feldspar ratios off northern Peru due to reduced amounts of plagioclase but also K-feldspars north of ∼15°S. However, we cannot detect a similarity of dispersal patterns of (clay)-minerals or grain-size distributions to surface current patterns, diverted west off northern Chile/southern Peru and northwest off central/northern Peru, in our data as suggested by Scheidegger and Krissek (1982). Instead, the north-northwest trending lobes of quartz, illite and plagioclase (Figs. 17a and b, Fig. 18a) in our opinion reflect the distribution of dust via the main wind field of the trade winds. However, we have also detected eolian input from the central Peruvian coastal deserts in a western direction. As mentioned above, easterlies are prevalent around 7 - 8°S from June - October, suggesting eolian transport off northern Peru in a westerly direction, and a northwesterly direction from the Atacama Desert, contrasting the interpretation of Scheidegger and Krissek (1982). The major differences of the two source areas, i.e., the coastal desert of Peru and the Atacama Desert in northern Chile, are the amounts of feldspars and chlorite (Figs. 17, 18). Quartz and feldspars are products of weathered volcanic rocks as well as physically weathered metamorphic rocks and are delivered from both source areas. However, feldspar weathers much faster than quartz and is usually an indicator of freshly weathered source rocks. It is reduced off northern Peru where the source rocks are mainly granitic intrusives instead of freshly weathered basaltic and gabbroic rocks. Especially weathered andesites deliver high amounts of plagioclase (Fig. 17b) (cf. Scheidegger and Krissek, 1982). Its absence off North-Central Peru corresponds to the gap in the volcanic chain of the Andean Cordillera (Zeil, 1986; Orme, 2007). Ignoring the sub-aqueous sources of plagioclase (see below), the spatial distributions of feldspars display a decreasing trend in north-northwestern direction and thus point toward the southern source in northern Chile (cf. Stuut et al., 2006). As a consequence, the ratio of quartz/feldspars depicts a dust plume extending from the coastal desert of Peru north of ∼15°S (Fig. 17c) as it was presented by Molina-Cruz and Price (1977).

In contrast to Scheidegger and Krissek (1982) who refer to the findings of Rosato and Kulm (1981) on clay-mineral abundances, we do think clay-mineral composition is a sensitive indicator of dispersal patterns providing information for the entire study area, not just for the continental margin. Besides, the study area of Rosato and Kulm (1981) is considerably smaller than ours, focusing on sediment input

from central Peru only. They did not relate their data to specific geologic provinces. Like quartz (Leinen et al., 1986), illite is a robust indicator of dust in the South Pacific (Windom, 1976). It strongly supports the hypothesis of dust entrainment from the semi- and hyperarid coastal areas and the Atacama Desert as inferred from the quartz distribution of this study. Our findings of 20-25% of illite around the Nazca Ridge agree well with the average illite concentration in all of the South Pacific of 26% (Windom, 1976), but disagree with the findings of Rosato and Kulm (1981) who detected illite contents of 30-50% in the Peru Basin. In contrast to quartz, illite contents are as high off northern Peru as off southern Peru (Figs. 17a, 18a) as it is derived from the desert dust and omnipresent weathered metamorphic rocks, and the outcropping Precambrian basement of the Coastal Cordillera. Unlike the feldspars or quartz, which decrease off central and northern Peru, it is not a product of Quaternary volcanic rocks that are absent between 2°S and 15°S due to the volcanic gap. Illite continuously decreases in a northern direction, even across the equator. This indicates dust transport from the southern source areas at least as far north as the austral summer position of the ITCZ.

Like quartz, chlorite displays highest contents further offshore on Nazca Ridge and in the southern Peru Basin rather than closer to the coast, indicating its southern origin. It points to a major source in the granites of southern Peru and the Atacama Desert in northern Chile. This interpretation differs from Rosato and Kulm (1981) who attribute the main source to the coastal batholith of Peru due to highest chlorite values on the continental margin.

In our results of the k-means cluster analysis, which allocates each sample to only one cluster center, the southern samples all cluster around center 1, which includes the highest illite and chlorite contents of all clusters, adding up to 36%. Inferred from the composition of this cluster center, this represents the dust-dominated sedimentation part of our study area (Fig. 19). It comprises the area of influence of both major dust source areas, the Nazca Ridge and the Peru Basin, extending onto the Galapagos Rise. This is also the area where the ubiquitous but much less abundant smectite originating from freshly weathered volcanic rock is obviously diluted by the other mineral groups. Kaolinite is highly variable (cf. Rosato and Kulm 1981) in this area and therefore does not contribute to the characterization of its sediments. Sediments from the Galapagos Rise also contain dust derived from the arid areas of Peru and Chile (see above and Figs. 17 a and b, 18 a), but are highly influenced by authigenic particle formation. They mainly cluster around cluster center 3, which displays rather high contents of kaolinite, typical of submarine weathering of K-feldspars (Rex and Martin, 1966) but still considerable amounts of illite from eolian input. High values of quartz and plagioclase on the Galapagos Rise, however, can be attributed to submarine volcanic activity, rather than to eolian input (Peterson and Goldberg, 1962; Bonatti and Arrhenius, 1970; Byerly et al., 1976; Wright, 2004).

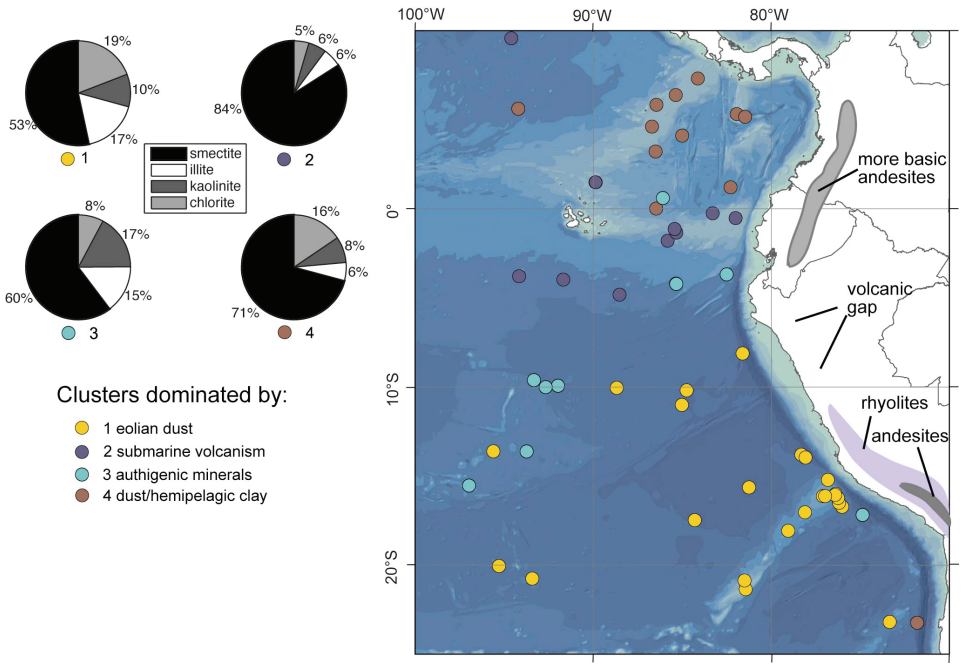

Figure 19: K-means cluster analysis of clay-mineral distributions (rel.%), identifying four clusters. The compositions of the four cluster centers and their attributed meaning are shown on the left. Indication of geological provinces taken from Zeil, 1986.

5.2 The Eolian Signal on Nazca Ridge and the Peru Basin

Eolian mineral dust grain-sizes in the SE Pacific are smaller than those found in the major dust study areas such as off West Africa (Fig. 14 this study; Dauphin, 1983; Stuut et al., 2005), but comparable in size to those found in northern Pacific sediments (medians of ∼3-8 μm (Rea and Hovan, 1995)). This is because most of the dust transported to the southeastern Pacific is not injected into the higher atmosphere but incorporated into the low level trade winds (Dauphin, 1983) and larger dust grains (>20 μm) are removed quickly due to gravitational fallout when transported offshore (Prospero and Bonatti, 1969). We attribute the two end-members with the finest dominant modes to eolian input to our study area (Fig. 16). EM1 represents nothing but eolian dust. It is spatially distributed in the Peru Basin with a constant distance from the South American coast as it represents the fine dust component sorted along its transportation path by gravitational fallout, as already suggested by Prospero and Bonatti (1969). The fine mode of EM1 (4.88 μm) agrees well with the modes of grain-size analyses of dust collected from the atmosphere by Prospero and Bonatti. During their dust collection study in the equatorial east Pacific, they determined dominant modal grain-sizes of 2-5 μm for single dust collections southwest of the Galapagos Islands (downwind in our study area) with a

particle settling technique. The findings of Dauphin (1983) for quartz grain-sizes from the Peru Basin match our results very well, even though we investigated the complete lithogenic silt fraction. Results from Dauphin show grain-size modes of 7-8 Φ for the Peru Basin, corresponding to 4-8 μm in our study (Fig. 14). By contrast, mean grain-sizes are coarser in our study area than dust collected south of 25°S (2.3 μm at 30°S (Wagener et al., 2008)). This difference marks the southern boundary of the dust pathways from the western South American deserts via the southeast trade winds.

The mapped proportions of EM1 (Fig. 16) are noticeably uniform in the deepest parts of the Peru Basin, all samples being equally well represented by this end member (proportions of 0.8-1). The uniformity in grain-size distribution is attributed to subsequent redistribution by bottom nepheloid layers in the basin as stated by Krissek et al. (1980). EM2 in our opinion is not a real end member but incorporates two different sediment populations that can be distinguished due to their geographical distribution: It approximates well most samples close to the South American continent between 3°S and 20°S and between 10°N and 0°. Combined with EM1, this represents the eolian input from the coastal deserts in Peru and the Atacama Desert in northern Chile, exhibiting a fining trend towards the open ocean. North of the equator the presence of EM2 suggests wet deposited dust in the doldrums (Fig. 16). The grain-size distributions of sediments from the Panama Basin represented by EMs 2 and 4 are a consequence of interfering transport agents and source areas. Some dust is transported via the Trade winds from Ecuador and northern Peru when it turns into a northeasterly direction offshore Ecuador. Prospero and Bonatti (1969) identified a dust source in the arid regions of western and southern Mexico for the northwestern Panama Basin. However, strong bottom water currents and thus sediment redistribution (Heath et al., 1974) play a major role in the redistribution of sediments (Lonsdale, 1976). Eolian input to the Panama Basin will be discussed in more detail later.

The seven samples retrieved from the Galapagos Rise are exceptional in their grain-size distribution as well as in all other proxies investigated. Sediments do not consist mainly of dust and biogenic opal and/or carbonate as sediments from Peru Basin, but are largely limited to authigenic particle formation at the ultra-slow spreading ridge (Wright, 2004), such as iron-manganese oxides or quartz and feldspars (cf. Bonatti and Arrhenius, 1968; Byerly et al., 1976). This makes their grain-size distributions exceptionally coarse. EM2 and EM4 best approximate grain-sizes in the area of the Galapagos Rise, since together they comprise the whole unsorted silt fraction of 2-63 μm. We thus corroborate the study of Krissek et al. (1980) who found considerable amounts of sand and silt-sized material in sediments from the Galapagos Rise originating from hydrothermal processes.

5.3 Terrigenous Input to the Carnegie Ridge and the Panama Basin

As mentioned above, the illite data indicate dust transported as far north as 5°N with the major wind field of the trade winds (Figs. 13, 18). This observation could not be resolved with the grain-size data. EM3, characteristic for sediments around the Galapagos Islands and Carnegie Ridge, together with EM4 represents very coarse-grained volcanic glass originating from the Galapagos Islands. It is the area of the highest smectite values that are fed by different sources. Wet chemical weathering of volcanic rocks and basic submarine volcanism are generally known to produce major amounts of smectite (Chamley, 1989). As precipitation and thus wet chemical weathering as well as continental and submarine volcanism are omnipresent in the area of the doldrums, so is smectite. Samples from the Carnegie Ridge and south of the Galapagos Islands thus cluster around cluster center 2 (average smectite content 84%) of the K-means cluster analysis (Fig. 19). The Equatorial Undercurrent (Strub et al., 1998) most likely distributes material from the Galapagos Islands to the east. Prospero and Bonatti (1969), however, found also considerable amounts of smectite in dust samples from northeast of the Galapagos Islands, which they related to semi-arid source areas in Ecuador and northern Peru. On the continent, the area dominated by cluster 2 corresponds to the area of extreme climatic contrasts with interchanging humid and arid conditions, i.e., wet-chemical weathering and (smectite-rich) dust production. The area experiences easterly winds in austral summer. The signal we retrieved from surface sediments very likely contains smectite from both windborne dust and submarine volcanic debris (cf. Heath et al., 1974), but also fluvial debris originating from the Gulf of Guayaquil on the eastern end of the Carnegie Ridge (Rincón et al., 2010). By contrast, dust samples from the atmosphere above the Panama Basin, the Cocos Ridge and the Guatemala Basin were dominated by plagioclase, pointing to a dust source in western and southern Mexico (Prospero and Bonatti, 1969). Our results for plagioclase also show increased values on the Cocos Ridge, but also across the saddle of the Carnegie Ridge. It is not clear, whether this reflects dust and/or submarine sources. Additionally, the quartz/feldspar ratio is increased on the Cocos and Coiba ridges extending south from Central America. Smectite, and especially chlorite are also increased on the ridges.

During boreal winter, strong winds cross the Panama Isthmus. Dominant northeast trade winds result in decreasing rainfall from east to west in the northern parts, while the equatorial low causes extreme (unstable convective thunderstorm) precipitation within the ITCZ (Bundschuh et al., 2007). Dust transported across Central America from above the Atlantic might thus be a minor contributor to these signals (Prospero and Bonatti, 1969; Prospero and Lamb, 2003; Liang et al., 2009), but chlorite and most likely quartz seem to be related to a local source in Costa Rica. Inland of the Cocos Ridge, the Cordillera de Talamanca corresponds to a gap of the

otherwise closely spaced Quaternary stratovolcanoes that are most likely sources of airborne smectite. The Cordillera de Talamanca, however, is interspersed with batholiths and granitoid intrusions (Abratis, 1998), and probably the provenance of quartz and chlorite. Despite the identification of the source area, we cannot prove the transport agent for these terrigenous sediments, which might be eolian as well as hemipelagic. After all, fluvial erosion is predominant due to heavy rainfalls in the doldrums (Bundschuh et al., 2007). According to Heath et al. (1974) fluvial input and further distribution by intermediate water currents are responsible for the increased chlorite contents on the ridges. Our K-means cluster analysis resulted in one cluster that is confined to Panama Basin. This cluster center 4 represents sediments relatively rich in chlorite, while smectites remain the predominant mineral group, emphasizing the dominant northern provenance of surface sediments in the Panama Basin.

6. Conclusions

Based on clay-mineral and grain-size distribution data obtained from surface sediment samples from the SE Pacific, the following conclusions can be drawn: (1) Clay-mineral compositions of surface sediments allow the identification of different geological provenances also in offshore areas of the SE Pacific. We were able to confine the smectite-dominated sedimentation areas to the continental areas influenced by extensive tropical rainfall related to the ITCZ. Furthermore, the smectite and plagioclase distributions in marine surface sediments mirror the volcanic gap between 2° and 15°S.

(2) The illite content in the clay fraction is a valuable indicator of dust supplied from the Atacama Desert as preserved in marine sediments in the SE Pacifc.

(3) Wind is the major transport agent of terrigenous sediments west of the Peru-Chile Trench between 5°S and 25°S. Dust is distributed over the ocean by the south-east trade winds.

(4) The Nazca Ridge receives considerable amounts of eolian-derived silt-sized material from the semi- and hyper-arid areas of South America and is therefore an area suitable for paleo-dust research.

(5) Different proxies are necessary to differentiate between hemipelagic and eolian sediment transport in the Panama Basin. Due to strong bottom water circulation overprinting the terrigenous supply to the basin we have not been able to identify transport agents satisfactorily.

(6) Areas of low sedimentation rates and authigenic particle production render the interpretation of end-member analysis results as presented here difficult, because some of the obtained end-members incorporate more than one original sediment population and are thus no true end-members by definition. Nevertheless, the area dominated by eolian-derived terrigenous supply was identified by combining the

results of clay-mineral compositions and grain-size distribution of the surface sediments.

7. Acknowledgements

We thank R. Fröhlking and S. Wiebe (AWI) for technical support in the lab and Hannes Schmidt for clay-mineral sample preparation. We also thank D. Heslop (University of Bremen) for analytical support. T. Laepple kindly provided his expertise plotting NCEP data. Core-top samples were provided by the Marine Geology Repository at the Oregon State University. We thank Bobbi Conrad and Alan Mix for support during sampling. G.-J. Weltje is acknowledged for providing the end-member modeling algorithm. The German Science Foundation financed this study within the project Ti 240/17 (DFG).

Supplementary Material

S1. Table of samples analyzed for this study

ship	cruise	hole/sample	latitude	longitude	water depth (m)	depth (cm)	device	year
Melville	FD75-3	FD75-3-9 MG1	-23.245	-71.392	7597	0-2	gravity corer	1975
Melville	FD75-3	FD75-3-15 MG4	-17.19	-74.862	4690	0-3	gravity corer	1975
Melville	FD75-3	FD75-3-16 MG2	-13.957	-78.085	4653	0-3	gravity corer	1975
Melville	ME0005A	ME0005A-14MC2	5.8465	-86.449	2045	0-2	multicorer	2000
Melville	ME0005A	ME0005A-15MC6	4.6137	-86.704	904	0-2	multicorer	2000
Melville	ME0005A	ME0005A-20MC8	3.2123	-86.486	2675	0-2	multicorer	2000
Melville	ME0005A	ME0005A-21MC3	0.0215	-86.463	2942	0-2	multicorer	2000
Melville	ME0005A	ME0005A-25MC5	-1.8534	-82.787	2203	0-2	multicorer	2000
Melville	ME0005A	ME0005A-29MC2	-0.5134	-81.995	1343	0-2	multicorer	2000
Melville	ME0005A	ME0005A-35MC1	4.1198	-85.005	3404	0-2	multicorer	2000
Melville	ME0005A	ME0005A-38MC2	7.3167	-84.113	1003	0-2	multicorer	2000
Melville	ME0005A	ME0005A-41MC2	7.8557	-83.608	1370	0-2	multicorer	2000
Melville	PLDS-2	PLDS-2 ST35 33G	0.605	-86.087	2708	0-3	gravity corer	1976
Melville	PLUTO-3	PLUTO-3-15	6.580	-92.942	3585	0-2	boxcorer	1981
Melville	VLCN-1	VLCN-1-50BC	6.530	-92.767	3578	0-2	boxcorer	1980
Oceanographer	OC170	OC170-186P	-13.612	-93.737	3784	0-2.5	gravity corer	1970
Oceanographer	OC170	OC170-182P	-13.612	-95.598	3811	0-3	gravity corer	1970
Oceanographer	OC73-3	OC73-3-6 MG2	-20.055	-95.295	4313	0-2	gravity corer	1973
Roger Revelle	RR9702A	RR9702A-50MC4	-23.606	-73.608	3396	0-2	multicorer	1997
Roger Revelle	RR9702A	RR9702A-52MC3	-23.193	-73.345	3418	0-2	multicorer	1997
Roger Revelle	RR9702A	RR9702A-54MC3	-21.359	-81.436	1323	0-2	multicorer	1997
Roger Revelle	RR9702A	RR9702A-60MC2	-20.878	-81.499	2480	0-2	multicorer	1997
Roger Revelle	RR9702A	RR9702A-62MC3	-18.085	-79.040	2937	0-2	multicorer	1997
Roger Revelle	RR9702A	RR9702A-64MC1	-17.035	-78.109	2930	0-2	multicorer	1997
Roger Revelle	RR9702A	RR9702A-66MC1	-16.127	-77.098	2575	0-2	multicorer	1997
Roger Revelle	RR9702A	RR9702A-68MC3	-16.007	-76.378	3228	0-2	multicorer	1997
Roger Revelle	RR9702A	RR9702A-72MC3	-16.506	-76.185	3782	0-2	multicorer	1997
Roger Revelle	RR9702A	RR9702A-70MC3	-16.725	-76.013	4124	0-2	multicorer	1997
Roger Revelle	RR9702A	RR9702A-76TC	-16.071	-76.406	3189	0-2	gravity corer	1997
Roger Revelle	RR9702A	RR9702A-74MC2	-16.244	-76.244	3476	0-2	multicorer	1997
Roger Revelle	RR9702A	RR9702A-77MC2	-16.134	-76.977	2588	0-2	multicorer	1997
Roger Revelle	RR9702A	RR9702A-79PC	-15.217	-76.819	3525	0-1	gravity corer	1997
T. Washington	VNTR01	VNTR01-11GC	0.14	-95.335	3345	0-2	gravity corer	1989
T. Washington	VNTR01	VNTR01-12GC	-3.01	-95.07	3535	0-2	gravity corer	1989
T. Washington	VNTR01	VNTR01-13GC	-3.092	-90.823	3304	0-2	gravity corer	1989
T. Washington	VNTR01	VNTR01-14GC	1.485	-89.855	1944	0-2	gravity corer	1989
T. Washington	VNTR01	VNTR01-15GC	1.485	-89.862	1955	0-2	gravity corer	1989
T. Washington	VNTR01	VNTR01-20GC	5.627	-94.197	3563	0-2	gravity corer	1989
T. Washington	VNTR01	VNTR01-21GC	9.588	-94.603	3710	0-2	gravity corer	1989
T. Thompson	TT9108	04GC	7.897	-89.943	3450	0-2	gravity corer	1991
Wecoma	W7706	W7706-16K TRAY	-15.637	-81.247	4521	0-2	gravity corer	1977
Wecoma	W7706	W7706-17	-17.487	-84.300	4573	0-2	boxcorer	1977
Wecoma	W7706	W7706-15 TRAY	-13.807	-78.305	4581	0-2	gravity corer	1977
Wecoma	W7706	W7706-21 TRAY	-23.245	-71.812	4400	0-2	gravity corer	1977
Wecoma	W7706	W7706-24K bag	-23.32	-71.128	5107	0-2	gravity corer	1977
Wecoma	W7706	W7706-24 TRAY	-23.32	-71.128	5107	0-2	gravity corer	1977
Wecoma	W7706	W7706-38 TRAY	-13.2	-77.252	1414	0-2	gravity corer	1977
Wecoma	W7706	W7706-62 TRAY	-8.217	-80.795	2670	0-2	gravity corer	1977
Wecoma	W7706	W7706-63K TRAY	-8.282	-80.923	4513	0-2	gravity corer	1977
Wecoma	W7706	W7706-65GC	-10.197	-84.747	4500	0-2	gravity corer	1977
Wecoma	W7706	W7706-68GC	-4.818	-88.512	3903	0-2	gravity corer	1977
Wecoma	W7706	W7706-71GC	-3.682	-82.505	1933	0-2	gravity corer	1977
Wecoma	W7706	W7706-70GC	-4.215	-85.328	3453	0-2	gravity corer	1977
Wecoma	W7706	W7706-69	-4.200	-85.340	3537	0-2	boxcorer	1977
Yaquina	Y71-03	Y71-03-06	6.39	-85.362	1945	0-2	gravity corer	1971
Yaquina	Y71-03	Y71-03-08 MG2	5.317	-81.938	3888	0-2	gravity corer	1971
Yaquina	Y71-03	Y71-03-09 MG1	5.172	-81.473	3601	0-2	gravity corer	1971
Yaquina	Y71-03	Y71-03-010A MG2	1.217	-82.277	3474	0-2	gravity corer	1971
Yaquina	Y71-03	Y71-03-11 MG3	-0.252	-83.285	2656	0-2	piston	1971
Yaquina	Y71-03	Y71-03-13 MG3	-1.795	-85.810	2798	0-2	piston	1971
Yaquina	Y71-03	Y71-03-20 MG1	-1.335	-85.323	2310	0-2	piston	1971
Yaquina	Y71-03	Y71-03-22 MG3	-1.138	-85.418	2338	0-2	gravity corer	1971

Yaquina	Y71-06	Y71-06-26 MG3	-15.268	-76.373	4813	0-2	gravity corer	1972
Yaquina	Y71-07	Y71-07-28 MG4	-11.017	-85.012	4491	0-2	gravity corer	1972
Yaquina	Y71-07	Y71-07-30 MG3	-10.052	-88.677	4237	0-2	gravity corer	1972
Yaquina	Y71-07	Y71-07-31 MG3	-9.932	-91.972	4114	0-2	gravity corer	1972
Yaquina	Y71-07	Y71-07-33 MG1	-10	-92.667	4093	0-2	gravity corer	1972
Yaquina	Y71-07	Y71-07-34 MG1	-9.607	-93.325	4622	0-2	gravity corer	1972
Yaquina	Y71-08	Y71-08-76 MG2	-8.117	-81.6	5122	0-2	gravity corer	1972
Yaquina	Y73-03	Y73-03-6	-3.782	-94.15	3714	0-2	gravity corer	1973
Yaquina	Y73-03	Y73-03-15 MG3	-13.007	-100.543	4425	0-2	gravity corer	1973
Yaquina	Y73-03	Y73-03-23 MG1	-15.528	-96.97	3656	0-2	gravity corer	1973
Yaquina	Y73-04	Y73-04-26 MG3	-20.77	-93.417	4394	0-2	gravity corer	1973
Yaquina	Y73-07	Y73-07-94	-16.845	-74.555	5920	0-2	gravity corer	1974
Yaquina	Y73-07	Y73-07-97	-13.957	-78.077	4620	0-2	gravity corer	1974
Yaquina	YALOC69	Y69-83 M1	-4.007	-92.015	3759	0-3	gravity corer	1969
Yaquina	YALOC69	Y69-84 M2	-3.98	-91.67	3748	0-2	gravity corer	1969
Yaquina	YALOC69	Y69-97 M1	0.53	-91.632	2362	0-2	gravity corer	1969

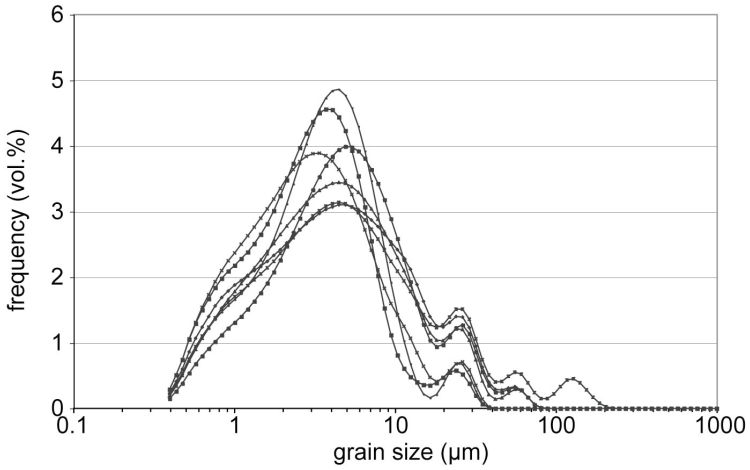

Figure 20: Grain-size distributions of bulk sediment samples from the Peru Basin. Dominant modes are in the same range as the grain-size distributions of the silt fractions (2-6 μm).

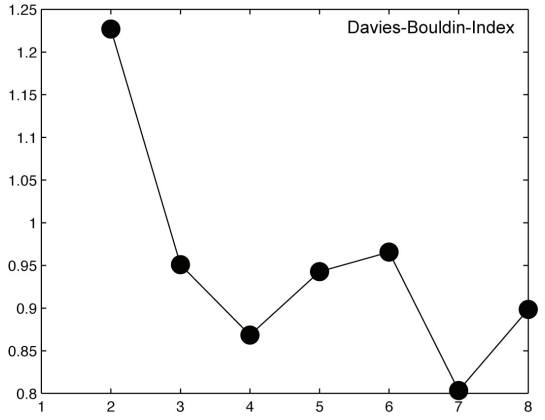

Figure 21: S3 Davies-Bouldin Index. Goodness of fit statistics for the K-means cluster analysis. Starting from the lowest number of calculated clusters the first local minimum appears for four clusters.

8. References

Abratis, M., 1998. Geochemical variations in magmatic rocks from southern Costa Rica as a consequence of Cocos Ridge subduction and uplift of the Cordillera de Talamanca, Universität Göttingen, Göttingen.

Arimoto, R., 2001. Eolian dust and climate: relationships to sources, tropospheric chemistry, transport and deposition. Earth Science Reviews 54(1-3), 29.

Biscaye, P.E., 1964. Distinction between kaolinite and chlorite in recent sediments by X-ray diffraction. American Mineralogist 49, 1282-1289.

Biscaye, P.E., 1965. Mineralogy and Sedimentation of Recent Deep-Sea Clay in the Atlantic Ocean and Adjacent Seas and Oceans. Geological Society of America Bulletin 76(7), 803-831.

Bonatti, E. and Arrhenius, G., 1970. Acidic Rocks on the Pacific Ocean Floor. In: A.E. Maxwell (Editor), The Sea. Jon Wiley & Sons, New York, pp. 445-464.

Boven, K.L., and Rea, D.K., 1998. Partitioning of eolian and hemipelagic sediment in eastern Equatorial Pacific core TR 163-31B and the late Quaternary paleoclimate of the Northern Andes: Journal of Sedimentary Research 68, 850-855.

Bruniard, E. D., 1982. La diagonal arida Argentina: un límite climático real (The Argentinian arid diagonal: a real climatic boundary). Revista Geográfica Intituto Panamericano de Geografía e Historia 95, 5-20.

Bundschuh, J., Winograd, M., Michael, D. and Alvarado, G.E., 2007. Regional Overview. In: J. Bundschuh and G.E. Alvarado (Editors), Central America: geology, resources, and hazards. Taylor & Francis/Balkema, Leiden, The Netherlands.

Byerly, G.R., Melson, W.G. and Vogt, P.R., 1976. Rhyodacites, andesites, ferrobasalts and ocean tholeiites from the Galapagos spreading center. Earth Planetary Science Letters 30, 215-221.

Chamley, H., 1989. Clay Sedimentology. Springer Verlag, Berlin, 623 pp.

Dauphin, J.P., 1983. Eolian Quartz Granulometry as a Paleowind Indicator in the Northeast Equatorial Atlantic, North Pacific and Southeast Equatorial Pacific, University of Rhode Island.

Davies, D. and Bouldin, D., 1979. A cluster separation measure. IEEE Trans. Patt. Anal. Machine Intell. PAMI-1, 224-227.

Dunne, T. and Mertes, L., 2007. Rivers. In: T.T. Veblen, K.R. Young and A.R. Orme (Editors), The Physical Geography of South America. Oxford regional environments series. Oxford University Press, Oxford.

Ehrmann, W.U., Melles, M., Kuhn, G. and Grobe, H., 1992. Significance of clay-mineral assemblages in the Antarctic Ocean. Marine Geology 107(4), 249-273.

Flores-Aqueveque, V., Vargas, G., Rutllant, J., Le Roux, J.P., 2009. Estacionalidad de la erosion y el transporte eólico de partículas en el desierto costero de Atacama, Chile (23°S). Andean Geology 36 (2), 288-310.

Flores-Aqueveque, V., Alfaro, S., Muñoz, R., Rutllant, J., Caquineau, S., Le Roux, J.P. and Vargas, G., 2010. Aeolian erosion and sand transport over the Mejillones Pampa in the coastal Atacama Desert of northern Chile. Geomorphology 120 (3-4), 312-325.

Garreaud, R., Vuille, M., Clement, A.C., 2003. The Climate of the Altiplano: Observed Current Conditions and Mechanisms of Past Changes. Palaeogeography, Palaeoclimatology, Palaeoecology 194(1-3), 5.

Garreaud, R.D. and Muñoz, R.C., 2005. The Low-Level Jet off the West Coast of Subtropical South America: Structure and Variability. Monthly Weather Review 133, 2246-2261.

Goudie, A.S. and Middleton, N.J., 2006. Desert Dust in the Global System. Springer, Heidelberg, 287 pp.

Harrison, S.P., Kohfeld, K.E., Roelandt, C. and Claquin, T., 2001. The role of dust in climate changes today, at the last glacial maximum and in the future. Earth Science Review 54(1-3), 43-80.

Heath, G.R., Moore, T.C. and Roberts, G.L., 1974. Mineralogy of surface sediments from the Panama Basin, Eastern Equatorial Pacific. Journal of Geology 82(2), 145-160.

Honjo, S., 1982. Seasonality and Interaction of Biogenic and Lithogenic Particulate Flux at the Panama Basin. Science 218, 883-884.

Holz, C., Stuut, J.-B. W., Henrich, R., 2004. Terrigenous sedimentation processes along the continental margin off NW Africa: implications from grain-size analysis of seabed sediments. Sedimentology 51, 1145-1154.

Howard, A.D., 1985. Interaction of sand transport with topography and local winds in the Northern Peruvian desert. In: O.E. Barndorff-Nielsen, J.T. Moller, K. Romer Rasmussen and B.B. Willetts (Editors), Workshop on the Physics of Blown Sand Memoirs. Department of Theoretical Statistics, Institute of Mathematics, University of Aarhus, Denmark, pp. 511-543.

Jickells, T.D., An, Z.S:, Andersen, K.K., Baker, A.R., Bergametti, G., Brooks, N. , Cao, J.J., Boyd, P.W., Duce, R.A., Hunter, K.A., Kawahata, H., Kubilay, N., laRoche, J., Liss, P. S., Mahowald, N., Prospero, J. M., Ridgwell, A. J., Tegen, I., Torres, R., 2005. Global Iron Connections Between Desert Dust, Ocean Biogeochemistry, and Climate. Science 308, 67-71.

Joussaume, S., 1990. Three-Dimensional Simulations of the Atmospheric Cycle of Deser Dust Particles Using a General Circulation Model. Journal of Geophysical Research 95(D2), 1909-1941.

Kalnay, E., Kanamitsu, M., Kistler, R., Collins, W., Deaven, D., Gandin, L., Iredell, M., Saha, S., White, G., Woollen, J., Zhu, Y., Leetmaa, A., Reynolds, R., Chelliah, M., Ebisuzaki, W., Higgins, W., Janowiak, J., Mo, K. C., Ropelewski, C., Wang, J., Jenne, R., Joseph, D., 1996. The NCEP&NCAR 40-Year Reanalysis

Project. Bulletin of American Meteorological Society 77(3), 437-471.

Kessler, W.S., 2006. The circulation of the eastern tropical Pacific: A review. Progressive Oceanography 69(2-4), 181-217.

Kienast, S.S., Kienast, M., Mix, A.C., Calvert, S.E. and François, R., 2007. Thorium-230 normalized particle flux and sediment focusing in the Panama Basin region during the last 30,000 years. Paleoceanography 22, PA2213.

Krissek, L.A., Scheidegger, K.F. and Kulm, L.D., 1980. Surface sediments of the Peru-Chile continental margin and the Nazca plate. Geological Society of America Bulletin 91(6), 321-331.

Kurgansky, M., Montecinos, A., Metzger, S., Villagran, V. and Verdejo, H., 2010. Filed study of atmospheric dust devils in the Atacama Desert. Geophysical Research Abstracts 12, EGU2010-1246, EGU General Assembly 2010.

Lamy, F., Hebbeln, D., Wefer, G. 1999. High-resolution marine record of climatic change in mid-latitude Chile during the last 28,000 years based on terrigenous sediment parameters. Quaternary Research 51, 83-93.

Leduc, G., Vidal, L., Cartapanis, O. and Bard, E., 2009. Modes of eastern equatorial Pacific thermocline variability: Implications for ENSO dynamics over the last glacial period. Paleoceanography 24, PA3202.

Leinen, M., Cwienk, D., Heath, G. R., Biscaye P. E., Kolla, V., Thiede, J., Dauphin, J. P., 1986. Distribution of biogenic silica and quartz in recent deep-sea sediments. Geology 14(3), 199-203.

Lettau, H. and Costa, J.R., 1978. Characteristic winds and boundary layer meteorology of the arid zones in Peru and Chile. In: H. Lettau and K. Lettau (Editors), Exploring the World's Driest Climate. Center for Climatic Research, Madison, WI, pp. 163-181.

Li, F., Ginoux, P. and Ramaswamy, V., 2008. Distribution, transport, and deposition of mineral dust in the Southern Ocean and Antarctica: Contribution of major sources. Journal of Geophysical Research 113, D10207.

Liang, J.-H., McWilliams, J.C., Gruber, N., 2009. High-frequency response of the ocean to mountain gap winds in the northeastern tropical Pacifc. Journal of Geophysical Research 114(C12005), 1-12.

Lonsdale, P., 1976. Abyssal Circulation of the Southeastern Pacific and Some Geological Implications. Journal of Geophysical Research 81(6), 1163-1176.

Lonsdale, P., 1977. Inflow of bottom water to the Panama Basin. Deep-Sea Research 24, 1065-1101.

Lyle, M., Pisias, N., Paytan, A., Martinez, J.I. and Mix, A., 2007. Reply to comment by R. Francois et al. on 'Do geochemical estimates of sediment focusing pass the sediment test in the equatorial Pacific?' Further explorations of 230Th normalization. Paleoceanography 22, PA1217.

Macharé, J. and Ortlieb, L., 1992. Plio-Quaternary Vertical Motions and the

Subduction of the Nazca Ridge, Central Coast of Peru. Tectonophysics 205 (1-3), 97.

Maher, B.A., Prospero, J.M., Mackie, D. , Gaiero, D., Hesse, P.P., Balkanski, Y., 2010. Global connections between Aeolian dust, climate and ocean biogeochemistry at the present day and at the last glacial maximum. Earth Science Review 99, 61-97.

Molina-Cruz, A. and Price, P., 1977. Distribution of opal and quartz on the ocean floor of the subtropical southeastern Pacific. Geology 5(2), 81-84.

NCEP Reanalysis data provided by the NOAA/OAR/ESRL PSD, Boulder, Colorado, USA, from their Web site at http://www.esrl.noaa.gov/psd/

Nur and Ben-Avraham, 1981. Volcanic gaps and the consumption of aseismic ridges in South America. Geological Society of America Memoir 154, 729-740.

Orme, A.R., 2007. The Tectonic Framework of South America. In: T.T. Veblen, K.R. Young and A.R. Orme (Editors), The Physical Geography of South America. Oxford regional environments series. Oxford University Press, Oxford.

Pawlowsky-Glahn, V. and Egozcue, J.J., 2006. Compositional data and their analysis: an introduction. In: A. Buccianti, G. Mateu-Figueras and V. Pawlowsky-Glahn (Editors), Compositional Data Analysis in the Geosciences: From Theory to Practice. Geological Society, London, pp. 1-10.

Peterson, M.N.A. and Goldberg, E.D., 1962. Feldspar Distributions in South Pacific Pelagic Sediments. Journal of Geophysical Research 67(9), 3477-3492.

Petschick, R., Kuhn, G. and Gingele, F., 1996. Clay-mineral distribution in surface sediments of the South Atlantic: sources, transport, and relation to oceanography. Marine Geology 130(3-4), 203-229.

Prins, M.A. and Weltje, G.J., 1999. End-member modelling of siliciclastic grain-size distributions: the Late Quaternary record of eolian and fluvial sediment supply to the Arabian Sea and its paleoclimatic significance. In: J.W. Harbaugh et al. (Editors), Numerical Experiments in Stratigraphy: Recent Advances in Stratigraphic and Sedimentologic Computer Simulations. SEPM Special Publication. Geological Society Publishing House, London.

Potter, P., 1994. Modern Sands of South America: Composition, Provenance and Global Significance. Geologische Rundschau 83(1), 212.

Prospero, J.M. and Bonatti, E., 1969. Continental Dust in the Atmosphere of the Eastern Equatorial Pacific. Journal of Geophysical Research 74, 3362-3371.

Prospero, J.M., Ginoux, P., Torres, O., Nicholson, S.E., Gill, T.E. (2002) Environmental characterization of global sources of atmospheric soil dust identified with the Nimbus 7 Total Ozone Mapping Spectrometer (TOMS) absorbing aerosol product. Review of Geophysics 40(1), RG1002.

Prospero, J.M. and Lamb, P.J., 2003. African Droughts and Dust Transport to the Caribbean; Climate Change Implications. Science 302, 1024-1027.

Pye, K., 1987. Aeolian Dust and Dust Deposits. Academic Press, London.

Rea, D.K., 1994. The paleoclimatic record provided by eolian deposition in the deep sea: the geologic history of wind. Review of Geophysics 32, 159-195.

Rea, D.K. and Hovan, S.A., 1995. Grain-size distribution and depositional processes of the mineral component of abyssal sediments: Lessons from the North Pacific. Paleoceanography 10(2), 251-258.

Rex, R.W. and Martin, B.D., 1966. Clay mineral formation in sea water by submarine weathering of K-feldspars, Clays Clay Mineralogy 14, 235-240.

Ridgwell, A.J., 2002. Dust in the Earth system: the biogeochemical linking of land, air and sea. Philosophical Transactions Mathematical Physical and Engineering Sciences 360, 2905-2924.

Rincón Martínez, D., Lamy, F., Contreras, S., Leduc, G., Bard, E., Saukel, C., Blanz, T., Mackensen, A., Tiedemann, R., 2010. More humid interglacials in Ecuador during the past 500 kyr linked to latitudinal shifts of the Equatorial Front and the Intertropical Convergence Zone in the eastern tropical Pacific. Paleoceanography, 25, PA2210, doi:10.1029/2009PA001868

Rincón Martínez, D., Steph, S., Lamy, F., Mix, A., Mackensen, A., Tiedemann, R., Tracking the Equatorial Front in the eastern equatorial Pacific Ocean by the isotopic and faunal composition of planktonic foraminifera. Marine Micropaleontology, in review.

Rosato, V.J., Kulm, L.D. and Derks, P.S., 1975. Surface Sediments of the Nazca Plate. Pacific Science 29(1), 117-130.

Rosato, V.J., Kulm, L.D., 1981. Clay mineralogy of the Peru continental margin and adjacent Nazca plate: Implications for provenance, sea level changes, and continental accretion. In: Kulm, L.D., Dymond, J., Dasch, E.J., Hussong, D.M., Roderick, R. (eds.) (1981): Nazca Plate: Crustal Formation and Andean Convergence. Geological Society of American Memoir 154, 545-568.

Rutllant, J., Fuenzalida, H., Aceituno, P., 2003. Climate dynamics along the arid northern coast of Chile: The 1997-1998 Dinámica del Clima de la Región de Antofagasta (DICLIMA) experiment. Journal of Geophysical Research 108(D17), 4538.

Sarnthein, M., Tetzlaff, G., Koopmann, B., Wolter, K. and Pflaumann, U., 1981. Glacial and Interglacial Wind Regimes over the Eastern Subtropical Atlantic and North-West Africa. Nature 293(5829), 193.

Scheidegger, K.F. and Krissek, L.A., 1982. Dispersal and deposition of eolian and fluvial sediments off Peru and northern Chile. Geological Society of American Bulletin 93(2), 150-162.

Schwerdtfeger, W., 1976. Climates of Central and South America. World Survey of Climatology, 12. Elsevier, Amsterdam.

Strub, P.T., Mesías, J.M., Montecino, V., Rutllant, J. and Salina, S., 1998.

Coastal Ocean Circulation off Western South America. In: A.R. Robinson and K.H. Brink (Editors), The Global Coastal Ocean. The Sea, Vol.11. John Wiley & Sons Inc., New York.

Stuut, J.-B.W., Prins, M.A., Schneider, R.R., Weltje, G.J., Jansen, J.H.F., Postma, G., 2002. A 300-kyr record of aridity and wind strength in southwestern Africa: inferences from grain-size distributions of sediments on Walvis Ridge, SE Atlantic. Marine Geology 180, 221-233.

Stuut, J.-B.W., Zabel, M., Ratmeyer, V. and Helmke, P., 2005. Provenance of present-day eolian dust collected off NW Africa. J. Geophys. Res. 110, D04202 1-14.

Stuut, J.-B., Marchant, M., Kaiser, J., Lamy, F., Mohtadi, M., Romero, O., Hebbeln, D. , 2006. The late Quaternary paleoenvironment of Chile as seen from marine archives. Geographica Helvetica 61(2), 135-151.

Tanaka, T.Y. and Chiba, M., 2006. A numerical study of the contributions of dust source regions to the global dust budget. Global and Planetary Change 52 (1-4), 88-104.

Tegen, I., Harrison, S.P., Kohfeld, K., Prentice, I.C., Coe, M., Heimann, M., 2002. Impact of vegetation and preferential source areas on global dust aerosol: Results from a model study. Journal of Geophysical Research 107: D21 4576.

Tucker, M.E., 1996. Methoden der Sedimentologie. Enke, Stuttgart.

Wagener, T., Guieu, C., Losno, R., Bonnet, S. and Mahowald, N., 2008. Revisiting atmospheric dust export to the Southern Hemisphere ocean: Biogeochemical Implications. Global Biogeochemical Cycles 22, GB2006 1-13.

Weltje, G., 1997. End-member modeling of compositional data: Numerical-statistical algorithms for solving the explicit mixing problem. Mathematical Geology 29(4), 503-549.

Weltje, G., Prins, M.A., 2003. Muddled or mixed? Inferring palaeoclimate from size distributions of deep-sea clastics. Sedimentary Geology 162, 39 - 62.

Werner, M., Tegen, I., Harrison, S.P., Kohfeld, K.E., Prentice, I.C., Balkanski, Y., Rodhe, H., Roelandt, C., 2002. Seasonal and interannual variability of the mineral dust cycle under present and glacial climate conditions. Journal of Geophysical Research 107, D24 4744.

Windom, H.L., 1976. Lithogenous Material in Marine Sediments. In: J.P. Riley and R. Chester (Editors), Chemical Oceanography. Academic Press, London, pp. 103-135.

Wright, J.C.M., 2004. Evolution of the Galapagos Rise and the Bauer Microplate: Implications for the Nazca Plate, Texas A&M University, College Station.

Wyrtki, K. and Meyers, G., 1976. The Trade Wind Field Over the Pacific Ocean. Journal of Applied Meteorology 15(7), 698-704.

Zeil, W., 1986. Südamerika. Geologie der Erde, 1. Enke, Stuttgart.

4.2 Late Quaternary Glacial-Interglacial Climate Variability of Western South America

Cornelia Saukel, Frank Lamy, Jerry McManus, Daniel Rincón Martínez, Jan-Berend W. Stuut, Gisela Winckler, Silke Steph, Ralf Tiedemann
(to be submitted to *Quaternary Science Reviews*)

Abstract The investigation of ocean-atmosphere linkages in the southeastern tropical Pacific allows inferences about continental climate variability in western South America. While previous studies mostly concentrated on paleoceanographic features, we focus our work on reconstructing changes in eolian transport and trade-wind strength. Measurements of independent dust proxies at Ocean Drilling Program (ODP) Site 1237 off the coast of southern Peru reveal higher supply of eolian dust during glacials than during interglacials of the past 500 ka. These results are in accordance with dust flux data from the eastern equatorial Pacific at 110°W (ODP Site 849). While glacial dust fluxes are twice as high as during interglacials at Site 1237, grain size characteristics do not vary on glacial-interglacial time scales, but remain rather constant, indicating no distinct changes in mean wind speed or direction. From these results we infer changes in continental aridity and southeast trade-wind vigor during the late Pleistocene. A change in the extent of the dust source regions (the Atacama Desert in northern Chile and the coastal deserts of Peru) due to a varying vegetation cover and a meridional shift of the atmospheric circulation system of the Southeast Pacific as well as enhanced gustiness are the driving forces for the glacial-interglacial variability of dust input during the past 500 ka. Our results necessitate a re-interpretation of previous dust studies of the equatorial east Pacific that originally suggested increased terrigenous supply during interglacials to be of eolian origin. While findings from the equatorial east Pacific reveal enhanced fluvial input from northwestern-most South America during wetter interglacials, our data suggest increased eolian-derived terrigenous supply during drier glacials from the arid areas south of 3°S.

Keywords: South America, paleoclimate, late Pleistocene, dust

1. Introduction

The variability of western South American climate history is tightly connected to changes in the atmosphere-ocean circulation system of the southeastern Pacific (Markgraf et al., 2000; Cane, 2005), which in turn is largely dependent on the regional topography of the Andean mountain range. The regional climate is further linked to a number of interacting factors including (1) the latitudinal sea sur-

face temperature (SST) gradient in the South Pacific along the west coast of South America, (2) the moisture balance, controlled by SSTs and evaporation in the South Pacific, (3) the El Niño - Southern Oscillation (ENSO) variability, (4) the latitudinal position of the Intertropical Convergence Zone (ITCZ), and (5) the intensity and direction of the southeast trade winds.
The large-scale atmospheric circulation in the tropical Pacific consists of two deep overturning circulation cells, the Hadley (meridional) cell, the near-surface component of which is represented by the trade winds, and the Walker (zonal) cell, which is associated with the east-west oceanography asymmetry. Surface winds, which control upwelling, the tilt of the thermocline, and thus the formation of the cold tongue in the Eastern Pacific, depend on changes in the Walker and Hadley cells (Reiter, 1979; Pierrehumbert, 2000). The resulting connection between surface winds and SSTs is the key to comprehending the behavior of the coupled ocean-atmosphere system.

South American climate reconstructions have been based on diverse but - compared to other continents - relatively sparse paleoclimate marine and continental records. Those studies partially reveal contradicting results concerning the relation of the five factors mentioned above on glacial-interglacial timescales. For example, some authors conclude that drier conditions in northern and central South America during glacials can be attributed to a stronger meridional SST gradient and a more northern position of the ITCZ (e.g., Martinez et al., 2003; Rincón et al., 2010), resembling a La Niña setting. Other studies suppose a southward displacement of the ITCZ (e.g., Rea et al., 1986; Broccoli et al., 2006), implying wetter conditions with weakened southeast trade winds during glacials (Boven and Rea, 1998) and a more El Niño-like situation (Koutavas et al., 2002; Koutavas and Lynch-Stieglitz, 2003).
In this respect, winds and their transport of dust play a key role in the understanding of glacial-interglacial changes in the SE Pacific and the adjacent continent as the atmospheric circulation system responds to and modulates the effects of continental and oceanographic changes. While larger (smaller) mean grain sizes can be an indication of increased (decreased) wind speeds (Sarnthein et al., 1981, Janecek and Rea, 1985), the abundance of eolian-derived deep-sea sediments allows inferences about changes in the environmental and climatic conditions of the dust source area (e.g., Clemens 1998). Mineral dust preserved in marine sediments is thus a useful proxy to reconstruct both climate-related changes of the atmospheric circulation pattern as well as periods of continental aridity vs. humidity (Kohfeld and Harrison, 2001; Stuut et al., 2002; Maher et al., 2010).
While the paradigm of greater dust fluxes during glacials compared to interglacials on a global scale has been widely accepted (e.g., Mahowald et al., 1999; Kohfeld and Harrison, 2001; Bauer and Ganopolski, 2010), this inference and its implica-

tions have been more controversial in the equatorial (south)-east Pacific. Rea et al. (1986; 1994) and Olivarez et al. (1991) found higher dust fluxes during interglacials in the eastern equatorial Pacific (DSDP 503B at 4°N, 95.6°W, Fig. 22) implying dry interglacial periods with enhanced atmospheric circulation and wet glacial periods accompanied by weaker atmospheric circulation in central and northern South America. Analogous to these findings, Rea (1994) interpreted higher siliciclastic input at site Y71-6-12 (16.26°S, 77.23°W; close to our core site) just before and during glacials as increased hemipelagic input and thus wetter climate conditions. Chuey et al. (1987) on the other hand, found enhanced eolian mass accumulation rates during glacials in the central equatorial Pacific (RC11-210 at 1.82°N, 140°W) between 800 ka and 300 ka before present and inferred drier conditions in the source areas of northwestern South America, but no significant change in wind intensities as seen in grain-size variability. Anderson et al. (2006) investigated a transect of sediment cores across the equator at the same longitude, revealing maximum dust fluxes also during glacials of the past 300 ka. Winckler et al. (2008) found an increase in dust flux by a factor of 2.5 during glacials compared to interglacials consistently throughout the equatorial Pacific since 500 ka B.P., corroborating the global view of greater dust flux during cold stages.

Here we present new proxy data from Ocean Drilling Program (ODP) Site 1237 drilled on the easternmost flank of Nazca Ridge, 140 km offshore (16.11°S, 76.37°W; 3212 m water depth), covering the past 500 ka. Its position below the path of eolian transport from the Atacama Desert and close to the arid coasts of Peru, but west of the deep-sea trench provides an excellent opportunity to reconstruct eolian input due to its undisturbed and complete sediment record (Mix et al., 2003). Our data represent the only continuous dust record from the SE Pacific south of 5°S covering the last 500 ka. The approach of using multiple proxies including grain-size distributions, thorium (Th-)isotopes, and the geochemical composition of the sediments, allows us to differentiate between changes in wind intensities and climatic changes in the source areas (cf. Rea et al., 1985; Olivarez et al., 1991). We compare our record to previously published dust flux data from the equatorial Pacific (Winckler et al., 2008) and to a multiproxy climate reconstruction at ODP site 1239 located on Carnegie Ridge off Ecuador, constraining latitudinal shifts of the ITCZ on glacial-interglacial timescales (Rincón et al., 2010).

2. Materials and Methods

The age model of site 1237 is based on a benthic δ^{18}O record tied to the chronology of the LR04 isotope stratigraphy of Lisiecki and Raymo (2005), applying the Analyseries software (Paillard, 1996). Due to partial dissolution of $CaCO_3$ - deduced from a large amplitude in Ca counts from XRF scans (not shown) and from

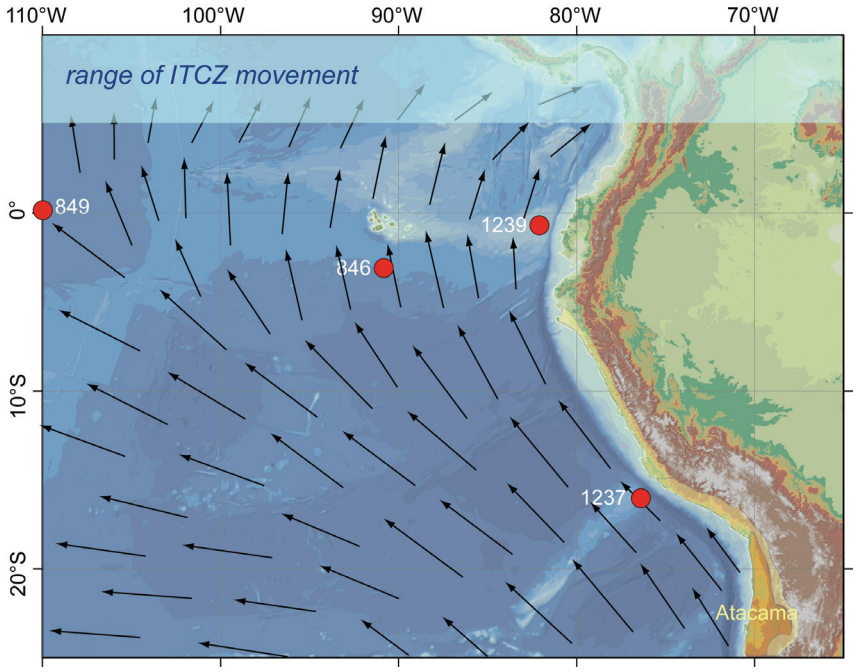

Figure 22: Study area. Red dots show core locations discussed in the text, black arrows indicate the direction of the dominant wind field. The light blue bar represents the meridional range of the seasonal ITCZ movement. The orange and yellow shadings represent the (hyper-)arid core and semi-arid parts of the Atacama Desert and Peru coastal deserts, respectively.

observed dissolution features on foraminifera of the coarse fraction (>63 μm) when selecting benthic foraminifers for isotope measurements - the δ^{18}O-record of ODP Site 1237 (Fig. 23B) is comparably noisy during MIS 2 - 5 and MIS 8, 9 and 12, and of comparatively low resolution during MIS 10 and 11. Ba-counts of the XRF-scans were therefore used for fine-tuning the age model (S1). The lack of sample material between 3.3 - 7.4 mcd (80 - 240 ka) at Site 1237 was compensated for by using samples from pre-site survey core RRV9702A-69PC (16.01°S, 76.33°W). The latter was aligned to ODP site 1237 using magnetic susceptibility data from both cores (S2).

The siliciclastic content of ODP site 1237 sediments represents the percentage of bulk sediment after subtracting measured percentages of biogenic opal, carbonate, and organic matter (TOC). The biogenic opal content (wt%) was determined with an automated leaching method, following procedures outlined in Müller and Schneider (1993). TOC and total carbon contents were analyzed with the LECO technique and a CNS elemental analyzer, respectively, before calculating $CaCO_3$ contents, following standard methods (e.g., Rincón-Martínez et al., 2010). The chemical composition of the sediment was analyzed applying X-ray fluorescence scanning

(XRF) (Aavatech 2^{nd} generation XRF Scanner at AWI) and Inductively Coupled Plasma - Optical Emission Spectrometry (ICP-OES in the Geochemistry Department at AWI). We scanned the split sediment cores in 1 cm intervals corresponding to a time-resolution of 300 - 800 years. Iron XRF counts were calibrated to absolute concentrations determined by ICP-OES on 35 samples (cf. Rincón et al., 2010). Linear sedimentation rates (LSR in cm ka^{-1}) were derived from the age model and multiplied by the dry bulk density (DBD in g cm^{-3}) obtained from borehole logging data at site 1237 (Mix et al., 2003) and by the concentration of an individual sediment component to calculate accumulation rates (AR in g cm^{-2} ka^{-1}).
The fine fractions ($<$63 μm) of a total of 35 samples were analyzed for thorium (Th) and uranium (U) isotopes by isotope dilution Inductively Coupled Plasma Mass Spectrometry. Fluxes were calculated using the ^{230}Th profiling method (e.g., Bacon 1984, Francois et al., 2004) to compare to the AR derived from the age model. Dust mass fluxes were calculated from common thorium (^{232}Th) according to Winckler et al. (2008), ^{232}Th being a trace element enriched in continental crust (e.g., McGee et al, 2007). Additional measurements of four bulk sediment samples were conducted to test the influence of grain-size separation on Th-isotope concentrations (cf. Kretschmer et al., 2010; McGee et al., 2010; S3).
We measured the grain-size distribution of the terrigenous siliciclastic sediment fraction with a Beckman-Coulter Laser Particle Sizer. To isolate the terrigenous sediment fraction, we followed the methods of Stuut et al. (2007) for the removal of other mainly biogenic constituents.

3. Results

To avoid dilution effects, we calculated accumulation rates (ARs) of individual sediment components. This resulted in siliciclastic and iron (Fe) ARs that are increased by factors of 2 - 3 during glacials compared to interglacials (Fig. 23D, E, S4). Glacial stages 4 and 6 start out with highest ARs of the terrigenous siliciclastic fraction. There seems to be a general decreasing trend throughout MIS 3. In order to have an age-model independent measure of dust accumulation rates, we determined the ^{232}Th- and Fe- fluxes to the ocean floor by applying the ^{230}Th-normalization method (e.g., Bacon, 1984; Francois et al., 2004). Age-model dependent ARs are usually limited in temporal resolution and integrated over time intervals between age control points, assuming a constant accumulation rate over each interval, which, however, cannot be ascertained (Francois et al., 2004; Loubere et al., 2004). In contrast, the ^{230}Th normalization method gives accumulation rates for discrete points in time. Absolute values of ^{230}Th-normalized Fe-fluxes reach only 35 - 65% of the values obtained by age-model dependent AR calculations (Fig. 23F). Nevertheless, results also suggest a twofold-increased input of siliciclastic material during glacials compared to interglacials and corroborate the general trend as seen in the

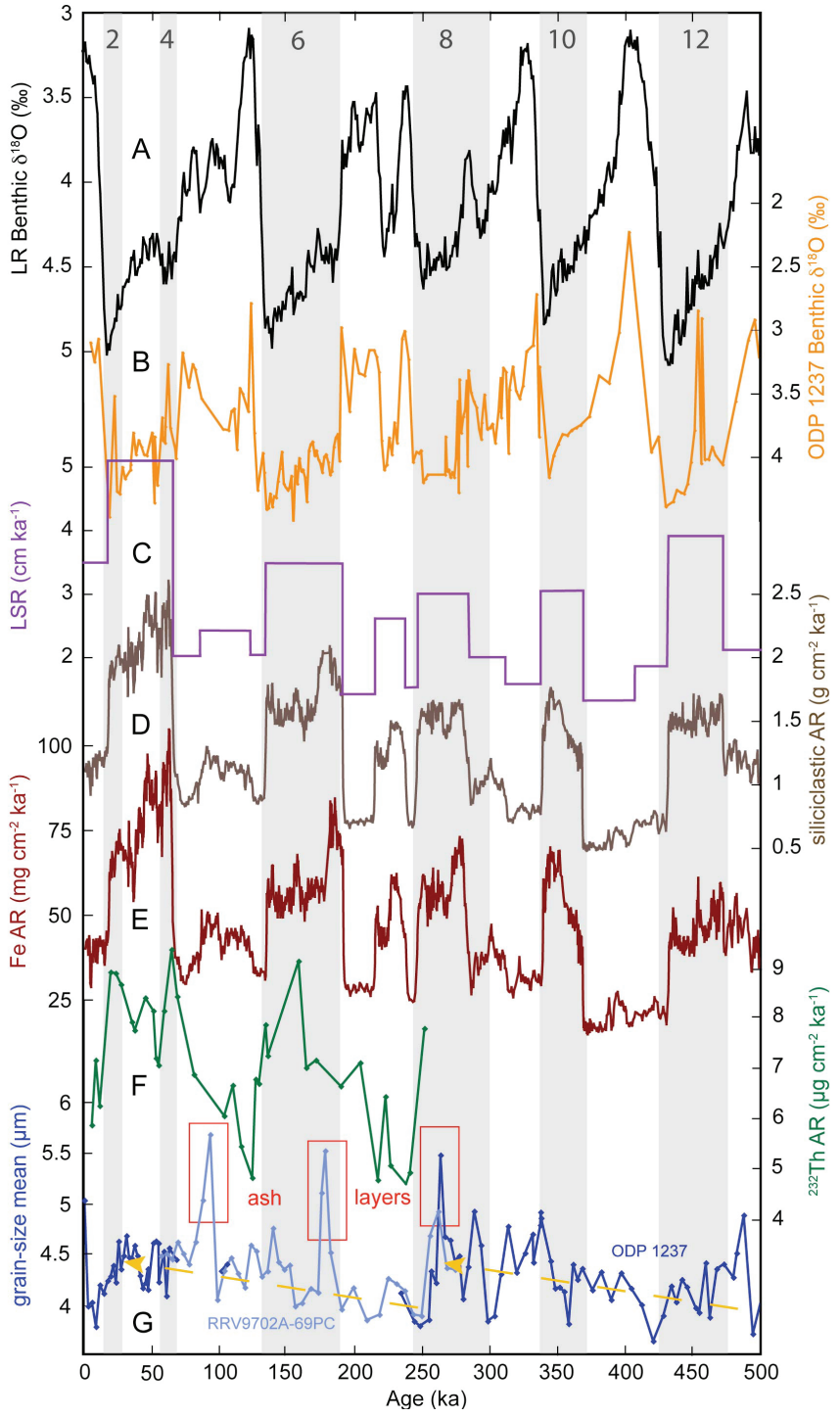

Figure 23: Records of eolian-derived sediment input to ODP Site 1237 over the last 500 ka. **(A)** Benthic oxygen isotope stack (Lisiecki and Raymo, 2005), **(B)** Benthic oxygen isotope record of ODP Site 1237, **(C)** Linear sedimentation rates (LSR, cm ka^{-1}), **(D)** siliciclastic accumulation rates (AR, g cm^{-2} ka^{-1}), **(E)** Iron accumulation rates (Fe AR, mg cm^{-2} ka^{-1}), **(F)** ^{232}Thorium flux (μg cm^{-2} ka^{-1}), **(G)** Mean grain size of siliciclastic sediment fraction (μm)

age-model dependent ARs. Loubere et al. (2004) also found very variable calcite accumulation rates for sediments from the equatorial east Pacific comparing the different MAR-approaches, where one explanation could be sediment redistribution leading to focusing during glacials. Focusing factors at ODP Site 1237 vary around 2 (not shown) throughout the time interval in consideration. There is therefore no evidence for major changes in sediment focusing that could explain the observed two-to threefold variations in the accumulation of bulk and constituent sediments at the study site. The combined results provide a more robust basis for paleoclimate interpretations, since the general trend and the amplitudes of the terrigenous input obtained by the two independent methods compare well (Fig. 24D, E).

In contrast to the variability in siliciclastic input, grain-size means (Fig. 23G) do not vary on orbital or glacial-interglacial time-scales but remain rather constant between 3.7 and 5 μm, except of 3 outlying peaks of $>$5.5 μm, representing sediment core sections contaminated by volcanic ash. However, grain-size means do increase on a longer timescale, from 500 ka to 260 ka, when they drop to $<$4 μm, only to slightly increase again from $\sim$250 ka until $\sim$30 ka, before another drop below 4 μm at 9 ka.

4. Discussion

4.1 Changes in dust flux on glacial-interglacial cycles

The data set presented in figure 23 is the first record obtained from below the major dust-transporting wind field in the SE Pacific close enough to the source area to record changes in dust supply and wind intensity (Fig. 22). Silt-sized material deposited in areas within a few hundred kilometers offshore is considered more reliable in recording these changes than the clay-sized fraction (e.g., Sarnthein et al., 1981; Tiedemann et al., 1989), which is the only fraction documented at the core locations of previous studies further offshore. The disadvantage of a study site as close to the coast as ODP Site 1237 is the hemipelagic sediment component one would usually expect, and which would contaminate the eolian input signal (Weltje and Prins, 2003; Weltje and Prins, 2007). However, we can rule out a hemipelagic component in the sediments of ODP cores 1237 as the site is located offshore an area where no major perennial rivers drain into the Pacific. The South American deep-sea trench represents a barrier catching the fluvial material from the minor, ephemeral rivers of southern Peru, making winds the most probable transport agent of the terrigenous fraction (Krissek et al., 1980).

Linear sedimentation rates (LSR) largely determine accumulation rates of the individual sediment components at our site (Fig. 23C-E). Ca-contents are higher during glacials, while siliciclastic contents are higher during interglacials (S4). Changes in

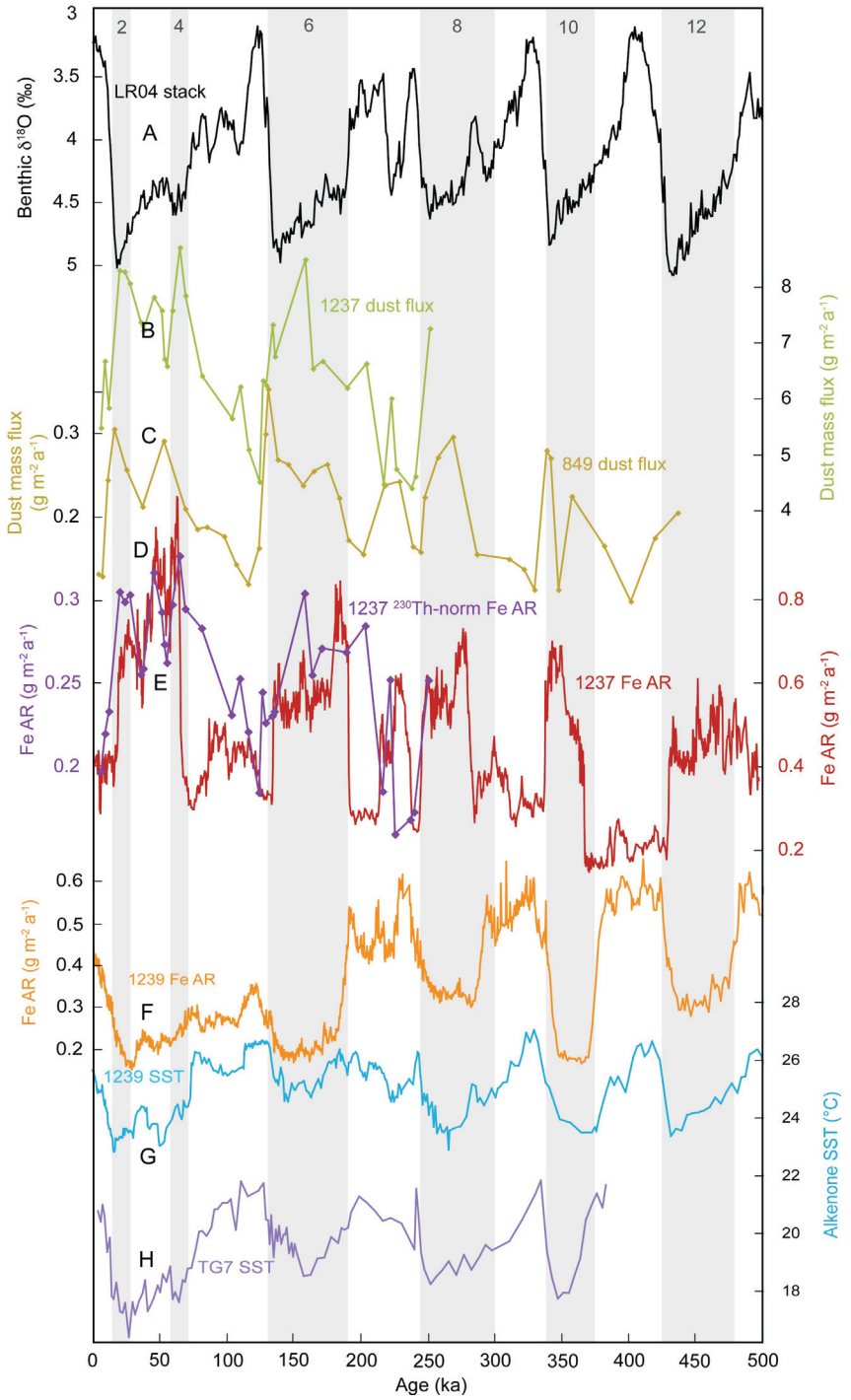

Figure 24: Comparison of eolian flux records in relation to SST records. **(A)** Benthic oxygen isotope stack (Lisiecki and Raymo, 2005), **(B)** Dust flux of ODP Site 1237 (g m^{-2} a^{-1}), **(C)** Dust flux of ODP Site 849 (g m^{-2} a^{-1}), **(D)** Fe accumulation rates (g m^{-2} a^{-1}) of ODP Site 1237, **(E)** ^{230}Th-normalized iron flux at ODP Site 1237 (g m^{-2} a^{-1}), **(F)** Fe accumulation rates (g m^{-2} a^{-1}) of ODP Site 1239 (Rincón Martínez et al., 2010), **(G)** Alkenone SSTs (°C) heavily influenced by the equatorial front, ODP Site 1239 (Rincón et al., 2010), **(H)** Alkenone SSTs (°C) off southern Peru, TG7 (Calvo et al., 2001).

ARs of dust provide a comprehensive picture of changes in the intensity of the dust cycle, including source, transport and deposition (Kohfeld and Tegen, 2007). Two different methods of calculating accumulation rates consistently show a 2-3-time increase of siliclastic material during glacials compared to interglacials at our site. Fe ARs calculated from LSRs and dry bulk density (DBD) show the same trend and amplitude of our ^{232}Th-dust record (Fig. 23E, F). Our records generally support the idea of dustier glacials compared to interglacials, in agreement with different modeling results for the last glacial maximum (LGM, Mahowald et al., 1999; Lunt and Valdes, 2002; Werner et al., 2002) and in particular support earlier results from the equatorial east Pacific (Winckler et al., 2008). The dust flux trends of ODP Site 1237 and Site 849 (Winckler et al., 2008), which is situated downwind from our core location (Fig. 22), fit very well in the location of their minima and maxima (Fig. 24B, C), even though they were measured in differing temporal resolution. The study sites are fed by the same dust source: the Atacama Desert of northern Chile and the coastal deserts of southern Peru. Dust fluxes at Site 1237 are 30 times those measured at Site 849, which can be explained by the proximal position of core 1237 relative to the distal core 849. Given the large distance between the cores, the coherence of the dust flux records between the two sites is surprisingly good, supporting the hypothesis of a common source and supporting our assumption that hemipelagic sedimentation plays a minor role at Site 1237, if at all. Since the hemipelagic contribution to the terrigenous sediment component is negligible at our study site, the derived proxy record allows a re-interpretation of previously published data. We propose the signal found by Rea (1994) for site Y71-6-12 (close to our site) not to record hemipelagic deposition as suggested by the author, but to record continental dust from the arid and semi-arid regions of western South America with maximal supply just before (related to their age model) and during glacials. Several scientists proposed higher dust fluxes in the tropical east Pacific during interglacials instead of during glacials. Rea et al. (1986) and Olivarez et al. (1991) interpreted their results to represent more arid conditions during the warm stages in northwestern South America. Our results clearly oppose this hypothesis. According to Rincón-Martínez et al. (2010), terrigenous input during interglacials at ODP Site 1239 (Fig. 22, 24) was increased due to enhanced precipitation that fed fluvial runoff in northwestern South America. We propose to alternatively interpret the higher terrigenous input at site 503B (4.05°N, 95.63°W) (Fig. 22) during interglacials (Rea et al. 1986; Rea 1994) as a consequence of wet deposition below the ITCZ, which is then shifted to a more southern location, rather than as increased dust supply due to more arid conditions on land (Rea et al. 1986; Rea 1994). According to Hovan (1995) and McGee et al. (2007) wet deposition below the ITCZ increases the accumulation rate of dust in comparison to core locations north or south of the tropical rainbelt. This dependency would explain the increased deposi-

tion of dust at site 503B during interglacials. In contrast, higher terrigenous input at core location V19-29 (3.58°S, 83.93°W) during glacials (Rea, 1994) in our opinion represents enhanced dust supply from the coastal deserts and the Atacama Desert because of the study site's position south of the Equatorial Front and south of the area influenced by wet deposition. Furthermore, it is too far west to receive any fluvial material originating from the Gulf of Guayaquil that is transported with ocean surface currents in a northward direction.

4.2 Climate Variability of Western South America Inferred from Continental Dust During the Past 500 ka

Continental Aridity

Dust flux is often used as a proxy for climate change in terms of aridity and the extent of vegetation cover (e.g., Clemens, 1998). Changes in the source areas in terms of vegetation cover are also the most important factor for the increased dust supply during the LGM according to modeling studies by Mahowald et al. (1999; 2006). Latorre et al. (2002) suggest dry conditions on the margin of the Atacama Desert during the LGM from the analysis of rodent midden. Our data support the idea of enlarged semi-arid areas surrounding the Atacama Desert during all glacials, which we attribute to decreased precipitation and vegetation cover on the western slopes of the central Andes in Peru and Chile as well as the coastal areas of Peru. If glacials can be interpreted analogous to La Niña-like conditions (Andreasen and Ravelo, 1997; Andreasen et al. 2001; Martinez et al., 2003), arid conditions predominated in the Atacama Desert due to reduced moisture transport from the south during austral summer (Houston, 2006). Less precipitation then leads to a reduced vegetation cover and thus a larger potential dust entrainment area on the western Andean slopes. Glacial sea-level low-stands additionally exposed the comparably narrow but noteworthy shelf areas on the west coast of South America, also contributing to an extension of the source areas. However, the extension of the desert in an eastern direction is limited by the Andean mountain range and is insufficient to explain a two- to threefold increase in dust flux due to the limitation in area. A spatial extension of the desert is more likely conceivable in a north-southern direction, towards southern Ecuador and central Chile. This latitudinal extension cannot be recorded at a single marine sediment drill site.

Wind Intensities and Direction

In order to investigate whether enhanced wind speeds during glacials were responsible for the increased dust supply, we additionally analyzed grain-size distributions of the land-derived sediment fraction. Because of increased meridional SST gradients that would imply stronger winds during the cold stages (Fig. 24F-H) one

would expect the dust grain-size distributions to record changes in wind intensities (Lindzen and Nigam, 1987) in terms of coarser grain-size means during glacials and finer means during interglacials, as found off west Africa, e.g. by Sarnthein et al. (1981). However, we do not recognize this relationship for the SE Pacific in our data (Fig. 23G). By comparing our dust flux data to SSTs of Site TG7 (Calvo, 2001) and ODP Site 1239 (Rincón et al., 2010), we can distinguish a clear co-occurrence of cooler (warmer) SSTs of the cold tongue and increased (decreased) dust accumulation rates (Fig. 3 B, F-H). Meridional SST gradients within the cold tongue (ODP Site 1239 - TG7) change in a glacial-interglacial pacing, the gradient being 4 - 5°C during interglacials and 6 - 7°C during glacials (Fig. 24G, H). While dust mass flux depicts considerable changes on glacial-interglacial time scales (Fig. 23D, E, F), grain-size means suggest only minor changes in mean wind intensities on longer time scales during the past 500 ka. Evidence of slight increases in wind velocity are recognized between 500 ka and 250 ka and also between 250 ka to 21 ka (Fig. 23G), when grain-size means suddenly decrease. According to Kohfeld and Tegen (2007), higher surface wind speeds in source areas can cause enhanced dislocation of smaller as well as larger particles compared with particle sizes dislocated at lower wind speeds. In other words, the mean/mode can remain unchanged while there is a change in intensity of the entraining winds. We thus cannot exclude an increase in wind speeds during glacials, but simply do not see it recorded at our core location.
The modeled transport of mass and energy within the winter hemisphere Hadley cell intensifies as the ITCZ is moved meridionally (Lindzen and Hou, 1988), either due to changes in insolation or due to the variability inherent to the atmosphere-ocean system, i.e. tropical SSTs. A longitude-independent Hadley circulation is typical for the Pacific because of its wide ocean basin reducing longitudinal variation of the atmospheric circulation (Pierrehumbert, 2000). Analogous to the southern hemisphere (SH) winter, evidence for a glacial northward shift of the atmospheric circulation system in the SE Pacific comes from several different studies of the southern Westerlies (e.g., Stuut and Lamy, 2004; Kaiser et al. 2005; Toggweiler, 2009), as well as the ITCZ (Martin et al., 1997; Rincón et al. 2010). Wind intensities comprise both the meridional (v) and zonal (u) wind components. Reiter (1979) suggested an extratropical trigger event to activate a self-enforcing feedback between the meridional trade-wind components v, the Hadley cell intensity and precipitation. As the subtropical anticyclone moves further to the north, it weakens but allows $v_{SouthernHemisphere(SH)}$ to increase in the east Pacific, extending into the northern hemisphere, without necessarily influencing the behavior of the zonal wind component u_{SH} (Reiter, 1979). Because of the southern Peruvian coast bending in a northwestern direction, the Andes constrict the airflow on the eastern flank of the anticyclone and accelerate it (Hay, 1996). In this respect, our dust flux data support the idea of MARs reflecting changes in wind intensities. As the meridional

component (v_{SH}) is enhanced, the capacity (dust load) of the southeast trade winds is increased, without necessarily changing the grain-size spectrum of the dust load. It remains questionable if the outlined mechanisms together with the limited extensions of the desert areas are sufficient to increase the supply in dust during the glacials by a factor of 2-3.

Additional enhanced gustiness during the cold stages (McGee et al., 2010) seems to be the most reasonable explanation for this increase, if we consider all our proxies and atmospheric circulation evidence taken together. McGee et al. (2010) found that enhanced gustiness in dust source areas appeared contemporaneous to greater meridional temperature gradients during glacial periods (as shown above), while mean wind speeds did not change considerably. More frequent dust outbreaks over enlarged source areas during cold periods then explain the amplitudes in dust supply to the ocean during the past 500 ka.

5. Summary and Conclusion

The results of this study demonstrate that western South America south of the Gulf of Guayaquil was more arid during glacials, and more humid during interglacials of the past 500 ka, corroborating the general idea of globally dustier glacials vs. more humid interglacials. Our findings seem to contradict earlier studies of South American continental climate presenting a wetter Altiplano during glacials (e.g., Thompson et al., 1998). However, these contrasting observations can be reconciled by considering that this situation corresponds to a typical La Niña-like austral summer season (Houston, 2006), when moisture transport by strong low-level easterly winds from Atlantic sources is increased so that wet episodes occur throughout the Altiplano, resulting in a rain shadow above the Western Cordillera as a consequence (Garreaud et al., 2003). During glacials, dust source areas around the Atacama were enlarged, the atmospheric circulation system including the ITCZ of the SE Pacific was located further to the north, and the meridional wind component and accordingly the Hadley cell were intensified. This led to an increased capacity, i.e. dust load, of the southeast trade winds.

The southeast trade wind system intensified only slightly between 500 and 250 ka and again between 250 ka and the LGM, but not on a glacial cyclicity. This is in contrast to findings in an analogous study area off the southwestern coast of Africa (Namibia) from Stuut et al. (2002), who recognized stronger southeast trade winds during glacials compared to interglacials.

The fact that grain sizes do not reveal increases in wind speed, the limited extension of the source areas, and the non-changing wind direction due to the Andean mountain range strongly speak for enhanced gustiness during the glacials as another important mechanism for the 2-3 fold increase in dust accumulation rates at ODP Site 1237. Future regional modeling and investigations of SST gradients along

the South American west coast and of the dust-entraining processes in the source area will further elucidate our hypotheses.

6. Acknowledgements

We thank Alan Mix for providing sample material from core RRV9702A-69PC. We thank Roseanne Schwartz (LDEO), Ingrid Stimac and Ilsetraut Stölting (AWI) for technical support in the laboratory and Marty Fleisher (LDEO) for ICP-MS analyses; Sven Kretschmer for helpful discussions and comments. This study was supported by the German Science Foundation (DFG).

Supplementary Material

Methodology: Th-Profiling Due to a lack of sample material, the fine fraction collected after washing the samples over 63 μm - meshes was collected to analyze them for their excess $^{230}Th_0$ and ^{232}Th concentrations. Most of the Thorium sinks to the ocean floor attached to the fine fraction $<$20 μm (cf. Kretschmer et al. 2010). The values for the bulk fraction are thus slightly decreased compared to the fine fraction, as the concentration in the bulk fraction is lower as expected, in our case by about 10%. However, we consider the disparity negligible for our interpretations.

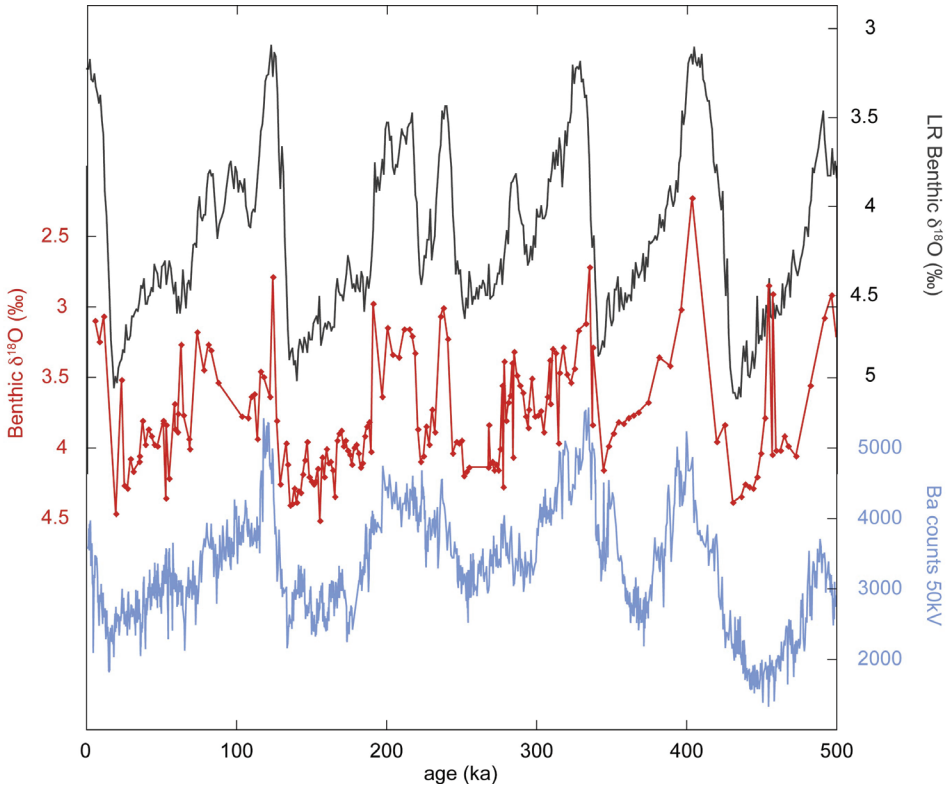

Figure 25: S1. Age model of ODP Site 1237. Alignment of the benthic δ^{18}O record from ODP site 1237 (red) to the LR04 stack (black), both in per mil, as refined with the Ba-counts (blue) of ODP Site 1237 XRF scans. For the benthic δ^{18}O record from ODP site 1237 different species had to be used: *Cibicidoides wuellerstorfi*, *Uvigerina peregrina*, *Uvigerina hispida*. The values obtained for the Uvigerina species were adjusted to *C. wuellerstorfi* by subtracting 0.64.

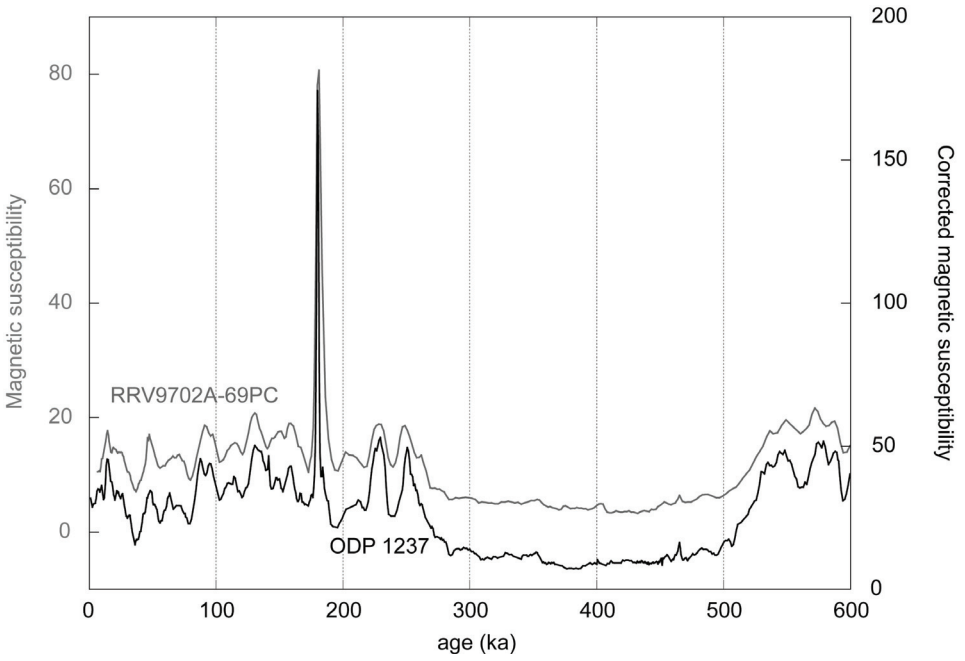

Figure 26: S2. Alignment of sediment cores investigated in this study. Magnetic Susceptibility of ODP Site 1237 (black) and RRV9702A-69PC (grey). The age model of ODP Site 1237 was thus used for pre-site survey core RRV9702A-69PC. The peak at ∼180 ka represents an ash layer present in ODP 1237 boreholes A and C, as well as RRV9702A-69PC.

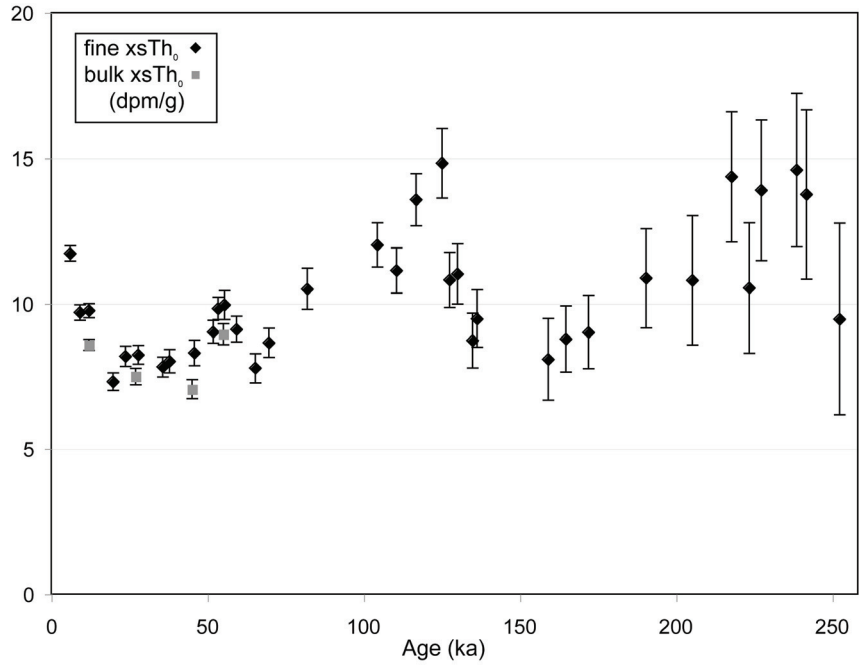

Figure 27: S3. Comparison of excess $^{230}Th_0$ (dpm/g) of the bulk sediment (grey squares) and the fine fraction (black diamonds). Error bars are shown for both, representing propagated errors associated with the calculation of the initial unsupported ^{230}Th concentration.

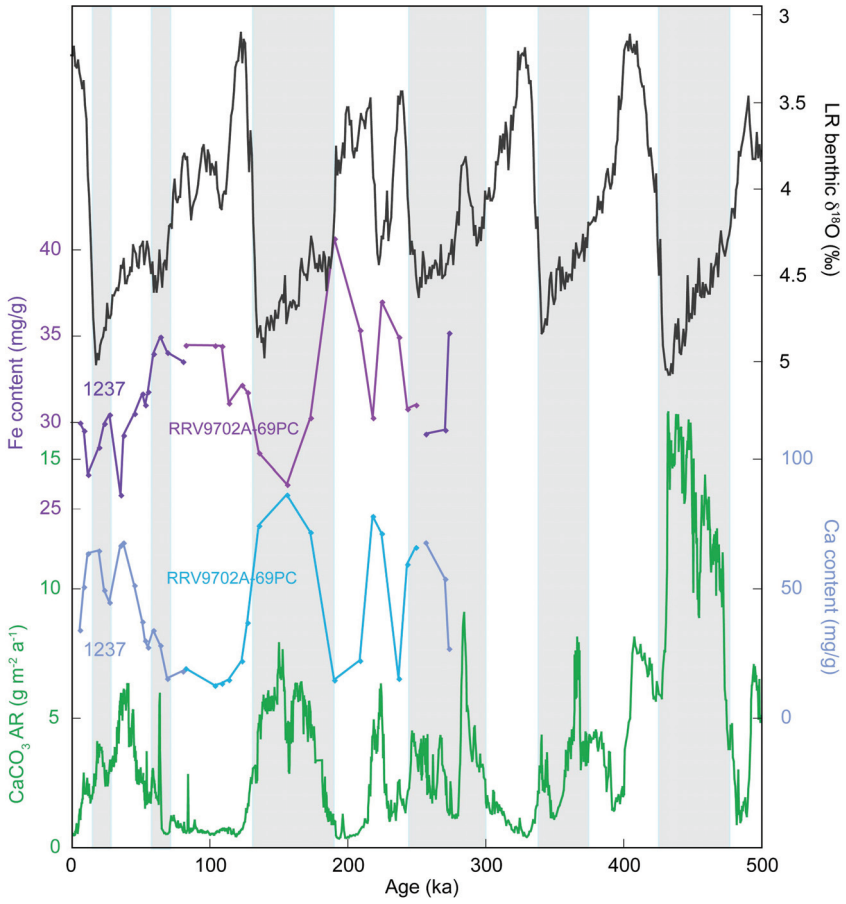

Figure 28: S4. **a** LR04 stack (black), **b** Iron (Fe) content (mg/g) (purple), **c** Calcium (Ca) content (mg/g) (blue) and d $CaCO_3$ mass accumulation rates (mg cm^{-2} ka^{-1}) (green) of ODP site 1237. Glacials are indicated with light blue bars. Ca-contents agree very well with $CaCO_3$ ARs, while Fe-contents are in anti-phase to both Calcium records. This is due to the $CaCO_3$ dissolution effect. Where $CaCO_3$ is well preserved, it dilutes the terrigenous sediment components, in this case Fe.

7. References

Anderson, R.F., Fleisher, M.Q., and Lao, Y., 2006, Glacial-interglacial variability in the delivery of dust to the central equatorial Pacific Ocean: Earth and Planetary Science Letters, v. 242, p. 406, doi:10.1016/j.epsl.2005.11.061

Andreasen, D.J., Ravelo, A.C., and Broccoli, A.J.2001, Remote forcing at the last glacial maximum in the tropical Pacific ocean: Journal of Geophysical Research, v. 106, p. 879-897, doi:10.1029/1999JC000087

Andreasen, D.J., and Ravelo, A.C., 1997, Tropical Pacific ocean thermocline depth reconstructions for the last glacial maximum: Paleoceanography, v. 12 (3), p. 395-413, doi:10.1029/97PA00822

Bacon, M.P., 1984, Glacial to interglacial changes in carbonate and clay sedimentation in the Atlantic Ocean estimated from 230Th measurements, Isot. Geosci., v. 2, 97-111.

Bauer, E. and Ganopolski A., 2010, Aeolian dust modeling over the past four glacial cycles with CLIMBER-2, Global and Planetary Change, v.74, p.49-60, doi:10.1016/j.gloplacha.2010.07.009

Bobst, A.L., Lowenstein, T.K., Jordan, T.E., Godfrey, L.V., Ku, T.-L., and Luo, S., 2001, a 106 ka paleocliamte record from drill core of the Salar de Atacama, northern Chile: Palaeogeography, Paleoclimatology, Palaeoecology, v. 173, p. 21-42

Boven, K.L., and Rea, D.K., 1998, Partitioning of eolian and hemipelagic sediment in eastern Equatorial Pacific core TR 163-31B and the late Quaternary paleoclimate of the Northern Andes: Journal of Sedimentary Research, v. 68, p. 850-855

Broccoli, A.J., Dahl, K.A., and Stouffer, R.J., 2006, Response of the ITCZ to Northern Hemisphere cooling: Geophysical Research Letters, v. 33, p. L01702, doi:10.1029/2005GL024546

Calvo, E., Pelejero, C., Herguera, J.C., Palanques, A., and Grimalt, J.O., 2001, Insolation dependence of the southeastern subtropical Pacific sea surface temperature over the last 400 kyrs: Geophysical Research Letters, v. 28, p. 2481, doi:10.1029/2000GL012024

Cane, M.A., 2005, The evolution of El Niño, past and future: Earth and Planetary Science Letters, v. 230, p. 227, doi:10.1016/j.epsl.2004.12.003

Chuey, J.M., Rea, D.K., and Pisias, N.G., 1987, Late Pleistocene paleoclimatology of the central equatorial Pacific: A quantitative record of eolian and carbonate deposition: Quaternary Research, v. 28, p. 323, doi:10.1016/0033-5894(87)90001-9

Clemens, S.C., 1998, Dust response to seasonal atmospheric forcing: Proxy evaluation and calibration: Paleoceanography, v.13, no.5, p.471-490, doi:10.1029/98PA02131

Francois, R., Frank, M., Rutgers van der Loeff, M.M., and Bacon, M.P., 2004,

230Th normalization: An essential tool for interpreting sedimentary fluxes during the late Quaternary: Paleoceanography, v. 19, p. PA1018, doi:10.1029/2003PA000939

Garreaud, R., Vuille, M., Clement, A.C., 2003, The climat
e of the Altiplano: observed current conditions and mechanisms of past changes: Palaeogeography, Palaeoclimatology, Palaeoecology, v. 194, p. 5, doi:10.1016/S0031-0182(03)00269-4 Hay, W.W., 1996, Tectonics and climate: Geologische Rundschau, v.85, p. 409-437

Hovan, S. A., 1995, Late Neogene atmospheric circulation intensity and climatic history recorded by eolian deposition in the eastern equatorial Pacific: Proc. ODP, Scientific Results, 138: College Station, TX (Ocean Drilling Program), p. 615-625

Houston, J., 2006, Variability of precipitation in the Atacama Desert: its causes and hydrological impact: International Journal of Climatology, v. 26, p. 2181.1097-0088, doi: 10.1002/joc.1359

Janecek, T.R., Rea, D.K., 1985, Quaternary fluctuations in the northern hemisphere trade winds and westerlies: Quaternary Research, v. 24, p. 150-163

Kaiser, J., Lamy, F., and Hebbeln, D., 2005, A 70-kyr sea surface temperature record off southern Chile (Ocean Drilling Program Site 1233): Paleoceanography, v. 20, p. PA4009.0883-8305, doi:10.1029/2005PA001146

Kohfeld, K.E., and Harrison, S.P., 2001, DIRTMAP: the geological record of dust: Earth-Science Reviews, v. 54, p. 81, doi:10.1016/S0012-8252(01)00042-3

Kohfeld, K.E., and Tegen, I., 2007, Record of Mineral Aerosols and Their Role in the Earth System. In: H.D. Holland and K. Turekian (eds.), Treatise on geochemistry, Elsevier

Koutavas, A., and Lynch-Stieglitz, J., 2003, Glacial-interglacial dynamics of the eastern equatorial Pacific cold tongue-Intertropical Convergence Zone system reconstructed from oxygen isotope records: Paleoceanography, v. 18, p. 1089, doi:10.1029/2003PA000894

Koutavas, A., Lynch-Stieglitz, J., Marchitto, T.M., Jr., and Sachs, J.P., 2002, El Niño-Like Pattern in Ice Age Tropical Pacific Sea Surface Temperature: Science, v. 297, p. 226-230. doi:10.1126/science.1072376

Kretschmer, S., Geibert, W., Rutgers van der Loeff, M.M., and Mollenhauer, G., 2010, Grain size effects on 230Thxs inventories in opal-rich and carbonate-rich marine sediments: Earth and Planetary Science Letters, v. 294, p. 131, doi:10.1016/j.epsl.2010.03.021

Krissek, L.A., Scheidegger, K.F., Kulm, L.D., 1980, Surface sediments of the Peru-Chile continental margin and the Nazca plate: Geological Society of America Bulletin, v. 91 (6), p. 321-331, doi:10.1130/0016-7606

Latorre, C., Betancourt, J.L., Rylander, K.A., Quade, J., 2002, Vegetation invasions into absolute desert: A 45000 yr rodent midden record from the Calama - Salar de Atacama basins, northern Chile (lat 22° - 24° S): Geological Society of

America Bulletin, v. 114, p. 349, doi:10.1130/0016-7606

Lawrence, K.T., Liu, Z., and Herbert, T.D., 2006, Evolution of the Eastern Tropical Pacific Through Plio-Pleistocene Glaciation: Science, v. 312, p. 79-83. doi:10.1126/science.1120395

Lindzen, R.S., and Nigam, S., 1987, On the Role of Sea Surface Temperature Gradients in Forcing Low-Level Winds and Convergence in the Tropics: Journal of Atmospheric Sciences, v. 44 (17), p. 2418-2436

Lindzen, R.S., and Hou, A.V., 1988, Hadley Circulations for Zonally Averaged Heating Centered off the Equator: Journal of the Atmospheric Sciences, v. 45, p. 2416, doi:10.1175/1520-0469

Loubere, P., Mekik, F., Francois, R., Pichat, S., 2004, Export fluxes of calcite in the eastern equatorial Pacific from the Last Glacial Maximum to present: Paleoceanography, v.19, p. PA2018, doi:10-1029/2003PA000986

Lisiecki, L.E., and Raymo, M.E., 2005, A Pliocene-Pleistocene stack of 57 globally distributed benthic δ^{18}O records: Paleoceanography, v. 20, p. PA1003, doi:10.1029/2004PA001071

Lunt, D.J, and Valdes, P.J., 2002, Dust deposition and provenance at the Last Glacial Maximum and present day: Geophysical Research Letters, v. 29, p. 2085, doi:10.1029/2002GL015656

Maher, B.A., Prospero, J.M., Mackie, D., Gaiero, D., Hesse, P.P., and Balkanski, Y., 2010, Global connections between aeolian dust, climate and ocean biogeochemistry at the present day and at the last glacial maximum: Earth-Science Reviews, v. 99, p. 61, doi:10.1016/j.earscirev.2009.12.001

Mahowald, N.M., Muhs, D.R., Levis, S., Rasch, P.J., Yoshioka, M., Zender, C.S., and Luo, C., 2006, Change in atmospheric mineral aerosols in response to climate: Last glacial period, preindustrial, modern, and doubled carbon dioxide climates: Journal of Geophysical Research, v. 111, p. D10202.0148-0227, doi:10.1029/2005JD006653

Mahowald, N., Kohfeld, K., Hansson, M., Balkanski, Y., Harrison, S.P., Prentice, I.C., Schulz, M., and Rodhe, H., 1999, Dust sources and deposition during the last glacial maximum and current climate: A comparison of model results with paleodata from ice cores and marine sediments: Journal of Geophysical Research, v. 104, p. 15895, doi:10.1029/1999JD900084

Markgraf, V., Baumgartner, T.R., Bradbury, J.P., Diaz, H.F., B. Dunbar, R., Luckman, B.H., Seltzer, G.O., Swetnam, T.W., and Villalba, R., 2000, Paleoclimate reconstruction along the Pole-Equator-Pole transect of the Americas (PEP 1): Quaternary Science Reviews, v. 19, p. 125, doi:10.1016/S0277-3791(99)00058-X

Martin, L., Bertaux, J., Corrège, T., Ledru, M.-P., Mourguiart, P., Sifeddine, A., Soubiès, F., Wirrmann, D., Suguio, K., and Turcq, B., 1997, Astronomical Forcing of Contrasting Rainfall Changes in Tropical South America between 12,400 and

8800 cal yr B.P: Quaternary Research, v. 47, p. 117, doi:10.1006/qres.1996.1866

Martinez, I., Keigwin, L., Barrows, T.T., Yokoyama, Y., Southon, J., 2003, La Niña-like conditions in the eastern equatorial Pacific and a stronger Choco jet in the northern Andes during the last glaciation: Paleocenaography, v. 18 (2), p.1033, doi: 10.1029/2002PA000877

McGee, D., Marcantonio, F., and Lynch-Stieglitz, J., 2007, Deglacial changes in dust flux in the eastern equatorial Pacific: Earth and Planetary Science Letters, v. 257, p. 215.0012-821X,
doi: 10.1016/j.epsl.2007.02.033

McGee, D., Broecker, W.S., Winckler, G., 2010, Gustiness: The driver of glacial dustiness?: Quaternary Science Reviews, v. 29, p.2340-2350,
doi:10.1016/j.quascirev.2010.06.009

Mix, A.C., Tiedemann, R., Blum, P. (eds.), 2003, Proc. ODP, Initial Reports Leg 202: College Station, TX, Ocean Drilling Program, p. 1-107, doi:10.2973/odp.proc.ir.202.2003

Müller, P.J., and Schneider, R., 1993, An automated leaching method for the determination of opal in sediments and particulate matter: Deep Sea Research Part I: Oceanographic Research Papers, v. 40, p. 425, doi:10.1016/0967-0637(93)90140-X

Olivarez, A.M., Owen, R.M., and Rea, D.K., 1991, Geochemistry of eolian dust in Pacific pelagic sediments: Implications for paleoclimatic interpretations: Geochimica et Cosmochimica Acta, v. 55, p. 2147, doi:10.1016/0016-7037(91)90093-K

Paillard, D., 1996, Macintosh Program performs time-series analysis: Eos Trans

Pierrehumbert, R.T., 2000, Climate change and the tropical Pacific: The sleeping dragon wakes: PNAS, v. 97, p. 1355-1358

Rea, D.K., 1994, The paleoclimatic record provided by eolian deposition in the deep sea: The geologic history of wind: Review of Geophysics, v. 32, p. 159, doi:10.1029/93RG03257

Rea, D.K., Chambers, L.W., Chuey, J.M., Janecek, T.R., Leinen, M., and Pisias, N.G., 1986, A 420,000-year record of cyclicity in oceanic and atmospheric processes from the eastern equatorial Pacific: Paleoceanography, v. 1, p. 577,
doi:10.1029/PA001i004p00577

Rea, D.K., Leinen, M., and Janecek, T.R., 1985, Geologic Approach to the Long-Term History of Atmospheric Circulation: Science, v. 227, p. 721-725. doi:10.1126/science.227.4688.721

Reiter, E.R., 1979, Trade-Wind Variability, Southern Oscillation, and Quasi-Biennial Oscillation: Archiv für Meteorologie, Geophysik und Bioklimatologie, v. 28, p. 113

Rincón-Martínez, D., Lamy, F., Contreras, S., Leduc, G., Bard, E., Saukel, C.,

Blanz, T., Mackensen, A., and Tiedemann, R., 2010, More humid interglacials in Ecuador during the past 500 kyr linked to latitudinal shifts of the equatorial front and the Intertropical Convergence Zone in the eastern tropical Pacific: Paleoceanography, v. 25, p. PA2210. doi:10.1029/2009PA001868

Sarnthein, M., Tetzlaff, G., Koopmann, B., Wolter, K., and Pflaumann, U., 1981, Glacial and interglacial wind regimes over the eastern subtropical Atlantic and North-West Africa: Nature, v. 293, p. 193. doi:10.1038/293193a0

Stuut, J.-B.W., Prins, M.A., Schneider, R.R., Weltje, G.J., Jansen, J.H.F., and Postma, G., 2002, A 300-kyr record of aridity and wind strength in southwestern Africa: inferences from grain-size distributions of sediments on Walvis Ridge, SE Atlantic: Marine Geology, v. 180, p. 221.0025-3227, doi:10.1016/S0025-3227(01)00215-8

Stuut, J.-B.W., and Lamy, F., 2004, Climate variability at the southern boundaries of the Namib (southwestern Africa) and Atacama (northern Chile) coastal deserts during the last 120,000 yr: Quaternary Research, v. 62, p. 301.0033-5894, doi: 10.1016/j.yqres.2004.08.001

Stuut, J.-B.W., Kasten, S., Lamy, F., and Hebbeln, D., 2007, Sources and modes of terrigenous sediment input to the Chilean continental slope: Quaternary International, v. 161, p. 67, doi:10.1016/j.quaint.2006.10.041

Tiedemann, R., Sarnthein, M., Stein, R., 1989, Climatic changes in the western Sahara: Aeolo-marine sediment record of the last 8 million years (Sites 657-661): Proceedings ODP, Scientific results, v. 108, p. 241

Thompson, L.G., Davis, M.E., Mosley-Thompson, E., Sowers, T.A., Henderson, K.A., Zagorodnov, V.S., Lin, P.N., Mikhalenko, V.N., Campen, R.K., Bolzan, J.F., Cole-Dai, J., and Francou, B., 1998, A 25,000-Year Tropical Climate History from Bolivian Ice Cores: Science, v. 282, p. 1858, 10.1126/science.282.5395.1858

Toggweiler, J.R., 2009, CLIMATE CHANGE: Shifting Westerlies: Science, v. 323, p. 1434-1435, doi: 10.1126/science.1169823

Werner, M., Tegen, I., Harrison, S.P., Kohfeld, K.E., Prentice, I.C., Balkanski, Y., Rodhe, H., and Roelandt, C., 2002, Seasonal and interannual variability of the mineral dust cycle under present and glacial climate conditions: Journal of Geophysical Research, v. 107, p. 4744, doi:10.1029/2002JD002365

Weltje, G.J., and Prins, M.A., 2007, Muddled or mixed? Inferring palaeoclimate from size distributions of deep-sea clastics: Sedimentary Geology, v. 162, p. 39.0037-0738, doi: 10.1016/S0037-0738(03)00235-5

Weltje, G.J., and Prins, M.A., 2003, Genetically meaningful decomposition of grain-size distributions: Sedimentary Geology, v. 202, p. 409.0037-0738, doi: 10.1016/j.sedgeo.2007.03.007

Winckler, G., Anderson, R.F., Fleisher, M.Q., McGee, D., and Mahowald, N., 2008, Covariant Glacial-Interglacial Dust Fluxes in the Equatorial Pacific and Ant-

arctica: Science, v. 320, p. 93, doi:10.1126/science.1150595

4.3 Glacial-Interglacial Variability in Dust Supply to the SE Pacific during the Plio-Pleistocene Transition (2-3.1 Ma)

Cornelia Saukel, Jan-Berend Stuut, Frank Lamy, Ralf Tiedemann
(Manuscript in preparation)

Abstract Plio-Pleistocene variations in southeast trade wind strength and its dust transport are considered missing links for a comprehensive understanding of the tropical Southeast Pacific paleoceanography, including thermocline dynamics and the amplification of oceanic upwelling and productivity. In order to reconstruct long-term changes in southeast trade wind intensities and South American continental aridity linked to the Northern Hemisphere Glaciation intensification, trade wind strength was reconstructed by analyzing the wind-blown sediment fraction at ODP Site 1237 for grain-size distribution and the geochemical composition of the bulk sediment.

An end-member modeling algorithm (EMMA) resolved the original grain-size populations of the terrigenous sediment fraction and allowed the identification of three different contributors: a coarse volcanic ash end member and a silt- and clay-sized dust end member, both attributed to eolian dust from the Atacama Desert. Ash layers characterized by extremely coarse grain sizes anticipate a clear pattern of the grain-size means or modes. The volcanic ash points to phases of major outbreaks between 2.9 and 2.7 Million years (Ma), at ∼2.6 Ma, between ∼2.33 - 2.25 Ma, and 2.13 - 2.08 Ma. The coarser of the dust end members co-varies with iron and titanium accumulation rates on glacial-interglacial cycles and with sea surface temperatures in the east Pacific Cold Tongue (ODP Site 846, Lawrence 2006). Taken together, the data indicate drier continental conditions and stronger southeast trade winds during cold periods versus less intense wind strength during warm stages between 2.7 - 2.0 Ma. Long-term increases in dust accumulation and wind strength between ∼2.7 Ma and 2.5 Ma, and 2.2 and 2.0 Ma are associated with times of global climate cooling and likely the result of a development of stronger atmospheric circulation in the equatorial Pacific.

Keywords: Tropical east Pacific, SE trade winds, dust, Plio-Pleistocene transition

1. Introduction

The Plio-Pleistocene transition was a phase of major global climatic reorganization resulting in major Northern Hemisphere Glaciation (NHG) between ∼3.1 and 2 Ma (e.g., Raymo, 1994; Shackleton et al., 1984) and marked by regular occurrence of ice-rafted debris in the North Atlantic and Pacific oceans from ∼2.7 Ma onwards

(e.g., Haug et al., 2005; Kleiven et al., 2002; Thiede et al., 1998). Conditions changed from relatively warm and ice-free climates in high latitudes to generally colder climates (e.g., Lisiecki and Raymo, 2005). The role of the tropics in global climate reorganization has attracted much attention in paleoclimate research during the past couple of decades (Cane, 1998; Mix, 2006; Pierrehumbert, 2000; Ravelo, 2010). For example, the low-latitude Pacific strongly contributes to the global atmosphere's sensible and latent heat budget (Cane, 1998; Pierrehumbert, 2000; Philander and Fedorov, 2003) influencing the ocean's thermohaline circulation. The tropical Pacific in turn can be influenced by extratropical forcing, such as changes in water masses that are subducted in the high latitudes and upwelled in the tropical regions (e.g., Fedorov and Philander, 2001; Strub, 1998). The interaction of high- and low-latitudes and the contribution of tropical processes to global climate variations are still under debate (e.g., Fedorov et al., 2006; Ravelo, 2010). Understanding atmosphere-ocean linkages is essential in this context as winds influence upwelling intensities and sea surface temperatures (SST), but in turn depend on ocean temperature gradients (e.g., Philander and Fedorov; 2003 Strub, 1998) .

While numerous studies have focused on Pliocene SSTs and changes in thermocline depth in the equatorial east Pacific (Dekens et al., 2007; Groeneveld et al., 2006; Lawrence et al., 2006; Philander and Fedorov, 2003; Steph et al., 2006; Wara et al., 2005), studies of proxies for atmospheric change in the area are rather sparse. Therefore, this study will focus on changes in trade wind strength and dust transport on orbital time scales, as these are considered missing links in understanding the Plio-Pleistocene changes in tropical Pacific oceanography and productivity, associated with changes in thermocline depth and upwelling.

Such links between wind strength and changes in oceanography have been described for other regions and time intervals. Marlow et al. (2000) attributed the gradual increase in upwelling and hence cooling SSTs in the Benguela Current off Namibia during the Plio-Pleistocene to the onset of NHG and concurrent strengthening of winds to larger pole-to-equator temperature gradients. In contrast, Rea (1994) stated there was no sign of paleoclimatic changes in southern hemisphere eolian records during the late Pliocene. Hovan (1995) documented a decreasing input of eolian material to the equatorial Pacific throughout the Neogene as a consequence of relatively wetter conditions in the continental eolian source areas since the late Pliocene. This interpretation, taken for face value, contradicts the link between global cooling and increasing aridification.

The aim of this study therefore is to reconstruct relative changes of Pacific southeast trade-wind strength and dust transport during the intensification of NHG to elucidate the role of the atmospheric component in paleoceanographic changes of the equatorial East Pacific (EEP) and in turn the potential influence of the EEP on the global feedback mechanism. We present the first high-resolution dust record of the

tropical Southeast (SE) Pacific covering the Plio-Pleistocene transition (3.1 - 2 Million years before present (Ma)). We document changes in dust accumulation rates and grain-size distributions at ODP Site 1237 ($\sim$140 km offshore southern Peru) as indicators of changes in South American continental aridity and SE trade wind strength, respectively (e.g.; Rea, 1994; Stuut et al., 2002).

2. Material and Methods

ODP Site 1237 is located at 16°S, 76°W on Nazca Ridge west of the deep-sea trench and has underlain the path of eolian transport from the Atacama Desert in Peru and northern Chile at least since early Pliocene time. During the Plio-Pleistocene transition (2-3.1 Ma), ODP Site 1237 located on the eastern flank of Nazca Ridge tectonically moved roughly 50 km towards the southern coast of Peru (Mix et al., 2003). Nevertheless, there is no visible trend in the data related to the tectonic backtrack during the time interval in consideration.

The age model is from Tiedemann et al. (2007a), based on a multi-proxy tuning approach, including benthic δ^{13}C and GRA density. To improve the age model of the Site 1237 we performed δ^{18}O measurements on 1 - 5 specimens of the epibenthic foraminifer *Cibicidoides wuellerstorfi* from the size fraction >250 - 400 μm on a FINNIGAN 253 mass spectrometer with a Kiel CARBO device at the Alfred-Wegener-Insitute (AWI) in Bremerhaven. Analytical reproducibility was $\sim$0.08 ‰for δ^{18}O. The benthic δ^{18}O record was tied to the chronology of the LR04 isotope stratigraphy of Lisiecki and Raymo (2005), applying the *Analyseries* software (Paillard, 1996) (Fig. 29).

The geochemical composition of the sediment was analyzed applying non-destructive X-ray fluorescence scanning (XRF) (Aavatech 2nd generation XRF Scanner at AWI) and Inductively Coupled Plasma - Optical Emission Spectrometry (ICP-OES in the Geochemistry Department at AWI). Split sediment cores were scanned in 2 cm intervals corresponding to a time-resolution of $\sim$650 - 2000 years. We show log-ratios of XRF-scan intensities as they closely mimic the patterns of log-ratio element abundances, providing interpretable signals of relative changes in the chemical composition of the sediment (Weltje and Tjallingii, 2008). Iron (Fe), titanium (Ti), and potassium (K) XRF counts were additionally calibrated to absolute concentrations determined by ICP-OES on 100 samples via linear correlation (e.g., Monien et al., 2010; Rincón et al. 2010).

Linear sedimentation rates (LSR, in cm ka^{-1}) were derived from the age model and multiplied by the dry bulk density (DBD in g cm^{-3}) obtained from borehole logging data at site 1237 (Mix et al., 2003) and element concentrations to calculate accumulation rates (AR, in g cm^{-2} ka^{-1}) of sediment components indicating terrigenous input:

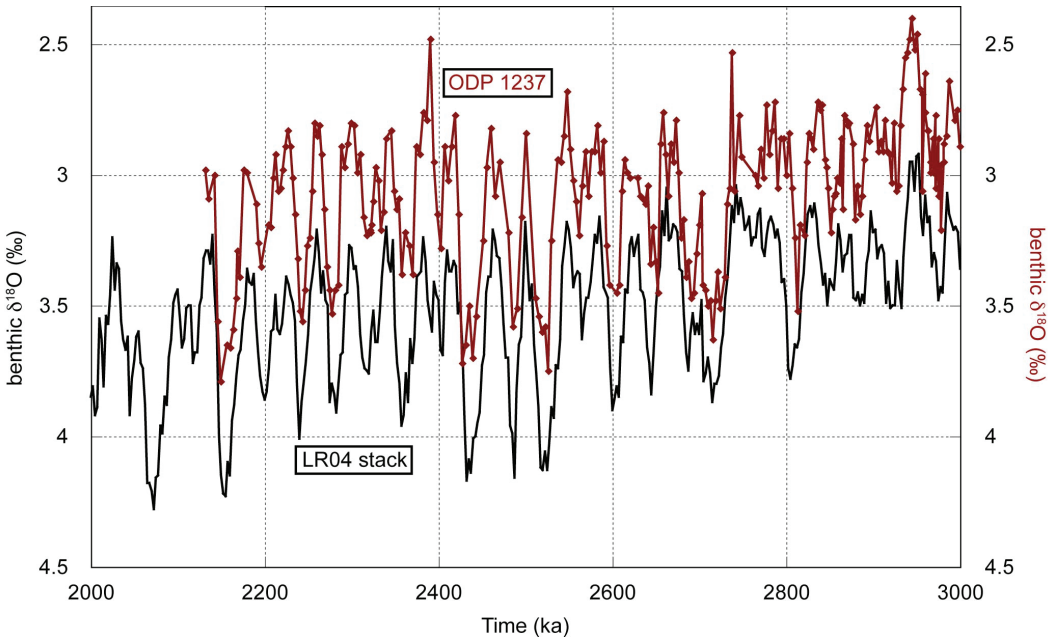

Figure 29: δ^{18}O records of Lisiecki and Raymo (2005) (black) and ODP Site 1237, this study (red)

$$\text{AR} = \rho_{dry} * \text{LSR} * \text{component of sediment } (\%).$$

We measured the grain-size distribution of the terrigenous siliciclastic sediment fraction of 165 samples with a Beckman-Coulter Laser Particle Sizer. To isolate the terrigenous sediment fraction, organic matter was removed boiling the samples with excess of a 10% H_2O_2 solution until reaction stopped. Carbonates and biogenic opal were removed boiling the samples with excess 10% HCl^{-1} for one minute and NaOH for 20 minutes, respectively (e.g., Stuut et al., 2007). Before the analysis, the sediment suspensions were brought to boil with a few mg of $NaPyPO_4$ in order to avoid coagulation of particles.

Subsequently, the end-member modeling algorithm (EMMA) of Weltje (1997) was applied to the siliciclastic grain-size data set in order to identify the original sediment populations, i.e. sources and transport mechanisms that are preserved in and can be retrieved from marine sediments. The minimum number of end members needed to model the variance in the data set satisfactorily is determined by a 'goodness of fit', the coefficients of determination for several different models. It is calculated for each size class and represents the squared correlation coefficient (r^2) of the input variables and their approximated values (Prins and Weltje, 1999; Weltje, 1997).

3. Results

A significant correlation of iron (Fe) and titanium (Ti) (wt%) (r^2=0.94) (S1) suggests a common terrigenous source of these elements. The strong correlation suggests no diagenetical remobilization of Fe, as Ti is hardly influenced by diagenetic processes (Richter et al., 2006). Fe and Ti accumulation rates (ARs) generally oscillate on glacial-interglacial cycles (Fig. 30B, C), where maxima coincide with glacials, and minima with interglacials. The Fe and Ti ARs both show increases from ∼2.8 Ma to ∼2.5 Ma. K ARs (Fig. 30D) generally co-vary with Fe and Ti ARs except of 12 sharp events concurrent with peaks in grain-size means that are associated with ash layers and patches of ash desribed in the sediment core (Mix et al., 2003). Some of the rare exceptional interglacial local maxima in Fe and Ti ARs are also concurrent with extremely coarse grain-size means (Fig. 30E).

The mean grain size of the terrigenous fraction ranges from 2.5 and 36 μm, generally varying between 2.5 and 8 μm (Fig. 30E), while means >8 μm correspond to the ash layers or ash lenses in the sediment core mentioned above (Mix et al., 2003).

The average grain-size distribution has a modal grain size of 4.44 μm (Fig.31a). A 3-end-member (EM) model provided the best compromise based on the coefficient of determination (r^2 mean = 0.85) (Fig.31b) and the need to keep the number of end members as small as possible. Overall, the model represents the grain-size data well, except of the size classes between 10-20 μm, where the coefficient of determination (r^2) reaches only 0.55 (Fig. 31c). EM1 is the coarsest end member with the dominant mode at 50.2 μm (Fig. 31d). Its long tail in the fine size classes is an artifact of the EM-analysis. EM2 and 3 overlap considerably, but show distinctly different modes at 2.31 μm and 6.45 μm respectively. Their two minor modes at the coarse end are residues from the statistical analysis and not of importance as their frequencies are very low (<1.5 vol. %).

The proportions of the three end members (Fig. 32) co-vary with changes in terrigenous accumulation rates and terrigenous element concentrations respectively. K ARs co-varies with EM1. K ARs show highest values and amplitudes between ∼2.7 and 2.93 Ma when EM1 proportions also increase sharply. EM2 and the log-ratio of Fe/K co-vary significantly in long- as well as short-term sequences (Fig. 32). Both increase from ∼2.8 Ma until ∼2.5 Ma. The dust character of EM2 is supported by the agreement of its grain-size distribution with grain-size distributions of present-day dust deposited on Nazca Ridge. The coarse present-day dust end-member in Saukel et al. (2011) displays a mode of 5.88 μm, comparable to the range of EM2 with a mode of 6.45 μm. EM3 is the finest of the three end members, representing clay-sized grain-size distributions. Proportions of EM3 vary around an average of 47%, while log(Al/K) displays a mean of -1.6, both showing a few neg-

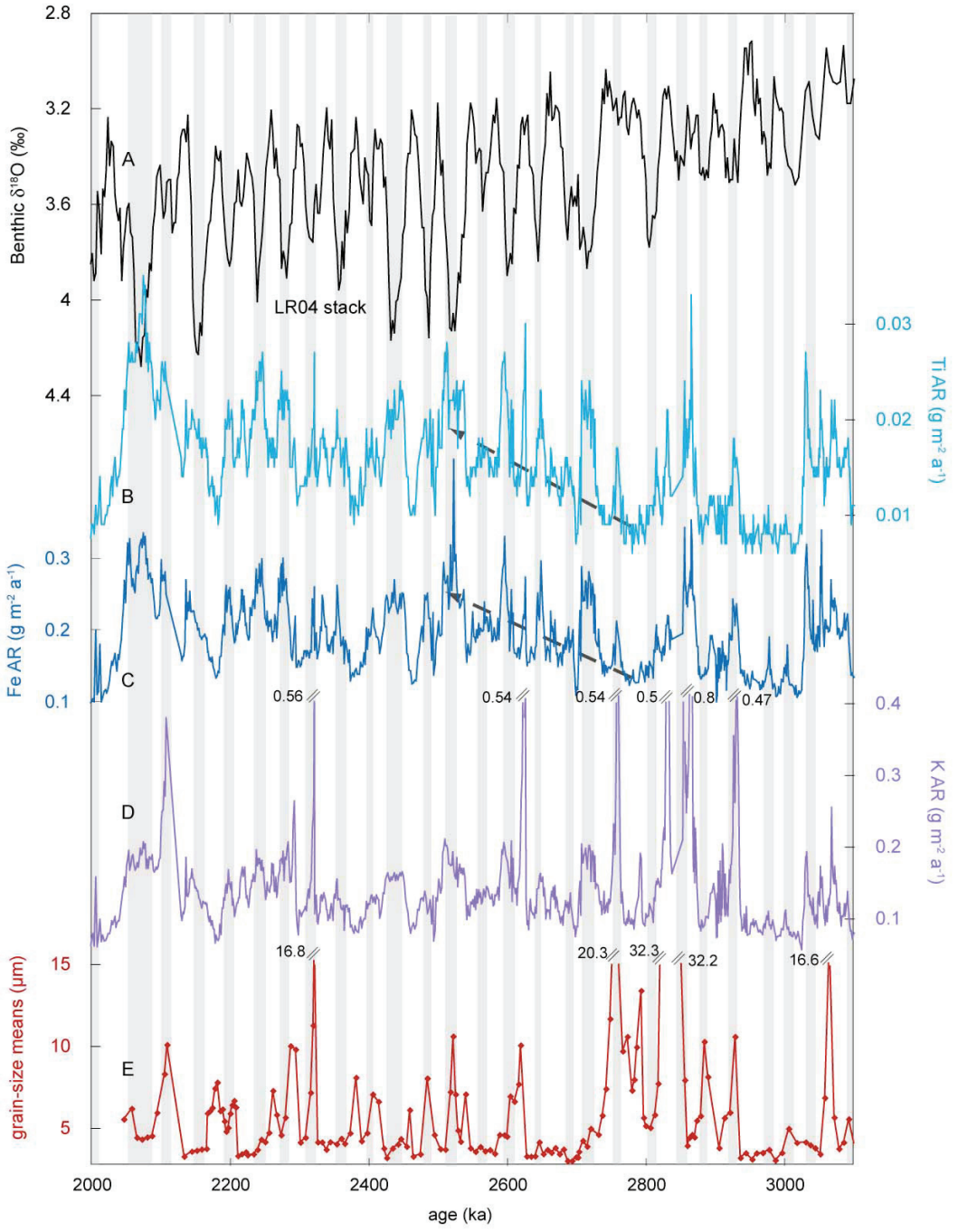

Figure 30: Accumulation rates of terrigenous elements representative of dust and average grain size. **A** δ^{18}O record of Lisiecki and Raymo (2005); **B** Titanium accumulation rates (g m^{-2} a^{-1}); **C** Iron accumulation rates (g m^{-2}a^{-1}); **D** Potassium accumulation rates (g m^{-2}a^{-1}); **E** Mean grain size of grain-size distributions (μm); grey bars indicate cold periods (glacials) as indicated by the oxygen isotope stack.

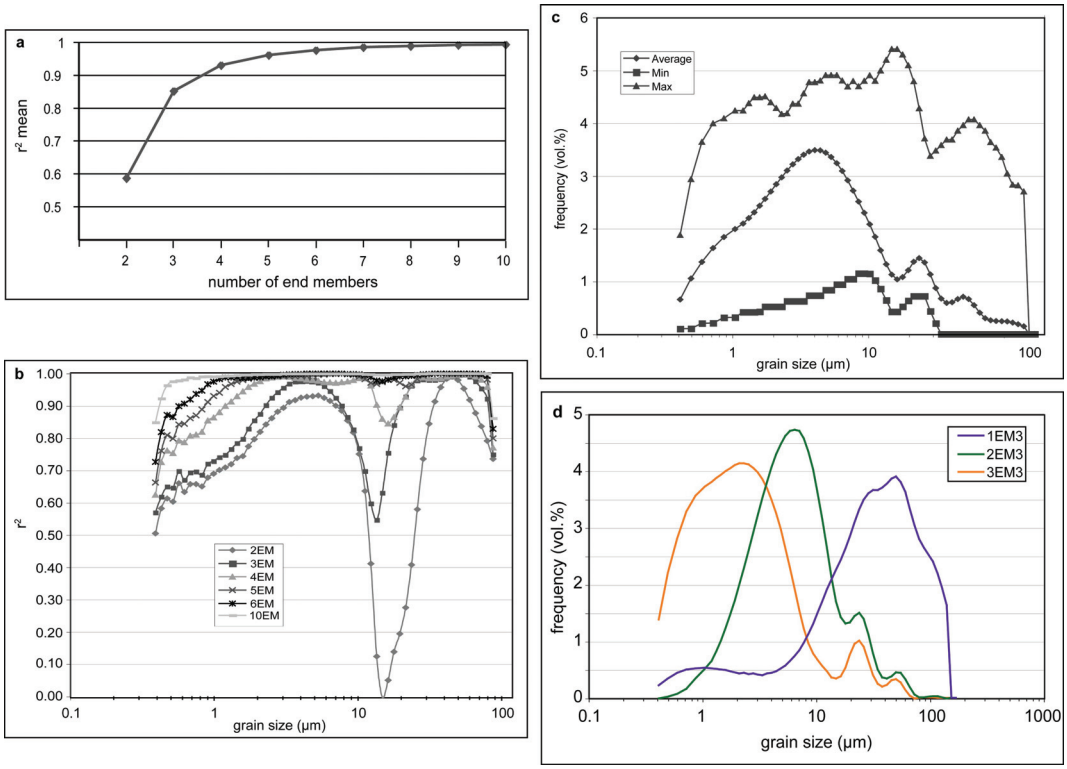

Figure 31: Grain-size end member analysis statistics. **a** Mean coefficient of determination (r^2 mean) for models with varying numbers of EMs; **b** Coefficient of determination (r^2) for each grain-size class for different models; **c** Average, minimum and maximum grain-size distributions of the entire data set; **d** Grain-size distributions of the 3 end members of the model applied for paleoclimate reconstruction in this study.

ative excursions, mostly concomitant with prominent ash layers (Fig. 32). There is no long-term trend visible in the record.

4. Discussion

The SE trade winds are the modern transporting agent of dust in the study area (Saukel et al., in press) and most probably have been during the Pliocene and Pleistocene as well. Due to its location west of the South American deep-sea trench that catches turbidites and riverine input, and the small number of perennial rivers in southern Peru and northern Chile, fluvial input can largely be excluded at the study site (Saukel et al., in press). Furthermore, 3.1 - 2 Ma ago, the study site was located further offshore, rendering the contribution of fluvial supply to sediment accumulation even less likely. Therefore, unlike the commonly accepted idea that terrigenous sediments with grain-size medians of >6 μm are attributed to eolian transport and <6 μm to hemipelagic transport (Clemens, 1998; Holz et al., 2004; Koopmann, 1981; Prins and Weltje, 1999; Sarnthein et al., 1981; Sirocko, 1991; Stuut et al., 2002), the terrigenous input to ODP Site 1237 consists predominantly of wind-blown material.

4.1 Volcanic Ash Components in Eolian-Derived SE Pacific Marine Sediments

Even though transported by winds, volcanic ash layers can be obstructive when retrieving paleoclimatic dust signals from marine sediments. Due to highest volcanic activitiy between 2.93 and 2.75 Ma, the interval is not useful for paleoclimate interpretations (Fig. 32). In several previous studies the activity of Andean volcanoes crowning the Western Cordillera of the central Andes has been studied investigating marine sediments (e.g., Leg 201 Hart and Miller, 2006; Leg 112 Pouclet et al., 1990). As the ash does not always form discrete sediment layers, it is difficult to omit all ash contributions when sampling. However, very coarse grain-size distributions (EM1) together with a potassium-rich geochemical composition, associated with Andean volcanism (Hart and Miller, 2006), precisely identify ash layers in sediments of ODP Site 1237 during the time of the Plio-Pleistocene transition (Fig. 32; Mix et al., 2003). Further evidence is given by the coarse character of EM1, which is attributed to abundant volcanic glass that was observed in the samples. Sand- and coarse silt-sized grain-size modes (up to 96.5 μm) of the terrigenous fraction and sharp peaks of K AR mark the intervals of 2.93 - 2.75 Million years (Ma), at $\sim$2.61 Ma, between 2.33 - $\sim$2.25Ma, and 2.13 - 2.08 Ma, pointing to phases of major volcanic activity in the Andes' central volcanic zone (16 - 28°S), probably related to subduction-induced uplift (Hart and Miller, 2006).

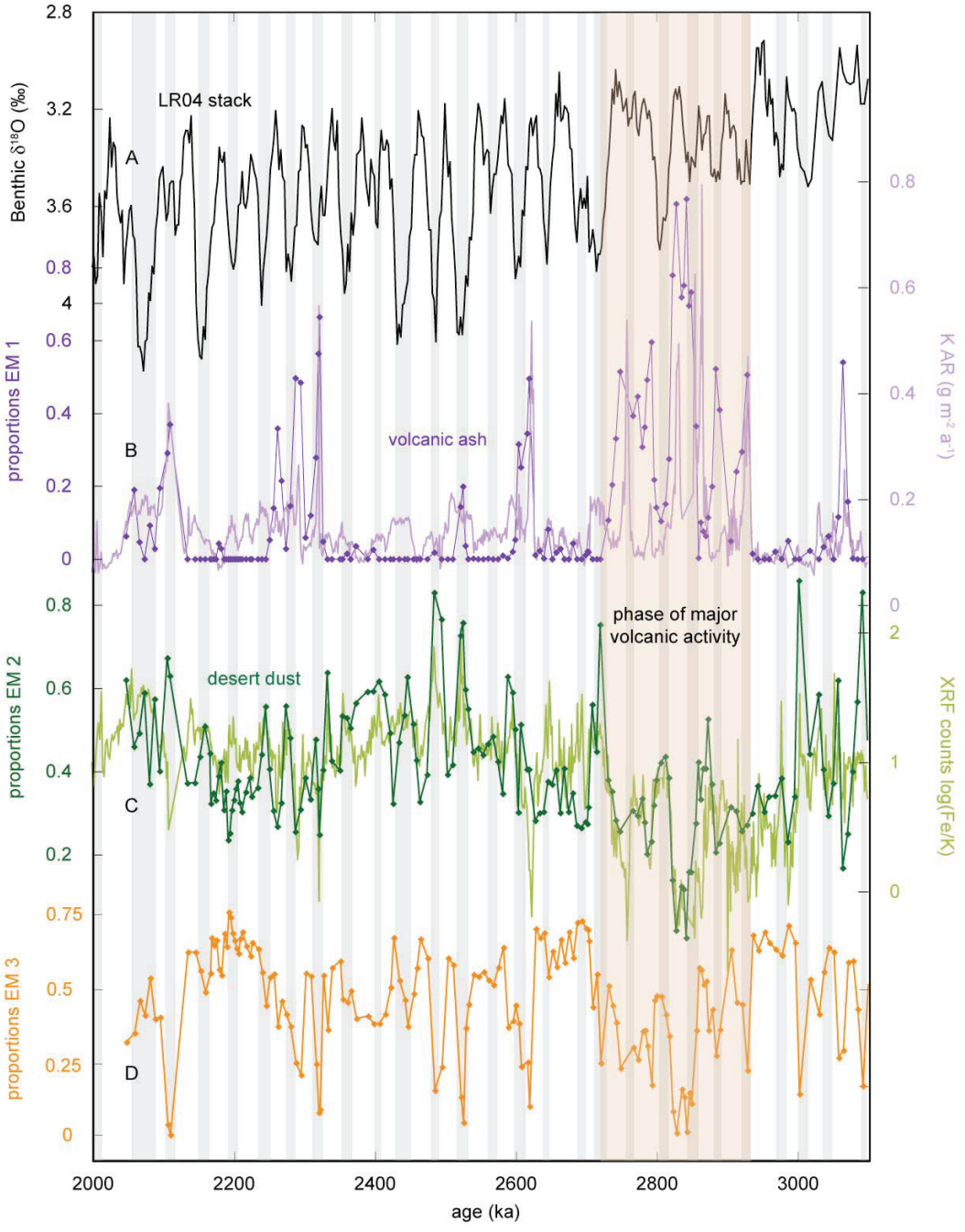

Figure 32: EM proportions and relative changes in geochemical composition plotted against time. **A** δ^{18}O record of Lisiecki and Raymo (2005); **B** K accumulation rates (g $m^{-2}a^{-1}$) (light purple), proportions of EM1 (dark purple); **C** Log ratio of Fe/K XRF counts (light green), proportions of EM2 (dark green); **D** Proportions of EM3 (orange); grey bars indicate cold periods (glacials) as indicated by the oxygen isotope stack; phases marked by black bars on top of plot indicate ash layers from ODP Leg 202 Initial Reports.

4.2 South American Continental Aridity and Changes in Wind Strength During Plio-Pleistocene Transition

End members 2 and 3 are interpreted as coarser (silt-sized) and finer (clay-sized) dust, respectively. The concurrent variability of EM2 proportions and of the log-ratio of (Fe/K) suggests desert dust to be the source. Fe is omnipresent in deserts through the coating of quartz grains of dust (e.g., Goudie and Middleton 2006), but can also be a component of volcanic ash (http://volcanoes.usgs.gov/ash/properties.-html#components). K, on the other hand, is abundant in andesitic volcanic ash (see above) and common in several clay minerals (Moore and Reynolds, 1997). Higher values for log (Fe/K) therefore represent desert soil dust rather than volcanic ash, while lower values suggest a higher abundance of ashes in the sediment. While the Fe/K ratio has been used as a proxy for humidity vs. aridity in Atlantic sediment cores off Senegal (Mulitza et al., 2008). This interpretation does not apply to our study area, where fluvial input is not significant.
The finer dust end member EM3 co-varies with the log-ratio of Al/K (not shown). As mentioned above, Al is very abundant in clay minerals. The proportion of EM3 co-varying with the log-ratio of Al/K suggests that EM3 represents a fine dust component blown out of the Atacama Desert and its surrounding semi-arid areas. There are no trends visible in the record, suggesting rather constant transport and deposition of fine dust at the study site.

Fe and Ti ARs (Fig. 30) as well as EM2 proportions (Fig. 32) are high before 3 Ma, when they suddenly drop suggesting slightly enhanced dust production and/or transport during the Mid-Pliocene warm period. The time interval before $\sim$3 Ma has been extensively studied in the PRISM Project (Dowsett et al., 1999) as it is a warm excursion in a globally cooling climate. The interval from 3.29 to 2.97 represents a phase of relatively stable climate, characterized by reduced continental ice volume and sea-ice, a +25 m higher sea level, increased SSTs in high latitudes, and expanded vegetation cover (Dowsett et al., 1999) compared to modern conditions. A dynamic global vegetation model (Haywood and Valdes, 2006) suggests a replacement of numerous arid areas by grasslands. This limitation of arid areas rather argues for decreased dust production than for an increased availability of dust. However, the core areas of the Atacama Desert stayed hyperarid during the Mid-Pliocene, while the surrounding areas displayed alternating more humid vs. more arid conditions (e.g., Hartley and Chong, 2002). In more humid conditions - meaning semi-arid rather than arid conditions in this context - wet-chemical weathering enhances the production of soils, and, when the soils dry up, dust. The alternation of humid and arid conditions is a likely explanation for the higher amplitudes in Fe and Ti ARs and grain size before 3 Ma, although not on a glacial-interglacial cyclicity. A similar pattern is found in the deserts in Africa

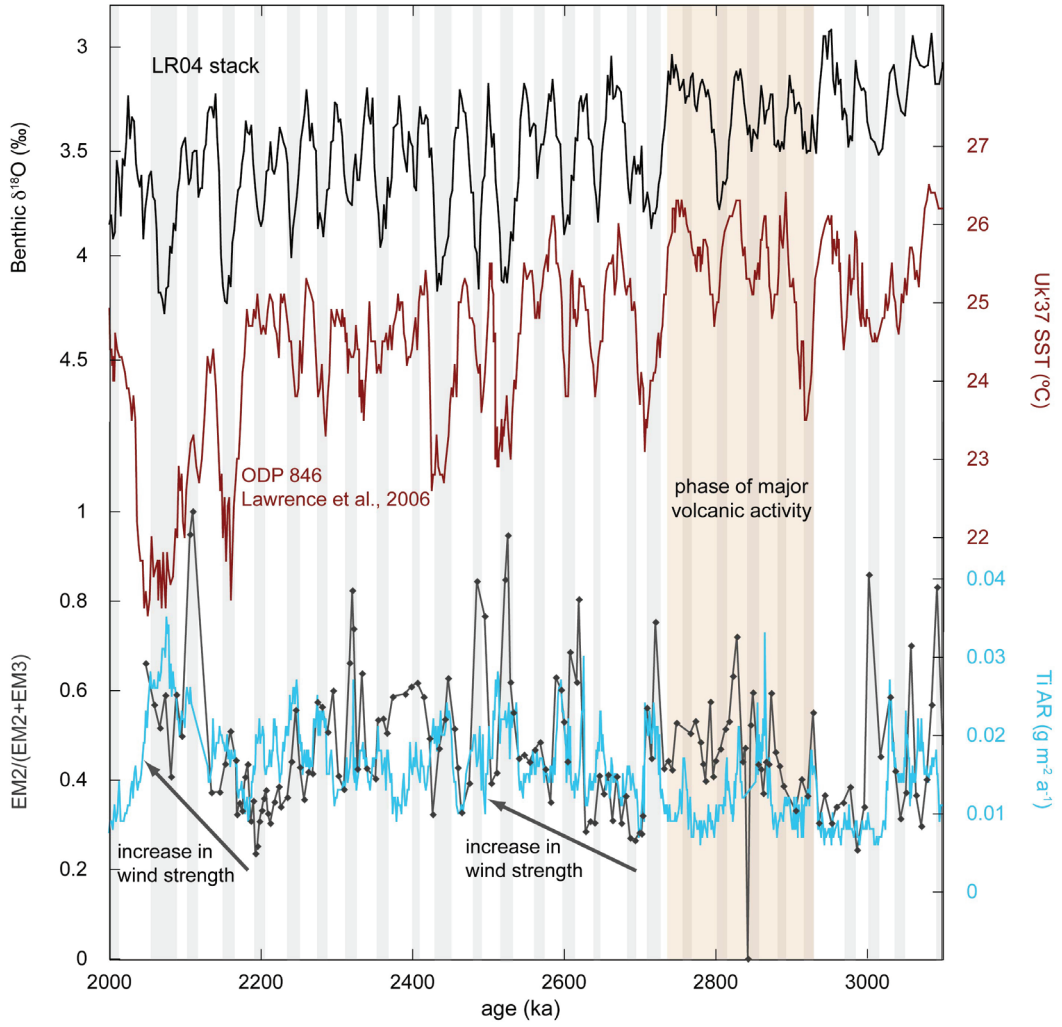

Figure 33: Variability of trade wind strength during the Plio-Pleistocene transition. δ^{18}O record of Lisiecki and Raymo (2005) (black); Alkenone-derived SSTs at ODP Site 846 from Lawrence et al. (2006) (red); Titanium accumulation rates (g $m^{-2}a^{-1}$) (cyan); ratio of EMs 2 and 3 representing changes in trade wind strength (dark grey); grey bars indicate cold periods (glacials) as indicated by the oxygen isotope stack.

during this time interval as well. Pollen indicators of trade winds in Africa for the time interval between 3.5 and 2.6 Ma, for example, show that forests occurred in Northwest Africa at irregular intervals (Leroy and Dupont, 1997). Trade winds generally increased between 3.3 and 2.5 Ma, while a strong aridification event at ∼3.2 in connection with enhanced trade winds was followed by more humid conditions (Haywood et al., 2002; Leroy and Dupont, 1997) until 2.97 Ma. However, like the Atacama, the Namib Desert persisted throughout the PRISM2 interval (Haywood et al., 2002). Unfortunately, the dust record of ODP Site 1237 is concealed by volcanic ash accumulations between 2.9 and 2.75 Ma. Nevertheless, it points to similar conditions to those prevalent in Africa.

Before the onset of major volcanic activity, all parameters indicate that the dust component remained comparably small. The high amplitudes in grain size as well as the ARs of the terrigenous elements suddenly drop at 2.99 Ma, at the end of the Mid-Pliocene warm period. Increases in Fe and Ti ARs as well as EM2 proportions and Fe/K log-ratios from 2.7 to ∼2.5 (Fig. 30, 32) indicate enhanced dust transport to ODP Site 1237. This is attributed to increasing trade wind strength induced by the development of pronounced meridional temperature gradients related to global cooling (Brierley and Fedorov, 2010; Lunt et al., 2008; Marlow et al., 2000; Tiedemann et al., 2007b), as expressed by an intensification of the NHG.

Concurrent with NHG ice sheet growth and the beginning of full glacial-interglacial conditions at ∼2.7 Ma (e.g., Haug et al., 2005; Kleiven et al., 2002; Raymo, 1994; Thiede et al., 1998), maxima in the Fe ARs, Ti ARs, and the dust end member EM2 occur during cold stages (Fig. 30A-C and 32C). The ratio of the coarse dust end member (EM2) over the two dust end members combined (EM2/(EM2+EM3)) (Fig. 33), reflecting the eolian grain size, is interpreted as an indicator of SE trade wind strength (Stuut et al., 2002). The record suggests an intensification of the trade winds between 2.7 and 2.5 Ma. The increasing strength of the SE trade winds is concurrent with findings from the East Atlantic, also suggesting increasing trade winds and aridification of Africa throughout the NHG intensification after 2.7 Ma (deMenocal, 1995; Hovan and Rea, 1991; Marlow et al., 2000; Ruddiman and Janecek, 1989; Tiedemann et al., 1994) driven by a steeper meridional (pole-equator) temperature gradient. After a decrease from ∼2.3 to 2.2 Ma, the grain-size ratio records another increase in wind strength from 2.2 Ma to the end of the record at 2.05 Ma. Etourneau et al. (2010) suggested the development of a stronger atmospheric circulation in the EEP based on an increase in the zonal and meridional temperature gradient in the Pacific during the same interval.

The wind strength is generally higher during glacials compared to interglacials, in anti-correlation with SST in the eastern Pacific cold tongue (Lawrence et al., 2006; Fig. 33). SSTs and productivity of the Pacific cold tongue change on obliquity cycles such that temperatures are lower and productivity higher during cold stages

(Lawrence et al., 2006). Coarser grain sizes in our record indicate enhanced trade-wind strength during glacials compared to interglacials, supporting the widely accepted hypothesis for the Plio-Pleistocene transition after ∼2.7 Ma: stronger SE trade winds enforce the East Pacific cold tongue through increased upwelling of cold, nutrient-rich waters offshore Peru during glacials, leading to increased nutrient availability at the surface, which allows an increase in productivity (Mudelsee and Raymo, 2005; Steph et al., 2010; Tiedemann et al., 2007b). Most prominent in all records representing dust supply and wind strengths in this study are MIS 98 and 100, in agreement with major cooling excursions in East Pacific cold tongue SSTs and in the LR04 benthic δ^{18}O-record (Fig. 32 and 33). As suspected by, e.g., Fedorov et al. (2006), SE trade winds vary with SSTs on obliquity cycles after at least 2.7 Ma. Importantly, our data clearly show an increase in trade winds at the time of NHG intensification at ∼2.7 Ma and thus disagree with findings by Rea (1994) who postulated little but stable eolian input into the South Pacific for this time interval.

5. Conclusion

(1) Three end members are recognized in the grain-size distributions of ODP Site 1237 from Nazca Ridge, using the end-member modeling algorithm of Weltje (1997). The coarsest end member nicely identifies volcanic debris. The two finer end members are interpreted as 'coarse' and 'fine' eolian dust.
(2) The ratio of the two eolian end members reflects the coarseness of dust. Its changes are therefore interpreted to mirror changes in SE trade wind intensities.
(3) Grain-size and geochemical analysis identify ash layers in the sediment. Ash layers between 2.93 and 2.75 Ma suggest major volcanic eruptions in the Andes while concealing signals of climate change.
(4) The wind strength record shows intensified trade winds during glacials compared to interglacials after ∼2.7 Ma, suggesting a causal relationship of colder surface waters, trade wind strength and productivity-favorable upwelling.
(5) The long-term behavior of SE trade wind strength during the Plio-Pleistocene transition is synchronous to trade wind changes in West Africa (deMenocal, 1995; Leroy and Dupont, 1997; Marlow et al., 2000) and the equatorial Pacific (Etourneau et al., 2010), implying that steeper pole-to-equator temperature gradients, which globally developed due to global climate cooling, caused and increased trade wind intensity.

6. Acknowledgements

We thank Ralf Rehage (Marum Bremen), Ilsetraut Stölting (AWI Bremerhaven), Ingrid Stimac (AWI Bremerhaven), Rita Fröhlking (AWI Bremerhaven), and Wolfgang Bevern (Marum Bremen) for technical support in the lab; Dr. Daniela Schmidt for last-minute corrections. The German Science Fondation (DFG) funded this

study.

Supplementary Material

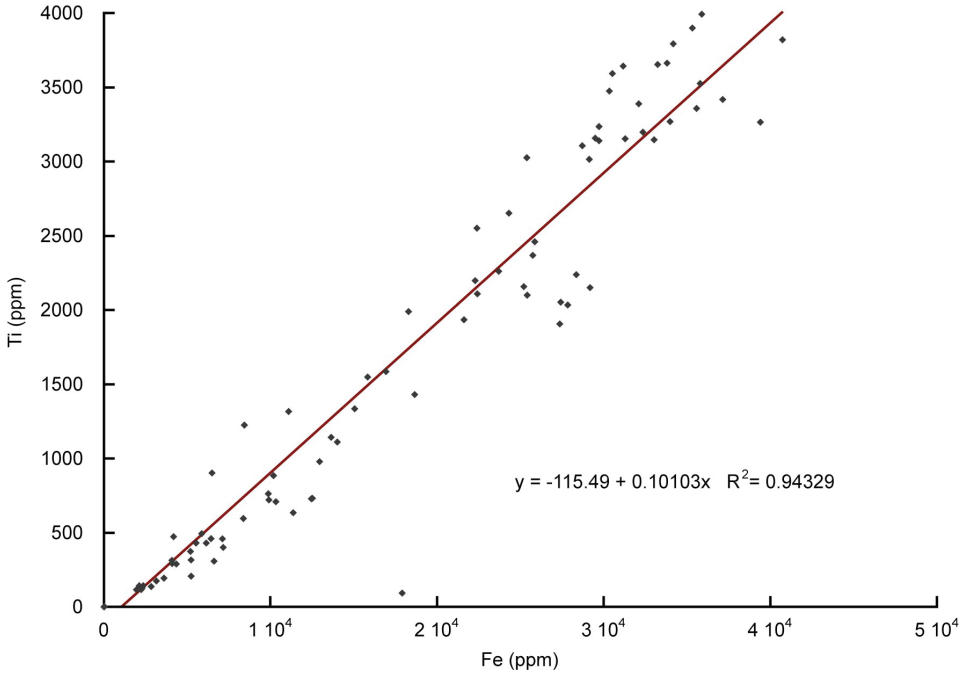

Figure 34: S1. Linear correlation of titanium and iron concentrations (ppm) from ICP-OES measurements

7. References

Brierley, C.M., Fedorov, A.V., 2010, Relative importance of meridional and zonal sea surface temperature gradients for the onset of the ice ages and Pliocene-Pleistocene climate evolution: Paleoceanography, v.25(2), doi:10.1029/2009PA001809

Cane, M.A., 1998, A Role fort he Tropical Pacific: Science, v. 282, p. 59-61, doi:10.1126/science.282.5368.59

Clemens, S.C., 1998, Dust response to seasonal atmospheric forcing; Proxy evaluation and calibration: Paleoceanography, v.13(5), p.471-490

Dekens, P.S., Ravelo, A.C., McCarthy, M.D., 2007, Warm upwelling regions in the Pliocene warm period: Paleoceanography, v.22(3), doi:10.1029/2006PA001394

Dowsett, H.J., Barron, J.A., Poore, R.Z., Thompson, R.S., Cronin, T.M., Ishman, S.E., and Willard, D.A., 1999, Middle Pliocene paleoenvironmental reconstruction: PRISM2, USGS Open File Report, v.99(535)

deMenocal, P., 1995, Plio-Pleistocene African Climate:Science, v.270, p.53-59, doi:10.1126/science.270.5233.53 Etourneau, J., Schneider, R., Blanz, T., and Martinez, P., 2010, Intensification of the Walker and Hadley atmospheric circulations during the Pliocene-Pleistocene climate transition: Earth and Planetary Sci-

ence Letters, v.297(1-2), p.103-110, doi:10.1016/j.epsl.2010.06.010

Fedorov, A.V., and Philander, S.G., 2001, A Stability Analysis of Tropical Ocean-Atmosphere Interactions: Bridging Measurements and Theory for El Niño: Journal of Climate, v. 14, p. 3086-3101

Fedorov, A.V., Dekens, P.S., McCarthy, M., Ravelo, A.C., deMenocal, P.B., Barreiro, R.C., Pacanowski, R.C., Philander, S.G., 2006, The Pliocene Paradox (Mechanisms for a Permanent El Niño: Science, v.312, p. 1485-1489, doi:10.1126/science.1122666

Goudie, A.S., and Middleton, N.J., 2006, Desert Dust in the Global System: Heidelberg, Springer, 287 p.

Groeneveld, J., Steph, S., Tiedemann, R., Garbe-Schönberg, D., Nürnberg, D., Sturm, A., 2006, Pliocene mixed-layer oceanography for site 1241, using combined Mg/Ca and d18O analysis of Globigerinoides sacculifer, in: Tiedemann, R., Mix, A.C., and Ruddiman, W.F. (eds.), Proceedings of the Ocean Drilling Program, Scientific Results Leg 202, College Station, TX

Hart, D. and Miller, D.J., 2006, Analysis and Correlation of Volcanic Ash in Marine Sediments from the Peru Margin: Explosive Volcanic Cycles of the North-Central Andes, in: Jorgensen, B.B., D'Hondt, S.L., and Miller, D.J. (eds.) Proceedings of the Ocean Drilling Program, Scientific Results Leg 201, College Station, TX

Hartley, A.J., and Chong, G., 2002, Late Pliocene age for the Atacama Desert: Implications for the desertification of western South America: Geology, v.30(1), p. 43-46

Haug, G.H., Ganopolski, A., Sigman, D.M., Rosell-Mele, A., Swann, G.E.A., Tiedemann, R., Jaccard, S.L., Bollmann, J., Maslin, M.A., Leng, M.J., Eglington, G., 2005, North Pacific seasonality and the glaciation of North America 2.7 million years ago: Nature, v.433, p. 821-825, doi:10.1038/nature03332

Haywood, A.M., Valdes, P.J., and Sellwood, B.W., 2002, Magnitude of climate variability during middle Pliocene warmth: a palaeoclimate modelling study: Palaeogeography, Palaeoclimatology, Palaeoecology, v.188(1-2), p.1-24, doi:10.1016/S0031-0182(02)00506-0

Haywood, A.M., and Valdes, P.J., 2006, Vegetation cover in a warmer world simulated using a dynamic global vegetation model for the Mid-Pliocene: Palaeogeography, Palaeoclimatology, Palaeoecology, v.237(2-4), p. 412-427, doi:10.1016/j.palaeo.2005.12.012

Holz, C., Stuut, J.-B. W., Henrich, R., 2004, Terrigenous sedimentation processes along the continental margin off NW Africa: implications from grain-size analysis of seabed sediments: Sedimentology, v. 51, p. 1145-1154, doi:10.111/j.1365-3091.2004.0065.x

Hovan, S.A., and Rea, D.K., 1991, Post-Eocene record of eolian deposition at

Sites 752, 754, and 756, in: Weissel, J., Pierce, J.,Taylor, E., Alt, J. et al., Proceedings of the Ocean Drilling Program, Scientific Results Leg 121, College Station, TX Hovan, S.A., 1995, Late Cenozoic atmospheric circiulation intensity and climatic history recorded by eolian deposition in the eastern equatorial Pacific Ocean, in: Pisias, N.G., Janecek, T.R., Palmer-Julson, A., van Andel, T.H. (eds.), Proceedings of the Ocean Drilling Program Scientific Results Leg 138, College Station, TX

http://volcanoes.usgs.gov/ash/properties.html#components, 03.01.2011

Kleiven, H.F., Jansen, E., Fronval, T. and Smith, T.M., 2002, Intensification of Northern Hemisphere glaciations in the circum Atlantic region (3.5 - 2.4 Ma) - ice-rafted detritus evidence, Palaeogeography Palaeoclimatology Palaeoecology, v.184, p. 213-223

Koopmann, B., 1981, Sedimentation von Saharastaub im subtropischen Nordatlantik wáhrend der letzten 25000 Jahre: Meteor Forschungsergebnisse, v. C35, p.23-59 Lawrence, K.T., Liu, Z., and Herbert, T.D., 2006, Evolution of the Eastern Tropical Pacific Through Plio-Pleistocene Glaciation: Science, v. 312, p. 79-83.doi:10.1126/science.1120395

Leroy, S.A.G., Dupont, L.M., 1997, Marine palynology of the ODP site 658 (N-W Africa) and its contribution to the stratigraphy of Late Pliocene: Geobios, v.30(3), p. 351-359, doi:10.1016/S0016-6995(97)80194-5

Lisiecki, L.E., and Raymo, M.E., 2005, A Pliocene-Pleistocene stack of 57 globally distributed benthic δ^{18}O records: Paleoceanography, v. 20, p. PA1003, doi:10.1029/2004PA001071

Lunt, D., Valdes, P., Haywood, A., and Rutt, I., 2008, Closure of the Panama Seaway during the Pliocene: implications for climate and Northern Hemisphere glaciation: Climate Dynamics, v. 30, p. 1.0930-7575

Marlow, J.R., Lange, C.B., Wefer, G., Rosell-Mele, A., 2000, Upwelling Intensification As Part of the Pliocene-Pleistocene Climate Transition: Science, v.290, p.2288-2291, doi:10.1126/science.290.5500.2288

Mix, A.C., Tiedemann, R., and Blum, P., 2003, Southeast Pacific Paleoceanographic Transects Sites 1232 - 1242, Initial Reports Leg 202, College Station, TX

Mix, A.C., 2006, Running hot and cold in the eastern equatorial Pacific, Quaternary Science Reviews, v.25, p.1147-1149, doi:10.1016/j.quascirev.2006.03.008

Monien, D., Kuhn, G., von Eynatten, H., Talarico, F.M., 2010, Geochemical provenance analysis of fine-grained sediment revealing Late Miocene to recent Paleo-Environmental changes in the Western Ross Sea, Antarctica: Global and Planetary Change, in press, doi:10.1016/j.gloplacha.2010.05.001

Moore, D.M., Reynolds, R.C. jr., 1997, X-Ray Diffraction and the Identification and Analysis of Clay Minerals, 2nd edition, Oxford University Press, New York

Mudelsee, M., and Raymo, M.E., 2005, Slow dynamics of the Northern Hemisphere glaciation: Paleoceanography, v.20(4), doi:10.1029/2005PA001153

Mulitza, S., Prange, M., Stuut, J.-B.W., Zabel, M., von Dobeneck, T., Itambi, A.C., Nizou, J., Schulz, M., and Wefer, G., 2008, Sahel megadroughts triggered by glacial slowdowns of Atlantic meridional overturning: Paleoceanography, v.23(4), doi:10.1029/2008PA001637

Paillard, D., 1996, Macintosh Program performs time-series analysis: Eos Trans.

Philander, S.G., Fedorov, A.V., 2003, Role of tropics in changing the response to Milankovich forcing some three million years ago: Paleoceanography, v.18(2), doi:10.1029/2002PA000837

Pierrehumbert, R.T., 2000, Climate change and the tropical Pacific: The sleeping dragon wakes: PNAS, v. 97, p. 1355-1358.

Pouclet, A., Cambray, H., Cadet, J.-P., Bourgois, J., and De Wever, P., 1990, Volcanic ash from Leg 112 off Peru, in: Suess, E., von Huene, R. et al., (eds.) Proceedings of the Ocean Drilling Program, Scientific Results Leg 112, ODP College Station, TX

Prins, M.A., and Weltje, G.J., 1999, End-member modelling of siliciclastic grain-size distributions: the Late Quaternary record of eolian and fluvial sediment supply to the Arabian Sea and its paleoclimatic significance, in Harbaugh, J.W., Watney, W.L., Rankey, E.C., Slingerland, R., Goldstein, R.H., and Franseen, E.K., eds., Numerical Experiments in Stratigraphy: Recent Advances in Stratigraphic and Sedimentologic Computer Simulations Volume 62: SEPM Special Publication London, Geological Society Publishing House.

Ravelo, A.C., 2010, Palaeoclimate: Warmth and glaciation: Nature Geosci, v. 3, p. 672.1752-089410.1038/ngeo965

Raymo, M.E., 1994, The Initiation of Northern Hemisphere Glaciation: Annual Review of Earth and Planetary Sciences, v. 22, p. 353-383

Rea, D.K., 1994, The paleoclimatic record provided by eolian deposition in the deep sea: The geologic history of wind: Rev. Geophys., v. 32, doi:10.1029/93RG03257

Richter, T.O, van der Gaast, S., Koster, B., Vaars, A., Gieles, R., De Stigter, H.C., and van Weering, T.C.E., 2006, The Avaatech XRF Core Scanner: technical description and applications to NE Atlantic sediments, in: Rothwell, R.G. (ed.) New Techniques in Sediment Core Analysis, Geological Society Special Publications, v.267, p.39-50

Rincón Martínez, D., Lamy, F., Contreras, S., Leduc, G., Bard, E., Saukel, C., Blanz, T., Mackensen, A., and Tiedemann, R., 2010, More humid interglacials in Ecuador during the past 500 kyr linked to latitudinal shifts of the equatorial front and the Intertropical Convergence Zone in the eastern tropical Pacific: Paleoceanography, v. 25, p. PA2210, doi:10.1029/2009PA001868

Ruddiman, W.F., and Janecek, T.R., 1989, Pliocene-Pleistocene biogenic and terrigenous fluxes at equatorial Atlantic Sites 662, 663, and 664, in: Ruddiman,

W.F., and Sarnthein, M., Proceedings of the Ocean Drilling Program, Scientific Results Leg 108, p.211-240, College Station, TX

Sarnthein, M., Tetzlaff, G., Koopmann, B., Wolter, K., and Pflaumann, U., 1981, Glacial and interglacial wind regimes over the eastern subtropical Atlantic and North-West Africa: Nature, v. 293, p. 193, doi:10.1038/293193a0

Saukel, C., Lamy, F., Stuut, J.-B.W., Tiedemann, R., Vogt, C., 2010, Distribution and Provenance of wind-blown SE Pacific surface sediments: Marine Geology, in press, doi:10.1016/j.margeo.2010.12.006

Shackleton, N.J., Backman, J., Zimmernmann, H., Kent, D.V., Hall, M.A., Roberts, D.G., Schnitker, D.G., Baldauf, J.G., Desprairies, A., Homrighausen, R., Huddlestun, P., Keene, J.B., Kaltenback, A.J., Krumsiek, K.A.O., Morton, A.C., Murray, J.W., Westberg-Smith, J., 1984, Oxygen isotope calibration of the onset of ice-rafting and history of glaciation in the North Atlantic region: Nature, v.307, p. 620-623, doi: 10.1038/307620a0

Sirocko, F., 1991, Deep-sea sediments of the Arabian Sea: a paleoclimatic record of the Southwest-Asian monsoon: Geologische Rundschau, v.80, p.557-566

Steph, S., Tiedemann, R., Groeneveld, J., Sturm, A., Nürnberg, D., 2006, Pliocene changes in tropical east Pacific upper ocean stratification: response to tropical gateways?, in: Tiedemann, R., Mix, A.C., and Ruddiman, W.F. (eds.), Proceedings of the Ocean Drilling Program, Scientific Results Leg 202, College Station, TX

Steph, S., Tiedemann, R., Prange, M., Groeneveld, J., Schulz, M., Timmermann, A., Nürnberg, D., Rühlemann, C., Saukel, C., and Haug, G.H., 2010, Early Pliocene increase in thermohaline overturning: A precondition for the development of the modern equatorial Pacific cold tongue: Paleoceanography, v. 25, p. PA2202.0883-8305

Strub, P.T., Mesías, J.M., Montecino, V., Rutllant, J., and Salina, S., 1998, Coastal Ocean Circulation off Western South America, in Robinson, A.R., and Brink, K.H., eds., The Sea, Volume 11, John Wiley & Sons Inc.

Stuut, J.-B.W., Kasten, S., Lamy, F., and Hebbeln, D., 2007, Sources and modes of terrigenous sediment input to the Chilean continental slope: Quaternary International, v. 161, p. 67, doi:10.1016/j.quaint.2006.10.041

Stuut, J.-B.W., Prins, M.A., Schneider, R.R., Weltje, G.J., Jansen, J.H.F., and Postma, G., 2002, A 300-kyr record of aridity and wind strength in southwestern Africa: inferences from grain-size distributions of sediments on Walvis Ridge, SE Atlantic: Marine Geology, v. 180, p. 221.0025-3227, doi:10.1016/S0025-3227(01)00215-8

Thiede, J., Winkler, A., Wolf-Welling, T., Eldholm, O., Myhre, A.M., Baumann, K.-H., Henrich, R., Stein, R., 1998, Late Cenozoic history of the polar North Atlantic: results from ocean drilling: Quaternary Science Review, v.17, p.185-208,

doi:10.1016/S0277-3791(97)00076-0

Tiedemann, R., Sarnthein, M., Shackleton, N.J., 1994, Astronomic Timescale for the Pliocene Atlantic δ^{18}O and Dust Flux Records of Ocean Drilling Program Site 659: Paleoceanography, v.9(4), p.619-638, doi:10.1029/94PS00208

Tiedemann, R., Sturm, A., Steph, S., Lund, S.P., Stoner, J.S., 2007a, Astronomically calibrated timescales from 8 to 2.5 Ma and benthic isotope stratigraphies, Site 1236, 1237, 1239, and 1241, in: Tiedemann, R., Mix, A.C., and Ruddiman, W.F. (eds.), Proceedings of the Ocean Drilling Program, Scientific Results Leg 202, College Station, TX

Tiedemann, R., Mix, A.C., 2007b, Leg 202 Synthesis: Southeast Pacific paleoceanography, in Tiedemann, R., Mix, A.C., and Ruddiman, W.F. (eds.), Proceedings of the Ocean Drilling Program, Scientific Results Leg 202, College Station, TX

Wara, M.W., Ravelo, A.C., and Delaney, M.L., 2005, Permanent El Niño-like Conditions During the Pliocene Warm Period: Science, v.309, p.758-76, doi:10.1126/science.1112596

Weltje, G., 1997, End-member modeling of compositional data: Numerical-statistical algorithms for solving the explicit mixing problem: Mathematical Geology, v. 29, p. 503, doi:10.1007/BF02775085

Weltje, G., Tjallingii, R., 2008, Calibration of XRF core scanners for quantitative geochemical logging of sediment cores: Theory and application: Earth and Planetary Science Letters, v.274, p.423-438

4.4 More humid interglacials in Ecuador during the past 500 kyr linked to latitudinal shifts of the equatorial front and the Intertropical Convergence Zone in the eastern tropical Pacific

Rincón Martínez, D., Lamy, F., Contreras, S., Leduc, G., Bard, E., Saukel, C., Blanz, T., Mackensen, A., Tiedemann, R., 2010, Paleoceanography, Vol. 25, PA2210, doi:10.1029/2009PA001868

PALEOCEANOGRAPHY, VOL. 25, PA2210, doi:10.1029/2009PA001868, 2010

Click Here for Full Article

More humid interglacials in Ecuador during the past 500 kyr linked to latitudinal shifts of the equatorial front and the Intertropical Convergence Zone in the eastern tropical Pacific

Daniel Rincón-Martínez,[1] Frank Lamy,[1] Sergio Contreras,[2] Guillaume Leduc,[3] Edouard Bard,[4] Cornelia Saukel,[1] Thomas Blanz,[3] Andreas Mackensen,[1] and Ralf Tiedemann[1]

Received 8 October 2009; revised 10 February 2010; accepted 24 March 2010; published 2 June 2010.

[1] Studying past changes in the eastern equatorial Pacific Ocean dynamics and their impact on precipitation on land gives us insight into how the Intertropical Convergence Zone (ITCZ) movements and the El Niño-Southern Oscillation modulate regional and global climate. In this study we present a multiproxy record of terrigenous input from marine sediments collected off the Ecuadorian coast spanning the last 500 kyr. In parallel we estimate sea surface temperatures (SST) derived from alkenone paleothermometry for the sediments off the Ecuadorian coast and complement them with alkenone-based SST data from the Panama Basin to the north in order to investigate SST gradients across the equatorial front. Near the equator, today's river runoff is tightly linked to SST, reaching its maximum either during the austral summer when the ITCZ migrates southward or during El Niño events. Our multiproxy reconstruction of riverine runoff indicates that interglacial periods experienced more humid conditions than the glacial periods. The north-south SST gradient is systematically steeper during glacial times, suggesting a mean background climatic state with a vigorous oceanic cold tongue, resembling modern La Niña conditions. This enhanced north-south SST gradient would also imply a glacial northward shift of the Intertropical Convergence Zone at least in vicinity of the cold tongue: a pattern that has not yet been reproduced in climate models.

Citation: Rincón-Martínez, D., F. Lamy, S. Contreras, G. Leduc, E. Bard, C. Saukel, T. Blanz, A. Mackensen, and R. Tiedemann (2010), More humid interglacials in Ecuador during the past 500 kyr linked to latitudinal shifts of the equatorial front and the Intertropical Convergence Zone in the eastern tropical Pacific, *Paleoceanography*, *25*, PA2210, doi:10.1029/2009PA001868.

1. Introduction

[2] Today the average state of the eastern equatorial Pacific (EEP) is characterized by a pronounced north-south sea surface temperature (SST) gradient, with warm and stratified waters remaining north of the equator (Eastern Pacific Warm Pool (EPWP)), while a cold tongue, associated with equatorial upwelling and advection of cold waters from the Peru Current, is located south of the equator. On interannual to decadal timescales these conditions are significantly modified through atmosphere-ocean changes related to El Niño-Southern Oscillation (ENSO) dynamics. During the warm (El Niño) phase of ENSO, warm waters spread eastward from the western Pacific warm pool, and SSTs in the cold tongue are substantially warm. Conversely, during the cold (La Niña) phase, the cold tongue strengthens, and the cross-equatorial SST gradient in the EEP is substantially larger [*McPhaden et al.*, 2006; *Wang and Fiedler*, 2006].

[3] Long-term ENSO changes on millennial, orbital, or even tectonic timescales throughout the Plio-Pleistocene and their role for global climate have been intensively discussed [*Markgraf and Diaz*, 2000; *Cane*, 2004; *Fedorov et al.*, 2006]. On glacial-interglacial timescales, some authors suggest that the average glacial state of the EEP was more similar to that occurring during modern El Niño years [*Koutavas et al.*, 2002; *Koutavas and Lynch-Stieglitz*, 2003], while others consider a mean glacial state similar to the cold La Niña phase [*Andreasen and Ravelo*, 1997; *Andreasen et al.*, 2001; *Martínez et al.*, 2003]. Low-latitude orbital forcing has been suggested to exert control on the mean state of ENSO as well [*Clement et al.*, 1999; *Pena et al.*, 2008]. Other authors again link SST changes in the EEP to high-latitude climate variability in the Southern Hemisphere without invoking ENSO changes [*Pisias and Mix*, 1997; *Lea et al.*, 2000; *Feldberg and Mix*, 2003; *Spero et al.*, 2003; *Lea et al.*, 2006].

[4] Hence, the scenarios drawn from these studies are diverse. Most studies focus on paleoceanographic features such as SST, paleoproductivity, or water stratification, whereas continental climate changes are rarely considered [e.g., *Pahnke et al.*, 2007]. Yet, modern atmosphere-ocean reorganizations

[1]Alfred Wegener Institute for Polar and Marine Research, Bremerhaven, Germany.
[2]Max Planck Institute for Marine Microbiology, Bremen, Germany.
[3]Institut für Geowissenschaften, Christian Albrecht Universität, Kiel, Germany.
[4]CEREGE, Aix-Marseille Université, CNRS, Collège de France, IRD, Europôle Méditerranéen de L'Arbois, Aix-en-Provence, France.

Copyright 2010 by the American Geophysical Union.
0883-8305/10/2009PA001868

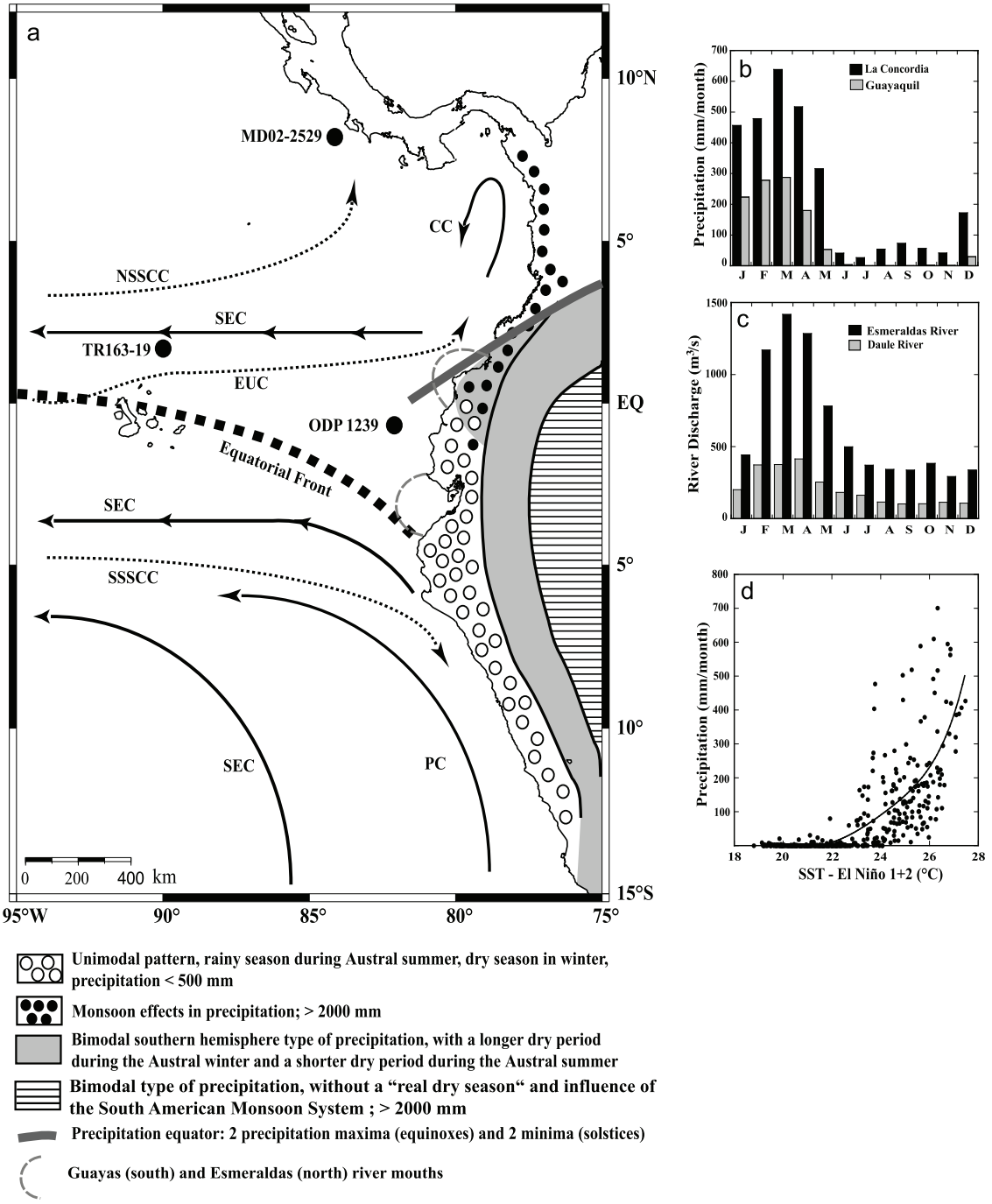
a
10°N
5°
EQ
5°
10°
15°S
95°W
90°
85°
80°
75°
MD02-2529
CC
NSSCC
SEC
TR163-19
EUC
ODP 1239
Equatorial Front
SEC
SSSCC
SEC
PC
0 200 400 km
b
La Concordia
Guayaquil
Precipitation (mm/month)
J F M A M J J A S O N D
c
Esmeraldas River
Daule River
River Discharge (m3/s)
J F M A M J J A S O N D
d
Precipitation (mm/month)
SST - El Niño 1+2 (°C)
Unimodal pattern, rainy season during Austral summer, dry season in winter, precipitation < 500 mm
Monsoon effects in precipitation; > 2000 mm
Bimodal southern hemisphere type of precipitation, with a longer dry period during the Austral winter and a shorter dry period during the Austral summer
Bimodal type of precipitation, without a "real dry season" and influence of the South American Monsoon System ; > 2000 mm
Precipitation equator: 2 precipitation maxima (equinoxes) and 2 minima (solstices)
Guayas (south) and Esmeraldas (north) river mouths

Figure 1

related to ENSO strongly impact onshore precipitation, particularly in northern Peru and coastal Ecuador. During El Niño phases, unusually warm EEP waters promote convection of the overlying atmosphere, while the Intertropical Convergence Zone (ITCZ) and associated precipitation anomalies shift farther south than during the regular seasonal cycle [*Horel and Cornejo-Garrido*, 1986; *Bendix*, 2000; *Bendix and Bendix*, 2006].

[5] Here, we present a combined analysis of proxy data that allude to paleoceanographic changes in the EEP and concomitant continental paleoclimate variations onshore during the past 500 kyr. The proxy profiles are derived from samples obtained from sediment cores off the coast of Ecuador and in the Panama Basin. A systematic pattern of changes in the terrigenous sediment input during glacial-interglacial periods can be linked to tropical rainfall changes over coastal Ecuador. These glacial-interglacial rainfall changes are paralleled by latitudinal shifts of the equatorial front (EF) moving southward during interglacials as is indicated by higher SST, enhanced surface water stratification, higher abundances of the foraminifera species *Globorotalia cultrata* relative to *Neogloboquadrina dutertrei*, and increases in mangrove biomarker accumulation rates. A comparison of our SST record with the EPWP SST record from Site MD02-2529 covering the past ~300 kyr indicates that fluctuations in the latitudinal SST gradients during glacial-interglacial periods across the EF in the EEP played a pivotal role in past precipitation changes in the region.

2. Modern Climatology and Oceanography at Studied Sites

[6] Our study is based on two sites in the EEP (Figure 1), the first of which is Ocean Drilling Program (ODP) Site 1239 (0°40.32′S, 82°4.86′W, 1414 m water depth) located at the northern margin of the eastern Pacific cold tongue close to the EF and ~120 km off the Ecuadorian coast. The area is characterized by a thermocline shoaling and local wind-driven upwelling that supplies nutrient-rich waters from the Equatorial Undercurrent (EUC) to the surface, creating highstanding stocks of phytoplankton and enhanced primary productivity rates [*Lukas*, 1986; *Fiedler et al.*, 1991; *Pennington et al.*, 2006]. The second site, MD02-2529 (08° 12.33′N, 84°07.32′W, 1619 m water depth), is situated close to the Costa Rica margin of the Panama Basin within the EPWP, where SSTs are above 27°C and sea surface salinities are below 33.2 practical salinity unit (psu) throughout the year [*Leduc et al.*, 2007].

2.1. EEP Oceanography

[7] A striking feature of the west coast of South America is the presence of unusually cool and highly saline ($T < 25$°C, $S > 34$ psu) surface waters extending westward slightly south of the equator. This cold tongue is fed by seasonal advection of cold waters from the Peru Current (PC) and by equatorial upwelling [*Pak and Zaneveld*, 1974; *Fiedler and Talley*, 2006]. The cold tongue is bounded by the EF, a narrow band located around the equator between the Peruvian coast and the Galapagos Islands (Figure 1). North of the EF, warm, low-salinity waters ($T < 25$°C, $S > 34$ psu) of the Panama Basin occur because of a large net heat flux, weak wind mixing, and intense rainfall beneath the ITCZ [*Pak and Zaneveld*, 1974; *Fiedler and Talley*, 2006].

[8] The cold tongue and associated frontal zone are persistent features, but their strength varies both seasonally and interannually. During austral winter, solar heating reinforces the meridional SST gradient, strengthening the southeasterly trade winds and the equatorial cold tongue and shifting the EF to its northernmost position. From January to April, SST increases south of the equator because of the subsidence of the southeast trades, resulting in a diffused southern position of the EF [*Pak and Zaneveld*, 1974; *Raymond et al.*, 2004; *de Szoeke et al.*, 2007]. The quasiperiodic El Niño-Southern Oscillation (ENSO) dominates the interannual variability in this region. The El Niño warm phase is related to anomalous eastward advection of warm water in the eastern Pacific cold tongue, associated with a weaker EF [*Pak and Zaneveld*, 1974; *Kessler*, 2006; *McPhaden et al.*, 2006; *Wang and Fiedler*, 2006]. At this time, variations in the water transports of the South Equatorial Current (SEC) and EUC induce a deepening of the thermocline, causing positive SST anomalies [*Kessler*, 2006]. The opposite conditions occur during the cool La Niña phase.

2.2. EEP Atmospheric Circulation

[9] The EEP atmospheric convection and its associated continental precipitation are mostly linked to the ITCZ and occur preferentially over the EPWP waters. This pattern is maintained most of the year by several positive feedbacks. First, the temperature asymmetry along the equator reinforces

Figure 1. (a) Schematic (sub)surface circulation in the eastern equatorial Pacific (modified after *Kessler* [2006]). Locations of ODP Site 1239, Site TR163-19, Site MD02-2529, and the Guayas and Esmeraldas river mouths and precipitation patterns over northern South America (modified after *Bendix and Lauer* [1992]). Upper layer currents (black arrows) are the SEC, South Equatorial Current; CC, Colombia Current; and PC, Peru or Humboldt Current. Subsurface currents (dashed arrows) are NSSCC, Northern Subsurface Countercurrent; SSSCC, Southern Subsurface Countercurrent; and EUC, Equatorial Undercurrent. (b) Mean monthly precipitation at Guayaquil (2.20°S, 79.90°W, 6 m above sea level (asl); Guayas Basin) and La Concordia (0.1°N, 79.30°W, 300 m asl; Esmeraldas Basin) metereological stations. (c) Mean monthly fluvial discharge of the Daule River (1.69°S, 79.99°W, 20 m asl; at La Capilla hydrological station), one of the main tributaries of the Guayas River, and the Esmeraldas River (0.52°N, 79.41°W, 50 m asl; at Esmeraldas hydrological station). (d) Polynomial fit between monthly SST at El Niño 1 + 2 region (0°S–10°S, 90°W–80°W) and monthly precipitation at Guayaquil meteorological station. SST data are generated from the World Ocean Atlas database [*Conkright et al.*, 2002]; precipitation [*Peterson and Russell*, 1997] and river discharges are from R-HydroNET (available at http://www.r-hydronet.sr.unh.edu/).

surface winds over the cold tongue, which further cools the water through evaporation and upwelling [*Xie and Philander*, 1994; *Xie*, 2004]. Second, the combination of cold surface waters with warm, dry air aloft results in large and persistent subtropical stratocumulus decks, which reflect much of the incoming solar radiation and help to maintain the cool SST of the "cold tongue" [*Klein and Hartmann*, 1993; *Raymond et al.*, 2004]. In addition, the northwest-southeast orientation of the coastline of South America combined with the topographic barrier of the Andes constrains winds to blow along the Peruvian coastline and induces coastal upwelling there [*Philander et al.*, 1996; *Xie*, 2004].

[10] During late austral summer, the north-south SST contrast is relaxed, the EF is weakest, and the ITCZ and associated precipitation migrate southward along the Colombian and Ecuadorian coasts [*Horel and Cornejo-Garrido*, 1986; *Bendix and Lauer*, 1992; *Hastenrath*, 2002; *Amador et al.*, 2006; *Poveda et al.*, 2006]. Conversely, a northward displacement of the ITCZ occurs during late austral winter, when the cold tongue is intensified and the advection of the Peru-Chile current is strongest [*Hastenrath*, 2002; *Amador et al.*, 2006; *Poveda et al.*, 2006; *de Szoeke et al.*, 2007].

[11] During an El Niño event the trade winds weaken along the equator, as atmospheric pressure rises in the western Pacific and falls in the eastern Pacific, and permit an eastward expansion of warm waters from the central Pacific [*McPhaden et al.*, 2006; *Wang and Fiedler*, 2006]. This phenomenon acts to weaken the Humboldt Current and the equatorial and coastal upwelling systems. Atmospheric convection cells and the associated precipitation of the ITCZ shift to the south, causing heavy rainfall over the northern Peruvian desert and coastal Ecuador [*Horel and Cornejo-Garrido*, 1986; *Neill and Jørgensen*, 1999; *Hastenrath*, 2002; *Waylen and Poveda*, 2002; *Poveda et al.*, 2006].

2.3. Guayas and Esmeraldas Drainage Systems, Precipitation, and Fluvial Runoff

[12] The Guayas and the Esmeraldas basins are the largest drainage systems in western Ecuador, both in terms of area (32,674 km^2 and 21,418 km^2, respectively) and water volume drained per area unit. Annual precipitation and river discharges in both basins, including the Coastal Mountain Range and the western slopes of the Andes at altitudes <1800 m above sea level, experience a unimodal pattern that is characterized by a rainy season from December to April. Precipitation and river runoff maxima occur in March and broadly coincide with the southernmost seasonal excursion of the ITCZ in the EEP and with the seasonal SST maximum at ODP Site 1239 (Figures 1b–1d). The rest of the year, precipitation is limited by the combined effects of low SST, atmospheric subsidence of dry air, and reduced insolation due to persistent low-level stratus decks [*Horel and Cornejo-Garrido*, 1986; *Bendix and Lauer*, 1992].

[13] Heavy precipitation and severe floods also affect the coastal area of Ecuador during El Niño events, with rainfall differences between normal years and El Niño events as large as 200% for Guayaquil (Guayas Basin). Extensive precipitation during El Niño years occurs during the normal rainy season when the Hadley circulation is increased, and the ITCZ is displaced southward because of the strong warming of the Niño 1 + 2 region (0°S–10°S, 90°W–80°W (Figure 1d)) [*Rossel et al.*, 1996; *Bendix and Bendix*, 2006].

3. Methods

3.1. Stratigraphic Framework (ODP Site 1239 and Site MD02-2529)

[14] Sampling of Site 1239 followed the meters composite depth scale that was developed for the multiple offset cores [*Shipboard Scientific Party*, 2003]. The age model of the uppermost ~17.4 m, representing the past ~500 kyr, is based on oxygen isotope stratigraphy. We correlated the $\delta^{18}O$ record of the benthic foraminifera *Cibicidoides wuellerstorfi* to the chronology of the LR04 stack [*Lisiecki and Raymo*, 2005] using the AnalySeries software [*Paillard et al.*, 1996] (Figure 2). Sedimentation rates range from ~2 to ~5 cm kyr^{-1}, with higher values occurring during interglacials (Figure 2). Stratigraphy at Site MD02-2529 over the past three climatic cycles is based on the benthic $\delta^{18}O$ record performed on *C. wuellerstorfi* and on a previously published chronostratigraphy for the last 90 kyr [*Leduc et al.*, 2007].

3.2. Paleoceanographic Proxies

3.2.1. Foraminifera Oxygen Isotopes

[15] We measured the stable oxygen isotope composition of the epibenthic foraminifer *Cibicidoides wuellerstorfi*, as well as of two planktonic foraminiferal species, the surface dweller *Globigerinoides ruber*, and the deep-dwelling *Globorotalia tumida*. Approximately 4 individuals of *C. wullerstorfi* and 10 individuals of each planktonic species were selected from the 315–355 μm and 355–400 μm fractions, respectively. Measurements of $\delta^{18}O$ were performed on a Finnigan 253 MS with a Kiel CARBO device at the Alfred-Wegener-Institut (AWI) (Bremerhaven, Germany) with an analytical reproducibility of ~0.08‰ for $\delta^{18}O$. The oxygen isotope composition values were calibrated using the NBS-19 standard and are reported relative to the International Atomic Energy Agency Vienna Pee Dee Belemnite standard. The resolution of sampling was defined on the basis of a preliminary age model from biostratigraphy in order to obtain intervals of 1000 years or less for benthic foraminifera and of 3000 years for planktonic foraminifera. The $\delta^{18}O$ difference between *G. ruber* ss and *G. tumida* is used as a proxy for water column thermal stratification (D. Rincón-Martínez et al., Tracking the equatorial front in the eastern equatorial Pacific Ocean by the isotopic and faunal composition of planktonic foraminifera, submitted to *Marine Micropaleontology*, 2010).

3.2.2. Alkenones

[16] Alkenones are a series of long-chain (C_{37}, C_{38}, and C_{39}) unsaturated methyl and ethyl ketones synthesized mainly by *Emiliania huxleyi* and some other species of the class Prymnesiophyceae that live in the uppermost meters of the euphotic zone. To obtain the total lipid extract, freeze-dried sediments (~1 g) from ODP Site 1239 were solvent extracted with 25 mL dichloromethane at 75°C at a pressure of 80 bars on an accelerated solvent extractor (Dionex ASE 200) at the Christian Albrecht University of Kiel. An internal standard (cholestane [$C_{27}H_{48}$] and hexatriacontane [$C_{36}H_{74}$]) was added and used to quantify organic compounds. Aliquots (1%–5%) of the total lipid fractions were separated using a

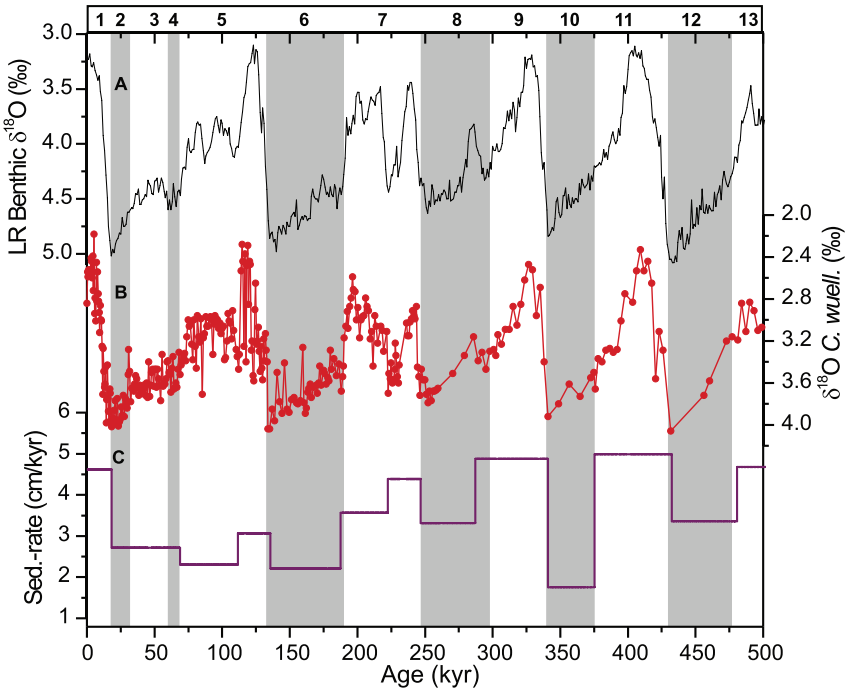

Figure 2. Oxygen isotope stratigraphy for the ODP Site 1239. (a) Benthic oxygen isotope stack [*Lisiecki and Raymo*, 2005]. (b) The $\delta^{18}O$ (‰) record of the benthic foraminifera *Cibicidoides wuellerstorfi* from ODP Site 1239. (c) Linear sedimentation rates (cm kyr^{-1}) of the uppermost ~17.4 m (past ~500 kyr) from ODP Site 1239. Shading highlights glacial marine isotopic stages.

double-column multidimensional gas chromatograph with two Agilent 6890 gas chromatographs for $C_{37:2}$ and $C_{37:3}$ alkenone identification and quantification. The procedure used at Centre Européen de Recherche et d'Enseignement des Géosciences de l'Environnement (Aix-Marseille Université) to extract and quantify $C_{37:2}$ and $C_{37:3}$ alkenones from MD02-2529 is fully described by *Sonzogni et al.* [1997] and *Pailler and Bard* [2002]. Alkenone-derived temperatures from MD02-2529 for the last 90 kyr have been previously published and discussed by *Leduc et al.* [2007]. The alkenone unsaturation index ($U^{K'}_{37}$) was calculated with the peak areas of the diunsaturated and triunsaturated C_{37} methyl alkenones using the ratio $(C_{37:2})/(C_{37:2} + C_{37:3})$. To reconstruct the SST, we used the alkenone unsaturation and the global calibration derived by *Müller et al.* [1998]:

$$U^{K'}_{37} = \langle 0.033 \times \mathrm{SST} \rangle + 0.044.$$

3.2.3. Foraminiferal Assemblage ($R_{c/d}$)

[17] The abundance ratio between *Globorotalia menardii cultrata* and *Neogloboquadrina dutertrei* (right coiling) has been used as an index for the influence of the Panama-Costa Rica Dome and the cold tongue upwelling systems and therefore is of value for locating the EF in the EEP [i.e., *Martinez and Bedoya*, 2001; *Martínez et al.*, 2006; Rincón-Martínez et al., submitted manuscript, 2010]. In this study we counted >300 specimens from the 355–400 μm size fraction, and the ratios were calculated according to Rincón-Martínez et al. (submitted manuscript, 2010):

$$R_{c/d} = \text{number of specimens of } \textit{G. cultrata} \,/(\text{number of specimens of } \textit{G. cultrata} + \textit{N. dutertrei})$$

3.3. Terrigenous Sediment Input

3.3.1. Siliciclastic Content

[18] The lithogenic record for ODP 1239 represents the residual sediment percentage obtained after subtraction of carbonate, opal, and organic matter:

$$\text{siliciclastic (wt \%)} = 100 - \%CaCO_3 - \%\text{biogenic opal} - \%\text{TOC}.$$

The determination of total organic carbon (TOC) was performed with the LECO technique (LECO Carbon-Sulfur Analyzer CS-125), and previous dissolution of the calcium carbonates was performed by adding 1 *M* solution of HCL to the dry sediment. Total carbon (TC) and total nitrogen (TN) were measured on the same TOC samples using a CNS elemental analyzer (Elementar Vario EL III). The carbonate content (wt %) was determined by the difference between TC and TOC:

$$CaCO_3(\text{wt \%}) = (\%\text{TC} - \%\text{TOC}) \times 8.33.$$

The concentration of biogenic silica (wt %) was quantified by using the automated leaching method according to *Müller and Schneider* [1993]. Biogenic opal was extracted from dry bulk sediment by using sodium hydroxide at ~85°C for ~45 min. The leaching solution was continuously analyzed for dissolved silicon by molybdenum-blue spectrophotometry. *DeMaster*'s [1981] mineral correction was consequently applied.

3.3.2. X-Ray Fluorescence Scanning and Inductively Coupled Plasma-Optical Emission Spectrometry Elemental Concentrations

[19] Elemental concentrations (unit is total elemental counts) were measured using an Avaatech^{TM} X-Ray Flourescence (XRF) Core Scanner (AWI, Bremerhaven) and a nondestructive measuring technique that allows rapid semi-quantitative geochemical analysis of split sediment cores [*Richter et al.*, 2006]. Sampling intervals ranged from 1 to 5 cm, resulting in a time resolution of 200 and 400 years for the upper ~350 kyr of the XRF records and 1000 to 1500 years for the oldest part. Iron (Fe) and titanium (Ti) XRF counts were calibrated to absolute elemental concentration by using Inductively Coupled Plasma-Optical Emission Spectrometry. Previous to analysis, all samples were freeze-dried, and 34 discrete sediment samples were digested using HF (23 *M*), HNO_3 (15 *M*), and HCl (12 *M*). Measurements were carried out in a TJA-IRIS-Intrepid spectrometer at the geochemistry laboratories of AWI, and the results were used to convert XRF counts to element concentrations in mg g^{-1} of sediment by means of linear regressions ($r^2 = 0.83$, $n = 32$ for Fe and $r^2 = 0.63$, $n = 33$ for Ti).

3.3.3. Taraxerol

[20] Taraxerol has been reported to dominate the free and bound lipid composition inside *Rhizophora mangle* leaves and has been used to track past changes in mangrove ecosystems [*Versteegh et al.*, 2004; *Grosjean et al.*, 2007]. Total lipid extracts (see section 3.2.2) were methylated with diazomethane and silylated with N, O-bis (trimethylsilyl) trifluoroacetamide in pyridine and then analyzed by GC-MS (Trace GC-MS, Thermo Finnigan) at the Max-Planck-Institute for Marine Microbiology in Bremen. The relative abundance of taraxerol was estimated by peak integration in the mass chromatograms using a characteristic *m/z* value of 204 [*Killops and Frewin*, 1994; *Versteegh et al.*, 2004].

3.3.4. Mass Accumulation Rates

[21] Linear sedimentation rates (LSR; cm kyr^{-1}) and mass accumulation rates (AR) are derived from the calculated ages of individual samples along with the high-resolution-corrected bulk density (HROM; g cm^{-3}) based on borehole logging at Site 1239 [*Shipboard Scientific Party*, 2003]:

$$AR_{component} = \text{concentration component} \times \text{LSR} \times \text{HROM},$$

where AR is in ng cm^{-2} kyr^{-1} for the taraxerol, mg cm^{-2} kyr^{-1} for the iron and titanium, and g cm^{-2} kyr^{-1} for the bulk siliciclastic fraction.

4. Results and Discussion

4.1. Terrigenous Sediment Supply to the ODP Site 1239

[22] Terrigenous sedimentation supply at Site 1239 (Figure 3) is reconstructed from three independent proxy data sets: (1) AR of siliciclastic material, (2) high-resolution XRF core scanning (Fe, Ti), and (3) lipid biomarker taraxerol, indicative of the supply of plant debris from mangroves at the Ecuadorian coast.

[23] The terrigenous records at Site 1239 exhibit a consistent glacial-interglacial pattern over the past 500 kyr (Figures 3 and 4f). Sediments are predominantly terrigenous during interglacials, with siliciclastic contents generally above 50% and reaching maximum values of up to 80% during marine isotope stage (MIS) 7 (Figure 3b). Glacial siliciclastic contents are substantially lower, within the range of 20% to 40% with lowest values during MIS 2 and MIS 12. As siliciclastic contents may be substantially affected by productivity changes and carbonate dissolution, we calculated siliciclastic AR (Figure 3c) as a more reliable proxy for terrigenous supply changes. In line with higher sedimentation rates during interglacials (Figure 2c), the siliciclastic AR record reveals pronounced interglacial maxima with values 3 to 5 times higher than that found during glacials. Highest AR are found in MIS 7 and MIS 11, whereas MIS 5 values are relatively low, and minimum AR occur in MIS 10. Similar results are recorded in Fe and Ti AR records (Figures 3d–3g). The strong similarity between the Fe and Ti records suggests that diagenetic alteration potentially affecting Fe has not been a critical factor at Site 1239. Moreover, when log ratios of Fe and Ti over calcium (Ca) are computed to account for dilution by carbonates and nonlinearities between XRF counts and elemental concentrations [*Weltje and Tjallingii*, 2008], the first-order sign of changes in terrigenous supply on glacial-interglacial timescales remains unchanged (data not shown). Low AR of terrigenous components during MIS 5 indicate variable glacial-interglacial amplitudes in terrigenous supply to Site 1239. However, total siliciclastic, Fe, and Ti contents during MIS 5 are similar to other interglacials (Figures 3b, 3d, and 3f), and the low siliciclastic AR during MIS 5 are solely the result of low sedimentation rates.

[24] Glacial-interglacial siliciclastic AR variations at Site 1239 are unlikely due to postdepositional processes such as horizontal focusing or winnowing. According to *Lyle et al.* [2005], sediment focusing preferentially increases from elevated regions to the deeper parts of the basins, and in the Panama and Peru basins, the bulk sediment burial matches surface water patterns. Moreover, the observed glacial-interglacial pattern in local sediment supply to ODP Site 1239 demonstrates that continental rainfall rather than glacioeustatic sea level variations was the main factor controlling the basinward terrestrial transport off Ecuador. For example, during glacial times when the global sea level was at lowstand, one would expect an oceanward migration of fluvial depocenters and widespread fluvial incision of the subaerially exposed continental shelf producing increased siliciclastic AR at ODP Site 1239. In contrast, our records show higher concentrations and AR of terrigenous material during interglacials that overcompensated any potential sea level influence on fluvial sediment supply.

[25] High terrigenous AR during interglacial periods also contradict the concept that in the equatorial Pacific, transport of terrigenous material was increased during glacial periods [*Anderson et al.*, 2006; *McGee et al.*, 2007; *Winckler*

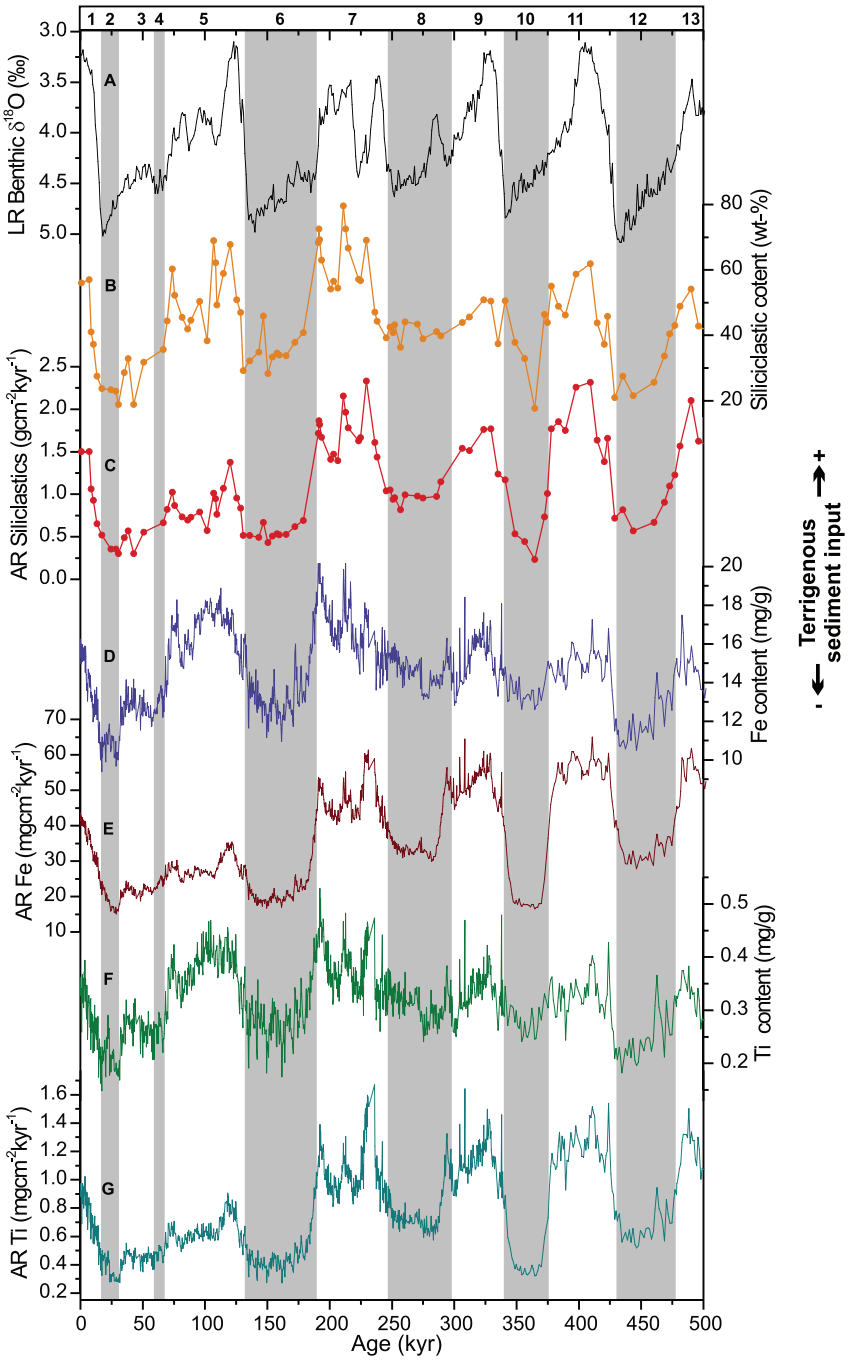

Figure 3. Records of changes in terrigenous sediment input to ODP Site 1239 over the last 500 kyr. (a) Benthic oxygen isotope stack [*Lisiecki and Raymo*, 2005] for stratigraphic reference. (b) Content (wt %) and (c) accumulation rates (AR, g cm^{-2} kyr^{-1}) of siliciclastics. (d) Iron contents (mg g^{-1}). (e) Iron AR (mg cm^{-2} kyr^{-1}). (f) Titanium contents (mg g^{-1}). (g) Titanium AR (mg cm^{-2} kyr^{-1}).

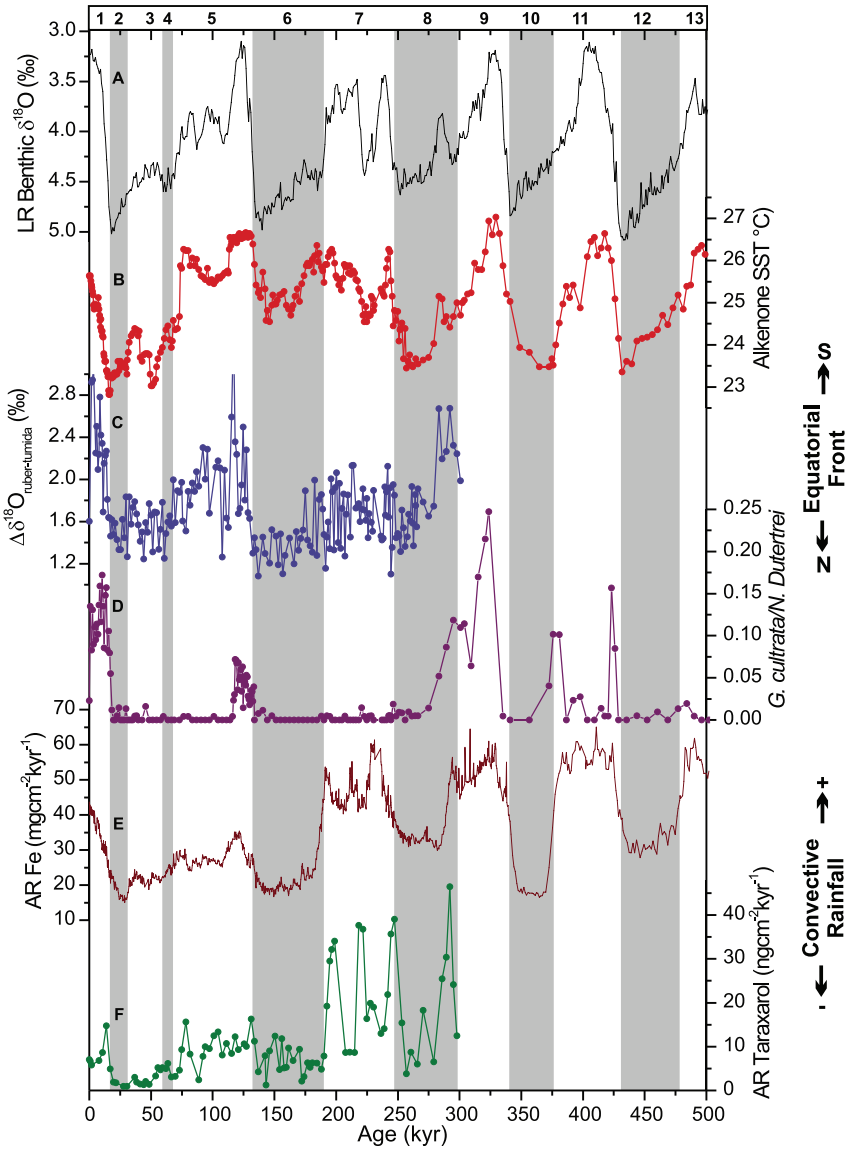

Figure 4. EEP paleoceanographic changes as reconstructed at ODP Site 1239. (a) Benthic oxygen isotope stack [*Lisiecki and Raymo*, 2005] for stratigraphic reference. (b) Alkenone sea surface temperature (SST) record. (c) $\Delta\delta^{18}O$ between *Globorotalia tumida* and *Globigerinoides ruber*. High values are indicative of strongly stratified waters north of the equatorial front. (d) Abundance ratio ($R_{c/d}$) between planktonic foraminifera *Globorotalia cultrata* and *Neogloboquadrina dutertrei*. High values are indicative of warm waters north of the equatorial front. (e) Iron AR (mg cm^{-2} kyr^{-1}). (f) Taraxerol AR (ng cm^{-2} kyr^{-1}). High values are interpreted as enhanced fluvial runoff as a result of increased continental rainfall.

et al., 2008]. We attribute the contrasting results to the fact that far from shore, the terrigenous component of deep-sea sediments consists of eolian dust and that these fluxes were generally greater during glacial periods than during interglacials [*Mahowald et al.*, 1999; *Kohfeld and Harrison*, 2001]. Hence, the rather nearshore location of Site 1239 suggests that fluvial input from the Guayas and/or Esmeraldas drainage systems was increased during interglacial periods relative to glacial periods.

[26] Our third proxy for terrigenous input is taraxerol AR, which was used as a proxy for sedimentation of mangrove leaf remains (*Rhizophora*) that were washed offshore by

riverine runoff [*Versteegh et al.*, 2004; *Grosjean et al.*, 2007]. The *Rhizophora* genus is the dominant mangrove along the Colombian and Ecuadorian coasts. and its distribution is associated with the presence of warm waters and humid coastal conditions north of the EF [*Heusser and Shackleton*, 1994; *Neill*, 1999]. Compared to glacials, taraxerol AR are higher during the Holocene and MIS 5 and reach extremely high values during MIS 7 (Figure 4f). These higher interglacial AR are consistent with our interpretation of predominantly fluvial terrigenous input induced by enhanced tropical rainfall. However, the supply of mangrove material may also be affected by sea level changes. For instance, in the nearby Angola Bight, *Kim et al.* [2005] showed that high taraxerol contents during terminations I and II were controlled by global sea level rise resulting in strong shelf erosion supplying preexisting deposits of mangrove material. Additional support for deglacial sea level control on EEP mangrove input into marine sediments comes from pollen analyses [*Heusser and Shackleton*, 1994; *González et al.*, 2006] and Mn/Ca of planktonic foraminifera [*Klinkhammer et al.*, 2009], which display maxima in mangrove pollen and dissolved terrestrial input to coastal surface waters during the last deglaciation. Our record shows early maxima in taraxerol AR during terminations I, II, and particularly III (Figure 4f) while taraxerol levels remain high during the whole interglacial period. Hence, we suggest that increased taraxerol sedimentary fluxes during interglacials are driven to some extent by increased riverine runoff.

4.2. SST, EF Latitudinal Position, and Their Relationship to Continental Precipitation

[27] Global compilations of SST estimations from modern sediments indicate that alkenones unsaturation, $U^{K'}_{37}$, is almost linearly related to annual mean SST from 0 to 10 m water depth [*Müller et al.*, 1998; *Conte et al.*, 2006; *Prahl et al.*, 2006]. $U^{K'}_{37}$ sensitivity to temperature has been assessed in laboratory cultures [*Prahl and Wakeham*., 1987], and second-order mechanisms such as salinity and alkenones synthesized by thermocline-dwelling coccolithophorids or diagenetic alterations are known to play a minor role on the alkenone-SST signal (see review by *Conte et al.* [2006]). It is unclear, however, why alkenones that are produced during an often discrete and short period of the annual cycle are representative of annual mean SST [*Prahl et al.*, 2000].

[28] Alkenone-derived SST at Site 1239 reveals pronounced glacial-interglacial cycles, with temperatures ranging from ~22.8 during MIS 2 to ~27°C during MIS 9 (Figure 4b). We find SST amplitudes of up to 3.5°C for the oldest glacial-interglacial cycles (MIS 8–13), ~2.5°C for the MIS 8–7 transition, only ~2°C for termination II (MIS 6–5), and again higher amplitudes of ~3°C for termination I (MIS 2–1). The magnitude of the deglacial SST increase during termination I is consistent with previous studies conducted in the eastern tropical Pacific that used Mg/Ca ratios and faunal assemblages [*Lea et al.*, 2000; *Pena et al.*, 2008; *MARGO Project Members*, 2009]. Glacial-interglacial SST amplitudes in other $U^{K'}_{37}$ estimations from the region are, however, somewhat lower (~1°C to ~2°C) [*Horikawa et al.*, 2006; *Pahnke et al.*, 2007; *Koutavas and Sachs*, 2008; *Dubois et al.*, 2009]. Sea surface temperature values at Site MD02-2529 range from minima of ~25°C during MIS 2 and 8 to maxima of ~28°C during the Holocene (Figure 5b). Glacial-interglacial SST amplitudes are generally smaller than at Site 1239, on the order of 2°C for terminations I (MIS 2−1) and III (MIS 8−7) and less than 1°C for termination II (MIS 6−5).

[29] Comparison of the global benthic $\delta^{18}O$ record (LR04 stack) with the Site 1239 SST estimates reveals several interesting features: (1) an early warming is recorded prior to terminations I, III, and IV; (2) SSTs during MIS 6 are warmer than those recorded during the other glacial periods; (3) an abrupt cooling occurs during early MIS 3 and is followed by a warming of the same magnitude at the end of MIS 3; and (4) SST estimates recorded during the Holocene reveal ~1°C lower SST when compared to other interglacial periods (Figure 4b). The early warming during the glacial terminations is also observed in other tropical records (see review by *Schneider et al.* [1999]) and has been suggested to be linked with low-latitude insolation forcing. Elevated glacial SSTs during MIS 6 are also found at Site MD02-2529 (Figure 5b) in the eastern Pacific cold tongue [*Calvo et al.*, 2001] and in many other Indian and Atlantic equatorial records (see review by *Schneider et al.* [1999]). In contrast, EEP $\delta^{18}O$ and Mg/Ca records of planktonic foraminifera suggest a colder MIS 6 in comparison with alkenone-based SSTs with a cooling of similar magnitude to those found on the preceding and following glacial periods [e.g., *Lea et al.*, 2000; *Pena et al.*, 2008].

[30] Given the importance of tropical SST patterns in determining present-day Ecuadorian rainfall formation and associated fluvial discharges [i.e., *Rossel et al.*, 1996; *Bendix and Bendix*, 2006] (Figures 1b–1d), past SST changes offshore Ecuador likely impacted the terrigenous material fluxes at ODP Site 1239. On the basis of this modern SST-rainfall correlation (Figure 1d), the range of glacial-interglacial SSTs plausibly resulted in substantial precipitation changes in coastal Ecuador (e.g., more than doubling of rainfall for the glacial-interglacial increase from 23.5°C to 26.5°C). Thus, we infer that higher accumulation of lithogenic sediments at Site 1239 generally reflects higher fluvial input and a wetter Ecuadorian coast, most likely coupled to warmer SSTs in combination with southward shifts of the EF-ITCZ system as observed today during austral summer or during El Niño years. Lower lithogenic accumulations during glacial periods indicate decreased fluvial input and arid conditions on the continent.

[31] Further support for EF-ITCZ southward excursions during interglacials comes from the $\delta^{18}O$ gradient between planktonic foraminifera living at different depths (hereafter referred to as $\Delta\delta^{18}O$) (Figure 4c) and the $R_{c/d}$ index (Figure 4d). Planktonic foraminifera $\Delta\delta^{18}O$ is indicative of water column stratification in the EEP (Rincón-Martínez et al., submitted manuscript, 2010). High interglacial $\Delta\delta^{18}O_{G.\ ruber-G.\ tumida}$ values (Figure 4c) indicate stratified waters north of the EF, where a strong thermal gradient occurs in the upper 100 m. Low glacial $\Delta\delta^{18}O_{G.\ ruber-G.\ tumida}$ values reflect intensified upwelling linked to a stronger Peru Current and a northward location of the EF-ITCZ complex. With the exception of MIS 7, glacial-interglacial patterns are also evident in the $R_{c/d}$ record (Figure 4d),

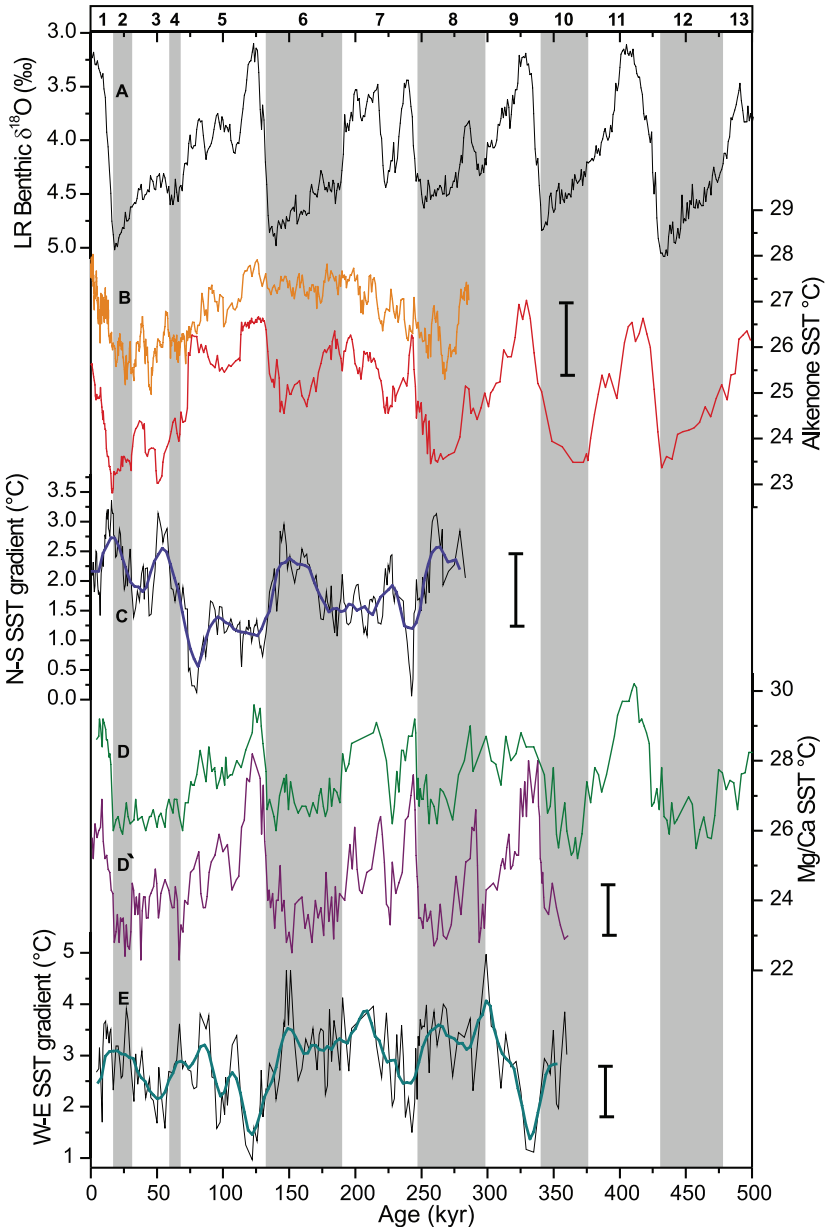

Figure 5. Comparison of eastern and western equatorial Pacific SST records. (a) Benthic oxygen isotope stack [*Lisiecki and Raymo*, 2005] for stratigraphic reference. (b) Alkenone-derived SST records from the two eastern equatorial Pacific sites. MD02-2529 (top line, this study) data represent the eastern Pacific warm pool; ODP Site 1239 data (bottom line, this study) represent the northernmost reach of the cold tongue. (c) SST gradient between the northern Site MD02-2529 (08°12.33′N) and the southern Site 1239 (0°40.32′S). Increased SST difference between the equator and the eastern Pacific warm pool represents La Niña-like mean conditions. (d) Mg/Ca SST record from ODP Site 806B (0°19.1′N, 159°21.7′E; top line) in the western Pacific warm pool [*Medina-Elizalde and Lea*, 2005] and Site TR163-19 (2°15′S, 90°57′W; bottom line) from north of the EEP cold tongue [*Lea et al.*, 2000]. (e) SST gradient between the eastern and western tropical Pacific sites. Reduced west-east SST gradients represent El Niño-like mean conditions.

which exhibits higher values during interglacials, indicating southward shifts of the EF-ITCZ. Low and minimum $R_{c/d}$ values recorded during MIS 5 and 7, respectively, are attributed to potential changes on ecologic factors such as food web or nutrient supply that might also exert control on the abundance of *G. cultrata* [i.e., *Martinez and Bedoya*, 2001; *Martínez et al.*, 2006; Rincón-Martínez et al., submitted manuscript, 2010].

[32] Glacial-interglacial relation of enhanced fluvial input patterns and thus tropical precipitation of coastal Ecuador to warmer offshore SSTs appears to be a robust feature. But low siliciclastic AR during MIS 5 (Figures 4b and 4e) and low $\Delta\delta^{18}O_{G.\ ruber-G.\ tumida}$ and $R_{c/d}$ values during MIS 7 beg the question of whether there is a consistent signature of rainfall response to the SST forcing. The specific mechanism behind the disproportion in the magnitude of lithogenic supply among interglacials is unknown. Differences in atmospheric CO_2 concentrations, astronomical forcing, and glacial ice volume [see *Tzedakis et al.*, 2009] plausibly fostered variations in moisture advection to the ITCZ and to the continent, stimulating variations in precipitation, vegetation cover, and fluvial suspended loads that are reflected in the variable magnitude between the different interglacials of terrestrial input to the EEP.

4.3. Changes of Equatorial Pacific Mean States During the Last 300,000 Years

[33] Tropical Pacific SST patterns translate into transequatorial and cross-equatorial equatorial pressure gradients that control the position and intensities of atmospheric convection over the Pacific Ocean. We apply this concept and investigate past changes in zonal and meridional SST gradients (Figures 5c and 5e) as indication of changes in the large-scale tropical atmospheric circulation, notably, the Walker and Hadley cells. The zonal SST gradient was estimated using published *Globigerinoides ruber* Mg/Ca measured at ODP Site 806B from the Ontong Java Plateau (0°19.1′N, 159°21.7′E, 2520 m water depth) [*Medina-Elizalde and Lea*, 2005] and at Site TR163-19 (2°15′S, 90°57′W, 2348 m water depth) just north of the EEP cold tongue [*Lea et al.*, 2000]. The meridional gradient was calculated using alkenone-derived SST from ODP Site 1239 and Site MD02-2529 (this study). Here we use the terms "El Niño-like" and "La Niña-like" to describe mean changes in the zonal and meridional SST gradients across the equatorial Pacific, either in the form of decreased (El Niño) or increased (La Niña) gradients without specifically implying changes in frequency or amplitude of ENSO variability.

[34] Previous studies comparing SST derived from alkenones and Mg/Ca in the EEP have reported contrasting results. For example, on millennial-scale alkenones and Mg/Ca SST, changes that have punctuated the last deglaciation are known to be out of phase [i.e., *Mix*, 2006; *Koutavas and Sachs*, 2008]. Other studies based on compilations of Holocene SST data have revealed divergent SST trends over the last 10 kyr, with warming versus cooling recorded by alkenone- versus Mg/Ca-based SST, respectively [i.e., *Leduc et al.*, 2010; *Sachs*, 2008; *Sachs et al.*, 2000]. These dissimilarities suggest that coccolithophorids and foraminifera do not record the same paleoceanographic features. For this reason we avoided using different proxies when we compiled the zonal and meridional SST gradients across the equatorial Pacific, and we assumed that these gradients best represent past changes in the equatorial SST mean state. Reported error bars in alkenone and Mg/Ca temperature estimates are ±1.5°C and ±0.6°C, respectively [*Müller et al.*, 1998; *Lea et al.*, 2000].

[35] The zonal SST gradient shows a distinct glacial-interglacial pattern, with minima during the interglacials and maxima during glacials (Figure 5e). For instance, during MIS 5e, MIS 7e, and MIS 9e the west-east SST gradient was ~1.5°C, while for MIS 2 and MIS 8 it was ~3°C and ~3.5°C, respectively. This suggests a weakened Walker circulation (El Niño-like conditions) during interglacials and intensified Walker circulation (La Niña-like conditions) during glacial periods. Such a scenario is consistent with reduced upwelling activity or intensity, an anomalous warming in the easternmost Pacific, an EF-ITCZ southward migration, and heavy rainfall on the Guayas and Esmeraldas basins during interglacials (Figure 3) [i.e., *Horel and Cornejo-Garrido*, 1986; *Hastenrath*, 2002; *Rossel et al.*, 1996; *Bendix and Bendix*, 2006].

[36] Systematic glacial-interglacial patterns are also recorded in the meridional SST gradient record (Figures 5b and 5c). Low meridional SST gradients occur during MIS 5 (0.8°C to1.4°C) and MIS 7 (1.4°C to 1.8°C) while MIS 2, 4, 6, and 8 were characterized by a steeper SST gradient (2.2°C to 2.6°C). Today, the annual mean position of the eastern Pacific ITCZ is located in the vicinity of 10°N and remains north of the equator because of a strong cross-equatorial SST gradient. During El Niño years, mainly during the months of March and April, the meridional gradient is weakened, leading to extensive precipitation over coastal Ecuador linked to an equatorward shift of the meridional position of the ITCZ. Taken together, the co-occurrence of weaker meridional and zonal SST gradients suggests an El Niño-like state during interglacial periods contrasting with La Niña-like conditions recorded during glacial periods. This result is consistent with reconstructions of the ENSO, suggesting reduced ENSO activity during the Last Glacial Maximum (LGM) [*Leduc et al.*, 2009]. Sea surface temperature reconstructions from the southeastern Pacific margin suggest that remote advection of cold waters from high latitudes is a valid mechanism for explaining the observed glacial La Niña-like state [*Kaiser et al.*, 2005].

[37] The zonal SST gradient is particularly well expressed during peak interglacials (i.e., MIS 5e, MIS 7e, and MIS 9e), while it does not show much change between late interglacials and glacials. In contrast, the meridional SST gradient clearly mimics glacial-interglacial patterns. One explanation for the disparate pattern of zonal and meridional SST gradients is that the zonal SST gradient was estimated from *G. ruber* Mg/Ca measurements, while the meridional SST gradient was calculated from alkenone ratios. The signal offset between both SST gradients might reflect contrasting sensitivities to different seasonal/interannual variations or depth distribution of proxy carriers [i.e., *Mix*, 2006; *Leduc et al.*, 2010], rather than disentanglement of the Hadley and Walker circulations. Alternatively, possible long-term

modifications of the tropical Pacific mean state, such as migration of the main centers of deep convection, could explain the divergent patterns of SST gradients, plausibly in conjunction with nonconventional El Niño, namely, the El Niño-modoki or pseudo-El Niño [i.e., *Yeh et al.*, 2009]. During such anomalous conditions, the maximum SST anomaly persists in the central Pacific, sandwiched between anomalous cooling in the east and west, modifying the atmospheric circulation and resulting in distinctly different global impacts than conventional El Niño conditions.

4.4. Comparison to Previous Paleoceanographic and Paleoclimatic Studies From the EEP and Adjacent South American Continent

[38] Our findings contradict the common view that during glacial times, the location of tropical rainfall zones experienced a southward displacement globally. Modeling studies simulate a southward displacement of the marine ITCZ in response to changes in continental ice volume at high latitudes [*Yin and Battisti*, 2001; *Chiang et al.*, 2003; *Chiang and Bitz*, 2005; *Broccoli et al.*, 2006]. However, today's climatology and variability of the eastern tropical Pacific SST have proven difficult to reproduce, even with current state-of-the-art coupled ocean-atmosphere general circulation models [*Mechoso et al.*, 1995; *Wang et al.*, 2005; *Wittenberg et al.*, 2006]. For instance, in simulations of the seasonal cycle, the modeled ITCZ tends to move across the equator following the seasonal movement of the Sun rather than remaining in the Northern Hemisphere as is suggested by monthly monitoring (i.e., http://trmm.gsfc.nasa.gov/). Moreover, in the current models, the ITCZ persists too long at a southern position compared to observations, causing a double ITCZ in the annual mean. Therefore, numerical models appear to overestimate the control of Northern Hemisphere ice sheets on the ITCZ and do not adequately implement low latitude air-sea interactions.

[39] Our results also challenge previous suggestions that a glacial relaxation of the SST asymmetry across the equator and a southward displacement of the marine ITCZ in the eastern Pacific were likely reflecting an El Niño-like pattern [*Koutavas et al.*, 2002; *Koutavas and Lynch-Stieglitz*, 2003]. Alternatively, the LGM reduction in the meridional $\delta^{18}O$ gradient reconstructed by *Koutavas and Lynch-Stieglitz* [2003] can be interpreted in terms of a northward migration of the EF-ITCZ system because their records are located primarily on the seasonal path of the EF-ITCZ system. Thus, a glacial northward shift of the EF would cause weaker meridional $\delta^{18}O$ gradients because of minimum changes in SST and salinity within the cold tongue. Other eastern Pacific alkenone-SST reconstructions [i.e., *Calvo et al.*, 2001; *Liu and Herbert*, 2004; *Horikawa et al.*, 2006; *Pahnke et al.*, 2007; *Koutavas and Sachs*, 2008; *Dubois et al.*, 2009], together with previous SST estimates based on marine microfossils [i.e., *Pisias and Mix*, 1997; *Feldberg and Mix*, 2003; *Martínez et al.*, 2003], support this view by demonstrating that sites located south of the EF experienced stronger cooling during the LGM and stronger warming during the last deglaciation compared to sites located north of the EF.

[40] Paleoclimate records from South America indicate southward ITCZ displacements during Northern Hemisphere ice sheet expansions (i.e., Amazon Basin [*Wang et al.*, 2004; *Jacob et al.*, 2007], Bolivian Altiplano [*Baker et al.*, 2001], Venezuela [*Rull*, 1996], ice cores [*Thompson et al.*, 1998; *Bradley et al.*, 2003], and glaciers [*Heine*, 2000]). This is in opposition to what is indicated by our marine data. The divergent behavior of the ITCZ in the continent plausibly relates to differences in heat flux patterns over the relatively dry continent as compared to the ocean where meridional temperature gradients were more prominent. This results in latitudinal ITCZ migrations over the continent that are much larger over the Amazon Basin and the Altiplano, while at the same time the ITCZ position over the EEP is defined by the geometry of the cold tongue-EF complex and the subtropical gyre circulation [i.e., *Horel et al.*, 1989; *Poveda et al.*, 2006; *Garreaud et al.*, 2009].

5. Summary and Conclusions

[41] We find prominent glacial-interglacial changes of fluvial sediment input that reflects more humid conditions along the Ecuadorian coast during interglacials. A warmer interglacial EEP cold tongue and a southward shift of the EF-ITCZ system likely control these humid interglacial conditions. Conversely, reduced fluvial input during glacials suggests more arid conditions coinciding with larger tropical Pacific SST gradients and a more northward location of the EF-ITCZ system. Despite this general tight coupling of rainfall changes in Ecuador to offshore oceanographic conditions, there are distinct differences between the individual interglacials, plausibly reflecting offsets in precipitation as well as duration and variability of interglacial climates of the past 500,000 years. Numerical modeling is required to test the sensitivity of past interglacial conditions and, notably, the distribution and intensity of tropical rainfall to variable atmospheric CO_2 concentrations, glacial ice volume, and orbital forcing.

[42] Zonal SST gradients in the eastern Pacific are reduced throughout interglacials and enhanced during glacials. With regards to long-term changes in the mean climate state, our data suggest a predominance of El Niño-like conditions off Ecuador during interglacials, while glacial conditions seem to more closely mimic La Niña-like conditions.

[43] Contrary to climate models our data indicate a northern EF-ITCZ position during glacials in the EEP. This was plausibly favored by the facts that (1) the cross-equatorial SST asymmetry was enhanced with stronger cooling south of the EF, which would drive the southeasterly trade winds across the equator, displacing the ITCZ to a northerly position [i.e., *Calvo et al.*, 2001; *Liu and Herbert*, 2004; *Horikawa et al.*, 2006; *Dekens et al.*, 2007; *Pahnke et al.*, 2007; *Koutavas and Sachs*, 2008; *Dubois et al.*, 2009; this study]; (2) the southeast-to-northwest tilted coastal geometry has not changed during the last 500 kyr, promoting coastal upwelling predominantly active south of the equator; and (3) the influence of the Andes and the South Pacific subtropical anticyclone on the regional atmospheric circulation remained reasonably stable during the entire time span, keeping the ocean surface cool through evaporation and suppressing deep convection in the Southern Hemisphere [e.g., *Takahashi and Battisti*, 2007].

[44] The glacial-interglacial latitudinal shifts of the EF-ITCZ system suggested by our data may be restricted to the EEP and the coastal area of northwest South America. Glacial cooling is particularly pronounced in the southeast Pacific [e.g., *Kaiser et al.*, 2005], which suggests a possibility that ITCZ migration in the region may be controlled by the northward advection of cold waters with the Humboldt Current system. Conversely, in the central and western Pacific, the magnitude of the cross-equatorial pressure gradient diminishes because the broad western Pacific warm pool dominates the SST pattern, leading to a potentially wider latitudinal range for ITCZ migrations during glacial times. Over the South American continent, away from the coast, the Andes and Amazon Basin impact atmospheric circulation patterns, allowing larger southward migrations of the ITCZ during glacial periods.

[45] **Acknowledgments.** At AWI, Reza Ahi assisted with TOC, opal, and CNS analyses and Lisa Schönborn provided invaluable assistance with oxygen isotopic measurement. Funding was provided through the German Science Foundation (grants Ha 2756/9-1 and TI240/17-2). D.R.M. and S.C. acknowledge Marcel Kuypers for his interest and support of this project and Gail Lee Arnold for her editorial comments. The authors further thank Frauke Rostek (CEREGE), who generated a considerable amount of alkenones data for Site MD02-2529, and Silvia Koch for her assistance at the biomarker laboratory at the CAU-IfG. This research used samples provided by the Integrated Ocean Drilling Program/Ocean Drilling Program (IODP/ODP) and the IMAGES program. Editorial comments by Rainer Zahn and critical reviews by George Philander and two anonymous reviewers substantially improved this manuscript.

References

Amador, J. A., E. J. Alfaro, O. G. Lizano, and V. O. Magaña (2006), Atmospheric forcing of the eastern tropical Pacific, *Prog. Oceanogr.*, *69*, 101–142, doi:10.1016/j.pocean.2006.03.007.

Anderson, R. F., M. Q. Fleisher, and Y. Lao (2006), Glacial-interglacial variability in the delivery of dust to the central equatorial Pacific Ocean, *Earth Planet. Sci. Lett.*, *242*, 406–414, doi:10.1016/j.epsl.2005.11.061.

Andreasen, D. J., and A. C. Ravelo (1997), Tropical Pacific Ocean thermocline depth reconstructions for the Last Glacial Maximum, *Paleoceanography*, *12*, 395–413, doi:10.1029/97PA00822.

Andreasen, D. J., A. C. Ravelo, and A. J. Broccoli (2001), Remote forcing at the Last Glacial Maximum in the tropical Pacific Ocean, *J. Geophys. Res.*, *106*, 879–897, doi:10.1029/1999JC000087.

Baker, P. A., G. O. Seltzer, S. C. Fritz, R. B. Dunbar, M. J. Grove, P. M. Tapia, S. L. Cross, H. D. Rowe, and J. P. Broda (2001), The history of South American tropical precipitation for the past 25,000 years, *Science*, *291*, 640–643, doi:10.1126/science.291.5504.640.

Bendix, J. (2000), Precipitation dynamics in Ecuador and northern Peru during the 1991/92 El Niño: A remote sensing perspective, *Int. J. Remote Sens.*, *21*, 533–548, doi:10.1080/014311600210731.

Bendix, A., and J. Bendix (2006), Heavy rainfall episodes in Ecuador during El Niño events and associated regional atmospheric circulation and SST patterns, *Adv. Geosci.*, *6*, 43–49.

Bendix, J., and W. Lauer (1992), Die Niederschlagsjahreszeiten in Ecuador und ihre Klimatdynamische interpretation, *Erdkunde*, *46*, 118–134, doi:10.3112/erdkunde.1992.02.04.

Bradley, R. S., M. Vuille, D. Hardy, and L. G. Thompson (2003), Low latitude ice cores record Pacific sea surface temperatures, *Geophys. Res. Lett.*, *30*(4), 1174, doi:10.1029/2002GL016546.

Broccoli, A. J., K. A. Dahl, and R. J. Stouffer (2006), Response of the ITCZ to Northern Hemisphere cooling, *Geophys. Res. Lett.*, *33*, L01702, doi:10.1029/2005GL024546.

Calvo, E., C. Pelejero, J. C. Herguera, A. Palanques, and J. O. Grimalt (2001), Insolation dependence of the southeastern subtropical Pacific sea surface temperature over the last 400 kyr, *Geophys. Res. Lett.*, *28*, 2481–2484, doi:10.1029/2000GL012024.

Cane, M. A. (2004), The evolution of El Niño, past and future, *Earth Planet. Sci. Lett.*, *230*, 227–240, doi:10.1016/j.epsl.2004.12.003.

Chiang, J. C. H., and C. M. Bitz (2005), Influence of high latitude ice cover on the marine Intertropical Convergence Zone, *Clim. Dyn.*, *25*, 477–496, doi:10.1007/s00382-005-0040-5.

Chiang, J. C. H., M. Biasutti, and D. S. Battisti (2003), Sensitivity of the Atlantic Intertropical Convergence Zone to Last Glacial Maximum boundary conditions, *Paleoceanography*, *18*(4), 1094, doi:10.1029/2003PA000916.

Clement, A. C., R. Seager, and M. A. Cane (1999), Orbital controls on the El Niño-Southern Oscillation and the tropical climate, *Paleoceanography*, *14*, 441–456, doi:10.1029/1999PA900013.

Conkright, M. E., R. A. Locarnini, H. E. Garcia, T. D. O'Brien, T. P. Boyer, C. Stephens, and J. I. Antonov (2002), World Ocean Atlas 2001: Objective analyses, data statistics, and figures, CD-ROM documentation, *Internal Rep. 17*, Natl. Oceanogr. Data Cent., NOAA, Silver Spring, Md.

Conte, M. H., M.-A. Sicre, C. Rühlemann, J. C. Weber, S. Schulte, D. Schulz-Bull, and T. Blanz (2006), Global temperature calibration of the alkenone unsaturation index (U) in surface waters and comparison with surface sediments, *Geochem. Geophys. Geosyst.*, *7*, Q02005, doi:10.1029/2005GC001054.

Dekens, P. S., A. C. Ravelo, and M. D. McCarthy (2007), Warm upwelling regions in the Pliocene warm period, *Paleoceanography*, *22*, PA3211, doi:10.1029/2006PA001394.

DeMaster, D. J. (1981), Measuring biogenic silica in marine sediments and suspended matter, in *Marine Particles: Analysis and Characterization*, *Geophys. Monogr. Ser.*, vol. 63, edited by D. C. Hurd and D. W. Spenser, pp. 363–368, AGU, Washington, D. C.

de Szoeke, S. P., S.-P. Xie, T. Piyama, K. J. Richards, and R. J. O. Small (2007), What maintains the SST front north of the eastern Pacific equatorial cold tongue?, *J. Clim.*, *20*, 2500–2514, doi:10.1175/JCLI4173.1.

Dubois, N., M. Kienast, C. Normandeau, and T. D. Herbert (2009), Eastern equatorial Pacific cold tongue during the Last Glacial Maximum as seen from alkenone paleothermometry, *Paleoceanography*, *24*, PA4207, doi:10.1029/2009PA001781.

Fedorov, A. V., P. S. Dekens, M. McCarthy, A. C. Ravelo, P. B. deMenocal, M. Barreiro, R. C. Pacanowski, and S. G. Philander (2006), The Pliocene Paradox (mechanisms for a permanent El Niño), *Science*, *312*, 1485–1489, doi:10.1126/science.1122666.

Feldberg, M. J., and A. C. Mix (2003), Planktonic foraminifera, sea surface temperatures, and mechanisms of oceanic change in the Peru and south equatorial currents, 0–150 ka BP, *Paleoceanography*, *18*(1), 1016, doi:10.1029/2001PA000740.

Fiedler, P. C., and L. D. Talley (2006), Hydrography of the eastern tropical Pacific: A review, *Prog. Oceanogr.*, *69*, 143–180, doi:10.1016/j.pocean.2006.03.008.

Fiedler, P. C., V. Philbrick, and F. P. Chavez (1991), Oceanic upwelling and productivity in the eastern tropical Pacific, *Limnol. Oceanogr.*, *36*(8), 1834–1850, doi:10.4319/lo.1991.36.8.1834.

Garreaud, R. D., M. Vuille, R. Compagnucci, and J. Marengo (2009), Present-day South American climate, *Palaeogeogr. Palaeoclimatol. Palaeoecol.*, *281*, 180–195, doi:10.1016/j.palaeo.2007.10.032.

González, C., L. E. Urrego, and J. I. Martínez (2006), Late Quaternary vegetation and climate change in the Panama Basin: Palynological evidence from marine cores ODP 677B and TR 163–38, *Palaeogeogr. Palaeoclimatol. Palaeoecol.*, *234*, 62–80, doi:10.1016/j.palaeo.2005.10.019.

Grosjean, E., G. A. Logan, N. Rollet, G. J. Ryan, and K. Glenn (2007), Geochemistry of shallow tropical marine sediments from the Arafura Sea, Australia, *Org. Geochem.*, *38*, 1953–1971, doi:10.1016/j.orggeochem.2007.06.017.

Hastenrath, S. (2002), The Intertropical Convergence Zone of the eastern Pacific revisited, *Int. J. Climatol.*, *22*, 347–356, doi:10.1002/joc.739.

Heine, K. (2000), Tropical South America during the Last Glacial Maximum: Evidence from glacial, periglacial and fluvial records, *Quat. Int.*, *72*, 7–21, doi:10.1016/S1040-6182(00)00017-3.

Heusser, L. E., and N. J. Shackleton (1994), Tropical climatic variation on the Pacific slopes of the Ecuadorian Andes based on a 25,000 year pollen record from deep-sea sediment core Tri163-31B, *Quat. Res.*, *42*, 222–225, doi:10.1006/qres.1994.1072.

Horel, J. D., and A. G. Cornejo-Garrido (1986), Convection along the coast of northern Peru during 1983: Spatial and temporal variations of clouds and rainfall, *Mon. Weather Rev.*, *114*, 2091–2105, doi:10.1175/1520-0493(1986)114<2091:CATCON>2.0.CO;2.

Horel, J. D., A. N. Hahmann, and J. E. Geisler (1989), An investigation of the annual cycle of convective activity over the tropical Americas, *J. Clim.*, *2*, 1388–1403, doi:10.1175/1520-0442(1989)002<1388:AIOTAC>2.0.CO;2.

Horikawa, K., M. Minagawa, M. Murayama, Y. Kato, and H. Asahi (2006), Spatial and temporal sea-surface temperatures in the eastern equatorial Pacific over the past 150 kyr, *Geophys. Res. Lett.*, *33*, L13605, doi:10.1029/2006GL025948.

Jacob, J., Y. Huang, J.-R. Disnar, A. Sifeddine, M. Boussafir, A. L. Spadano, and B. Turcq (2007), Paleohydrological changes during the last deglaciation in northern Brazil, *Quat. Sci. Rev.*, *26*, 1004–1015, doi:10.1016/j.quascirev.2006.12.004.

Kaiser, J., F. Lamy, and D. Hebbeln (2005), A 70-kyr sea surface temperature record off southern Chile (Ocean Drilling Program Site 1233), *Paleoceanography*, *20*, PA4009, doi:10.1029/2005PA001146.

Kessler, W. S. (2006), The circulation of the eastern tropical Pacific: A review, *Prog. Oceanogr.*, *69*, 181–217, doi:10.1016/j.pocean.2006.03.009.

Killops, S. D., and N. L. Frewin (1994), Triterpenoid diagenesis and cuticular preservation, *Org. Geochem.*, *21*, 1193–1209, doi:10.1016/0146-6380(94)90163-5.

Kim, J.-H., L. Dupont, H. Behling, and G. J. M. Verteegh (2005), Impacts of rapid sea-level rise on mangrove deposit erosion: Application of taraxerol and *Rhizophora* records, *J. Quat. Sci.*, *20*, 221–225, doi:10.1002/jqs.904.

Klein, S. A., and D. L. Hartmann (1993), The seasonal cycle of low stratiform clouds, *J. Clim.*, *6*, 1587–1606, doi:10.1175/1520-0442(1993)006<1587:TSCOLS>2.0.CO;2.

Klinkhammer, G. P., A. C. Mix, and B. A. Haley (2009), Increased dissolved terrestrial input to the coastal ocean during the last deglaciation, *Geochem. Geophys. Geosyst.*, *10*, Q03009, doi:10.1029/2008GC002219.

Kohfeld, K. E., and S. P. Harrison (2001), DIRTMAP: The geological record of dust, *Earth Sci. Rev.*, *54*, 81–114, doi:10.1016/S0012-8252(01)00042-3.

Koutavas, A., and J. Lynch-Stieglitz (2003), Glacial-interglacial dynamics of the eastern equatorial Pacific cold tongue-Intertropical Convergence Zone system reconstructed from oxygen isotope records, *Paleoceanography*, *18*(4), 1089, doi:10.1029/2003PA000894.

Koutavas, A., and J. P. Sachs (2008), Northern timing of deglaciation in the eastern equatorial Pacific from alkenone paleothermometry, *Paleoceanography*, *23*, PA4205, doi:10.1029/2008PA001593.

Koutavas, A., J. Lynch-Stieglitz, T. M. Marchitto, and J. Sachs (2002), El Niño-like pattern in Ice Age tropical Pacific sea surface temperature, *Science*, *297*, 226–230, doi:10.1126/science.1072376.

Lea, D. W., D. K. Pak, and H. J. Spero (2000), Climate impact of late Quaternary equatorial Pacific sea surface temperature variations, *Science*, *289*, 1719–1724, doi:10.1126/science.289.5485.1719.

Lea, D. W., D. K. Pak, C. L. Belanger, H. J. Spero, M. A. Hall, and N. J. Shackleton (2006), Paleoclimate history of Galápagos surface waters over the last 135,000 yr, *Quat. Sci. Rev.*, *25*, 1152–1167, doi:10.1016/j.quascirev.2005.11.010.

Leduc, G., L. Vidal, K. Tachikawa, F. Rostek, C. Sonzogni, L. Beaufort, and E. Bard (2007), Moisture transport across Central America as a positive feedback on abrupt climatic changes, *Nature*, *445*, 908–911, doi:10.1038/nature05578.

Leduc, G., L. Vidal, O. Cartapanis, and E. Bard (2009), Modes of eastern equatorial Pacific thermocline variability: Implications for ENSO dynamics over the last glacial period, *Paleoceanography*, *24*, PA3202, doi:10.1029/2008PA001701.

Leduc, G., R. Schneider, J.-H. Kim, and G. Lohmann (2010), Holocene and Eemian sea surface temperature trends as revealed by alkenone and Mg/Ca paleothermometry, *Quat. Sci. Rev.*, *29*, 989–1004, doi:10.1016/j.quascirev.2010.01.004.

Lisiecki, L. E., and M. E. Raymo (2005), A Pliocene-Pleistocene stack of 57 globally distributed benthic $\delta^{18}O$ records, *Paleoceanography*, *20*, PA1003, doi:10.1029/2004PA001071.

Liu, Z., and T. D. Herbert (2004), High-latitude influence on the eastern equatorial Pacific climate in the early Pleistocene epoch, *Nature*, *427*, 720–723, doi:10.1038/nature02338.

Lukas, R. (1986), The termination of the Equatorial Undercurrent in the eastern Pacific, *Prog. Oceanogr.*, *16*, 63–90, doi:10.1016/0079-6611(86)90007-8.

Lyle, M., N. Mitchell, N. Pisias, A. Mix, J. I. Martínez, and A. Paytan (2005), Do geochemical estimates of sediment focusing pass the sediment test in the equatorial Pacific?, *Paleoceanography*, *20*, PA1005, doi:10.1029/2004PA001019.

Mahowald, N., K. Kohfeld, M. Hansson, Y. Balkanski, S. P. Harrison, I. C. Prentice, M. Schulz, and H. Rodhe (1999), Dust sources and deposition during the Last Glacial Maximum and current climate: A comparison of model results with paleodata from ice cores and marine sediments, *J. Geophys. Res.*, *104*, 15,895–15,916, doi:10.1029/1999JD900084.

MARGO Project Members (2009), Constraints on the magnitude and patterns of ocean cooling at the Last Glacial Maximum, *Nat. Geosci.*, *2*, 127–132, doi:10.1038/ngeo411.

Markgraf, V., and H. F. Diaz (2000), The past ENSO record: A synthesis, in *El Niño and the Southern Oscillation Multiscale Variability and Global and Regional Impacts*, edited by H. F. Diaz and V. Markgraf, pp. 465–488, Cambridge Univ. Press, New York.

Martínez, I., L. Keigwin, T. T. Barrows, Y. Yokoyama, and J. Southon (2003), La Niña-like conditions in the eastern equatorial Pacific and a stronger Choco Jet in the northern Andes during the last glaciation, *Paleoceanography*, *18*(2), 1033, doi:10.1029/2002PA000877.

Martínez, I., D. Rincon, Y. Yokoyama, and T. Barrows (2006), Foraminifera and coccolithophorid assemblage change in the Panama Basin during the last deglaciation: Response to sea-surface productivity induced by a transient climate change, *Palaeogeogr. Palaeoclimatol. Palaeoecol.*, *234*, 114–126, doi:10.1016/j.palaeo.2005.10.022.

Martinez, J. I., and G. Bedoya (2001), Recent planktonic foraminifera from deep-sea sediments from the eastern equatorial Pacific: Proxies of the equatorial front in the late Quaternary, *J. Mar. Coastal Res.*, *30*, 151–176.

McGee, D., F. Marcantonio, and J. Lynch-Stieglitz (2007), Deglacial changes in dust flux in the eastern equatorial Pacific, *Earth Planet. Sci. Lett.*, *257*, 215–230, doi:10.1016/j.epsl.2007.02.033.

McPhaden, M. J., S. E. Zebiak, and M. H. Glantz (2006), ENSO as an integrating concept in Earth science, *Science*, *314*, 1740–1745, doi:10.1126/science.1132588.

Mechoso, C. R., et al. (1995), The seasonal cycle over the tropical Pacific in coupled ocean-atmosphere general circulation models, *Mon. Weather Rev.*, *123*, 2825–2838, doi:10.1175/1520-0493(1995)123<2825:TSCOTT>2.0.CO;2.

Medina-Elizalde, M., and D. W. Lea (2005), The mid-Pleistocene transition in the tropical Pacific, *Science*, *310*, 1009–1012, doi:10.1126/science.1115933.

Mix, A. C. (2006), Running hot and cold in the eastern equatorial Pacific, *Quat. Sci. Rev.*, *25*, 1147–1149, doi:10.1016/j.quascirev.2006.03.008.

Müller, P. J., and R. Schneider (1993), An automated leaching method for the determination of opal in sediments and particulate matter, *Deep Sea Res., Part I*, *40*(3), 425–444, doi:10.1016/0967-0637(93)90140-X.

Müller, P. J., G. Kirst, G. Ruhland, I. von Storch, and A. Rosell-Melé (1998), Calibration of the alkenone paleotemperature index $U^{K'}_{37}$ based on core-tops from the eastern South Atlantic and the global ocean (60°N–60°S), *Geochim. Cosmochim. Acta*, *62*(10), 1757–1772, doi:10.1016/S0016-7037(98)00097-0.

Neill, D. A. (1999), Vegetation, in *Catalogue of the Vascular Plants of Ecuador*, *Monogr. Syst. Bot.*, vol. 75, edited by P. M. Jørgensen and S. León-Yánez, pp. 8–13, Mo. Bot. Garden, St. Louis.

Neill, D. A., and P. M. Jørgensen (1999), Climates, in *Catalogue of the Vascular Plants of Ecuador*, *Monogr. Syst. Bot.*, vol. 75, edited by P. M. Jørgensen and S. León-Yánez, pp. 13–25, Mo. Bot. Garden, St. Louis.

Pahnke, K., J. P. Sachs, L. Keigwin, A. Timmermann, and S.-P. Xie (2007), Eastern tropical Pacific hydrologic changes during the past 27,000 years from D/H ratios in alkenones, *Paleoceanography*, *22*, PA4214, doi:10.1029/2007PA001468.

Paillard, D., L. Labeyrie, and P. Yiou (1996), Macintosh program performs time-series analysis, *Eos Trans. AGU*, *77*(39), 379, doi:10.1029/96EO00259.

Pailler, D., and E. Bard (2002), High frequency paleoceanographic changes during the past 140 000 yr recorded by the organic matter in sediments of the Iberian margin, *Palaeogeogr. Palaeoclimatol. Palaeoecol.*, *181*, 431–452, doi:10.1016/S0031-0182(01)00444-8.

Pak, H., and J. R. V. Zaneveld (1974), Equatorial front in the eastern Pacific Ocean, *J. Phys. Oceanogr.*, *4*, 570–578, doi:10.1175/1520-0485(1974)004<0570:EFITEP>2.0.CO;2.

Pena, L. D., I. Cacho, P. Ferretti, and M. A. Hall (2008), El Niño-Southern Oscillation-like variability during glacial terminations and interlatitudinal teleconnections, *Paleoceanography*, *23*, PA3101, doi:10.1029/2008PA001620.

Pennington, J. T., K.-L. Mahoney, V. S. Kuwahare, D. D. Kolber, R. Calienes, and F. P. Chavez (2006), Primary production in the eastern tropical Pacific: A review, *Prog. Oceanogr.*, *69*, 285–317, doi:10.1016/j.pocean.2006.03.012.

Peterson, T. C., and S. V. Russell (1997), An overview of the Global Historical Climatology Network temperature data base, *Bull. Am. Meteorol. Soc.*, *78*, 2837–2849, doi:10.1175/1520-0477(1997)078<2837:AOOTGH>2.0.CO;2.

Philander, S. G. H., D. Gu, D. Halpern, G. Lambert, N. C. Lau, T. Li, and R. C. Pacanowski (1996), Why the ITCZ is mostly north of the equator,

J. Clim., *9*, 2958–2972, doi:10.1175/1520-0442(1996)009<2958:WTIIMN>2.0.CO;2.

Pisias, N. G., and A. Mix (1997), Spatial and temporal oceanographic variability of the eastern equatorial Pacific during the late Pleistocene: Evidence from radiolaria microfossils, *Paleoceanography*, *12*, 381–393, doi:10.1029/97PA00583.

Poveda, G., P. R. Waylen, and R. S. Pulwarty (2006), Annual and inter-annual variability of the present climate in northern South America and southern Mesoamerica, *Palaeogeogr. Palaeoclimatol. Palaeoecol.*, *234*, 3–27, doi:10.1016/j.palaeo.2005.10.031.

Prahl, F. G., and S. G. Wakeham (1987), Calibration of unsaturation patterns in long-chain ketone compositions for paleotemperature assessment, *Nature*, *330*, 367–369, doi:10.1038/330367a0.

Prahl, F. G., T. Herbert, S. C. Brassell, N. Ohkouchi, M. Pagani, D. Repeta, A. Rosell-Melé, and E. Sikes (2000), Status of alkenone paleothermometer calibration: Report from Working Group 3, *Geochem. Geophys. Geosyst.*, *1*(11), 1034, doi:10.1029/2000GC000058.

Prahl, F. G., A. C. Mix, and M. A. Sparrow (2006), Alkenone paleothermometry: Biological lessons from marine sediment records off western South America, *Geochim. Cosmochim. Acta*, *70*, 101–117, doi:10.1016/j.gca.2005.08.023.

Raymond, D. J., S. K. Esbensen, C. Paulson, M. Gregg, C. S. Bretherton, W. A. Petersen, R. Cifelli, L. K. Shay, C. Ohlmann, and P. Zudeima (2004), EPIC2001 and the coupled ocean-atmosphere system of the tropical east Pacific, *Bull. Am. Meteorol. Soc.*, *85*, 1341–1354, doi:10.1175/BAMS-85-9-1341.

Richter, T. O., S. van der Gaast, B. Koster, A. Vaars, R. Gieles, H. C. de Stigter, H. de Haas, and T. C. E. van Weering (2006), The Avaatech XRF Core Scanner: Technical description and applications to NE Atlantic sediments, in *New Techniques in Sediment Core Analysis*, edited by R. G. Rothwell, *Geol. Soc. Spec. Publ.*, *267*, 39–50.

Rossel, F., E. Cadier, and G. Gómez (1996), Las inundaciones en la zona costera Ecuatoriana: Causas, obras de proteccion existentes y previstas, *Bull. Inst. Fr. Etud. Andines*, *25*(3), 399–420.

Rull, V. (1996), Late Pleistocene and Holocene climates of Venezuela, *Quat. Int.*, *31*, 85–94, doi:10.1016/1040-6182(95)00024-D.

Sachs, J. P. (2008), Divergent trends in Holocene SSTs derived from alkenones and Mg/Ca in the equatorial Pacific, *Eos Trans. AGU*, *89*(53), Fall Meet Suppl., Abstract PP23C-1486.

Sachs, J. P., R. R. Schneider, T. I. Eglinton, K. H. Freeman, G. Ganssen, J. F. McManus, and D. W. Oppo (2000), Alkenones as paleoceanographic proxies, *Geochem. Geophys. Geosyst.*, *1*(11), 1035, doi:10.1029/2000GC000059.

Schneider, R., P. J. Müller, and R. Acheson (1999), Atlantic alkenone sea surface temperature records, in *Reconstructing Ocean History: A Window Into the Future*, edited by I. Abrantes and A. C. Mix, pp. 33–55, Plenum, New York.

Shipboard Scientific Party (2003), Site 1239, *Proc. Ocean Drill Program Initial Rep.*, *202*, 1–93, doi:10.2973/odp.proc.ir.202.110.2003.

Sonzogni, C., E. Bard, F. Rostek, D. Dollfus, A. Rosell-Melé, and G. Eglington (1997), Temperature and salinity effects on alkenone ratios measured in surface sediments from the Indian Ocean, *Quat. Res.*, *47*, 344–355, doi:10.1006/qres.1997.1885.

Spero, H. J., K. M. Mielke, E. M. Kalve, D. W. Lea, and D. K. Pak (2003), Multispecies approach to reconstructing eastern equatorial Pacific thermocline hydrography during the past 360 kyr, *Paleoceanography*, *18*(1), 1022, doi:10.1029/2002PA000814.

Takahashi, K., and D. S. Battisti (2007), Processes controlling the mean tropical Pacific precipitation pattern: I. The Andes and the eastern Pacific ITCZ, *J. Clim.*, *20*, 3434–3451, doi:10.1175/JCLI4198.1.

Thompson, L. G., et al. (1998), A 25,000-year tropical climate history from Bolivian ice cores, *Science*, *282*, 1858–1864, doi:10.1126/science.282.5395.1858.

Tzedakis, P. C., D. Raynaud, J. F. McManus, A. Berger, V. Brovkin, and T. Kiefer (2009), Interglacial diversity, *Nat. Geosci.*, *2*, 751–755, doi:10.1038/ngeo660.

Versteegh, G. J. M., E. Schefuβ, L. Dupont, F. Marret, J. S. Sinninghe Damsté, and J. H. F. Jansen (2004), Taraxerol and *Rhizophora* pollen as proxies for tracking past mangrove ecosystems, *Geochim. Cosmochim. Acta*, *68*, 411–422, doi:10.1016/S0016-7037(03)00456-3.

Wang, C., and P. C. Fiedler (2006), ENSO variability and the eastern tropical Pacific: A review, *Prog. Oceanogr.*, *69*, 239–266, doi:10.1016/j.pocean.2006.03.004.

Wang, W., S. Saha, H.-L. Pan, S. Nadiga, and G. White (2005), Simulation of ENSO in the new NCEP coupled forecast system model (CFS03), *Mon. Weather Rev.*, *133*, 1574–1593, doi:10.1175/MWR2936.1.

Wang, X., A. S. Auler, R. L. Edwards, H. Cheng, P. Cristalli, P. L. Smart, D. A. Richards, and C.-C. Shen (2004), Wet periods in northeastern Brazil over the past 210 kyr linked to distant climate anomalies, *Nature*, *432*, 740–743, doi:10.1038/nature03067.

Waylen, P., and G. Poveda (2002), El Niño-Southern Oscillation and aspects of western South American hydro-climatology, *Hydrol. Processes*, *16*, 1247–1260, doi:10.1002/hyp.1060.

Weltje, G.-J., and R. Tjallingii (2008), Calibration of XRF core scanning for quantitative geochemical logging of sediment cores: Theory and application, *Earth Planet. Sci. Lett.*, *274*, 423–438, doi:10.1016/j.epsl.2008.07.054.

Winckler, G., R. F. Anderson, M. Q. Fleisher, D. McGee, and N. Mahowald (2008), Covariant glacial-interglacial dust fluxes in the equatorial Pacific and Antarctica, *Science*, *320*, 93–96, doi:10.1126/science.1150595.

Wittenberg, A. T., A. Rosati, N.-C. Lau, and J. J. Ploshay (2006), GFDL's CM2 global coupled climate models. Part III: Tropical Pacific climate and ENSO, *J. Clim.*, *19*, 698–722, doi:10.1175/JCLI3631.1.

Xie, S. P. (2004), The shape of continents, air-sea interaction, and the rising branch of the Hadley circulation, in *The Hadley Circulation: Present, Past and Future*, *Adv. Global Change Res.*, vol. 21, edited by H. R. Díaz and R. S. Bradley, pp. 121–152, doi:10.1007/978-1-4020-2944-8_4, Kluwer Acad., Dordrecht, Netherlands.

Xie, S. P., and S. G. H. Philander (1994), A coupled ocean-atmosphere model of relevance to the ITCZ in the eastern Pacific, *Tellus, Ser. A*, *46*, 340–350, doi:10.1034/j.1600-0870.1994.t01-1-00001.x.

Yeh, S. W., J. S. Kug, B. Dewitte, M. H. Kwon, B. P. Kirtman, and F. F. Jin (2009), El Niño in a changing climate, *Nature*, *461*, 511–514, doi:10.1038/nature08316.

Yin, J. H., and D. A. Battisti (2001), The importance of tropical sea surface temperature patterns in simulations of Last Glacial Maximum climate, *J. Clim.*, *14*, 565–581, doi:10.1175/1520-0442(2001)014<0565:TIOTSS>2.0.CO;2.

E. Bard, CEREGE, Aix-Marseille Université, CNRS, Collège de France, IRD, Europôle Méditerranéen de L'Arbois, BP 80, F-13545 Aix-en-Provence CEDEX 4, France.

T. Blanz and G. Leduc, Institut für Geowissenschaften, Christian Albrecht Universität, D-24118 Kiel, Germany.

S. Contreras, Max Planck Institute for Marine Microbiology, Celsiusstrasse 1, D-28359 Bremen, Germany.

F. Lamy, A. Mackensen, D. Rincón-Martínez, C. Saukel, and R. Tiedemann, Alfred Wegener Institute for Polar and Marine Research, Columbusstrasse, D-27568 Bremerhaven, Germany. (daniel.rincon.martinez@awi.de)

4.5 Early Pliocene increase in thermohaline overturning: A precondition for the development of the modern equatorial Pacific cold tongue

Steph, S., Tiedemann, R., Prange, M., Groeneveld, J., Schulz, M., Timmermann, A., Nürnberg, D., Rühlemann, C., Saukel, C. and Haug, G. H., 2010, Paleoceanography, Vol. 25, PA2202, doi:10.1029/2008PA001645

PALEOCEANOGRAPHY, VOL. 25, PA2202, doi:10.1029/2008PA001645, 2010

Click Here for Full Article

Early Pliocene increase in thermohaline overturning: A precondition for the development of the modern equatorial Pacific cold tongue

Silke Steph,[1,2,3] Ralf Tiedemann,[1] Matthias Prange,[4] Jeroen Groeneveld,[4] Michael Schulz,[4] Axel Timmermann,[5] Dirk Nürnberg,[6] Carsten Rühlemann,[7] Cornelia Saukel,[1] and Gerald H. Haug[3,8]

Received 28 May 2008; revised 29 July 2009; accepted 15 October 2009; published 15 April 2010.

[1] Unraveling the processes responsible for Earth's climate transition from an "El Niño–like state" during the warm early Pliocene into a modern-like "La Niña–dominated state" currently challenges the scientific community. Recently, the Pliocene climate switch has been linked to oceanic thermocline shoaling at ~3 million years ago along with Earth's final transition into a bipolar icehouse world. Here we present Pliocene proxy data and climate model results, which suggest an earlier timing of the Pliocene climate switch and a different chain of forcing mechanisms. We show that the increase in North Atlantic meridional overturning circulation between 4.8 and 4.0 million years ago, initiated by the progressive closure of the Central American Seaway, triggered overall shoaling of the tropical thermocline. This preconditioned the turnaround from a warm eastern equatorial Pacific to the modern equatorial cold tongue state about 1 million years earlier than previously assumed. Since ~3.6–3.5 million years ago, the intensification of Northern Hemisphere glaciation resulted in a strengthening of the trade winds, thereby amplifying upwelling and biogenic productivity at low latitudes.

Citation: Steph, S., R. Tiedemann, M. Prange, J. Groeneveld, M. Schulz, A. Timmermann, D. Nürnberg, C. Rühlemann, C. Saukel, and G. H. Haug (2010), Early Pliocene increase in thermohaline overturning: A precondition for the development of the modern equatorial Pacific cold tongue, *Paleoceanography*, *25*, PA2202, doi:10.1029/2008PA001645.

1. Introduction

[2] Understanding the causal chain of Pliocene climate forcing may help to improve predictions of future climate change, including the ultimate role of the ocean circulation in a globally warmer world [*Jansen et al.*, 2007]. During the Pliocene warm period from ~5.5 to ~3 Ma, mean global surface temperatures were ~3°C warmer than today, atmospheric CO_2 concentrations were close to modern ones [*Foster et al.*, 2009], the modern Northern Hemisphere ice cap was absent, and sea level was ~25 m higher than today [e.g., *Raymo et al.*, 1996; *Dowsett et al.*, 1999; *Ravelo et al.*, 2004; *Mudelsee and Raymo*, 2005]. Growing evidence from early Pliocene paleoclimate data suggests that sea surface temperatures (SST) in the eastern equatorial Pacific (EEP) cold tongue were similar to those of the western tropical Pacific Warm Pool [*Chaisson and Ravelo*, 2000; *Molnar and Cane*, 2002; *Ravelo et al.*, 2004; *Wara et al.*, 2005]. Warm surface water, a deep thermocline, and low biogenic productivity characterized the low-latitude to midlatitude upwelling regions [*Fedorov et al.*, 2006; *Dekens et al.*, 2007].

[3] The timing and mechanisms for the development of the modern EEP cold tongue state have so far been linked to the mid-Pliocene intensification of Northern Hemisphere glaciation (NHG) [*Fedorov et al.*, 2006]. According to a recent hypothesis [*Fedorov et al.*, 2006], cooling of the deep ocean, associated with enhanced oceanic heat loss at high latitudes and a balanced increase in heat gain at low latitudes, caused the tropical thermocline to shoal. This thermocline shoaling has been proposed to reach a critical threshold at ~3 Ma, allowing trade winds to bring cooler waters to the surface in equatorial and coastal upwelling zones.

[4] However, there is also evidence that cooling of the upwelling regions off California [*Fedorov et al.*, 2006; *Dekens et al.*, 2007; *Liu et al.*, 2008; *Brierley et al.*, 2009], West Africa [*Marlow et al.*, 2000] and within the EEP cold tongue [*Lawrence et al.*, 2006; *Dekens et al.*, 2007]

[1]Alfred Wegener Institute for Polar and Marine Research, Bremerhaven, Germany.
[2]Geology and Geophysics Department, Woods Hole Oceanographic Institution, Woods Hole, Massachusetts, USA.
[3]Now at DFG–Leibniz Center for Surface Process and Climate Studies, Institute for Geosciences, Potsdam University, Potsdam, Germany
[4]MARUM–Center for Marine Environmental Sciences and Department of Geosciences, University of Bremen, Bremen, Germany.
[5]IPRC, SOEST, University of Hawai'i at Mānoa, Honolulu, Hawaii, USA.
[6]Leibniz Institute of Marine Sciences at University of Kiel (IFM-GEOMAR), Kiel, Germany.
[7]Bundesanstalt für Geowissenschaften und Rohstoffe, Hannover, Germany.
[8]Geological Institute, Department of Earth Sciences, ETH Zurich, Zurich, Switzerland.

Copyright 2010 by the American Geophysical Union.
0883-8305/10/2008PA001645

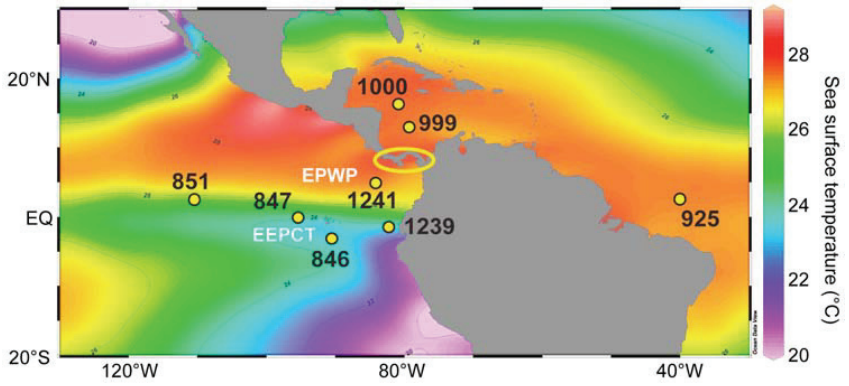

Figure 1. Map showing modern annual sea surface temperatures in the tropical eastern Pacific and western Atlantic/Caribbean (NODC, 2001 [*Conkright et al.*, 2002]). Yellow dots show the locations of ODP sites discussed in this study (Site 846, 3°06′S, 90°49′W, 3296 m water depth; Site 847, 0°12′N, 95°19′W, 3334 m water depth; Site 851, 2°46′N, 110°34′W, 3761 m water depth; Site 925, 4°12′N, 43°29′W, 3041 m water depth; Site 999, 12°45′N, 78°44′W, 2828 m water depth; Site 1000, 16°33′N, 79°52′W, 916 m water depth; Site 1239, 0°40′S, 82°05′W, 1414 m water depth; Site 1241, 5°51′N, 86°27′W, 2027 m water depth). The ellipse is indicating the final openings of the Central American Seaway. EEPCT, eastern equatorial Pacific cold tongue; EPWP, East Pacific Warm Pool.

started more than 600 kyr earlier (~4.5–3.6 Ma). Here, we present new proxy data that strongly corroborate an early development of the EEP cold tongue. This timing questions the intensification of NHG as exclusive forcing mechanism. Instead, it suggests an additional link to the early Pliocene threshold in the closure history of the Central American Seaway (CAS), which was associated with an increase in Atlantic meridional overturning circulation (AMOC) [e.g., *Haug and Tiedemann*, 1998]. Using Pliocene proxy data as well as results from a coupled climate model, we test the hypothesis that changes in the strength of the AMOC can trigger global adjustments of the thermocline depth (TCD). Such a link has been proposed by theoretical and modeling studies [e.g., *Huang et al.*, 2000; *Timmermann et al.*, 2005], but has so far not been observed or verified by proxy data.

2. Material and Methods

2.1. Sample Material

[5] We present new Pliocene planktonic foraminiferal $\delta^{18}O$ and Mg/Ca-derived temperatures, alkenone ($U^{K'}_{37}$) SSTs, opal accumulation rates, and benthic foraminiferal $\delta^{13}C$ from tropical eastern Pacific Ocean Drilling Program (ODP) sites 1239 (0°40′S, 82°05′W, 1414 m water depth) and 1241 (5°51′N, 86°27′W, 2027 m water depth) [*Mix et al.*, 2003] as well as from Caribbean ODP sites 999 (12°45′N, 78°44′W, 2828 m water depth) and 1000 (16°33′N, 79°52′W, 916 m water depth) [*Sigurdsson et al.*, 1997] (Figure 1). The preservation of foraminiferal carbonate shells is generally good according to the relatively shallow site locations well above the lysocline [*Sigurdsson et al.*, 1997; *Mix et al.*, 2003]. The proxy records span the time interval from ~2.1 Ma to 5.5 Ma. Pliocene age models for all sites are based on orbital tuning (see *Tiedemann et al.* [2007] for tropical eastern Pacific sites 1239 and 1241 and *Haug and Tiedemann* [1998] and *Steph et al.* [2006a] for Caribbean sites 999 and 1000).

2.2. Stable Isotope Measurements

[6] The samples were freeze-dried and washed through a 63 μm mesh. For $\delta^{18}O$ measurements on planktonic foraminifera, ten to fifteen specimens of *Neogloboquadrina dutertrei* (thermocline dweller) were selected from the 315–400 μm size fraction of samples from Caribbean sites 999 and 1000. Due to the lower amount of planktonic foraminifers in samples from equatorial eastern Pacific Site 1239, we picked ten to fifteen specimens of *Globigerinoides sacculifer* (mixed layer dweller) and *Globorotalia tumida* (habitat near the bottom of the photic zone) from the >250 μm size fraction. For benthic $\delta^{13}C$ measurements at Site 1000, we selected one to five tests of the epibenthic foraminifera *Cibicidoides wuellerstorfi* (>315 μm). Prior to analysis, visibly contaminated specimens were slightly crushed and ultrasonically cleaned with methanol. The excess liquid and mud were siphoned off and the samples were dried at 60°C.

[7] Stable isotope analyses on planktonic and epibenthic foraminifers were carried out at IFM-GEOMAR (Kiel), using either a Finnigan Delta-Plus-Advantage mass spectrometer coupled to a Finnigan Gas Bench II (with analytical precision better than ±0.07 ‰ for $\delta^{18}O$ and better than ±0.05 ‰ for $\delta^{13}C$; ±1σ), or a Finnigan MAT 252 mass spectrometer with automated Kiel carbonate preparation device (with analytical precision better than ±0.07 ‰ for $\delta^{18}O$ and ±0.04 ‰ for $\delta^{13}C$; ±1σ). Both machines were intercalibrated using a house standard, which was calibrated to the National Bureau of Standards NBS-19. The ratios of $^{18}O/^{16}O$ and $^{13}C/^{12}C$ are reported with reference to the Pee Dee Belemnite (PDB) standard.

2.3. Mg/Ca Analyses

[8] For Mg/Ca measurements, 20–25 specimens of *N. dutertrei* (sites 999, 1000) and *G. tumida* (Site 1239) were picked from the same size fraction as used for stable isotope analyses. Specimens visibly contaminated by ferromanganese oxides were not selected for analysis. After gentle crushing, the samples were cleaned according to the cleaning protocol for Mg/Ca of *Barker et al.* [2003]. To remove clays, the samples were rinsed four to six times with distilled deionized water and twice with methanol (suprapure) with ultrasonical cleaning steps (2 to 3 min) after each rinse. Subsequently, samples were treated with a hot (97°C) oxidizing 1% $NaOH/H_2O_2$ solution (10 ml 0.1 N NaOH (analytical grade); 100 μl 30% H_2O_2 (suprapure)) for 10 min to remove organic matter. Every 2.5 min, the vials were rapped on the bench top to release any gaseous buildup. After 5 min, the samples were placed in an ultrasonic bath for a few seconds to maintain contact between reagent and sample. This treatment was repeated after refreshment of the oxidizing solution. The remaining oxidizing solution was removed during three rinsing steps with distilled deionized water. After transferring the samples into clean vials, a weak acid leach with 250 μl 0.001 M HNO_3 (subboiled distilled) was applied with 30 s ultrasonic treatment and subsequent two rinses with distilled deionized water. After cleaning, the samples were dissolved in 0.075 M nitric acid (HNO_3) (subboiled distilled) and diluted several times, until all samples obtained calcium concentrations in the range of 30–70 ppm.

[9] Analyses were performed on an ICP-AES (ISA Jobin Yovin-Spex Instruments S.A. GmbH) at IFM-GEOMAR (Kiel) or on a simultaneous, radially viewing ICP-OES (Ciros CCD SOP, Spectro A. I., Germany) at the Institute of Geosciences (Kiel University, Germany). The long-term precision of the Mg/Ca analyses estimated from an internal laboratory standard was 0.1%. Replicate analyses on the same samples, which were cleaned and analyzed during different sessions, showed a standard deviation of 0.09 mmol/mol, introducing a temperature error of about 0.5°C.

2.4. Calculation of Mg/Ca-Derived Paleotemperatures

[10] For this study, *G. sacculifer* Mg/Ca temperatures were calculated using the *Dekens et al.* [2002] Mg/Ca temperature calibration for *G. sacculifer* with core-depth-based dissolution corrections for the Pacific (Site 1241) and for the Atlantic (sites 999, 1000). *N. dutertrei* Mg/Ca ratios from Caribbean sites 999 and 1000 were converted into temperature using the *Dekens et al.* [2002] Mg/Ca temperature calibration for *N. dutertrei* with a core-depth-based dissolution correction for the Atlantic. We used the *Anand et al.* [2003] multispecies Mg/Ca temperature calibration to calculate *G. tumida* Mg/Ca paleotemperatures at Pacific sites 1239 and 1241 and we included the *Dekens et al.* [2002] core-depth-based Pacific dissolution correction for *G. sacculifer*, because species-specific dissolution corrections for *G. tumida* are not available for the Pacific.

$$\mathrm{Mg/Ca} = 0.38 \exp 0.09[\mathrm{T} - 0.36(\text{core depth in km}) - 2.0^{\circ}\mathrm{C}] \quad (1)$$

[11] Yet we are aware that Mg/Ca *G. tumida* might have a different sensitivity to carbonate dissolution than Mg/Ca *G. sacculifer*, which would in turn affect the resulting absolute *G. tumida* Mg/Ca temperature estimates. Absolute Mg/Ca temperature estimates of course depend on the selection of Mg/Ca temperature calibrations used for the calculations, but the relative changes in vertical temperature gradients are robust regardless of which calibration is used. Our conclusions, which are mainly based on the evolutionary long-term changes of vertical temperature gradients between the mixed layer and the bottom of the photic zone, would therefore not be affected by the application of other Mg/Ca temperature calibrations.

2.5. Calculation of Opal Accumulation Rates

[12] To estimate opal accumulation rates at Site 1239, we quantified the concentrations of biogenic silica (opal) for 15 samples by using the automated leaching method according to *Müller and Schneider* [1993]. The opaline material was extracted from the dry and ground bulk sediment by sodium hydroxide at ~85°C for ~45 min. The leaching solution was continuously analyzed for dissolved silicon by molybdate blue spectrophotometry. The *DeMaster* [1981] mineral correction was consequently applied. The excellent linear correlation of opal concentrations with shipboard grape density data [*Mix et al.*, 2003] (R = 0.8) allowed for the calculation of a high-resolution opal percentage record. Mass accumulation rates (g cm^{-2} kyr^{-1}) were then calculated using the sedimentation rate (in cm kyr^{-1}) between age control points [*Tiedemann et al.*, 2007], dry bulk density data calculated from grape density and shipboard physical properties data [*Mix et al.*, 2003], and the opal concentrations (%).

2.6. Alkenone Analysis

[13] Samples of 2 g freeze-dried and homogenized sediment were mixed with an internal standard and ultrasonically extracted for 3 min (UP200H ultrasonication disrupter probe; S3 micropoint, amplitude 0.5, pulse 0.5), using successively less polar mixtures of methanol and methylene chloride (CH_3OH, CH_3OH/CH_2Cl_2 1:1, CH_2Cl_2). After centrifuging, the supernatants were combined, desalted with deionized water, dried with Na_2SO_4 and rotary evaporated to complete dryness. The residues were dissolved in CH_2Cl_2 and additionally purified using a silica cartridge (Varian Bond Elut; 1CC/100 mg). To eliminate interference with wax esters, the clean extracts were hydrolyzed with 0.1 N KOH in Methanol (90/10 CH_3OH/H_2O) at 80°C for 2 h, and the neutral fraction containing the alkenones was obtained by partitioning into hexane. Finally, the extracts were concentrated under N_2 and taken up in 25 μl of the 1:1 CH_3OH/CH_2Cl_2 mixture. Gas chromatography was performed using a HP5890 series II gas chromatograph equipped with a split/splitless injector, a 60 m × 0.32 mm × 0.1 μm nonpolar fused silica capillary column DB-5MS and flame ionization detector. An aliquot of 3 μl was injected in split mode (one tenth) with helium as the carrier gas. The oven temperature was programmed from 50°C to 250°C at 25°/min, 250°C to 290°C at 1°/min and a final heating from 290°C to 310°C at 30°/min. Compounds were quantified using octacosane acid methyl ester as an internal standard and the relative response

of the C38 n-alkane. The ketone unsaturation index $U_{37}^{K'}$ was converted to temperature according to *Conte et al.* [2006]:

$$T(^{\circ}C) = -0.957 + 54.3\left(U_{37}^{K'}\right) - 52.9\left(U_{37}^{K'}\right)^2 + 28.3\left(U_{37}^{K'}\right)^3. \quad (2)$$

[14] We applied the nonlinear $U_{37}^{K'}$/temperature calibration of *Conte et al.* [2006] because it is based on alkenones from surface water particulates collected in the world ocean (i.e., the natural environment of the alkenone producers) and associated temperatures measured at sampling depth. Moreover, this calibration accounts for the asymptotic behavior of $U_{37}^{K'}$ at the warmest SSTs. The analytical precision ($\pm 1\sigma$) based on duplicates and multiple extractions of a sediment sample used as an internal laboratory reference sample was better than 0.003 $U_{37}^{K'}$ units or 0.1°C.

2.7. Climate Model Experiments

[15] For our sensitivity experiments, we used the global atmosphere-ocean model ECBILT-CLIO version 3. The coupled model derives from the atmosphere model ECBILT [*Opsteegh et al.*, 1998] and the ocean/sea ice model CLIO [*Goosse and Fichefet*, 1999]. The atmospheric component solves the quasi-geostrophic equations and ageostrophic correction terms in T21 resolution using three layers. The primitive equation, free surface ocean component has a horizontal resolution of 3 degrees and 20 levels in the vertical. It is coupled to a thermodynamic-dynamic sea ice model with viscous plastic rheology. There is no *local* flux correction in ECBILT-CLIO. However, precipitation over the Atlantic and Arctic basins is reduced by 8.5% and 25%, respectively, and homogeneously redistributed over the North Pacific. The implementation of this regional flux adjustment considerably improves the simulation of the present-day climate and produces a realistic AMOC. Its reliability in the simulation of other climates than the present one, however, is elusive. For the sensitivity studies presented in this paper, the potential errors in surface hydrography and AMOC that are induced by the flux adjustment are acceptable since we are interested in the *qualitative* relationship between the AMOC and the thermocline, rather than in precise numbers. More information about the model and a complete list of references is available at http://www.knmi.nl/onderzk/CKO/ecbilt-papers.html.

[16] Beside a 5000 years control run (experiment CTL), simulating the present-day (preindustrial) climate, we conducted an experiment with open Central American Seaway (experiment CAS) and a freshwater hosing experiment (experiment OFF). These experiments were designed to elucidate the relationship between AMOC and tropical TCD. The freshwater hosing is a convenient method to shut off the AMOC, providing an estimate for the maximum response of tropical TCD to pure AMOC slowing. We note that we do not imply corresponding meltwater events in the early Pliocene.

[17] In experiment CAS, the Panama Seaway has a sill depth of 700 m and is defined on three velocity grid points, corresponding to a width of approximately 1000 km. All other boundary conditions are the same as in the control run. Therefore, experiment CAS should be viewed as a sensitivity study to elucidate tropical thermocline dynamics rather than a simulation of early Pliocene climate. In experiment OFF Panama is closed, but NADW formation is completely shut off by an anomalous freshwater input to the North Atlantic (0.5 Sv between 50°N and 70°N). In both experiments CAS and OFF, the model was integrated another 2250 years to reach a new equilibrium, starting from the control run's final state as initial condition. Model results presented in this paper are annual averages determined from the last 50 years of each experiment.

[18] Generally, the thermocline is defined as the depth at which the vertical temperature gradient is at a maximum. In a numerical ocean model such as CLIO, the search for this maximum would always result in thermocline depths that correspond exactly to the depths of grid points (in ECBILT-CLIO these are located at 5 m, 16 m, 29 m, 45 m, 65 m, 90 m, 122 m, etc.). Hence, changes that are smaller than the vertical grid spacing could not be observed when using the maximum temperature gradient for the calculation of TCD. Therefore, alternative indicators for TCD are generally used in numerical models. As an indicator for tropical TCD, we use the depth of the 20°C isotherm (the depth of an isotherm is not bound to the grid spacing; an isotherm can well reside between two grid points in the vertical and its depth can easily be found by linear interpolation of the gridded temperature field). In both observational data and the ECBILT-CLIO climate model, the depth of the maximum temperature gradient is almost identical to the depth of the 20°C isotherm in the central (~150 m) and eastern (less than 50 m on average) equatorial Pacific.

3. Results

3.1. Equatorial Eastern Pacific Site 1239

3.1.1. Planktonic $\delta^{18}O$ and Mg/Ca Paleotemperature Records

[19] The $\delta^{18}O$ record of the mixed layer dweller *G. sacculifer* as well as $\delta^{18}O$ and Mg/Ca temperature records of the deep dweller *G. tumida* (habitat close to the bottom of the photic zone [*Ravelo and Fairbanks*, 1992; *Ravelo and Andreasen*, 1999]) serve to reconstruct Pliocene changes in upper ocean stratification at equatorial eastern Pacific Site 1239 (Figure 2a). Small (large) surface/subsurface temperature differences, and hence small (large) $\delta^{18}O$ differences between shallow- and deep-dwelling planktonic foraminifera indicate a deep (shallow) thermocline [e.g., *Ravelo and Fairbanks*, 1992; *Ravelo and Andreasen*, 1999; *Steph et al.*, 2009].

[20] At Site 1239, $\delta^{18}O$ values of the mixed layer dweller *G. sacculifer* remained relatively constant between 5.0 and 3.9 Ma (average $\delta^{18}O$ of −1.1‰). From 3.9 to 2.7 Ma, the $\delta^{18}O$ values of *G. sacculifer* increased by ~0.4‰ (average $\delta^{18}O$ of −0.7‰ between 2.7 and 2.9 Ma) with a major step around ~3.7 Ma (Figure 2a). The Mg/Ca temperature and $\delta^{18}O$ records of the deep dweller *G. tumida*, however, suggest larger temperature changes at the bottom of the photic zone. Average *G. tumida* $\delta^{18}O$ values increased by

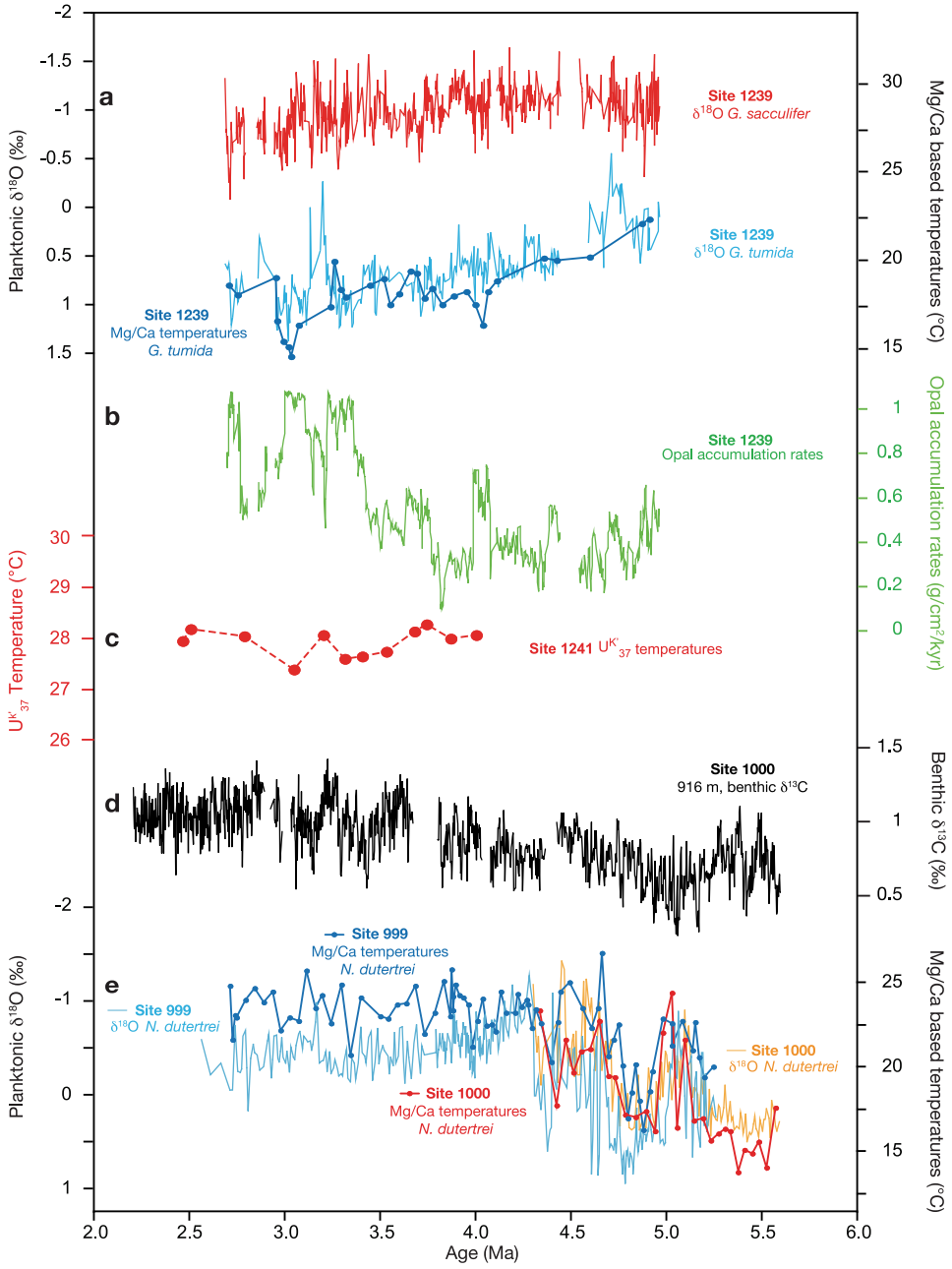

Figure 2. New proxy data presented in this study, spanning the time interval from ~5.6 Ma to 2.1 Ma. (a) *G. sacculifer* δ^{18}O data (red line), *G. tumida* δ^{18}O data (light blue line) and Mg/Ca temperature data (dark blue) from equatorial eastern Pacific ODP Site 1239. (b) Biogenic opal accumulation rates, Site 1239 (green line). (c) $U^{K'}_{37}$ sea surface temperature data from tropical eastern Pacific Site 1241 (red). (d) Epibenthic δ^{13}C record from Caribbean Site 1000 (*C. wuellerstorfi*, black line). (e) The δ^{18}O records of the thermocline dweller *N. dutertrei* (dextral variety) from Caribbean sites 999 (light blue) and 1000 (orange) and Mg/Ca temperature records of *N. dutertrei* (dextral variety) from sites 999 (dark blue) and 1000 (red).

~0.5‰ between 4.8 and 4.0 Ma, and by an additional ~0.3‰ between 3.8 and 3 Ma (Figure 2a). The low-resolution *G. tumida* Mg/Ca temperature record at Site 1239 shows a similar pattern; temperatures decrease by ~5°C during the early Pliocene, with a major step between ~4.8 and ~4.0 Ma (Figure 2a). This subsurface cooling and the increasing $\delta^{18}O$ gradient between the mixed layer and the bottom of the photic zone point to a TCD decrease at Site 1239 during the early Pliocene. Between 4.0 and 2.7 Ma, *G. tumida* Mg/Ca temperatures remained relatively stable, except for a pronounced cool interval between 3.3 and 3.0 Ma (Figure 2a).

3.1.2. Biogenic Opal Accumulation Rates

[21] We use biogenic opal accumulation rates calculated from equatorial eastern Pacific Site 1239 shipboard grape density data [*Mix et al.*, 2003] as an estimate for changes in diatom productivity (Figure 2b). Between 5.0 and 3.6 Ma, opal accumulation rates were low (on average ~0.4 g cm^{-2} kyr^{-1}) and the variability was relatively small, except for a short interval with higher opal accumulation rates (up to 0.7 g cm^{-2} kyr^{-1}) around 4.0 Ma. Between 3.6 and 3.5 Ma, opal accumulation rates at Site 1239 doubled rapidly to average values of ~0.8 g cm^{-2} kyr^{-1} (reaching maximum values of 1.05 g cm^{-2} kyr^{-1}), suggesting a distinct increase of diatom productivity at Site 1239 after 3.6–3.5 Ma (Figure 2b).

3.2. Tropical Eastern Pacific Site 1241

[22] We measured a low-resolution $U^{K'}_{37}$ record spanning the time interval from 4.0 to 2.5 Ma in order to get hold of SST changes in the upper 10 m of the water column, the preferred habitat of alkenone-producing coccolithophores. The Site 1241 $U^{K'}_{37}$ temperatures vary between 27.4°C and 28.3°C and show no long term trend (Figure 2c), suggesting that Pliocene SSTs in the uppermost water column were relatively constant in time and only slightly warmer than today (modern SSTs are ~27.0°C at the 4 Ma paleolocation and 27.4°C at the 2 Ma paleolocation of Site 1241).

3.3. Caribbean Sites 999 and 1000

3.3.1. Site 1000 Benthic $\delta^{13}C$ Record (*C. wuellerstorfi*)

[23] The $\delta^{13}C$ record of the epibenthic foraminifer *C. wuellerstorfi* serves as a proxy for changes in deep water ventilation [e.g., *Zahn et al.*, 1986; *McCorkle and Keigwin*, 1994], because the $\delta^{13}C$ of seawater is closely linked to nutrient and oxygen contents, whereas higher $\delta^{13}C$ values indicate lower nutrient contents and better ventilation [*Kroopnick*, 1985]. Caribbean Site 1000 (916 m water depth) provides information about ventilation changes at the Atlantic intermediate water level. Benthic $\delta^{13}C$ at Site 1000 decreased during the earliest Pliocene, reaching the lowest level between ~5.2 Ma and 4.9 Ma (average $\delta^{13}C$ = 0.6 ‰) (Figure 2d). Between ~4.9 and 3.6 Ma, Site 1000 benthic $\delta^{13}C$ increased to average values of ~1.1‰. These high $\delta^{13}C$ persisted until 2.2 Ma. The overall early Pliocene $\delta^{13}C$ trend suggests an increase in intermediate water ventilation (Figure 2d).

3.3.2. *N. dutertrei* $\delta^{18}O$ and Mg/Ca Paleotemperature Records

[24] We use $\delta^{18}O$ and Mg/Ca temperature records measured on the thermocline dweller *N. dutertrei* in order to reconstruct Pliocene Caribbean subsurface temperature changes, because the deep dweller *G. tumida* is absent in the Pliocene sections of sites 999 and 1000. The subsurface temperature development was very similar at both Caribbean sites (Figure 2e). Between 4.8 and 4.3 Ma, average $\delta^{18}O_{N.\ dutertrei}$ decreased by more than 1‰, whereas the *N. dutertrei* Mg/Ca temperature records indicate a synchronous subsurface temperature increase of ~4°C. Between 4.3 and 4.0 Ma, $\delta^{18}O_{N.\ dutertrei}$ increased while *N. dutertrei* Mg/Ca temperatures stayed stable, hinting to an increase in Caribbean subsurface salinity (Figure 2e). After 4.0 Ma, small long-term variations in the $\delta^{18}O$ and Mg/Ca temperature records of *N. dutertrei* indicate no major change in thermocline temperature and/or salinity at Caribbean Site 999.

3.4. Model Results

[25] Introducing a Panama Seaway in experiment CAS results in a mean total volume transport of 14 Sv (1 Sv = 10^6 m^3s^{-1}) from the Pacific into the Atlantic over the entire depth (700 m) of the strait. The inflow of relatively fresh Pacific surface water masses into the Atlantic reduces the salinity contrast between the two oceans and, as a result, the AMOC decreases. This is a robust result which has already been found in previous modeling studies and which is essentially independent of other boundary conditions [cf. *Maier-Reimer et al.*, 1990; *Klocker et al.*, 2005; *Lunt et al.*, 2008]. In our model, convection in the Labrador Sea, and hence UNADW formation, stops. The strength of the AMOC (measured by the net export of NADW to the Southern Ocean) is 15 Sv in the control run and 9 Sv in experiment CAS [cf. *Prange and Schulz*, 2004]. Figure 3a illustrates global changes in the depth of the 20°C isotherm (which is a good indicator for tropical TCD; see above) in response to the closure of the CAS. The pattern indicates an overall decrease in tropical TCD, except for the Caribbean, where the thermocline deepens (Figure 3a). Except for the Caribbean, the global pattern of TCD change between experiments CTL and OFF provides a very similar picture, albeit with a larger magnitude of thermocline shoaling in most areas of the world ocean as compared to experiment CAS (Figure 3b).

4. Discussion

4.1. Changes in Tropical Eastern Pacific Thermocline Depth

[26] We use new and previously published Mg/Ca temperature records and $\delta^{18}O$ values of the shallow-dwelling planktonic foraminifer *G. sacculifer* and of the deep dweller *G. tumida* to assess Pliocene variations in tropical eastern Pacific TCD (Figure 4). ODP Site 1241 is located at ~6°N close to the present-day Intertropical Convergence Zone (ITCZ) at the southern edge of the East Pacific Warm Pool, where upwelling is absent and tropical wind stress convergence is largest (doldrums; Figure 1). It has therefore an ideal position to monitor oceanic adjustments in TCD. Pliocene alkenone-derived SSTs at Site 1241 were high and relatively constant (~28°C; Figure 4a) and temperature fluctuations derived from $Mg/Ca_{G.\ sacculifer}$ were also small (~2°C) [*Groeneveld et al.*, 2006] (Figure 4a). Pliocene

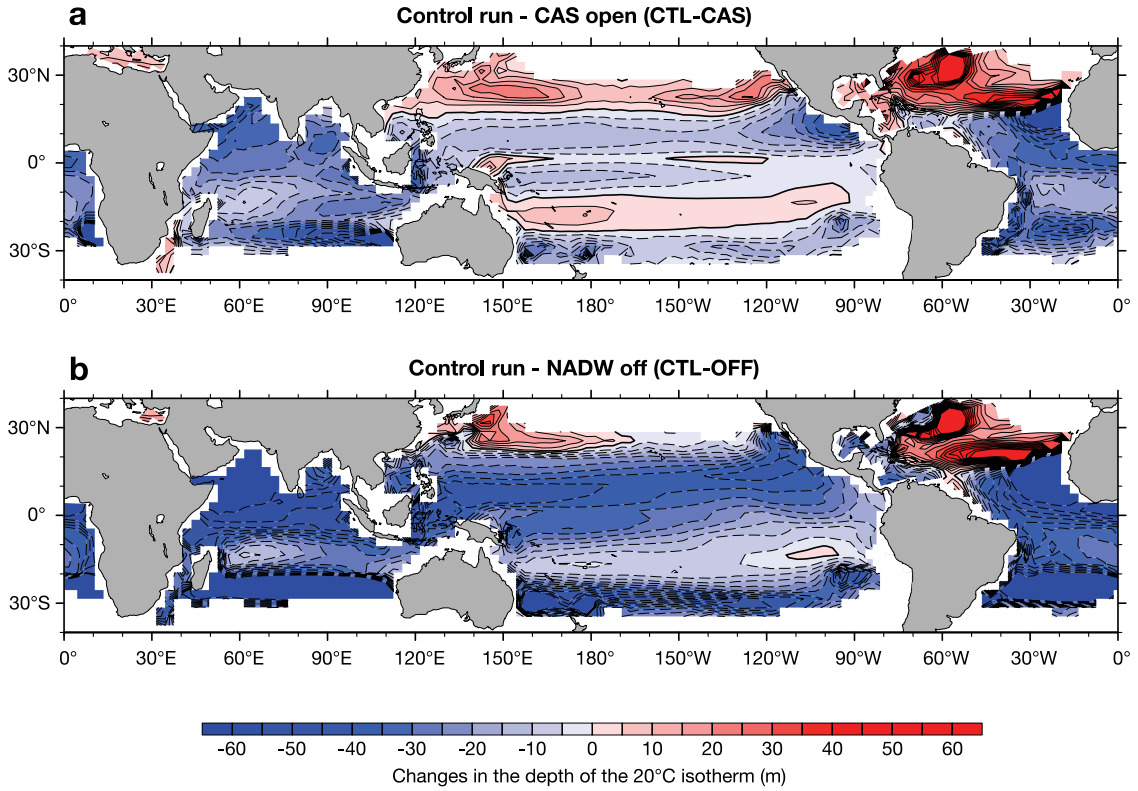

Figure 3. Differences in the depth of the 20°C isotherm (annual mean) between the present-day control run CTL and (a) experiment CAS with open Central American Seaway and (b) experiment OFF with NADW formation shut off completely by a strong anomalous freshwater input to the North Atlantic.

$Mg/Ca_{G.\ sacculifer}$ paleotemperature estimates at Site 1241 are on average ~1°C lower than alkenone-derived temperatures if using the *Dekens et al.* [2002] *G. sacculifer* calibration with Pacific dissolution correction factors for Mg/Ca temperature calculations. This relatively small temperature offset may either be related to differences in seasonality or to the fact that $U^{K'}_{37}$ provides SST's within the uppermost water column (~0–10 m water depth) while $Mg/Ca_{G.\ sacculifer}$ displays mixed layer temperatures (the modern average calcification depth of *G. sacculifer* in the Panama Basin is ~30–50 m [e.g., *Fairbanks et al.*, 1982]). Today, the temperature difference between 0 m and 30 m water depth at the 4–2 Ma paleolocations of Site 1241 amounts to ~1.5°C.

[27] In contrast, large temperature changes occurred at the bottom of the photic zone (Figure 4a). At East Pacific Warm Pool Site 1241, the temperature record of *G. tumida* reveals a long-term decrease of 6°C during the early Pliocene with a major step between ~4.8 and ~4.0 Ma [*Steph et al.*, 2006b]. The corresponding increase in the temperature gradient between the mixed layer and the bottom of the photic zone has been interpreted as a decrease in TCD [*Steph et al.*, 2006b]. The thermocline at Site 1241 remained shallow between ~4.0 and ~3.0 Ma. The subsurface temperature changes monitored by $Mg/Ca_{G.\ tumida}$ at equatorial upwelling Site 1239 off Ecuador (Figures 1 and 4a) are very similar to those observed at Site 1241, and also point to thermocline shoaling during the early Pliocene. Since Pliocene changes in Mg/Ca temperatures and $\delta^{18}O$ recorded by *G. tumida* show approximately the same pattern at sites 1241 and 1239 (Figure 4a), we are confident that $\delta^{18}O_{G.\ tumida}$ predominantly reflects temperature changes at the bottom of the photic zone (although biased by a certain amount of salinity change [*Steph et al.*, 2006b]). The fact that the *G. tumida* $\delta^{18}O$ records from tropical eastern Pacific sites 847 [*Chaisson and Ravelo*, 2000; *Wara et al.*, 2005] and 851 [*Cannariato and Ravelo*, 1997] bear a striking similarity to those from sites 1239 and 1241 suggests that the early Pliocene TCD decrease in the tropical eastern Pacific between 4.8 and 4.0 Ma was a large-scale phenomenon that spread across tropical oceanic fronts (Figures 1 and 4b). The temperature increase at the bottom of the photic zone after ~3.0 Ma observed at doldrum Site 1241 (derived from $Mg/Ca_{G.tumida}$) points to thermocline deepening outside the EEP cold tongue region (Figure 4a), and does hence not support the hypothesis of general thermocline shoaling around 3 Ma in response to global cooling [*Fedorov et al.*, 2006].

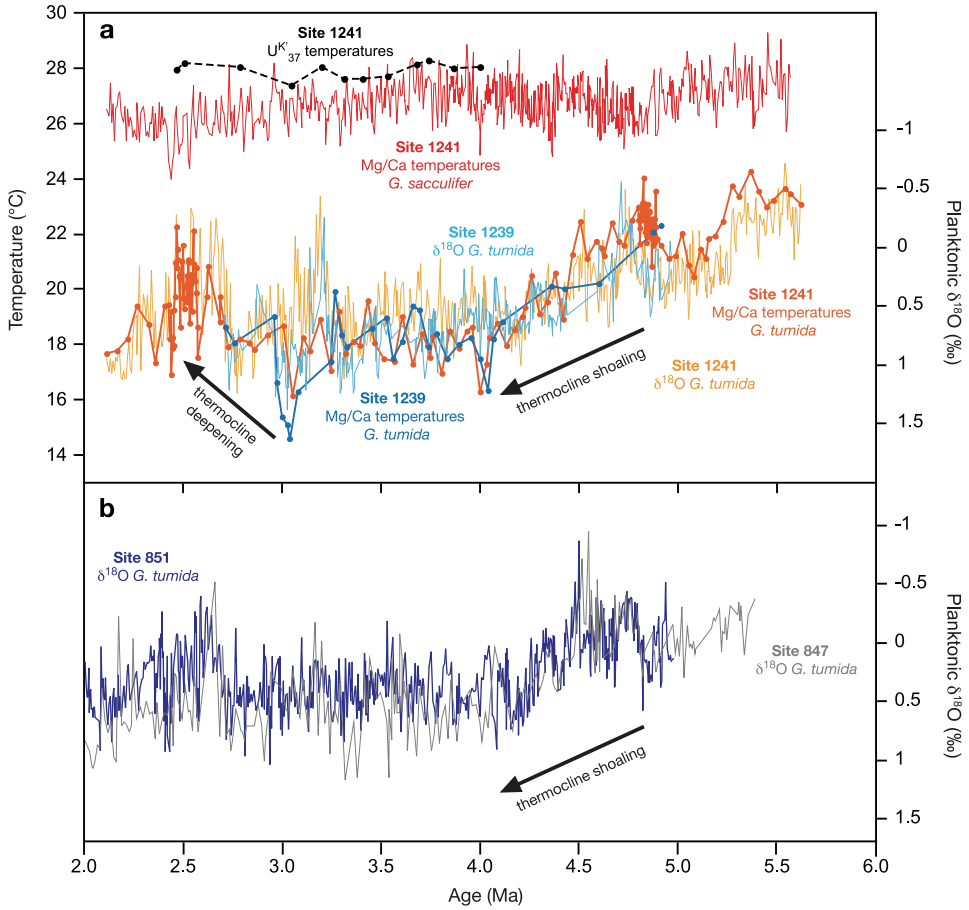

Figure 4. (a) Pliocene changes in tropical eastern Pacific upper ocean stratification. Top lines show $U^{K'}_{37}$ SSTs from East Pacific Warm Pool Site 1241 (this study, black dashed line with dots) and Mg/Ca mixed layer temperatures (*G. sacculifer*) from Site 1241 (red line) [*Groeneveld et al.*, 2006]. Bottom lines show *G. tumida* Mg/Ca temperature records (bottom of the photic zone, ~80–100 m water depth) from sites 1241 (red line with dots) [*Steph et al.*, 2006b] and 1239 (dark blue, EEP cold tongue, this study), as well as *G. tumida* δ^{18}O data from sites 1241 (orange) [*Steph et al.*, 2006b] and 1239 (light blue, this study). (b) Pliocene *G. tumida* δ^{18}O data from tropical eastern Pacific sites 851 (dark blue) [*Cannariato and Ravelo*, 1997] and 847 (gray) [*Wara et al.*, 2005].

4.2. Pliocene Changes in AMOC

[28] The timing of the observed regional TCD changes in the eastern tropical Pacific suggests a close link to changes in AMOC, as indicated by a comparison of benthic δ^{13}C data from tropical western Atlantic Site 925 [*Bickert et al.*, 1997; *Tiedemann and Franz*, 1997; *Shackleton and Hall*, 1997] and from Caribbean Site 1000. Specifically, the shoaling of the thermocline between 4.8 and 4.0 Ma was associated with AMOC strengthening, whereas the observed thermocline deepening at Site 1241 after 3 Ma was associated with a decrease in AMOC (Figure 5).

[29] Caribbean Site 1000, located at 916 m water depth, provides a window into the tropical Atlantic intermediate water level. Tropical Atlantic Site 925, located on the Ceara Rise at 3041 m water depth, is situated within the modern core depth of Lower North Atlantic Deep Water (LNADW) (Figure 1). The comparison of changes in δ^{13}C at sites 925 and 1000 provides information about the relative proportion of northern component (high-δ^{13}C) and southern component (low-δ^{13}C) water and the interplay between Upper North Atlantic Deep Water (UNADW) and LNADW formation (Figure 5). Approximations for Pliocene δ^{13}C end-member values indicative of Southern Ocean intermediate water (Site 1236; southeast Pacific, 1323 m water depth [*Tiedemann et al.*, 2007]) and Southern Ocean deep water (Site 1237; southeast Pacific, 3212 m water depth [*Tiedemann et al.*, 2007]) are provided in Figure 5 (see arrows). Unfortunately, no Pliocene end-member values are available for North

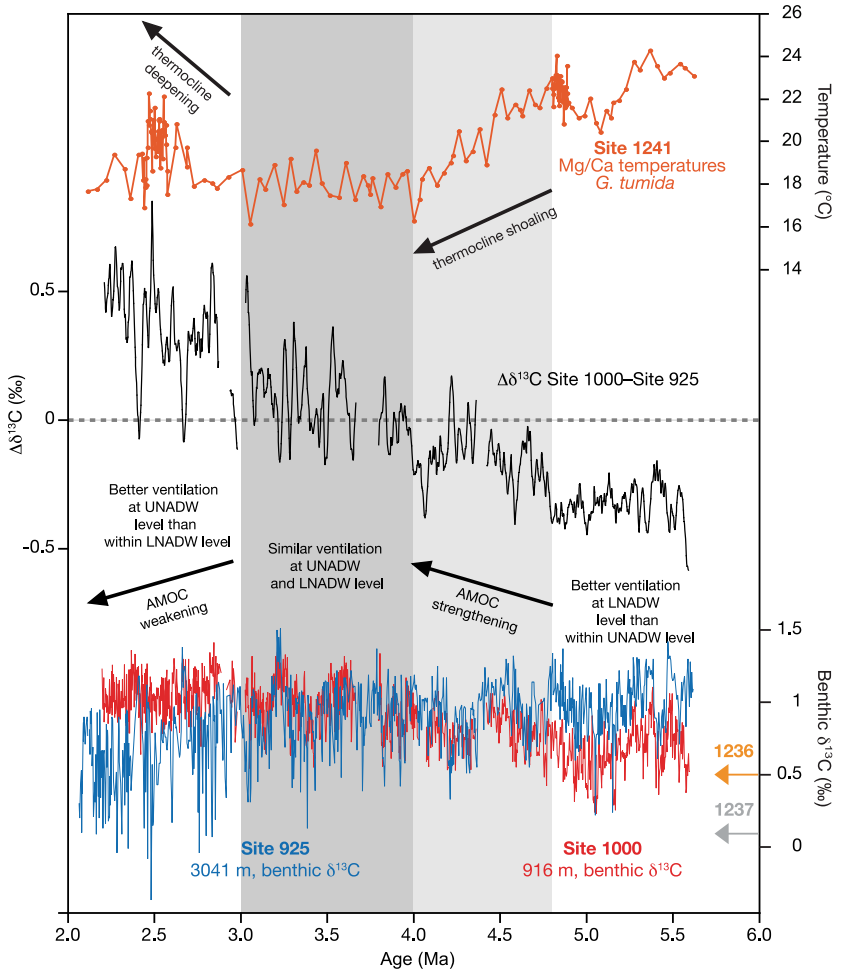

Figure 5. (top) *G. tumida* Mg/Ca temperature record from eastern Pacific Warm Pool Site 1241 (red line with dots) showing Pliocene changes in tropical eastern Pacific thermocline depth. (middle) $\Delta\delta^{13}C$ between Site 1000 (this study) and Site 925 [*Bickert et al.*, 1997; *Tiedemann and Franz*, 1997; *Shackleton and Hall*, 1997]. Before calculating the $\delta^{13}C$ difference between sites, both $\delta^{13}C$ records were evenly sampled at 2 kyr steps and smoothed using a 10-point running mean. This plot serves to clarify the timing of changes in the $\delta^{13}C$ difference between sites 1000 and 925 as mentioned in the text. Prior to 4.8 Ma, values < 0 suggest a large component of southern sourced water masses at the UNADW level (since intermediate water records from Caribbean Site 1000 and southeast Pacific Site 1236 [*Tiedemann et al.*, 2007] have similar $\delta^{13}C$ values) and weak AMOC. The decrease in $\Delta\delta^{13}C$ from ~4.8 Ma to ~4.0 Ma is marked by an increase in northern component water at the UNADW level and indicates AMOC strengthening. $\Delta\delta^{13}C$ values around 0 between 4 Ma and 3 Ma indicate a similar degree of ventilation at the UNADW and LNADW level. As $\delta^{13}C$ values at both sites are high during this interval, this points to enhanced AMOC. $\Delta\delta^{13}C$ values > 0 after ~3 Ma result from decreasing $\delta^{13}C$ values at LNADW Site 925. This indicates a larger component of southern sourced water masses at the LNADW level and reflects AMOC weakening, especially during harsh climate episodes. (bottom) Comparison of benthic $\delta^{13}C$ records from Caribbean Site 1000 (red, this study) and western Atlantic Site 925 (blue) [*Bickert et al.*, 1997; *Tiedemann and Franz*, 1997; *Shackleton and Hall*, 1997]. Arrows approximate average Pliocene $\delta^{13}C$ end-members of southern sourced water masses (orange arrow is for Site 1236, 21°22′S, 81°26′W, 1323 m water depth, Southern Ocean intermediate water [*Tiedemann et al.*, 2007]; gray arrow is for Site 1237, 16°00′S, 76°23′W, 3212 m water depth, Southern Ocean circumpolar deep water [*Tiedemann et al.*, 2007]).

Atlantic intermediate water masses. However, $\delta^{13}C$ values at Site 1000 higher than ~0.5‰ (average Pliocene $\delta^{13}C$ value at Southern Ocean intermediate water Site 1236) can only be explained by admixture of northern sourced (comparatively high $\delta^{13}C$) intermediate water masses. At the core depth of LNADW (Site 925), $\delta^{13}C$ values between 5.5 and 3.0 Ma were always too high to be explained by a significant contribution of southern sourced water masses. This suggests that the $\delta^{13}C$ contrast between northern and southern endmembers was strong and relatively constant during the early to middle Pliocene.

[30] Our findings generally support previous studies, which documented that changes in AMOC were linked to a threshold in the closure history of the CAS during the early Pliocene and to the mid-Pliocene intensification of NHG [e.g., *Keigwin*, 1978; *Oppo et al.*, 1995; *Haug and Tiedemann*, 1998; *Haug et al.*, 2001]. Between 5.5 and 3.2 Ma, average $\delta^{13}C$ values at Site 925 were relatively high (~1 ‰), indicating the continuous presence of well-ventilated LNADW (Figure 5). At Site 1000, however, $\delta^{13}C$-depleted Southern Ocean intermediate water masses dominated before ~4.9–4.8 Ma. After 4.8 Ma, the $\delta^{13}C$ difference between sites 925 and 1000 started to decrease until benthic $\delta^{13}C$ at Site 1000 reached values identical to those at Site 925 by ~4.0 Ma (Figure 5). This points to a first maximum in UNADW production in the Labrador Sea. The long-term $\delta^{13}C$ increase at UNADW Site 1000 was paralleled by thermocline shoaling in the tropical eastern Pacific. The intensification of UNADW formation has been attributed to enhanced salt transfer into the high northern latitudes via the Gulf Stream in response to shoaling of the CAS [e.g., *Keigwin*, 1978; *Haug and Tiedemann*, 1998].

[31] By comparing early Pliocene changes in benthic $\delta^{13}C$ at sites 1000 and 925, we obtain basically the same results as *Haug and Tiedemann* [1998] and *Haug et al.* [2001], who used benthic $\delta^{13}C$ records from Caribbean Site 999 (2828 m water depth), east Atlantic ODP Site 659 (3070 m water depth) and ODP Site 849 (deep Pacific end-member). It was recently questioned, however, whether benthic $\delta^{13}C$ changes at Site 999 (which is located ~1000 m below the Atlantic/Caribbean sill depth) indeed reflect Pliocene changes in Atlantic intermediate water circulation [*Molnar*, 2008]. The significant advantage of our new $\delta^{13}C$ record from Site 1000 (916 m water depth) is that it monitors changes in water mass characteristics well above the Atlantic/Caribbean sill depth (~1900 m), where the exchange between Atlantic and Caribbean intermediate waters was unhampered. Although the long-term trend of $\delta^{13}C$ changes is similar at sites 999 and 1000, absolute $\delta^{13}C$ values at Site 1000 are significantly higher than those from Site 999 [*Haug and Tiedemann*, 1998]. This demonstrates the comparatively stronger influence of UNADW at the shallower Site 1000 (with $\delta^{13}C$ values of up to 1.1 ‰; Figure 5). Such high $\delta^{13}C$ values are not observed in Southern Ocean sourced deep and intermediate water masses [*Tiedemann et al.*, 2007].

[32] High and nearly identical benthic $\delta^{13}C$ values at sites 1000 (UNADW) and 925 (LNADW) persisted between ~4.0 and 3.0 Ma (Figure 5). This corroborates the general consensus of a "superconveyor" with strong UNADW and LNADW formation [e.g., *Raymo et al.*, 1996; *Ravelo and Andreasen*, 2000] and coincides with the establishment and persistence of a shallow thermocline in the tropical east Pacific. Along with the first appearance of larger ice sheets on northern continents, $\delta^{13}C$ values started to decrease at Site 925, but remained high at Site 1000 (Figure 5). During harsh climate episodes, UNADW production stayed high (high $\delta^{13}C$ values at UNADW Site 1000) whereas LNADW formation was reduced [*Oppo et al.*, 1995], allowing poorly ventilated bottom waters from the Southern Ocean to penetrate to shallower water depths and farther to the north (low $\delta^{13}C$ values at LNADW Site 925). This weakening of the AMOC was paralleled by a moderate thermocline deepening in the tropical eastern Pacific (Figure 5).

4.3. Changes in Caribbean Thermocline Depth

[33] In order to assess Pliocene variations in TCD at Caribbean sites 999 and 1000, we compare Mg/Ca temperature and $\delta^{18}O$ data of the thermocline dweller *N. dutertrei* to previously published Mg/Ca temperature data of the mixed layer dweller *G. sacculifer* from Caribbean sites 999 and 1000 [*Groeneveld*, 2005; *Groeneveld et al.*, 2008] (Figure 6). A recent tropical Atlantic/Caribbean core top study indicates that $\delta^{18}O_{N.\ dutertrei} - \delta^{18}O_{G.\ sacculifer}$ can serve as a faithful recorder of TCD in the western Atlantic and Caribbean. Core top $\delta^{18}O_{N.\ dutertrei}$, and hence $\delta^{18}O_{N.\ dutertrei} - \delta^{18}O_{G.\ sacculifer}$, decreases significantly with increasing TCD, although *N. dutertrei* tends to calcify deeper in the water column if the thermocline is deep [*Steph et al.*, 2009].

[34] In this study, we use *G. sacculifer* Mg/Ca temperature records instead of $\delta^{18}O_{G.\ sacculifer}$, because early Pliocene mixed layer $\delta^{18}O$ changes in the Caribbean were predominantly driven by salinity [e.g., *Haug et al.*, 2001; *Steph et al.*, 2006a]. Mixed layer temperatures at both Caribbean sites show only small variations during the early Pliocene (Figure 6), whereas the *Dekens et al.* [2002] dissolution-corrected Mg/Ca temperature estimates suggest ~1.5°C higher temperatures at Site 1000 (on average 26.8°C) than at Site 999 (on average 25.3°C; Figure 6). Without dissolution corrections (using, i.e., the Mg/Ca temperature calibration of *Anand et al.* [2003]), the temperature difference between both sites would amount to ~3°C. Today, temperatures at 40–80 m water depth (estimated modern calcification depth of *G. sacculifer* in the Caribbean [*Steph et al.*, 2006a]) are ~1°C higher at Site 1000 than at Site 999 (NODC, 2001 [*Conkright et al.*, 2002]). Yet it is possible that this temperature difference was slightly enlarged during the early Pliocene, since Site 999 was located closer to the final openings of the CAS than Site 1000 (which was probably less affected by the comparatively cool Pacific inflow as discussed by *Steph et al.* [2006a] (see Figure 1)). Accordingly, mixed layer temperatures at Pacific Site 1241 and at Caribbean Site 999 should have been similar as long as Pacific surface water entered the Caribbean via the CAS (not necessarily at Site 1000, since it was located at a greater distance from the final openings of the gateway [see *Steph et al.*, 2006a]). Indeed, the measured Mg/Ca ratios of *G. sacculifer* are similar at sites 999 and 1241. Using the *Dekens et al.* [2002] Mg/Ca temperature calibration with Pacific dissolution correction factors for Site 1241 and Atlantic dissolution correction factors for Caribbean Site

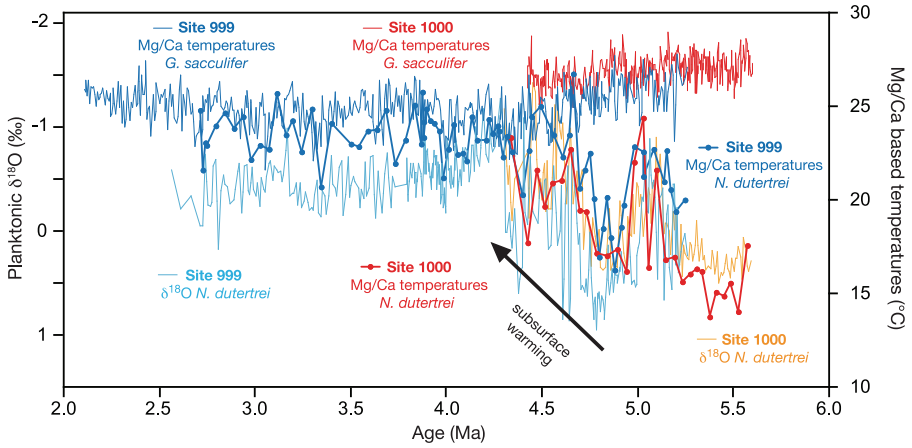

Figure 6. Changes in Caribbean upper ocean water mass signatures at ODP sites 999 and 1000 during the time interval from 5.6 to 2.1 Ma. Mg/Ca-based mixed layer temperature records (*G. sacculifer*) from sites 999 (dark blue line) [*Groeneveld*, 2005] and 1000 (red line) [*Groeneveld et al.*, 2008]. The $\delta^{18}O$ records of the thermocline dweller *N. dutertrei* dextral from sites 999 (light blue line) and 1000 (orange line) and Mg/Ca temperature records of *N. dutertrei* (dextral variety) from sites 999 (thick dark blue line with dots) and 1000 (thick red line with dots).

999, however, the resulting absolute mixed layer temperature estimates are generally higher at Site 1241 than at Site 999, especially between ~4.6 and 2.5 Ma (compare Figures 4a and 6). This may either indicate that early Pliocene carbonate dissolution patterns were different from the modern ones (with relatively stronger carbonate dissolution in the Caribbean and/or enhanced carbonate preservation in the Pacific with respect to today), or that relatively cool water masses (not originating from the East Pacific Warm Pool; Site 1241) entered the Caribbean from the EEP cold tongue region. Yet this would imply that parts of the EEP cold tongue were already significantly cooler than the East Pacific Warm Pool during the early Pliocene (which is not supported by the alkenone SST record from EEP cold tongue Site 846 [*Lawrence et al.*, 2006]).

[35] Since Pliocene mixed layer temperatures at Caribbean sites 999 and 1000 remained relatively constant through time, the observed increase in *N. dutertrei* Mg/Ca temperatures after ~4.8 Ma and the resulting decrease in the temperature gradient between mixed layer (*G. sacculifer*) and the thermocline (*N. dutertrei*), as well as the contemporaneous decrease in $\delta^{18}O_{N.\ dutertrei}$ (Figure 6) point to a deepening/warming of the Caribbean thermocline synchronous with thermocline shoaling in the tropical eastern Pacific [e.g., *Cannariato and Ravelo*, 1997; *Steph et al.*, 2006b, chapter 4.1]. The timing of this event corresponds roughly to the restriction of Pacific-Caribbean surface water exchange after 4.7–4.6 Ma [e.g., *Keigwin*, 1982; *Haug et al.*, 2001; *Steph et al.*, 2006a].

4.4. Numerical Experiments

[36] In the ECBILT-CLIO experiments, the closure of the CAS induces an overall decrease in tropical TCD, except for the Caribbean, where the thermocline deepens (Figure 3a). This is consistent with our Pliocene TCD reconstructions for Caribbean sites 999 and 1000 (Figure 6), and with results from previously published modeling studies [*Schneider and Schmittner*, 2006]. We thus interpret the Caribbean TCD increase after ~4.8 Ma to indicate the development of the modern Caribbean Warm Pool in response to shoaling of the CAS, when the inflow of relatively cold subsurface water from the Pacific into the Caribbean became significantly reduced [e.g., *Keigwin*, 1982; *Haug et al.*, 2001; *Steph et al.*, 2006a; *Groeneveld et al.*, 2008]. Except for the Caribbean, the global pattern of TCD change between experiments CTL and OFF shows a very similar picture in most areas of the world ocean (Figure 3b). This result provides insight into the mechanism of thermocline shoaling: Enhanced NADW formation leads to an increase in the volume of the cold water sphere and, hence, to upward thermocline shifts in the global ocean [*Huang et al.*, 2000; *Timmermann et al.*, 2005]. This finding suggests that the thermocline shoaling in the tropical east Pacific during the early Pliocene was the result of a global oceanic adjustment process in response to AMOC amplification, which, in turn, was induced by substantial shoaling of the CAS. Changes in wind stress owing to AMOC intensification were unlikely to account for the thermocline shoaling in the eastern equatorial Pacific (compared to experiments CAS and OFF an eastward surface wind stress anomaly is found over the entire equatorial Pacific in CTL, which tends to *deepen* the tropical thermocline in the eastern equatorial Pacific; see auxiliary material).[1] However, the simulated trade wind intensification in the southeastern tropical Pacific leads to cooling via increased evaporation and Ekman pumping that may lead to local thermocline shoaling [cf. *Timmermann et*

[1] Auxiliary materials are available in the HTML. doi:101029/2008PA001645.

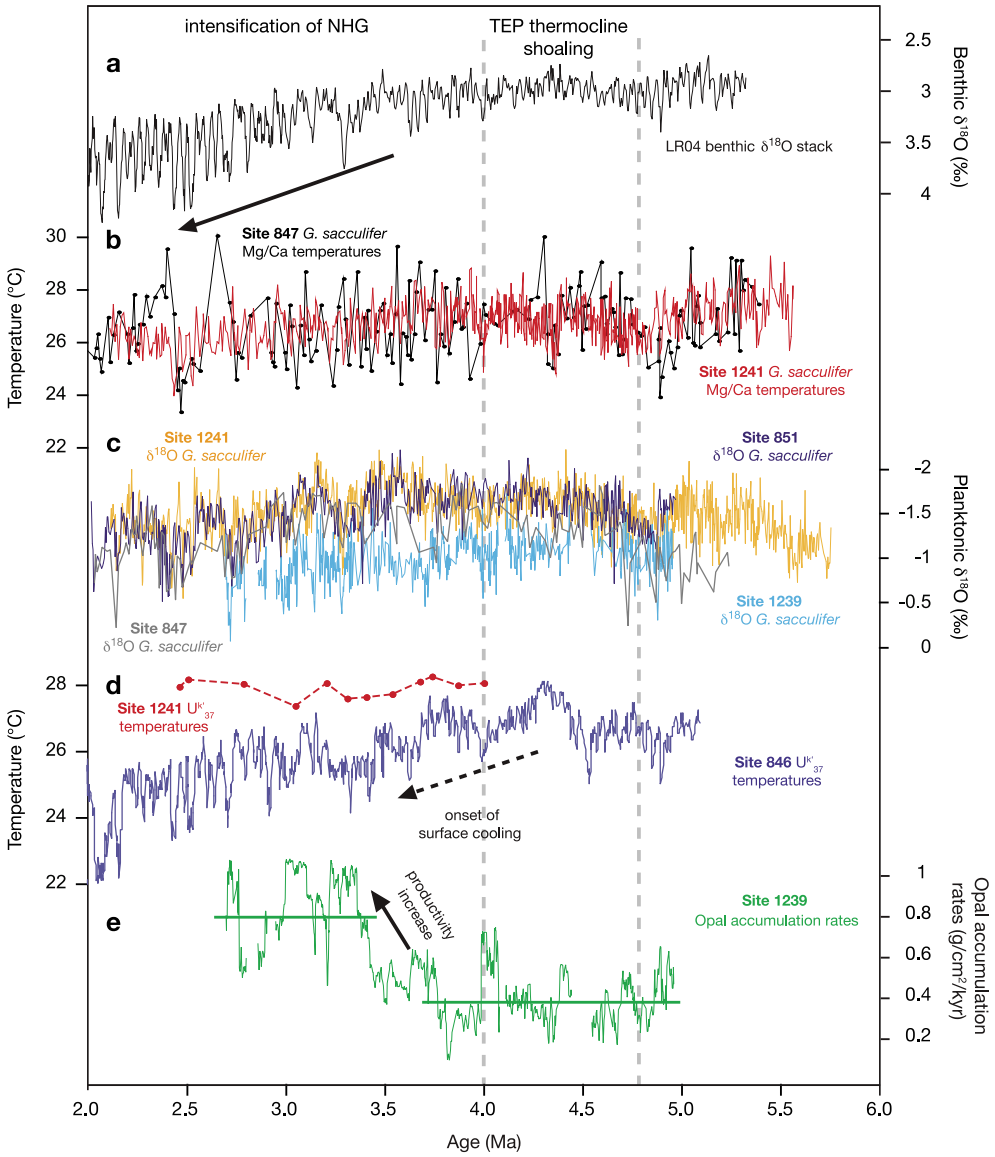

Figure 7. (a) LR04 benthic $\delta^{18}O$ stack [*Lisiecki and Raymo*, 2005] (black), mainly reflecting global changes in ice volume and deep water temperature. (b) Comparison of Pliocene *G. sacculifer* Mg/Ca temperatures from ODP Site 847 (black) [*Wara et al.*, 2005] and ODP Site 1241 (red) [*Groeneveld et al.*, 2006]. (c) Pliocene *G. sacculifer* $\delta^{18}O$ data from tropical eastern Pacific sites 1241 (orange) [*Steph et al.*, 2006b], 851 (dark blue) [*Cannariato and Ravelo*, 1997], 847 (gray) [*Wara et al.*, 2005], and 1239 (light blue, this study). (d) $U^{K'}_{37}$ SSTs from the Pacific doldrum region (Site 1241, red line, this study) and $U^{K'}_{37}$ SSTs from EEP cold tongue Site 846 (blue line) [*Lawrence et al.*, 2006]. (e) Biogenic opal accumulation rates, Site 1239 (green line).

al., 2007b]. The early Pliocene formation of the modern Caribbean Warm Pool more than compensated for the effect of AMOC-induced thermocline shoaling on Caribbean TCD.

4.5. Development of the EEP Cold Tongue

[37] While the temperature evolution at the bottom of the photic zone in the tropical eastern Pacific was synchronous across the equator (Figure 4), a meridionally different de-

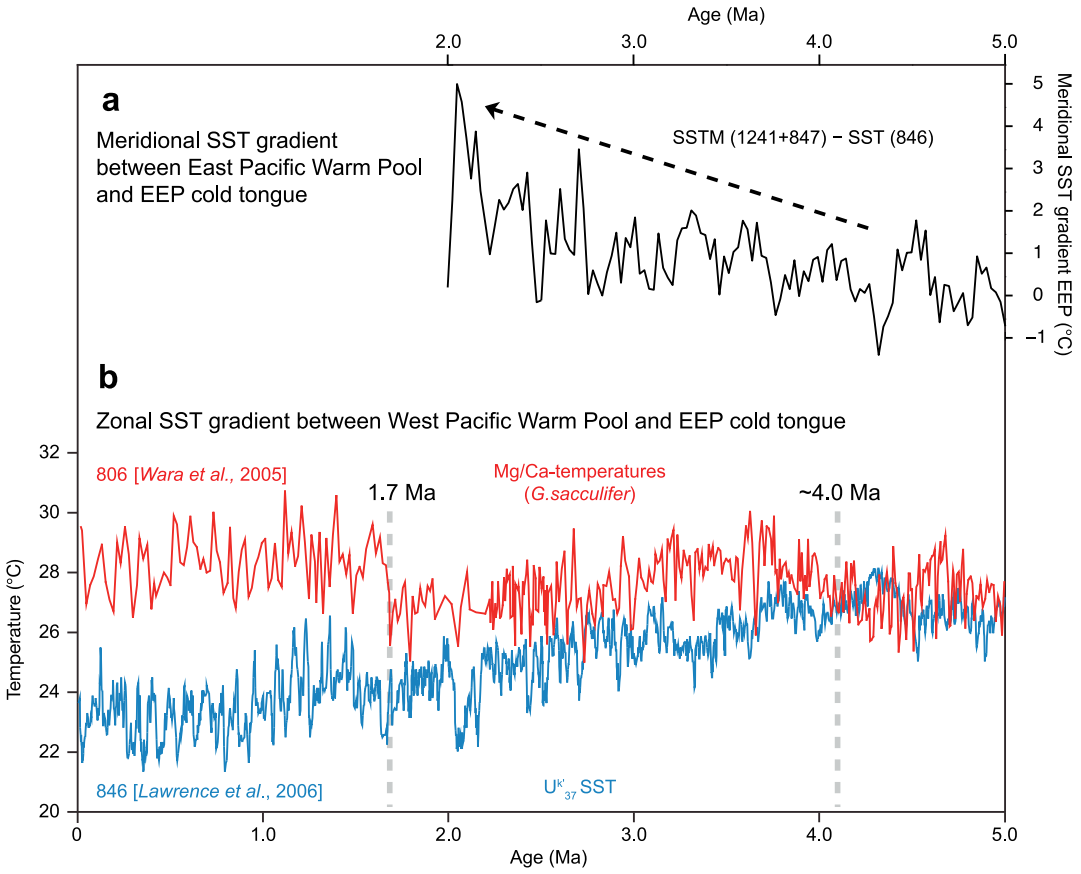

Figure 8. (a) Eastern equatorial Pacific meridional temperature gradient (°C) estimated from the difference between the mean of the Mg/Ca-based SST reconstructions from sites 1241 and 847 (northeastern equatorial Pacific [*Groeneveld et al.*, 2006; *Wara et al.*, 2005]) and the alkenone-based SST from site 846 (southeastern equatorial Pacific [*Lawrence et al.*, 2006]). All SST data were filtered with a three-point running mean, and the resulting time series were interpolated onto an equidistant grid with intervals of 25,000 years using a cubic spline. The strength of the meridional SST gradient determines the position of the ITCZ in the EEP, the strength of the cross-equatorial trade winds, and hence the efficiency of equatorial upwelling [*Timmermann et al.*, 2007a]. (b) The comparison of $U^{K'}_{37}$ temperatures from cold tongue Site 846 (blue) [*Lawrence et al.*, 2006] with $Mg/Ca_{G.\ sacculifer}$ derived temperatures from West Pacific Warm Pool Site 806 (red) [*Wara et al.*, 2005; *Fedorov et al.*, 2006] indicates that the development of the equatorial Pacific east-west SST gradient started as early as ~4.0 Ma, with a second major step occurring at 1.7 Ma as previously suggested by, e.g., *Fedorov et al.* [2006].

velopment of surface hydrography between the doldrums and the EEP cold tongue may reflect regional differences in wind stress. The similar mixed layer temperature evolution (derived from $Mg/Ca_{G.\ sacculifer}$) at doldrum Site 1241 [*Groeneveld et al.*, 2006] and at Site 847 [*Wara et al.*, 2005], today located at the northern edge of the EEP cold tongue, suggests that both sites were located in warm surface water outside the EEP cold tongue region during the early to middle Pliocene (Figures 1 and 7b). Absolute $\delta^{18}O$ *G. sacculifer* values and fluctuations are also similar at sites 1241, 847, and at ODP Site 851 (today located north of the modern EEP cold tongue region) [*Cannariato and Ravelo*, 1997; *Wara et al.*, 2005; *Steph et al.*, 2006b] (Figures 1 and 7c). Yet the pattern of long-term changes in $\delta^{18}O$ records displays larger deviations from their associated Mg/Ca temperature records, especially during the earliest Pliocene (Figure 7). This suggests that the $\delta^{18}O$ *G. sacculifer* signal at these sites is partly modulated by changes in mixed layer salinity.

[38] Within the EEP cold tongue region, the development of a shallow thermocline between ~4.8 and 4.0 Ma should have increased the potential of trade winds to decrease SST by initiating coastal and equatorial upwelling. Indeed, the *G. sacculifer* $\delta^{18}O$ record from equatorial upwelling Site 1239

diverges from the site 1241, 851, and 847 $\delta^{18}O_{G.\ sacculifer}$ records after ~3.9 Ma, and more clearly after ~3.7 Ma, displaying relatively higher $\delta^{18}O$ values (Figure 7c). This indicates a different development of mixed layer hydrography within the EEP cold tongue region, with lower temperatures (and/or higher salinity) compared to the East Pacific Warm Pool. A more faithful recorder of the SST development within the cold tongue is the $U^{K'}_{37}$ SST record from Site 846 [*Lawrence et al.*, 2006] (Figure 7d). Today, this site is located within the center of the EEP cold tongue, where the upwelling of cold waters is driven by Ekman divergence. The Site 846 SST estimates suggest that sea surface cooling within the EEP cold tongue region (~1°C/Ma) started between ~4.3 Ma and 3.6 Ma [*Lawrence et al.*, 2006]. Moderate early sea surface cooling (beginning around 4 Ma) is also observed in the upwelling area off the California margin [e.g., *Dekens et al.*, 2007; *Liu et al.*, 2008; *Brierley et al.*, 2009], but is neither reflected in the low-resolution $U^{K'}_{37}$ SST record nor in the $Mg/Ca_{G.\ sacculifer}$ derived mixed layer temperature record from East Pacific Warm Pool Site 1241 (Figures 7b and 7d). Decreasing SST in the EEP cold tongue region accordingly led to strengthening of the meridional SST gradient between the northeastern (sites 847, 1241) and southeastern (Site 846) equatorial Pacific during the early Pliocene (Figure 8a). This finding is supported by our modeling results, which also indicate that intensification of the AMOC related to CAS closing resulted in lower SST in the southeastern equatorial Pacific, whereas SST in the northeastern equatorial Pacific increased (see Figure S1 in Text S1). The mechanisms involved in establishing this meridional SST gradient have been described in detail by *Zhang and Delworth* [2005], *Timmermann et al.* [2007b] and *Xie et al.* [2008]. They play a key role in establishing the annual cycle of SST on the equator and in modulating ENSO variability.

[39] Comparing the $U^{K'}_{37}$ SST record from EEP cold tongue Site 846 [*Lawrence et al.*, 2006] with the $Mg/Ca_{G.sacculifer}$ temperature record from West Pacific Warm Pool Site 806 [*Wara et al.*, 2005; *Fedorov et al.*, 2006] furthermore suggests the initial development of an equatorial Pacific east-west SST gradient around 4.0 Ma (Figure 8b), consistent with early cooling observed in the EEP cold tongue region [e.g., *Lawrence et al.*, 2006; *Dekens et al.*, 2007]. In contrast, *Fedorov et al.* [2006] concluded that the transequatorial SST gradient was constantly weak during the time interval before ~1.7 Ma by comparing temperature records from Site 806 and tropical northeast Pacific Site 847. Yet the $U^{K'}_{37}$ SST record from EEP cold tongue Site 846 might be better suited for assessing the Pliocene development of the transequatorial temperature gradient than Site 847, because the similarity of mixed layer temperatures at Site 847 and at East Pacific Warm Pool Site 1241 (Figure 7b) indicates that

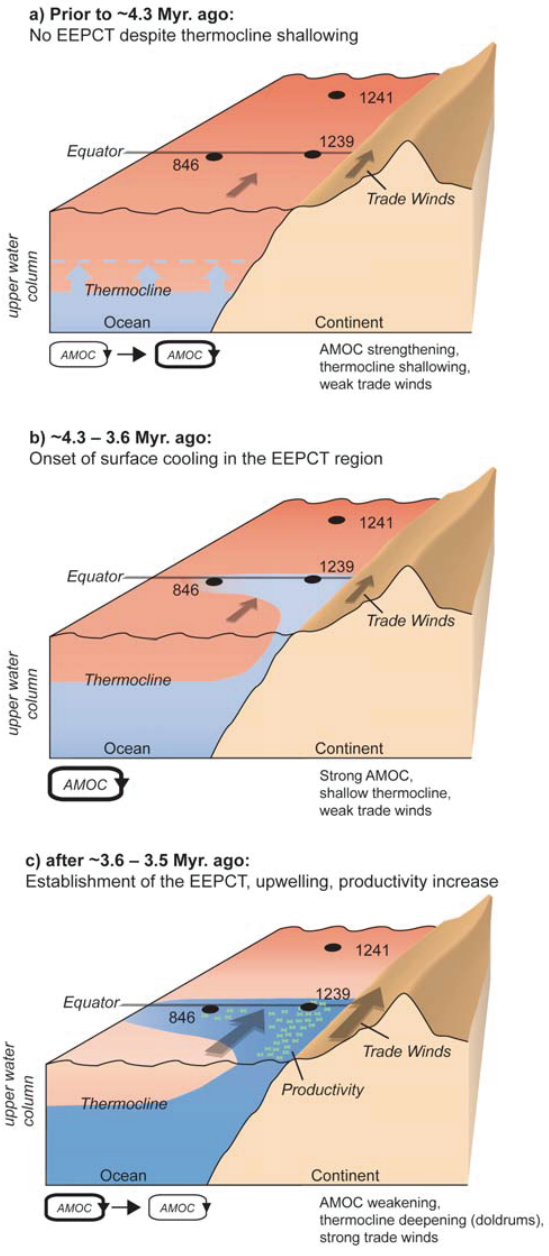

Figure 9. Schematic relationships between AMOC-induced changes in TCD and wind stress with respect to the development of the modern EEP cold tongue (EEPCT). (a) Thermocline shoaling in the tropical eastern Pacific at 4.8–4.0 Ma yielded an important precondition for the turnaround from a warm eastern equatorial Pacific to the modern EEP cold tongue state. (b) Although EEP cold tongue sea surface cooling may have started as early as ~4.3–4.0 Ma ago [*Lawrence et al.*, 2006] southeast trade winds were probably too weak to significantly amplify equatorial and coastal upwelling in a warm world prior to ~3.6 Ma. (c) Since 3.6–3.5 Ma, changes in the tropical wind field might then have tipped the scale for an increase in upwelling and productivity parallel to the intensification of NHG [*Mudelsee and Raymo*, 2005].

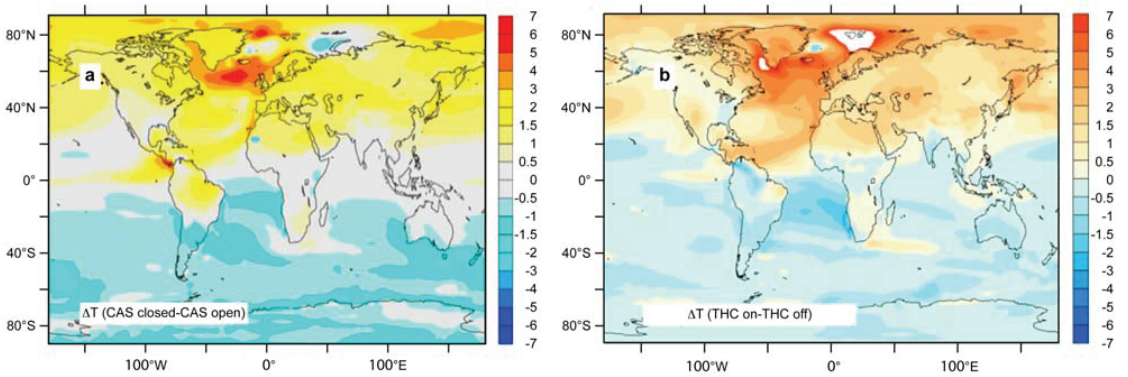

Figure 10. (a) SST response (°C) to closing of the CAS (from *Lunt et al.* [2008] with kind permission of Springer Science and Business Media) as simulated by the HadCM3 coupled model. (b) SST response (°C) to intensification of the AMOC as simulated by the HadCM3 model [*Timmermann et al.*, 2007b; *Dong and Sutton*, 2007].

Site 847 was probably not located in the center of the EEP cold tongue region during the early and middle Pliocene.

[40] Changes in biogenic opal accumulation rates, a proxy for biological productivity, provide additional evidence for enhanced early Pliocene upwelling in the EEP cold tongue, since this region developed as the equatorial center of diatom productivity after ~4.4 Ma [*Farrell et al.*, 1995]. Diatom productivity at EEP cold tongue Site 1239 increased significantly around 3.6–3.5 Ma, when opal accumulation rates doubled (Figure 7e). This change coincides with an increase in the SST gradient between doldrum Site 1241 and EEP cold tongue Site 846 (Figure 7d) and may indicate both, enhanced upwelling or an increase in nutrient concentration, which might be related to a change in advective nutrient supply. We surmise that strengthening of the pole-to-equator temperature gradient in response to the intensification of NHG enhanced trade wind strength [*Timmermann et al.*, 2004] and low-latitude upwelling since 3.6 Ma. If productivity changes are considered as additional evidence for the development of the EEP cold tongue, it occurred at least as early as 3.6–3.5 Ma.

5. Summary and Conclusions

[41] Both the early thermocline shoaling in the tropical eastern Pacific (4.8–4.0 Ma) and the early start of EEP cold tongue cooling (between ~4.3 Ma and 3.6 Ma) [e.g., *Lawrence et al.*, 2006; *Dekens et al.*, 2007] suggest a chain of forcing mechanisms for the development of the modern EEP cold tongue, which is different from the well-cited hypothesis that this Pliocene climate switch was predominantly linked to the major intensification of NHG (after ~3.0 Ma) [e.g., *Wara et al.*, 2005; *Fedorov et al.*, 2006]. Instead, the timing of these events suggests a close link to the gradual closure of the CAS, which reached a critical threshold during the earliest Pliocene, leading to the development of the modern Atlantic-Pacific salinity contrast and to the amplification of AMOC [e.g., *Keigwin*, 1982; *Haug and Tiedemann*, 1998; *Haug et al.*, 2001; *Steph et al.*, 2006a].

[42] Although the impact of the gradual CAS closure on global climate change has recently been questioned [*Molnar*, 2008], our study brings the CAS back into play by providing for the first time a consistent link between the observed decrease in tropical east Pacific TCD and an increase in the strength of the AMOC during the early Pliocene (4.8–4.0 Ma) that was triggered by a threshold in the closure history of the CAS (Figure 9). Our new Caribbean proxy data also suggests that this threshold in the CAS closure led to the formation of the modern Caribbean Warm Pool (starting at ~4.8 Ma), which more than compensated for AMOC-induced shoaling of the Caribbean thermocline. In contrast to previous studies, we identify changes in AMOC as a potential forcing mechanism, which consistently explains the Pliocene long-term evolution of tropical east Pacific TCD as well as the early onset of sea surface cooling in the EEP cold tongue [e.g., *Lawrence et al.*, 2006; *Dekens et al.*, 2007] and the development of a meridional SST gradient in the EEP during the early Pliocene (Figure 9).

[43] Further support for our main conclusions comes from a recent modeling study by *Lunt et al.* [2008]. Using the HadCM3 model, these authors find that closure of the CAS leads to strengthening of the AMOC as well as to warming of the Northern Hemisphere and cooling of the Southern Hemisphere (Figure 10a). This SST response to CAS closure is very similar to the SST response of the HadCM3 model to an intensification of the AMOC [*Timmermann et al.*, 2007b] (Figure 10b) and to the ECBILT-CLIO SST response to CAS closing (see auxiliary material). The enhancement of the EEP cold tongue results from a northward shift of the ITCZ and an associated southeasterly trade wind intensification south of the equator, while the wind-evaporation-SST feedback helps to maintain this feature. Summarizing, independent modeling and paleoproxy evidence suggests that the CAS played a key role in determining the strength of the AMOC, the position of the

ITCZ, the strength of the meridional SST gradient in the EEP and the existence of the EEP cold tongue.

[44] The observed increase in biogenic productivity and upwelling within the EEP cold tongue after 3.6–3.5 Ma likely resulted from enhanced trade wind strength due to strengthening of the pole-to-equator temperature gradient in response to the intensification of NHG (Figure 9). Yet the thermocline deepening at doldrum Site 1241 after 3.0 Ma was presumably linked to AMOC weakening in response to the intensification of NHG. This contradicts the hypothesis that cooling of the deep ocean after 3.0 Ma led to a global decrease in tropical TCD.

[45] A recent analysis of IPCC model results examining the next 100 years indicates a thermodynamically driven weakening of the Walker circulation in response to global warming, possibly favoring El Niño–like climate conditions [*Vecchi and Soden*, 2007]. Our results further suggest changes in AMOC as an important factor for the assessment of future changes in tropical climate dynamics. If global warming led to a reduction in both AMOC strength and trade wind intensity, the consequent increase in TCD would support the disappearance of the EEP cold tongue. Whether this mechanism may be adopted to assess future changes in ENSO variability remains to be shown.

[46] **Acknowledgments.** We thank A. Schmittner, F. Lamy, L. Reuning, and A. Sturm for discussions and criticism and D. Garbe-Schönberg, L. Haxhiaj, S. Koch, U. Nielsen, and A. Jesußek for technical assistance. We also thank the Associate Editor (David Lea) and three anonymous reviewers for their helpful comments. This research used samples and data provided by the Ocean Drilling Program, which is sponsored by the U.S. National Science Foundation and participating countries under management of Joint Oceanographic Institutions. Funding for this research was provided by the Deutsche Forschungsgemeinschaft (DFG) through projects Ti 240/7, Ti 240/12 (being part of the DFG Research Unit, FOR 451: Impact of Gateways on Ocean Circulation, Climate, and Evolution at Kiel University), and Ti 240/17 and through the DFG Research Center/Excellence Cluster "The Ocean in the Earth System" at the University of Bremen. A. Timmermann is supported by the Japan Agency for Marine-Earth Science and Technology through its sponsorship of the International Pacific Research Center.

References

Anand, P., H. Elderfield, and M. H. Conte (2003), Calibration of Mg/Ca thermometry in planktonic foraminifera from a sediment trap time series, *Paleoceanography*, *18*(2), 1050, doi:10.1029/2002PA000846.

Barker, S., M. Greaves, and H. Elderfield (2003), A study of cleaning procedures used for foraminiferal Mg/Ca paleothermometry, *Geochem. Geophys. Geosyst.*, *4*(9), 8407, doi:10.1029/2003GC000559.

Bickert, T., W. B. Curry, and G. Wefer (1997), Late Pliocene to Holocene (2.6–0 Ma) western equatorial Atlantic deep-water circulation: Inferences from benthic stable isotopes, *Proc. Ocean Drill. Program Sci. Results*, *154*, 239–254.

Brierley, C. M., A. V. Fedorov, Z. Liu, T. D. Herbert, K. T. Lawrence, and J. P. LaRiviere (2009), Greatly expanded tropical warm pool and weakened Hadley Circulation in the early Pliocene, *Science*, *323*, 1714–1718, doi:10.1126/science.1167625.

Cannariato, K. G., and A. C. Ravelo (1997), Pliocene-Pleistocene evolution of eastern tropical Pacific surface water circulation and thermocline depth, *Paleoceanography*, *12*, 805–820, doi:10.1029/97PA02514.

Chaisson, W. P., and A. C. Ravelo (2000), Pliocene development of the east-west hydrographic gradient in the equatorial Pacific, *Paleoceanography*, *15*, 497–505, doi:10.1029/1999PA000442.

Conkright, M. E., R. A. Locarnini, H. E. Garcia, T. D. O'Brien, T. P. Boyer, C. Stephens, and J. I. Antonov (2002), World Ocean Atlas 2001: Objective analyses, data statistics, and figures—CD-ROM documentation, *Internal Rep. 17*, 17 pp., Nat. Oceanogr. Data Cent., Silver Spring, Md.

Conte, M. H., M.-A. Sicre, C. Rühlemann, J. C. Weber, S. Schulte, D. Schulz-Bull, and T. Blanz (2006), Global temperature calibration of the alkenone unsaturation index ($U^{K'}_{37}$) in surface waters and comparison with surface sediments, *Geochem. Geophys. Geosyst.*, *7*, Q02005, doi:10.1029/2005GC001054.

Dekens, P. S., D. W. Lea, D. K. Pak, and H. J. Spero (2002), Core top calibration of Mg/Ca in tropical foraminifera: Refining paleotemperature estimation, *Geochem. Geophys. Geosyst.*, *3*(4), 1022, doi:10.1029/2001GC000200.

Dekens, P. S., A. C. Ravelo, and M. D. McCarthy (2007), Warm upwelling regions in the Pliocene warm period, *Paleoceanography*, *22*, PA3211, doi:10.1029/2006PA001394.

Dong, B., and R. Sutton (2007), Enhancement of ENSO variability by a weakened Atlantic thermohaline circulation in a coupled GCM, *J. Clim.*, *20*, 4920–4939, doi:10.1175/JCLI4284.1.

Dowsett, H. J., J. Barron, R. Z. Poore, R. S. Thompson, T. M. Cronin, S. E. Ishman, and D. A. Willard (1999), Middle Pliocene paleoenvironmental reconstruction: PRISM2, *U.S. Geol. Surv. Open File Rep.*, *99-535*, 13 pp.

DeMaster, D. J. (1981), Measuring biogenic silica in marine sediments and suspended matter, in *Marine Particles: Analysis and Characterization*, *Geophys. Monogr. Ser.*, vol. 63, edited by D. C. Hurd and D. W. Spenser, pp. 363–368, AGU, Washington, D. C.

Fairbanks, R. G., M. Sverdlove, R. Free, P. H. Wiebe, and A. W. H. Bé (1982), Vertical distribution and isotopic fractionation of living planktonic foraminifera from the Panama Basin, *Nature*, *298*, 841–844.

Farrell, J. W., I. Raffi, T. R. Janecek, D. W. Murray, M. Levitan, K. A. Dadey, K. C. Emeis, M. Lyle, J. A. Flores, and S. Hovan (1995), Late Neogene sedimentation patterns in the eastern equatorial Pacific Ocean, *Proc. Ocean Drill. Program Sci. Results*, *138*, 717–756.

Fedorov, A. V., P. S. Dekens, M. McCarthy, A. C. Ravelo, P. B. deMenocal, M. Barreiro, R. C. Pacanowski, and S. G. Philander (2006), The Pliocene paradox (mechanisms for a permanent El Niño), *Science*, *312*, 1485–1489, doi:10.1126/science.1122666.

Foster, G. L., O. Seki, R. D. Pancost, and D. N. Schmidt (2009), pCO_2 and climate: Evidence from boron based proxies of pH and pCO_2, *Geochim. Cosmochim. Acta*, *73*(13), suppl. 1, A391.

Goosse, H., and T. Fichefet (1999), Importance of ice-ocean interactions for the global ocean circulation: A model study, *J. Geophys. Res.*, *104*, 23,337–23,355, doi:10.1029/1999JC900215.

Groeneveld, J. (2005), Effect of the Pliocene closure of the Panamanian Gateway on Caribbean and East Pacific sea surface temperatures and salinities by applying combined Mg/Ca and ^{18}O measurements (5.6–2.2 Ma), Ph.D. thesis, 161 pp., Univ. of Kiel, Kiel, Germany.

Groeneveld, J., S. Steph, R. Tiedemann, D. Garbe-Schönberg, D. Nürnberg, and A. Sturm (2006), Pliocene mixed-layer oceanography for site 1241, using combined Mg/Ca and $\delta^{18}O$ analyses of *Globigerinoides sacculifer*, *Proc. Ocean Drill. Program Sci. Results*, *202*, 1–27, doi:10.2973/odp.proc.sr.202.209.

Groeneveld, J., D. Nürnberg, R. Tiedemann, G.-J. Reichart, S. Steph, L. Reuning, D. Crudeli, and P. Mason (2008), Foraminiferal Mg/Ca increase in the Caribbean during the Pliocene: Western Atlantic Warm Pool formation, salinity influence, or diagenetic overprint?, *Geochem. Geophys. Geosyst.*, *9*(1), Q01P23, doi:10.1029/2006GC001564.

Haug, G. H., and R. Tiedemann (1998), Effect of the formation of the Isthmus of Panama on Atlantic Ocean thermohaline circulation, *Nature*, *393*, 673–676, doi:10.1038/31447.

Haug, G. H., R. Tiedemann, R. Zahn, and A. C. Ravelo (2001), Role of Panama uplift on oceanic freshwater balance, *Geology*, *29*, 207–210, doi:10.1130/0091-7613(2001)029<0207:ROPUOO>2.0.CO;2.

Huang, R. X., M. A. Cane, N. Naik, and P. Goodman (2000), Global adjustment of the thermocline in response to deepwater formation, *Geophys. Res. Lett.*, *27*, 759–762, doi:10.1029/1999GL002365.

Jansen, E., et al. (2007), Palaeoclimate, in *Climate Change 2007: The Physical Science Basis: Working Group I Contribution to the Fourth Assessment Report of the Intergovernmental Panel on Climate Change*, edited by S. Solomon et al., pp. 433–497, Cambridge Univ. Press, New York.

Keigwin, L. D. (1978), Pliocene closing of the Isthmus of Panama, based on biostratigraphic

evidence from nearby Pacific Ocean and Caribbean Sea cores, *Geology*, *6*, 630–634, doi:10.1130/0091-7613(1978)6<630:PCOTIO>2.0.CO;2.

Keigwin, L. D. (1982), Isotopic paleoceanography of the Caribbean and East Pacific: Role of Panama uplift in late Neogene time, *Science*, *217*, 350–352, doi:10.1126/science.217.4557.350.

Klocker, A., M. Prange, and M. Schulz (2005), Testing the influence of the Central American Seaway on orbitally forced Northern Hemisphere glaciation, *Geophys. Res. Lett.*, *32*, L03703, doi:10.1029/2004GL021564.

Kroopnick, P. M. (1985), The distribution of ^{13}C in the world oceans, *Deep Sea Res., Part A*, *32*, 57–84, doi:10.1016/0198-0149(85)90017-2.

Lawrence, K. T., Z. Liu, and T. D. Herbert (2006), Evolution of the eastern tropical Pacific through Plio-Pleistocene glaciation, *Science*, *312*, 79–83, doi:10.1126/science.1120395.

Lisiecki, L. E., and M. E. Raymo (2005), A Pliocene-Pleistocene stack of 57 globally distributed benthic $\delta^{18}O$ records, *Paleoceanography*, *20*, PA1003, doi:10.1029/2004PA001071.

Liu, Z., M. A. Altabet, and T. D. Herbert (2008), Plio-Pleistocene denitrification in the eastern tropical North Pacific: Intensification at 2.1 Ma, *Geochem. Geophys. Geosyst.*, *9*, Q11006, doi:10.1029/2008GC002044.

Lunt, D. J., P. J. Valdes, A. Haywood, and I. C. Rutt (2008), Closure of the Panama Seaway during the Pliocene: Implications for climate and Northern Hemisphere glaciation, *Clim. Dyn.*, *30*, 1–18, doi:10.1007/s00382-007-0265-6.

Maier-Reimer, E., U. Mikolajewicz, and T. Crowley (1990), Ocean general circulation model sensitivity experiments with an open Central American Isthmus, *Paleoceanography*, *5*, 349–360, doi:10.1029/PA005i003p00349.

Marlow, J. R., C. B. Lange, G. Wefer, and A. Rosell-Melé (2000), Upwelling intensification as part of the Pliocene-Pleistocene climate transition, *Science*, *290*, 2288–2291.

McCorkle, D. C., and L. D. Keigwin (1994), Depth profiles of $\delta^{13}C$ in bottom water and core top *C. wuellerstorfi* on the Ontong Java Plateau and Emperor seamounts, *Paleoceanography*, *9*, 197–208, doi:10.1029/93PA03271.

Mix, A. C., et al. (2003), *Proceedings of the Ocean Drilling Program: Initial Reports*, vol. 202, Ocean Drill. Program, College Station, Tex.

Molnar, P. (2008), Closing of the Central American Seaway and the Ice Age: A critical review, *Paleoceanography*, *23*, PA2201, doi:10.1029/2007PA001574.

Molnar, P., and M. A. Cane (2002), El Niño's tropical climate and teleconnections as a blueprint for pre–Ice Age climates, *Paleoceanography*, *17*(2), 1021, doi:10.1029/2001PA000663.

Mudelsee, M., and M. E. Raymo (2005), Slow dynamics of the Northern Hemisphere glaciation, *Paleoceanography*, *20*, PA4022, doi:10.1029/2005PA001153.

Müller, P. J., and R. Schneider (1993), An automated leaching method for the determination of opal in sediments and particulate matter, *Deep Sea Res., Part I*, *40*, 425–444, doi:10.1016/0967-0637(93)90140-X.

Oppo, D. W., M. E. Raymo, G. P. Lohmann, A. C. Mix, J. D. Wright, and W. L. Prell (1995), A $\delta^{13}C$ record of upper North Atlantic deep water during the past 2.6 million years, *Paleoceanography*, *10*, 373–394, doi:10.1029/95PA00332.

Opsteegh, J. D., R. J. Haarsma, F. M. Selten, and A. Kattenberg (1998), ECBILT: A dynamic alternative to mixed boundary conditions in ocean models, *Tellus, Ser. A*, *50*, 348–367.

Prange, M., and M. Schulz (2004), A coastal upwelling seesaw in the Atlantic Ocean as a result of the closure of the Central American Seaway, *Geophys. Res. Lett.*, *31*, L17207, doi:10.1029/2004GL020073.

Ravelo, A. C., and D. H. Andreasen (1999), Using planktonic foraminifera as monitors of the tropical surface ocean, in *Reconstructing Ocean History—A Window Into the Future*, edited by F. Abrantes and A. Mix, pp. 217–244, Plenum, New York.

Ravelo, A. C., and D. H. Andreasen (2000), Enhanced circulation during a warm period, *Geophys. Res. Lett.*, *27*, 1001–1004, doi:10.1029/1999GL007000.

Ravelo, A. C., and R. G. Fairbanks (1992), Oxygen isotopic composition of multiple species of planktonic foraminifera: Recorders of the modern photic zone temperature gradient, *Paleoceanography*, *7*, 815–832, doi:10.1029/92PA02092.

Ravelo, A. C., D. H. Andreasen, M. Lyle, A. O. Lyle, and M. W. Wara (2004), Regional climate shifts caused by gradual global cooling in the Pliocene epoch, *Nature*, *429*, 263–267, doi:10.1038/nature02567.

Raymo, M. E., B. Grant, M. Horowitz, and G. H. Rau (1996), Mid-Pliocene warmth: Stronger greenhouse and stronger conveyor, *Mar. Micropaleontol.*, *27*, 313–326, doi:10.1016/0377-8398(95)00048-8.

Schneider, B., and A. Schmittner (2006), Simulating the impact of the Panamanian Seaway closure on ocean circulation, marine productivity and nutrient cycling, *Earth Planet. Sci. Lett.*, *246*, 367–380, doi:10.1016/j.epsl.2006.04.028.

Shackleton, N. J., and M. A. Hall (1997), The late Miocene stable isotope record: Site 926, *Proc. Ocean Drill. Program Sci. Results*, *154*, 367–373.

Sigurdsson, H., et al. (1997), *Proceedings of the Ocean Drilling Program: Initial Reports*, vol. 165, Ocean Drill. Program, College Station, Tex.

Steph, S., R. Tiedemann, M. Prange, J. Groeneveld, D. Nürnberg, L. Reuning, M. Schulz, and G. H. Haug (2006a), Changes in Caribbean surface hydrography during the Pliocene shoaling of the Central American Seaway, *Paleoceanography*, *21*, PA4221, doi:10.1029/2004PA001092.

Steph, S., R. Tiedemann, J. Groeneveld, A. Sturm, and D. Nürnberg (2006b), Pliocene changes in tropical East Pacific upper ocean stratification: Response to tropical gateways?, *Proc. Ocean Drill. Program Sci. Results*, *202*, 1–51, doi:10.2973/odp.proc.sr.202.211.2006.

Steph, S., M. Regenberg, R. Tiedemann, S. Mulitza, and D. Nürnberg (2009), Stable isotopes of planktonic foraminifera from tropical Atlantic/Caribbean core-tops: Implications for reconstructing upper ocean stratification, *Mar. Micropaleontol.*, *71*, 1–19, doi:10.1016/j.marmicro.2008.12.004.

Tiedemann, R., and S. O. Franz (1997), Deepwater circulation, chemistry, and terrigenous sediment supply in the equatorial Atlantic during the Pliocene, 3.3–2.6 Ma and 5–4.5 Ma, *Proc. Ocean Drill. Program Sci. Results*, *154*, 299–318.

Tiedemann, R., A. Sturm, S. Steph, S. P. Lund, and J. S. Stoner (2007), Astronomically calibrated time scales from 6–2.5 Ma and benthic isotope stratigraphies of sites 1236, 1237, 1239 and 1241, *Proc. Ocean Drill. Program Sci. Results*, *202*, 1–69, doi:10.2973/odp.proc.sr.202.210.2007.

Timmermann, A., F. B. Justino, F.-F. Jin, and H. Goosse (2004), Surface temperature control in the North and tropical Pacific during the Last Glacial Maximum, *Clim. Dyn.*, *23*, 353–370, doi:10.1007/s00382-004-0434-9.

Timmermann, A., S.-I. An, U. Krebs, and H. Goosse (2005), ENSO suppression due to weakening of the North Atlantic thermohaline circulation, *J. Clim.*, *18*, 3122–3139, doi:10.1175/JCLI3495.1.

Timmermann, A., S. J. Lorenz, S.-I. An, A. Clement, and S.-P. Xie (2007a), The effect of orbital forcing on the mean climate and variability of the tropical Pacific, *J. Clim.*, *20*, 4147–4159, doi:10.1175/JCLI4240.1.

Timmermann, A., et al. (2007b), The influence of a weakening of the Atlantic meridional overturning circulation on ENSO, *J. Clim.*, *20*, 4899–4919, doi:10.1175/JCLI4283.1.

Vecchi, G. A., and B. J. Soden (2007), Global warming and the weakening of the tropical circulation, *J. Clim.*, *20*, 4316–4340, doi:10.1175/JCLI4258.1.

Wara, M. W., A. C. Ravelo, and M. L. Delaney (2005), Permanent El Niño–like conditions during the Pliocene warm period, *Science*, *309*, 758–761, doi:10.1126/science.1112596.

Xie, S.-P., Y. Okumura, T. Miyama, and A. Timmermann (2008), Influences of Atlantic climate change on the tropical Pacific via the Central American Isthmus, *J. Clim.*, *21*, 3914–3928, doi:10.1175/2008JCLI2231.1.

Zahn, R., K. Winn, and M. Sarnthein (1986), Benthic foraminiferal $\delta^{13}C$ and accumulation rates of organic carbon: *Uvigerina peregrina* group and *Cibicidoides wuellerstorfi*, *Paleoceanography*, *1*, 27–42, doi:10.1029/PA001i001p00027.

Zhang, R., and T. Delworth (2005), Simulated tropical response to a substantial weakening of the Atlantic thermohaline circulation, *J. Clim.*, *18*, 1853–1860, doi:10.1175/JCLI3460.1.

J. Groeneveld, M. Prange, and M. Schulz, Department of Geosciences, University of Bremen, D-28359 Bremen, Germany.

G. H. Haug, Geological Institute, Department of Earth Sciences, ETH Zurich, CH-8092 Zürich, Switzerland.

D. Nürnberg, Leibniz Institute of Marine Sciences at University of Kiel (IFM-GEOMAR), D-24148 Kiel, Germany.

C. Rühlemann, Bundesanstalt für Geowissenschaften und Rohstoffe, D-30655 Hannover, Germany.

C. Saukel and R. Tiedemann, Alfred Wegener Institute for Polar and Marine Research, D-27568 Bremerhaven, Germany.

S. Steph, DFG–Leibniz Center for Surface Process and Climate Studies, Institute for Geosciences, Potsdam University, D-14476 Potsdam, Germany. (ssteph@whoi.edu)

A. Timmermann, IPRC, SOEST, University of Hawai'i at Mānoa, Honolulu, HI 96822, USA.

5 Changes in Dust Supply on Tectonic and Orbital Timescales during the Past 5 Ma - A Synthesis

Following the paradigm of taking 'the present as a key to the past, and the past as a key to the future' (Mathieson, 2002), this study was designed to reconstruct the atmospheric changes in the tropical Southeast (SE) Pacific over the past 5 Ma, focussing on continent-ocean-atmosphere linkages. Even though dust transport out of the Atacama Desert and the coastal deserts of Peru into the adjacent ocean is considerably less than in other prominent dust study areas offshore the major deserts of the Earth, such as the Sahara and Namib (West Africa), the Rub' al-Khali (Arabian Peninsula), the Loess plateaus and the Gobi (China), or the Lake Eyre Basin (Australia), dust contributes substantially to the comparably slow pelagic sedimentation in the SE Pacific of ∼1-3 cm ka^{-1} (Mix et al., 2003). Although a complex sedimentary environment made the retrieval of the most recent eolian signal a challenging task, analyzing grain-size distributions and clay-mineral compositions of surface sediments has identified the modern pattern of dust input (chapter 4.1). A dust lobe extending offshore Peru and northern Chile south of 5°S represents the modern pattern of dust deposition that is transported within the main field of the SE trade winds (chapter 4.1; Figs. 13 and 19).
Ocean Drilling Program (ODP) Site 1237 is located well within the extension of the dust lobe, about 140 km offshore the Peruvian coast and several hundreds of kilometers from the core region of the Atacama Desert in northern Chile (Fig. 5). Its position west of the Peru-Chile Trench on a topographic rise makes ODP Site 1237 a suitable site to study the history of changes in SE trade wind strength over time. Dust grain-size modes around 6 μm and means of 4 - 8 μm characterize recent sample material from the southeastern flank of Nazca Ridge, where ODP Site 1237 was drilled.

In total, a record of 5 Million years has been investigated (Fig. 35). It covers the Pliocene warm period (∼5.5 to ∼3 Ma) and the subsequent global cooling related to the Northern Hemisphere Glaciation (starting between ∼3.5 and 3 Ma), as well as the Mid-Pleistocene Climate Transition (c. 1.2 - 0.5 Ma), when the glacial/interglacial variability changed from a dominant periodicity of 41 ka to 100 ka, and amplitudes became more pronounced. Since the Pliocene warm period, mean global surface temperatures cooled by approximately 3°C (Dowsett et al., 1999; Robinson et al., 2008), Antarctic ice sheets grew larger, Northern Hemisphere ice sheets developed, and desert areas expanded (Dowsett et al., 1999). Atmospheric temperature gradients increased due to a more severe cooling of the high latitudes compared to the low latitudes (e.g., Timmermann et al., 2004). While the Earth

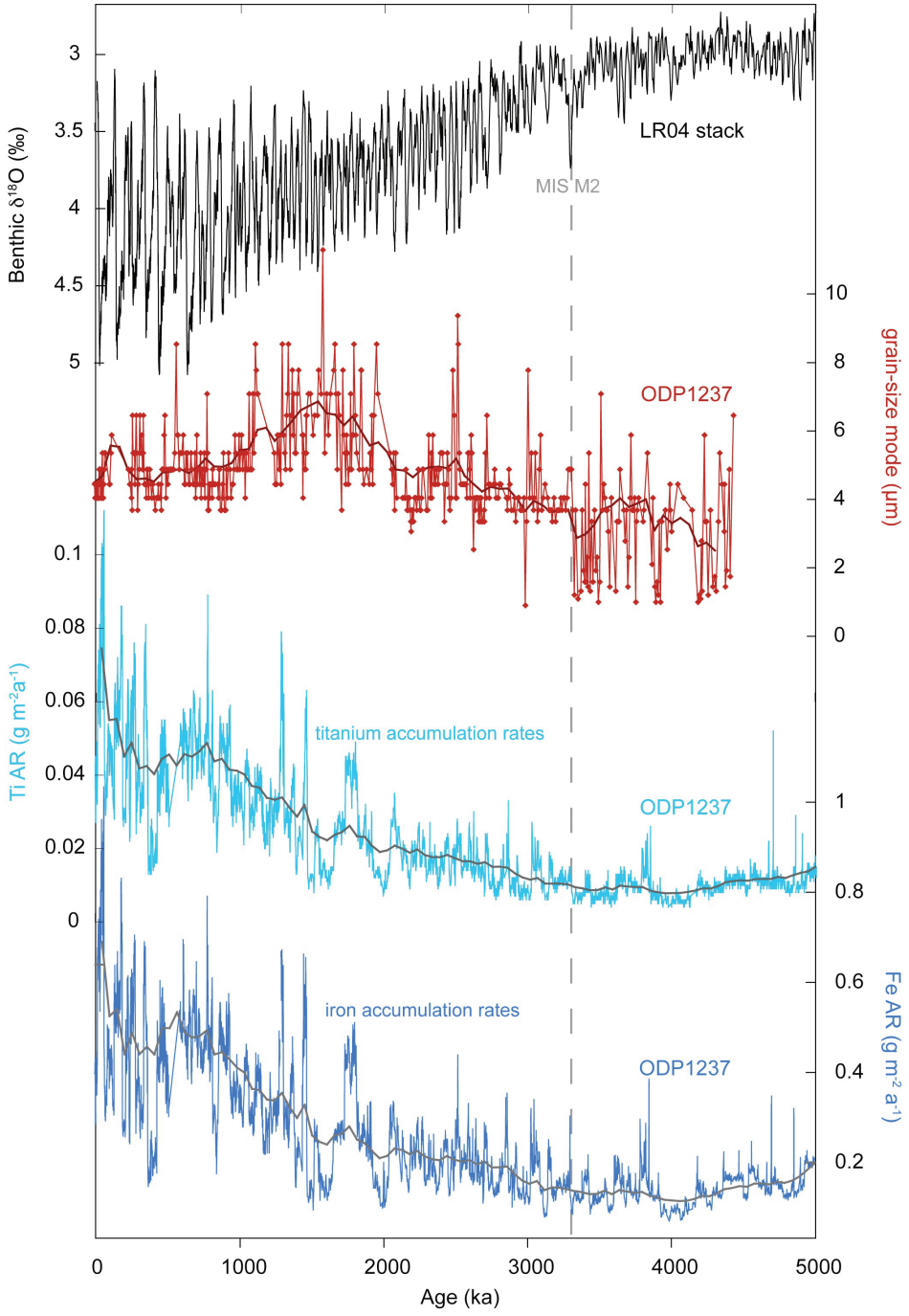

Figure 35: Grain-size modes, titanium (Ti) and iron (Fe) accumulation rates (ARs) of the past 5 Ma. Benthic oxygen isotope stack from Lisiecki and Raymo (2005); grain-size modes (μm) in red, smoothed curve fit in dark red; Ti AR (g m^{-2} a^{-1}) in light blue; Fe AR (g m^{-2} a^{-1}) in dark blue; smoothed curve fits in grey. MIS M2 at $\sim$3.3

became cooler and more arid, titanium (Ti) and iron (Fe) accumulation rate (AR) records from ODP Site 1237 suggest a long-term increase in dust supply to the SE Pacific after ∼3.3 Ma which is more pronounced after 1.6 Ma. The latter increase lasted until 0.8 Ma, followed by a slight decrease until 0.4 Ma. After 0.4 Ma mean dust supply increased again (Fig. 35). Although part of the increasing trend might result from the eastward tectonic drift of ODP Site 1237 toward the eolian dust source area (Fig. 36), these long-term changes coincide with the timing of major long-term phases of global cooling, suggesting a dominant climate control. Another tectonic factor, the Pliocene uplift of the Andes, may have provided additional feedbacks that especially influenced climate by intensifying the weathering rates in the source areas as well as the dust-transporting wind system that is controlled by the height of the Andes. However, these slow tectonic factors are considered to have played no essential role for the orbital-scale variability (19-100kyr) or relatively abrupt shifts within the proxy-records.

The increase in dust supply from ∼3.3 to 1.6 Ma is paralleled by an increase in grain-size modes. However, the second and more pronounced increase in dust supply after 1.6 Ma is not paralleled by increasing grain-sizes. Instead, grain-size modes decrease until ∼0.9 Ma. Modes vary from <1 - 4 μm before 4 Ma to 4 - 6.5 μm between 1 - 0 Ma. They show a long-term pattern very similar to the grain-size ratio of dust end members as calculated in chapter 4.3 (Fig. 37C) and thus depict increasing wind strength from ∼3.3 Ma to 1.6 Ma. The major step after which the increase begins occurs concurrent with Marine Isotope Stage (MIS) M2. This abrupt change in grain size and thus in the indicator of wind strength (chapter 4.3, Fig. 37C), suggests that changes at ∼3.3 Ma may be related to a threshold in climate and/or tectonic evolution. The concurrence with MIS M2 suggests the former, as MIS M2 represents the first large negative excursion in benthic δ^{18}O, depicting a major cooling event (e.g., Lisiecki and Raymo, 2005). Also, warm Pliocene conditions in the Ross embayment, Antarctica, ended with MIS M2 (Naish et al., 2009). The Early Pliocene is characterized by very large amplitudes in grain-size modes (Fig. 35) in comparison to the subsequent time intervals. Minima <2 μm that frequently occur before ∼3.3 Ma disappear parallel to the general increase in accumulation rates of indicators of eolian dust (Fig. 35). After the sudden switch a coarser grain-size population outweighs the fine component that was alternately dominant before.

Paleoceanographic studies from the tropical Pacific suggest the Pliocene climate switch to have already commenced around 4.8 Ma, or at least 600 ka earlier than previously thought (chapter 4.5). During the generally warm Early Pliocene, the thermocline depth in the tropical East Pacific (EEP) as recorded at ODP Site 1241

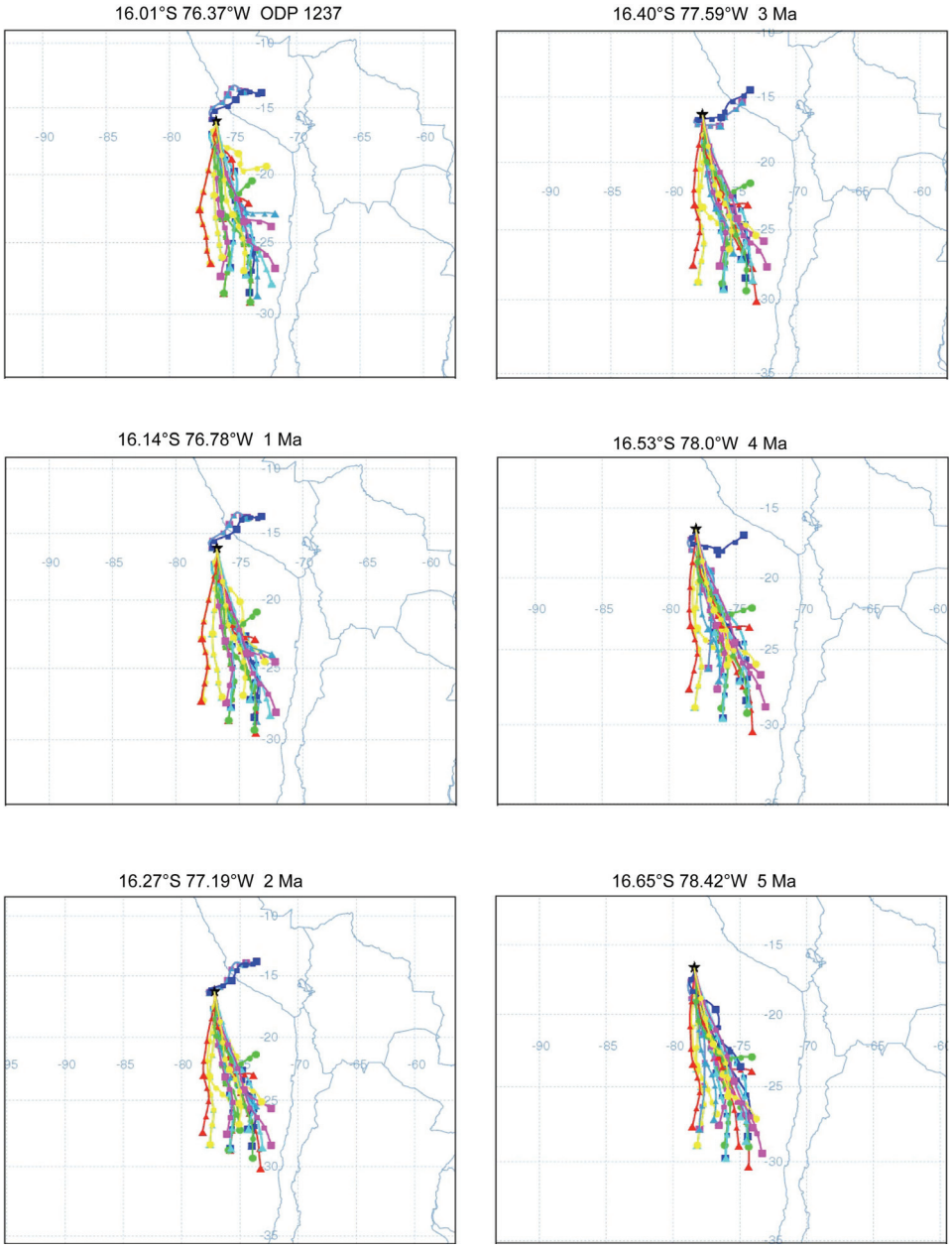

Figure 36: NOAA HYSPLIT MODEL ensemble backward trajectories based on NCEP Reanalysis data (Kalnay et al., 1996) for study site locations according to its tectonic backtrack (Mix et al., 2003) 0 - 5 Million years ago (1 Million year steps). Start time for each run: August 1^{st}, 2003; total run time 72 hours; vertical motion: model vertical velocity; level 1 height: 0 AMSL.

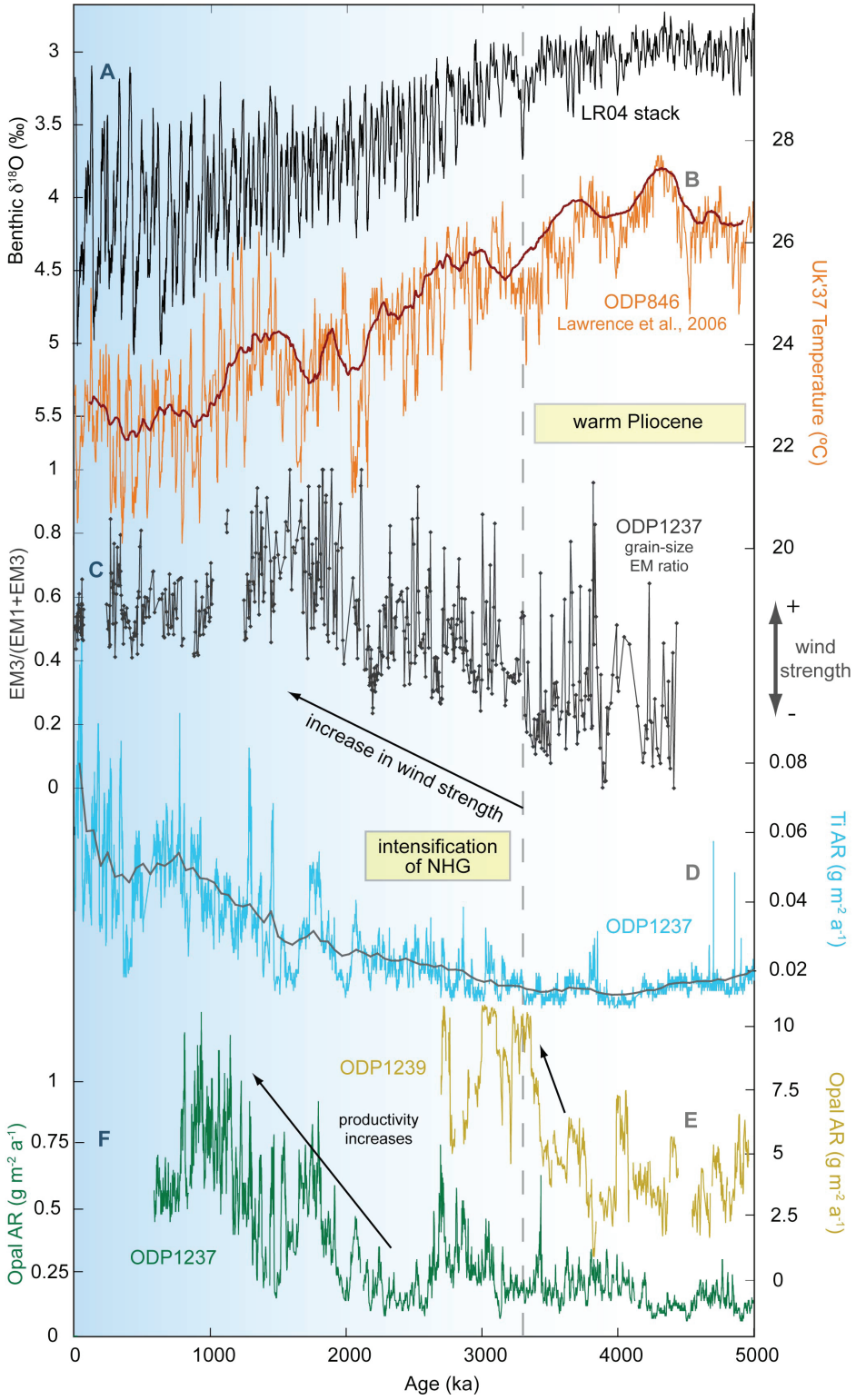

Figure 37: Changes in wind strength of the past 5 Ma. **A** benthic oxygen isotope stack from Lisiecki and Raymo (2005); **B** Alkenone SSTs (°C) heavily influenced by the equatorial front, ODP Site 846 from Lawrence et al. (2006), linear interpolation of data in dark red; **C** ratio of dust endmembers as calculated in chapter 4.3; **D** Titanium (Ti) accumulation rates (ARs) (g m^{-2} a^{-1}), smoothed curve fit of data in grey; **E** opal AR (g m^{-2} a^{-1}) ODP Site 1239; **F** opal AR (g m^{-2} a^{-1}) ODP Site 1237

started to decrease. This shallowing between 4.8 and 4.0 Ma was a large-scale phenomenon related to a strengthening of the Atlantic Meridional Overturning Circulation (AMOC) that in turn was induced by the shoaling the Central American Seaway (CAS). The timing marks a critical threshold during the closure history of the CAS when the exchange of surface water masses between the Pacific and the Caribbean was significantly reduced, thereby initiating global changes in ocean circulation (chapter 4.5). The thermocline shoaling in the EEP during the Early Pliocene was the result of an adjustment process of global ocean circulation in response to AMOC amplification, which was initiated by the closure of the CAS. Sea surface temperature (SST) estimates from ODP Site 846 (Lawrence et al., 2006, Fig. 37B) compared to an SST record from West Pacific Warm Pool (WPWP) Site 806 (Wara et al., 2005; Fedorov et al., 2006) suggest the development of an east-west SST gradient. Surface waters started cooling in the EEP between ∼4.3 and 3.6 Ma ago, reflecting the initiation of the EEP cold tongue. A shallowing thermocline within the EEP cold tongue region between 4.8 and 4 Ma should have reached a critical depth for strong winds to further decrease SSTs by initiating coastal and equatorial upwelling. In a simulation by Timmermann et al. (2007), trade-wind intensification in the southeastern tropical Pacific leads to cooling via increased evaporation and Ekman pumping that may lead to local thermocline shoaling. However, due to the different timing of the shallowing thermocline as seen at ODP Site 1241 and the increase in wind strength at ODP Site 1237 (Fig. 37C) this cannot be confirmed. Wind intensities seem to have been only strong enough after ∼3.3 Ma to control the upwelling of cool water masses from below while the thermocline remained in its shallow state (cf. Philander and Fedorov, 2003). If changes in productivity are considered as evidence for enhanced upwelling, opal ARs from ODP Site 1239 located at the rim of the EEP cold tongue support this hypothesis with a doubling of diatom productivity between 3.4 and 3.3 Ma (Fig. 37E). Opal ARs at ODP Site 1237 do not show this pattern because Site 1237 was either outside the zone of Peruvian coastal upwelling before 3 Ma due to its tectonic backtrack (see chapter 2, Figs. 36 and 37E), or strong coastal upwelling was initiated only much later.

Before 4 Ma, high amplitudes in the wind strength indicator point to a pronounced variability. While wind strength was generally weaker, conditions in the source areas during the Early Pliocene were semi-arid, with alternating more humid and more arid periods (Hartley and Chong, 2002). The presence of water and thus wet-chemical weathering as well as the regular drying of soils provided abundant small-grained dust before the climate switch. Theoretically, the tectonic backtrack might come into play here as well, as ODP Site 1237 was located at 78.4°W. Hysplit model backward trajectories based on data of August (when trade winds are

strongest) of an ordinary year (neither El Niño nor La Niña) suggest that the study site received dust mainly from the more southern part of the Atacama Desert (Fig. 36). Although, one must bear in mind that the backtracks show three single days in August 2003, not an average of a time series. Nevertheless, the distance from source to sink was larger in the Early Pliocene. Gravitational fall-out due to longer transport pathways is a probable explanation for smaller grain-size distributions before ∼3.3 Ma. If the tectonic backtrack were the pivotal cause, there would be an increasing trend in the grain-size data between 4.5 and 3.3 Ma as the site moved closer towards the source area. However, such a trend cannot be detected in the grain-size record (Figs. 35 and 37C).

Arid to semi-arid conditions predominated also in the core area of the Atacama (Berger, 1997; Hartley, 2003), turning into hyper-arid conditions in the Pliocene (between 4 and 3 Ma) (Hartley and Chong, 2002). Increasing accumulation rates of Fe and Ti starting at approximately the same time as the trade winds become stronger suggest a common mechanism that caused a more prominent aridity on the continent and higher wind intensities. Further uplift of the Andean mountain chain that might increase the SE trade winds parallel to the South American coast seems an unlike cause at the time, because the Central Andes were largely in place by then (chapter 2).

Stein (1985) found a distinct increase of accumulation rates of terrigenous matter and enhanced paleo-trade wind speeds at Deep Sea Drilling Project (DSDP) Site 397 located below the major dust transport pathway of the northeast trade winds off West Africa after ∼3.2 Ma and inferred an increase in aridity of the Northwest African continent. Leroy and Dupont (1997) and Marlow et al. (2000) found synchronous evidence for an onset of aridity in Africa and enhanced (SE) trade wind strength. Considering that the age model of DSDP Site 397 might be slightly off, the rather abrupt increases of dust accumulation and trade-wind strength in both oceans and hemispheres occurred at roughly the same time, also coinciding with MIS M2 or happening shortly thereafter. This concurrence suggests a relation to general global climate cooling. Hartley and Chong (2002) compared periods of increased aridification in the Atacama, Sahara and Namib deserts with temperature curves for the Southern Ocean and came to the same conclusion.

Zooming into the phase of NHG intensification from 3.1 to 2.4 Ma, wind strength kept increasing after the mid-Pliocene warmth, when variability again was rather high (chapter 4.3). While a thermocline deepening outside the EEP cold tongue linked to AMOC weakening after 3 Ma is inferred from the 1241 temperature records, modeling studies suggest that the enhancement of the EEP cold tongue results from a northward shift of the ITCZ (chapter 4.5). The increase in SE trade wind intensity until ∼2.5 Ma is related to a steeper pole-to-equator temperature

gradient developing during NHG intensification. More evidence for enhanced atmospheric circulation is given by an increase in the equatorial Pacific zonal SST gradient between 3.1 and 2.3 Ma (Wara et al., 2005) and a concurrent strengthening of the Walker Circulation (Medina-Elizalde and Lea, 2010). Strong winds seem to have further decreased SSTs by controlling equatorial upwelling in the cold tongue region. SE trade winds are also intensified during glacials compared to interglacials (Fig. 32), concurrent with SST minima in the EEP cold tongue (Lawrence et al., 2006, Fig. 37B), oscillating on an orbital scale of 41 ka.
From 3.1 to ∼2.5 Ma, opal ARs at ODP Site 1237 point to an increase in upwelling-induced productivity, that is followed by a sudden decline, when trade-wind strength slightly decreases from 2.5 to 2.2 Ma (Fig 37C, F). The onset of a major wind strength increase thereafter (Fig. 37C) is concomitant with increases in Fe and Ti ARs, as well as opal ARs at ODP Site 1237 (Figs. 35 and 37F). By 2.2 Ma, ODP Site 1237 was located closer to the continent, so that it also received dust from the southern coastal deserts of Peru and northern Chile, contributing further to the accumulation rates. However, the increase in wind strength and productivity are synchronous with an intensification of the Walker and Hadley Circulation as inferred from a steeper zonal SST gradient along the equatorial Pacific and an enhancement of equatorial upwelling between ∼2.2 and 2 Ma as described by Etourneau et al. (2010). Changes due to the tectonic backtrack thus seem negligible.

Wind strength slightly declines from 1.6 Ma until ∼900 ka and oscillates around the same level thereafter. This behavior is in agreement with an EEP cold tongue warming and productivity decline (this study and ODP Site 846 from Lawrence et al., 2006) between 1.6 and 1 Ma, pointing towards trade wind-controlled upwelling roughly until the Mid-Pleistocene Transition, when glacial oscillations change from 41 ka-cycles in an obliquity-dominated world to 100 ka eccentricity cycles.
Dust accumulation rates at ODP Site 1237, on the other hand, steeply increase from ∼1.6 to 0.8 Ma and then decrease until ∼0.4 Ma. Changes in South American continental climate (aridity vs. humidity) thus seem to be decoupled from wind strength variability after 1.6 Ma.

During the Late Pleistocene, dust accumulation and grain-size distributions at ODP Site 1237 still show different patterns. While grain-size distributions do not indicate any distinct changes in wind speed (Fig. 23), dust ARs oscillate on glacial cycles. This is largely attributed to changes in the source area and to meridional shifts of the atmospheric circulation system (chapter 4.2). During glacials, the South Pacific Anticyclone and the ITCZ were located further north and the Hadley Cell was intensified. While only the meridional wind component was enhanced, gen-

eral wind speeds did not change, but an enhanced availability of dust in the source area and an increased gustiness provided for a 2 - 3 fold increase in dust ARs at ODP Site 1237. At the same time, a steeper north-south SST gradient is recorded between equatorial ODP Site 1239 and MD02-2529 4.4 during glacials, also suggesting a vigorous oceanic cold tongue. In contrast, enhanced fluvial input at ODP Site 1239 during interglacials, is caused by more humid conditions. The southern movement of the ITCZ during interglacials leads to higher precipitation on the continent that in turn causes enhanced river runoff (chapter 4.4).

In conclusion, there is no single valid chain of forcing mechanisms for changes in western South American climate during the past 5 Ma. Hartley (2003) attributed the shift to hyper-arid conditions in the Atacama Desert to a combination of global climate cooling and enhanced upwelling of the Humboldt Current generated by the closure of the CAS between 3.5 and 3 Ma. While the onset of hyper-aridity in South America seems indeed to be related to a combination of the two, changes in ocean circulation and thermocline depth adjustments in the tropical East Pacific happened already before 4 Ma, preconditioning changes that were initiated by global cooling some 700 ka later. In the process of global climate cooling, a threshold was passed around 3.3 Ma, the mechanism of which is still to be explored. With the onset of the NHG and the amplification of the 41 ka climate variability as well as during the Plio-Pleistocene Transition the southeast trade winds strengthened upwelling in the eastern equatorial cold tongue and thereby further decreased SSTs. After $\sim$1.6 Ma when SSTs became higher again for a short period of time, this relationship seems no longer stable. Southeast trade winds decreased until roughly 900 ka and varied around a lower average until the present, while productivity in the coastal upwelling areas kept increasing until $\sim$900 ka, and dust accumulation rates even until present, oscillating on glacial-interglacial cycles.

6 Perspectives

Due to its continuous and complete sedimentary sequence, ODP Site 1237 has provided a number of paleo-environmental reconstructions in the SE Pacific (this study, Haywood et al., 2005; Holbourn et al., 2005; Fedorov et al., 2006; Dekens et al., 2007). It has an excellent stratigraphic framework (Tiedemann et al., 2007) that allows for precise paleoclimate comparisons. In the following, some ideas are outlined for further research at the site and/or the larger study area.

(1) A question that remained unanswered in this study concerns the trigger of the abrupt increase in SE trade-wind strength at $\sim$3.3 Ma ago. Comparing data from different study areas elucidated this change around MIS M2 to be of global scale. The grain-size data and terrigenous element accumulation rates suggest some threshold was passed, after which conditions did not return to their previous state.

(2) The five Million year record of this study indicates paleo-environmental changes in the tropical SE Pacific and on the adjacent continent during the Mid-Pleistocene Transition (MPT $\sim$1.2 - 0.5 Ma). The relationship of stronger winds, enhanced upwelling, lower sea surface temperatures, and a more pronounced continental aridity during glacials found in the period from 3 to 1.6 Ma (see chapter 4.3) is not apparent during the last 500 ka. The underlying mechanisms for this change in glacial-interglacial behavior are not yet understood. A close-up of the MPT would thus be important for further insight in the history of continent-ocean-atmosphere linkages in the SE Pacific.

(3) The enforcing of the SE trade winds by enhanced pole-to-equator water temperature gradients need some more data validation. High-resolution long-term temperature records should be generated at meridionally distributed study sites along the west coast of South America and subsequently compared to the wind strength proxy record.

(4) Global dust models have been used for (paleo-)climate research for more than a decade (e.g., Mahowald et al., 1999; Lunt and Valdes, 2002; Tegen et al., 2002; Werner et al., 2002; Mahowald et al., 2006; Tanaka and Chiba, 2006). Developing models on a regional scale to capture changes in the dust exporting areas would be helpful to disentangle the regional-scale processes that are responsible for the observed patterns in continental aridity and trade wind strength.

(5) The investigation of the geochemical composition including the rare earth element composition of dust samples from the Atacama Desert, from the regional

atmosphere as well as from SE Pacific surface sediments would help to further constrain the exact source area(s) of the dust that is deposited on the ocean floor.

References

Abratis, M. (1998). *Geochemical Variations in Magmatic Rocks from Southern Costa Rica as a Consequence of Cocos Ridge Subduction and Uplift of the Cordillera De Talamanca*. PhD thesis, Universität Göttingen.

Aravena, R. (1995). Isotope hydrology and geochemistry of nothern chile groundwaters. In *Aguas, Glaciares y Cambios Climaticos en los Andes Tropicales*, pages 109–117, La Paz. ORSTOM/UMSA/SENAMHI/CONAPHI.

Arimoto, R. (2001). Eolian dust and climate: Relationships to sources, tropospheric chemistry, transport and deposition. *Earth-Science Reviews*, 54(1-3):29.

Bacon, M. P. (1984). Glacial to interglacial changes in carbonate and clay sedimentation in the atlantic ocean estimated from 230th measurements. *Isotope Geoscience*, 2:97–111.

Barkan, J. and Alpert, P. (2010). The linkage between solar insolation and dust in the major world deserts. *The Open Atmospheric Science Journal*, 4:101–113.

Bartoli, G., Sarnthein, M., Weinelt, M., Erlenkeuser, H., Garbe-SchË†nberg, D., and Lea, D. (2005). Final closure of panama and the onset of northern hemisphere glaciation. *Earth and Planetary Science Letters*, 237(1-2):33 – 44.

Berger, I. (1997). *Arid Zone Geomorphology: Process, Form and Change in Drylands*, chapter 24 South America, pages 543–562. John Wiley and Sons Inc., Chichester, UK, 2 edition.

Berger, W., Vincent, E., and Thierstein, H. (1981). *The deep-sea record: Major steps in Cenozoic ocean evolution*, volume 32 of *The Deep Sea Drilling Project: a decade of progress*, pages 489–504. Soc. Econom. Paleontol. Mineral. Spec. Publ.

Berggren, W. and Hollister, C. (1974). *Paleogeography, paleobiogeography, and the history of circulation of the Atlantic Ocean*, volume 20 of *Studies in Paleoceanography*, pages 126–186. Soc. Econom. Paleontol. Mineral. Spec. Publ.

Bobst, A. L., Lowenstein, T. K., Jordan, T. E., Godfrey, L. V., Ku, T.-L., and Luo, S. (2001). A 106 ka paleoclimate record from drill core of the salar de atacama, northern chile. *Palaeogeography,Palaeoclimatology,Palaeoecology*, 173(1-2):21–42.

Breitsprecher, K. and Thorkelson, D. (2009). Neogene kinematic history of nazca-antarctic-phoenix slab windows beneath patagonia and the antarctic peninsula. *Tectonophysics*, 464:10–20.

Bundschuh, J., Winograd, M., Michael, D., and Alvarado, G. E. (2007). *Regional Overview*. Taylor and Francis/Balkema, Leiden, The Netherlands.

Cane, M. A. (1998). A role for the tropical pacific. *Science*, 282(5386):59–61.

Cane, M. A. (2005). The evolution of el niño, past and future. *Earth and Planetary Science Letters*, 230(3-4):227.

Clemens, S. (1998). Dust response to seasonal atmospheric forcing: Proxy evaluation and calibration. *Paleoceanography*, 13(5):471–490.

Dekens, P. S., Ravelo, A. C., and McCarthy, M. D. (2007). Warm upwelling regions in the pliocene warm period. *Paleoceanography*, 22(3).

Dengo, G. (1985). *Tectonic setting for the Pacific margin from southern Mexico to Northwestern Columbia*, pages 123–180. Number 7A in The Pacific Ocean: The ocean basins and margins. Plenum Press.

Dowsett, H. J., Barron, J., Poore, R., Thompson, R., Cronin, T., Ishman, S., and Willard, D. (1999). Middle pliocene paleoenvironmental reconstruction: Prism2. *USGS Open File Report*, 99(535).

Dowsett, H. J. and Caballero Gill, R. P. (2010). Pliocene climate. *Stratigraphy*, 7(2-3):106–110.

Etourneau, J., Schneider, R., Blanz, T., and Martinez, P. (2010). Intensification of the walker and hadley atmospheric circulations during the pliocene-pleistocene climate transition. *Earth and Planetary Science Letters*, 297(1-2):103 – 110.

Farrell, J., Murray, D., McKenna, V., and Ravelo (1995). Upper ocean temperature and nutrient contrasts inferred from pleistocene planktonic foraminifera d18o and d13c in the eastern equatorial pacific. In Pisias, N. G., Mayer, L. A., Palmer-Julson, A., and van Andel, T. H., editors, *Proceedings of the Ocean Drilling Program, Scientific Results*, volume 138, pages 289–319, College Station, TX. IODP, IODP.

Fedorov, A. V., Dekens, P. S., McCarthy, M., Ravelo, A., deMenocal, P. B., Barreiro, R. C., Pacanowski, R. C., and Philander, S. G. (2006). The pliocene paradox (mechanisms for a permanent el niño). *Science*, 312(5779):1485–1489.

Foster, G., Seki, O., Pancost, R., and Schmidt, D. (2009). pco_2 and climate: Evidence from boron based proxies of ph and pco_2. *Geochimica et Cosmochimica Acta*, 73(13).

Francois, R., Frank, M., Rutgers van der Loeff, M. M., and Bacon, M. P. (2004). 230th normalization: An essential tool for interpreting sedimentary fluxes during the late quaternary. *Paleoceanography*, 19(1):PA1018.

Garzione, C. N., Molnar, P., Libarkin, J. C., and MacFadden, B. J. (2006). Rapid late miocene rise of the bolivian altiplano: Evidence for removal of mantle lithosphere. *Earth and Planetary Science Letters*, 241(3-4):543.

Gregory-Wodzicki, K. M. (2000). Uplift history of the central and northern andes: A review. *Geological Society of America Bulletin*, 112(7):1091–1105.

Groeneveld, J., Steph, S., Tiedemann, R., Garbe-Schönberg, D., Nürnberg, D., and A., S. (2006). Pliocene mixed-layer oceanography for site 1241, using combined mg/ca and δ^{18}O analsys of globigerinoides sacculifer. In Tiedemann, R., Mix, A., and Ruddiman, W., editors, *Scientific Results*, volume 202 of *Proceedings of the Ocean Drilling Program*, College Station, TX. IODP.

Haq, B. (1981). Paleogene paleoceanography: early cenozoic oceans revisited. *Oceanol. Acta*, 4:71–82.

Harrison, S. P., Kohfeld, K. E., Roelandt, C., and Claquin, T. (2001). The role of dust in climate changes today, at the last glacial maximum and in the future. *Earth-Science Reviews*, 54(1-3):43.

Hart, D. and Miller, D. (2006). Analysis and correlation of volcanic ash in marine sediments from the peru margin: Explosvie volcanic cycles of the north-central andes. In Jorgensen, B. B., D'Hondt, S. L., and Miller, D. J., editors, *Ocean Drilling Program Leg 201*, College Station, TX. ODP, Ocean Drilling Programm.

Hartley, A. J. (2003). Andean uplift and climate change. *Journal of Geological Society*, 160:7–10.

Hartley, A. J. and Chong, G. (2002). Late pliocene age for the atacama desert: Implications for the desertification of western south america. *Geology*, 30(1):43–46.

Haug, G. and Tiedemann, R. (1998). Effect of the formation of the isthmus of panama on atlantic ocean thermohaline circulation. *Nature*, 393:673–676.

Haug, G., Tiedemann, R., Zahn, R., and Ravelo, A. (2001). Role of panama uplift on oceanic freshwater balance. *Geology*, 29:207–210.

Hay, W. (1996). Tectonics and climate. *Geologische Rundschau*, 85:409–437.

Haywood, A. M. (2005). The climate of the future: Clues from three million years ago. *Geology Today*, 21(4):138–143.

Haywood, A. M., Dekens, P., Ravelo, A. C., and Williams, M. (2005). Warmer tropics during the mid-pliocene? evidence from alkenone paleothermometry and a fully coupled ocean-atmosphere gcm. *Geochem. Geophys. Geosyst.*, 6(3).

Haywood, A. M. and Valdes, P. J. (2004). Modelling pliocene warmth: contribution of atmosphere, oceans and cryosphere. *Earth and Planetary Science Letters*, 218(3-4):363 – 377.

Henderson, G. and Anderson, R. F. (2003). The u-series toolbox for paleoceanography. *Reviews in Mineralogy and Geochemistry*, 525(1):493–531.

Holbourn, A., Kuhnt, W., Schulz, M., and Erlenkeuser, H. (2005). Impacts of orbital forcing and atmospheric carbon dioxide on miocene ice-sheet expansion. *Nature*, 438(7067):483–487.

Hovan, S. A. (1995). Late cenozoic atmospheric circulation intensity and climatic history recorded by eolian deposition in the eastern equatorial pacific ocean. In Pisias, N. G., Janecek, T. R., Palmer-Julson, A., and van Andel, T. H., editors, *Proceedings of the Ocean Drilling Program, Scientific Results*, volume 138, pages 615 – 625.

Ibaraki, M. (1997). Closing of the central american seaway and neogene coastal upwelling along the pacific coast of south america. *Tectonophysics*, 281:99–104.

Jaillard, E., Hérail, G., Monfret, T., Díaz-Martínez, E., Baby, P., Lavenu, A., and Dumont, J. (2000). *Tectonic Evolution of the Andes of Ecuador, Peru, Bolivia and Northernmost Chile*, pages 481–559. Rio de Janeiro.

Jickells, T. D., An, Z. S., Andersen, K. K., Baker, A. R., Bergametti, G., Brooks, N., Cao, J. J., Boyd, P. W., Duce, R. A., Hunter, K. A., Kawahata, H., Kubilay, N., laRoche, J., Liss, P. S., Mahowald, N., Prospero, J. M., Ridgwell, A. J., Tegen, I., and Torres, R. (2005). Global iron connections between desert dust, ocean biogeochemistry, and climate. *Science*, 308(5718):67–71.

Kalnay, E., Kanamitsu, M., Kistler, R., Collins, W., Deaven, D., Gandin, L., Iredell, M., Saha, S., White, G., Woollen, J., Zhu, Y., Leetmaa, A., Reynolds, R., Chelliah, M., Ebisuzaki, W., Higgins, W., Janowiak, J., Mo, K. C., Ropelewski, C., Wang, J., Jenne, R., and Joseph, D. (1996). The ncep/ncar 40-year reanalysis project. *Bulletin of the American Meteorological Society*, 77(3):437–471.

Keigwin, L. (1978). Pliocene closing of the isthmus of panama, based on biostratigraphic evidence from nearby pacific ocean and caribbean sea cores. *Geology*, 6:630–634.

Kessler, W. S. (2006). The circulation of the eastern tropical pacific: A review. *Progress In Oceanography*, 69(2-4):181.

Kohfeld, K. E. and Harrison, S. P. (2001). Dirtmap: The geological record of dust. *Earth-Science Reviews*, 54(1-3):81.

Kohfeld, K. E. and Tegen, I. (2007). *Treatise on Geochemistry*, chapter Record of Mineral Aerosols and Their Role in the Earth System. Number 4.13. Elsevier, Amsterdam.

Kretschmer, S., Geibert, W., Rutgers van der Loeff, M. M., and Mollenhauer, G. (2010). Grain size effects on 230thxs inventories in opal-rich and carbonate-rich marine sediments. *Earth and Planetary Science Letters*, In Press, Corrected Proof.

Lahsen, A. (1982). Upper cenozoic volcanism and tectonism in the andes of northern chile. *Earth-Science Reviews*, 18(3-4):285.

Laity, J. (2008). *Deserts and Desert Environments*. Wiley Blackwell, Chichester, UK.

Larrain, H., Velásquez, F., and Cereceda, P. e. a. (2002). Fog measurements at the site "falda verde" north of chañaral compared with other fog stations of chile. *Atmospheric Research*, 64:273–84.

Laskar, J. (1993). Frequency analysis for multi-dimensional systems. global dynamics and diffusion. *Physica D: Nonlinear Phenomena*, 67(1-3):257 – 281.

Latorre, C., Betancourt, J., and Rech, J. e. a. (2005). *23°S: Archeology and Environmental HIstory of the Southern Deserts*, chapter Late Quaternary history of the Atacama Desert. National Museum of Australia Press, Canberra.

Lawrence, K. T., Liu, Z., and Herbert, T. D. (2006). Evolution of the eastern tropical pacific through plio-pleistocene glaciation. *Science*, 312(5770):79–83.

Leroy, S. A. and Dupont, L. M. (1997). Marine palynology of the odp site 658 (n-w africa) and its contribution to the stratigraphy of late pliocene. *Geobios*, 30(3):351 – 359.

Lisiecki, L. E. and Raymo, M. E. (2005). A pliocene-pleistocene stack of 57 globally distributed benthic δ^{18}O records. *Paleoceanography*, 20(1):PA1003.

Lisiecki, L. E. and Raymo, M. E. (2007). Plio-pleistocene climate evolution: trends and transitions in glacial cycle dynamics. *Quaternary Science Reviews*, 26(1-2):56 – 69.

Lundelius, E. (1987). *The North American Quaternary sequence*, pages 211–235. Cenozoic mammals of North America. University of California Press.

Lunt, D., Valdes, P., Haywood, A., and Rutt, I. (2008). Closure of the panama seaway during the pliocene: Implications for climate and northern hemisphere glaciation. *Climate Dynamics*, 30(1):1:0930–7575.

Lunt, D. J. and Valdes, P. J. (2002). Dust deposition and provenance at the last glacial maximum and present day. *Geophys. Res. Lett.*, 29(22):2085.

Macharé, J. and Ortlieb, L. (1992). Plio-quaternary vertical motions and the subduction of the nazca ridge, central coast of peru. *Tectonophysics*, 205(1-3):97.

Mahowald, N., Kohfeld, K., Hansson, M., Balkanski, Y., Harrison, S. P., Prentice, I. C., Schulz, M., and Rodhe, H. (1999). Dust sources and deposition during the last glacial maximum and current climate: A comparison of model results with paleodata from ice cores and marine sediments. *J. Geophys. Res.*, 104(D13):15895.

Mahowald, N. M., Muhs, D. R., Levis, S., Rasch, P. J., Yoshioka, M., Zender, C. S., and Luo, C. (2006). Change in atmospheric mineral aerosols in response to climate: Last glacial period, preindustrial, modern, and doubled carbon dioxide climates. *J. Geophys. Res.*, 111(D10):D10202:0148–0227.

Marlow, J., Lange, C., Wefer, G., and Rosell-Mele, A. (2000). Upwelling intensification as part of the pliocene-pleistocene climate transition. *Science*, 290(5500):2288–2291.

Marshall, L. (1988). Land mammals and the great american interchange. *American Scientist*, 76:380–388.

Marshall, L., Webb, S., Sepkoski Jr., J., and Raup, D. (1982). Mammalian evolution and the great american interchange. *Science*, 215:1351–1357.

Mathieson, E. (2002). The present is the key to the past is the key to the future. Cordilleran Section - 98th Annual Meeting, Abstract.

McGee, D., Broecker, W. S., and Winckler, G. (2010). Gustiness: The driver of glacial dustiness? *Quaternary Science Reviews*, 29(17-18):2340.

McGregor, G. and Nieuwolt, S. (1998). *Tropical Climatology - An Introduction to the Climates of the Low Latitudes*. John Wiley and Sons Inc., UK, 2nd edition.

Medina-Elizalde, M. and Lea, D. W. (2010). Late pliocene equatorial pacific. *Paleoceanography*, 25(2):PA2208.

Megard, F. (1984). The andean orogenic period and its major structures in central and northern peru. *Journal of the Geological Society*, 141:893–900.

Mix, A. (2006). Running hot and cold in the eastern equatorial pacific. *Quaternary Science Reviews*, 25:1147–1149.

Mix, A., Tiedemann, R., and Blum, P. (2003). Southeast pacific paleoceanographic transects sites 1232 - 1242. In Mix, A., Tiedemann, R., and Blum, P., editors, *Initial Reports Leg 202*, volume 202 of *Proceedings of the Ocean Drilling Program*, College Station, TX. IODP, IODP.

Molnar, P. (2008). Closing of the central american seaway and the ice age: A critical review. *Paleoceanography*, 23(2).

Molnar, P. and Cane, M. A. (2002). El niño's tropical climate and teleconnections as a blueprint for pre-ice age climates. *Paleoceanography*, 17(2).

Monien, D. (2010). *Rapid environmental changes in the Ross Sea Embayment using a geochemical approach*. PhD thesis, University of Bremen, Bremen.

Mudelsee, M. and Raymo, M. E. (2005). Slow dynamics of the northern hemisphere glaciation. *Paleoceanography*, 20(4).

Mulitza, S., Prange, M., Stuut, J.-B., Zabel, M., von Dobeneck, T., Itambi, A. C., Nizou, J., Schulz, M., and Wefer, G. (2008). Sahel megadroughts triggered by glacial slowdowns of atlantic meridional overturning. *Paleoceanography*, 23(4).

Müller, P. J. and Schneider, R. (1993). An automated leaching method for the determination of opal in sediments and particulate matter. *Deep Sea Research Part I: Oceanographic Research Papers*, 40(3):425.

Naish, T., Powell, R., Levy, R., Wilson, G., Scherer, R., Talarico, F., Krissek, L., Niessen, F., Pompilio, M., Wilson, T., Carter, L., DeConto, R., Huybers, P., McKay, R., Pollard, D., Ross, J., Winter, D., Barrett, P., Browne, G., Cody, R., Cowan, E., Crampton, J., Dunbar, G., Dunbar, N., Florindo, F., Gebhardt, C., Graham, I., Hannah, M., Hansaraj, D., Harwood, D., Helling, D., Henrys, S., Hinnov, L., Kuhn, G., Kyle, P., Laufer, A., Maffioli, P., Magens, D., Mandernack, K., McIntosh, W., Millan, C., Morin, R., Ohneiser, C., Paulsen, T., Persico, D.,

Raine, I., Reed, J., Riesselman, C., Sagnotti, L., Schmitt, D., Sjunneskog, C., Strong, P., Taviani, M., Vogel, S., Wilch, T., and Williams, T. (2009). Obliquity-paced pliocene west antarctic ice sheet oscillations. *Nature*, 458(7236):322–328.

Norabuena, E., Leffler-Griffin, L., Mao, A., Dixon, T., Stein, S., Sacks, I. S., Ocola, L., and Ellis, M. (1998). Space geodetic observations of nazca-south america convergence across the central andes. *Science*, 279(5349):358–362.

Orme, A. R. (2007). *Tectonism, Climate, and Landsacpe Change*, volume 7 of *Oxford Regional Environments Series*, chapter 2, pages 23–44. Oxford University Press, Oxford.

Pälike, H., Shackleton, N., and Röhl, U. (2001). Astronomical forcing on late eocene marine sediments. *Earth and Planetary Science Letters*, 193:589–602.

Philander, S. G. and Fedorov, A. V. (2003). Role of tropics in changing the response to milankovich forcing some three million years ago. *Paleoceanography*, 18(2).

Picard, M., Sempere, T., and Plantard, O. (2008). Direction and timing of uplift propagation in the peruvivan andes deduced from molecular phylogenetics of highland biotaxa. *Earth and Planetary Science Letters*, 271(1-4):326–336.

Pierrehumbert, R. T. (2000). Climate change and the tropical pacific: The sleeping dragon wakes. *PNAS*, 97(4):1355–1358.

Poore, R. (2007). Paleoclimate reconstruction — pliocene environments. In Elias, S. A., editor, *Encyclopedia of Quaternary Science*, pages 1948 – 1958. Elsevier, Oxford.

Prins, M. A. and Weltje, G. J. (1999). *End-Member Modelling of Siliciclastic Grain-Size Distributions: The Late Quaternary Record of Eolian and Fluvial Sediment Supply to the Arabian Sea and Its Paleoclimatic Significance*, volume 62 of *Sepm Special Publication*. Geological Society Publishing House, London.

Prospero, J. M., Ginoux, P., Torres, O., Nicholson, S. E., and Gill, T. E. (2002). Environmental characterization of global sources of atmospheric soil dust identified with the nimbus 7 total ozone mapping spectrometer (toms) absorbing aerosol product. *Rev. Geophys.*, 40.

Pye, K. (1987). *Aeolian Dust and Dust Deposits*. Academic Press, London.

Ravelo, A., Andreasen, D., Lyle, M., Lyle, A., and Wara, M. (2004). Regional climate shifts caused by gradual global cooling in the pliocene epoch. *Nature*, 429:263–267.

Raymo, M. E. (1994). The initiation of northern hemisphere glaciation. *Annual Review of Earth and Planetary Sciences*, 22:353–383.

Rea, D. K. (1994). The paleoclimatic record provided by eolian deposition in the deep sea: The geologic history of wind. *Rev. Geophys.*, 32.

Richter, T., van der Gaast, S., Koster, B., Vaars, A., Gieles, R., De Stigter, H., De Haas, H., and van Weering, T. (2006). The avaatech xrf core scanner: technical description and applications to ne atlantic sediments. In Rothwell, R., editor, *New Techniques in Sediment Core Analysis*, volume 267 of *Special Publications*, pages 39–50. Geological Society.

Rincón-Martinez, D., Lamy, F., Contreras, S., Leduc, G., Bard, E., Saukel, C., Blanz, T., Mackensen, A., and Tiedemann, R. (2010). More humid interglacials in ecuador during the past 500 kyr linked to latitudinal shifts of the equatorial front and the intertropical convergence zone in the eastern tropical pacific. *Paleoceanography*, 25(2):PA2210.

Robinson, M., Dowsett, H. J., and Chandler, M. (2008). Pliocene role in assessing future climate impacts. *Eos Trans.*, 89:501–502.

Ruddiman, W. F. and Prell, W. L. (1997). *Tectonic Uplift and Climate Change*, chapter Introduction to the Uplift-Climate Hypotheses. Plenum Press, New York and London.

Sarnthein, M., Tetzlaff, G., Koopmann, B., Wolter, K., and Pflaumann, U. (1981). Glacial and interglacial wind regimes over the eastern subtropical atlantic and north-west africa. *Nature*, 293(5829):193.

Sarnthein, M., Winn, K., Duplessy, J.-C., and Fontugne, M. (1988). Global variations of surface ocean productivity in low and mid latitudes: Influence on CO_2 reservoirs of the deep ocean atmosphere during the last 21,000 years. *Paleoceanography*, 3(3):361–399.

Sepulchre, P., Sloan, L. C., Snyder, M., and Fiechter, J. (2009). Impacts of andean uplift on the humboldt current system: A climate model sensitivity study. *Paleoceanography*, 24(4):PA4215.

Stein, R. (1985). Late neogene changes of paleoclimate and paleoproductivity off northwest africa (d.s.d.p. site 397). *Palaeogeography, Palaeoclimatology, Palaeoecology*, 49(1-2):47 – 59.

Steinmann, M., Hungerbühler, D., Seward, D., and Winkler, W. (1999). Neogene tectonic evolution and exhumation of the southern ecuadorian andes: a combined stratigraphy and fission-track approach. *Tectonophysics*, 307:255–279.

Steph, S., Tiedemann, R., Groeneveld, J., A., S., and Nürnberg, D. (2006). Pliocene changes in tropical east pacific upper ocean stratification: response to tropical gateways? In Tiedemann, R., Mix, A., and Ruddiman, W., editors, *Scientific Results*, volume 202 of *Proceedings of the Ocean Drilling Program*, College Station, TX. IODP.

Steph, S., Tiedemann, R., Prange, M., Groeneveld, J., Schulz, M., Timmermann, A., NÂ¸rnberg, D., RÂ¸hlemann, C., Saukel, C., and Haug, G. H. (2010). Early pliocene increase in thermohaline overturning: A precondition for the development of the modern equatorial pacific cold tongue. *Paleoceanography*, 25(2):PA2202.

Strub, P. T., Mesías, J. M., Montecino, V., Rutllant, J., and Salina, S. (1998). *Coastal Ocean Circulation Off Western South America*, volume 11. John Wiley and Sons Inc.

Stuut, J.-B. W. (2001). *Late Quaternary Southwestern African terrestrial-climate signals in the marine record of Walvis Ridge, SE Atlantic Ocean*. PhD thesis, University of Utrecht.

Takahashi, K. and Battisti, D. (2006). Processes controlling the mean tropical pacific precipitation pattern: I. the andes and the eastern pacific itcz. *Journal of Climate*, 20:3434–3451.

Tanaka, T. Y. and Chiba, M. (2006). A numerical study of the contributions of dust source regions to the global dust budget. *Global and Planetary Change*, 52(1-4):88 – 104. Monitoring and Modelling of Asian Dust Storms.

Tegen, I., Harrison, S. P., Kohfeld, K., Prentice, I. C., Coe, M., and Heimann, M. (2002). Impact of vegetation and preferential source areas on global dust aerosol: Results from a model study. *J. Geophys. Res.*, 107.

Thiel, M., Macaya, E., Acuña, E., Arntz, W., Bastias, H., Brokordt, K., Camus, P., Castilla, J., Castro, L., Cortés, M., Dumont, C., and et al. (2007). The humboldt current system of northern and central chile. *Oceanography and Marine Biology: An Annual Review*, 45:195–344.

Tiedemann, R., A., S., Steph, S., Lund, S., and Stoner, J. (2007). Astronomically calibrated timescales from 6 to 2.5 ma and benthic isotope stratigraphies, site 1236, 1237, 1239, and 1241. In Tiedemann, R., Mix, A., Richter, C., and Ruddiman, W., editors, *Proc. ODP, Sci. Results, 202*, volume 202 of *Scientific Results*, pages 1–69. IODP, IODP.

Tiedemann, R. and Mix, A. C. (2007). Leg 202 synthesis: Southeast pacific paleoceanography. In Tiedemann, R., Mix, A., Richter, C., and Ruddiman, W., editors, *Proceedings of the Ocean Drilling Program, Scientific Results*, number 202, pages 1–56, College Station, TX.

Timmermann, A., Justino, F., Jin, F., and Goosse, H. (2004). Surface temperature control in the north and tropical pacific during the last glacial maximum. *Climate Dynamics*, 23(3-4):353–370.

Timmermann, A., Okumura, Y., An, S.-I., Clement, A., Dong, B., Guilyardi, E., Hu, A., Jungclaus, J. H., Renold, M., Stocker, T. F., Stouffer, R. J., Sutton, R., Xie, S.-P., and Yin, J. (2007). The influence of a weakening of the atlantic meridional overturning circulation on enso. *Journal of Climate*, 20(19):4899–4919.

Tsuchi, R. (1997). Marine climatic responses to neogene tectonics of the pacific ocean seaways. *Tectonophysics*, 281(1-2):113–124.

Wallace, J. M., Rasmusson, E. M., Mitchell, T. P., Kousky, V. E., Sarachik, E. S., and von Storch, H. (1998). On the structure and evolution of enso-related climate variability in the tropical pacific: Lessons from toga. *J. Geophys. Res.*, 103(C7):14241–14259.

Wara, M., Ravelo, A., and Delaney, M. (2005). Permanent el niño-like conditions during the pliocene warm period. *Science*, 309(5735):758–761.

Weltje, G. (1997). End-member modeling of compositional data: Numerical-statistical algorithms for solving the explicit mixing problem. *Mathematical Geology*, 29(4):503.

Weltje, G. J. and Prins, M. A. (2003). Muddled or mixed? inferring palaeoclimate from size distributions of deep-sea clastics. *Sedimentary Geology*, 162(1-2):39.

Weltje, G. J. and Prins, M. A. (2007). Genetically meaningful decomposition of grain-size distributions. *Sedimentary Geology*, 202(3):409.

Weltje, G. J. and Tjallingii, R. (2008). Calibration of xrf core scanners for quantitative geochemical logging of sediment cores: Theory and application. *Earth and Planetary Science Letters*, 274(3-4):423–438.

Werner, M., Tegen, I., Harrison, S. P., Kohfeld, K. E., Prentice, I. C., Balkanski, Y., Rodhe, H., and Roelandt, C. (2002). Seasonal and interannual variability of the mineral dust cycle under present and glacial climate conditions. *J. Geophys. Res.*, 107.

Wipf, M. (2006). *Evolution of the Western Cordillera and Coastal Margin of Peru: Evidence from Low-Temperature Thermochronology and Geomorphology*. Phd, ETH.

Wyrtki, K. and Meyers, G. (1976). The trade wind field over the pacific ocean. *Journal of Applied Meteorology*, 15:698 –704.

Zeil, W. (1986). *Südamerika. Geologie der Erde*, volume 1. Enke, Stuttgart.

List of Figures

1 Climate variability of the past 5 Ma 4
2 Atmospheric circulation patterns 8
3 Ocean-atmosphere circulation patterns 9
4 Climatic zones of western South America 12
5 Core and sample locations 15
6 Tectonic backtracks 16
7 Processed samples 18
8 Preparation steps of downcore sample material 20
9 Linear correlation of Fe counts from XRF scans and Fe concentrations 21
10 Test results removing biogenic opal 25
11 Preparation steps of surface sample material 26
12 Working Area 31
13 Wind Field 33
14 Results from grain-size analysis with Atterberg settling method . . . 37
15 Statistics of end-member modeling 39
16 Proportions of end members 40
17 Quartz and feldspars in clay fraction 41
18 Clay-mineral distributions 42
19 K-means cluster analysis of clay-mineral distributions 47
20 Grain-size distributions of bulk sediment samples from the Peru Basin 54
21 Davies-Bouldin Index 54
22 Core locations and wind field 65
23 Terrigenous input at ODP Site 1237 67
24 Comparison of eolian flux records 69
25 S1 Age model of ODP Site 1237 75
26 S2 Alignment of sediment cores ODP1237 and RRV9702A 76
27 S3 Comparison of excess $^{230}Th_0$ 76
28 S4 $CaCO_3$ mass accumulation rates 77
29 $\delta^{18}O$ record 87
30 Accumulation rates of terrigenous elements representative of dust . 89
31 Grain-size end member analysis statistics 90
32 End-member proportions plotted against time 92
33 Variability of trade wind strength during the Plio-Pleistocene transition 94
34 S1 Linear correlation of Fe and Ti 97
35 Ti and Fe accumulation rates of past 5 Ma 138
36 Hysplit back-trajectories 140
37 Changes in wind strength of the past 5 Ma 141

N a m e : ..... Datum .....

Anschrift : .....

E r k l ä r u n g

Hiermit versichere ich, dass ich

1. die Arbeit ohne unerlaubte fremde Hilfe angefertigt habe,

2. keine anderen als die von mir angegebenen Quellen und Hilfsmittel benutzt habe und

3. die den benutzten Werken wörtlich oder inhaltlich entnommenen Stellen als solche kenntlich gemacht habe.

_____, den .....

(Unterschrift)